Seasat Final Report

Volume IV: Attitude Determination

Alfred J. Treder

July 1, 1980

National Aeronautics and
Space Administration

Jet Propulsion Laboratory
California Institute of Technology
Pasadena, California

JPL PUBLICATION 80-38, VOLUME IV

Seasat Final Report

Volume IV: Attitude Determination

Alfred J. Treder

July 1, 1980

National Aeronautics and
Space Administration

Jet Propulsion Laboratory
California Institute of Technology
Pasadena, California

The research described in this publication was carried out by the Jet Propulsion Laboratory, California Institute of Technology, under NASA Contract No. NAS7-100.

PREFACE

The Seasat satellite was launched at 01:12:44 GMT on 27 June 1978 from the Western Test Range at Vandenberg Air Force Base, Lompoc, California. The spacecraft was injected into Earth orbit to demonstrate techniques for global monitoring of the dynamics of the air-sea interface and to explore operational applications. To achieve these objectives, a payload of sensors emphasizing all-weather, active and passive microwave capabilities was carried on the satellite. The mission was prematurely terminated on 10 October 1978 after 106 days of operation by a catastrophic failure in the satellite power subsystem.

Major mission accomplishments were:

(1) Demonstration of the orbital techniques required to support the mission and sensor operations.

(2) Demonstration of the simultaneous operation of all sensors for periods of time significant to global monitoring.

(3) The collection of an important data set for sensor evaluation and scientific use.

The early mission termination precluded:

(1) Demonstration of the planned operational features of the end-to-end data system.

(2) Collection of a global data set to meet overall geodetic and seasonal objectives and plans.

This report, in four volumes, includes results of the sensor evaluations and some preliminary scientific results from the initial experiment team activities. Scientific and applications studies will continue through FY 80, and will be included in the final version of this report.

ABSTRACT

On 7 July 1978 all sensors had been turned on, and Seasat began its successful mission. The attitude record from that date to the end of the mission has been archived on magnetic tape. In addition, a plot has been made of the available attitude data from each of the 1360 orbital revolutions, one plot per revolution, provided as a supplement to this report.

Attitude behavior tended to be quite repetitive, revolution to revolution and day to day, for many days at a time. There were four major mission segments in this respect, each of which has been characterized by a single whole-revolution plot in pitch, roll and yaw. Each of these graphs shows the mean function of orbital phase, mean ± standard deviation of attitude variation, and the envelope of extreme values. The overall characteristics of attitude behavior can be inferred from these curves without reference to the individual revolution plots.

The Seasat sun sensors constituted the only source of yaw attitude data. The sensor fields-of-view limited direct yaw measurement to about half of the mission time, though each 6040-s revolution had at least a 900-s period of such measurement. Yaw data gaps caused by those limits were filled by use of a suboptimal interpolation algorithm.

Of the four sun sensor heads, three observed the sun during the abbreviated mission and two of those showed misalignments on the order of 1/4 deg. Comparative analysis of data from one of the two misaligned heads produced an alignment calibration of accuracy sufficient to correct all the data from this head. The other misaligned head affected yaw accuracy during part of each revolution in the last nine days of the mission.

The 3σ accuracy of attitude determination (AD) was about 0.25 deg in pitch, 0.16 deg in roll, and between 0.05 and 0.31 deg in yaw. Pitch and roll AD accuracy varied 25 to 50 percent with latitude, due to "cold cloud" error effects largely confined to lower latitudes. Yaw AD accuracy varied with sun position in the sensor field-of-view, cross-coupling of pitch and roll AD error into yaw, and alignment accuracy of the sensor head. Accuracy of yaw data gap interpolation was 0.6 to 2.0 deg (3σ) in the middle part of the mission, when the right Scanwheel experienced periodic sun interference, and the accuracy was 0.95 deg (3σ) in the latter, quiescent part of the mission.

CONTENTS

Figures

Tables

SECTION I

INTRODUCTION

This volume documents the actual implementation of the Seasat Attitude Determination (AD) system and the contents of the attitude data files generated by that system. Also included are the deviations from plan caused by the anomalous sun interference with horizon sensors, inflight calibration of sun sensor head 2 alignment and horizon sensor biases, estimation of yaw interpolation parameters, sun and horizon sensor error sources, and yaw interpolation accuracy. Examples are given of flight attitude data from all modes of the Orbital Attitude Control System (OACS), of the ground processing effects on attitude data, and of "cold cloud" effects on pitch and roll data. Although not formally published, a supplemental set of plots, one for each orbital revolution, has been assembled for all definitive attitude data from 7 July 1978 (day 188) through the end of the mission on 10 October 1978 (day 283).*

The Seasat attitude control subsystem controlled the satellite actively in pitch and roll using error signals referenced to the horizon (see Section II of Volume II). Yaw was maintained in a stable condition by pitch momentum bias that cross-coupled yaw momentum into roll momentum as the satellite moved around the orbit.

Knowledge of satellite attitude was required to a greater accuracy than control to properly locate the sensor measurements on the Earth's surface and to provide inputs for SASS data processing. The mission specification required: 0.5 (deg (3σ) for control about each of the spacecraft control axes, and 0.2 deg (3σ) for determination about any axis.

Because of resource limits, the reference source selected for yaw was a set of sun sensors, which provided only partial coverage during the mission. The expectation was that the requirements could be met for all those times at which sun position information was available from these sensors. At other times, yaw attitude would be estimated by interpolation techniques, and the requirements for attitude knowledge would not be met completely.

During the mission, several anomalies were encountered (see Section VII of Volume II) that further affected the attitude control and knowledge accuracy.

Because of these events and the importance of attitude knowledge to the user of the sensor data, a special effort has been made to describe the actual attitude history for the mission and to estimate the associated errors. The results of this work are summarized in the following sections, and attitude histories are being made available as part of the basic data record.

*In custody of Dr. Hiroshi Ohtakay, Guidance and Control Section (343), Jet Propulsion Laboratory, 4800 Oak Grove Drive, Pasadena, CA 91103.

Other activities of this project are documented in separate volumes of this series:

Volume I	Program Summary
Volume II	Flight Systems
Volume III	Ground Systems

Abbreviations and acronyms used in this volume are defined in the appendix.

SECTION II

DESCRIPTION OF AD SYSTEM

The Seasat AD system (Reference 2-1), for purposes of this report, consisted of that satellite hardware and ground processing software which provided satellite orientation information in a geocentric orbital reference frame. The inputs to the system were the sun, Earth horizon, and satellite environment. The output was a set of time-ordered estimates and corresponding uncertainties of the offset angles between the Satellite Alignment Reference Axes (SARA) and the geocentric orbital reference axes. The system hardware consisted of attitude sensors (two infrared horizon scanners and two sets of sun aspect sensors) and their electronics, telemetry system, and science instruments, and the satellite structure on which the hardware was mounted. The ground software consisted of the Definitive Attitude Determination (DAD) software that provided a time history of the attitude of the satellite reference axes in the form of digital computer tape files. LMSC provided the hardware and GSFC designed, built, operated, and maintained the ground software. The DAD tape files were input to the JPL footprint determination software in support of scientific sensor data processing.

A. COORDINATE SYSTEMS

Figure 2-1 (Reference 2-2) shows the on-orbit configuration of the Seasat satellite. Nominal spacecraft axes (X_O, Y_O, and Z_O) are identified in the figure relative to the flight path and Earth (nadir) directions.

1. Satellite Alignment Reference Axes

Based on knowledge of mass properties relative to the Agena geometric axes (through spacecraft drawings), the orientation of the overall spacecraft principal axes (predicted) was known to some accuracy. SARA (Reference 2-3), a convenient optical tool reference frame, was defined within the alignment tool. It was defined by a rotation relative to the transferred spacecraft reference axes that aligned SARA to the predicted orientation of the spacecraft principal axes. The predicted principal axes were expected to lie within 0.2 deg (3σ) of the true spacecraft principal axes. In any case, SARA was the reference frame to which all other reference frames embedded in specific hardware were rotationally aligned. In flight, SARA was actually indeterminate, but it could be recreated with sufficient accuracy by use of the ground-measured alignment transformations. In the case of sun sensor head 2, this was augmented by inflight calibration, which will be discussed in subsequent sections.

2. Orbit Reference Axes (Geocentric, Geodetic)

As characterized in Reference 2-4, these coordinate systems were orbit-dependent. Generally, the X-axis pointed in the direction of flight and was

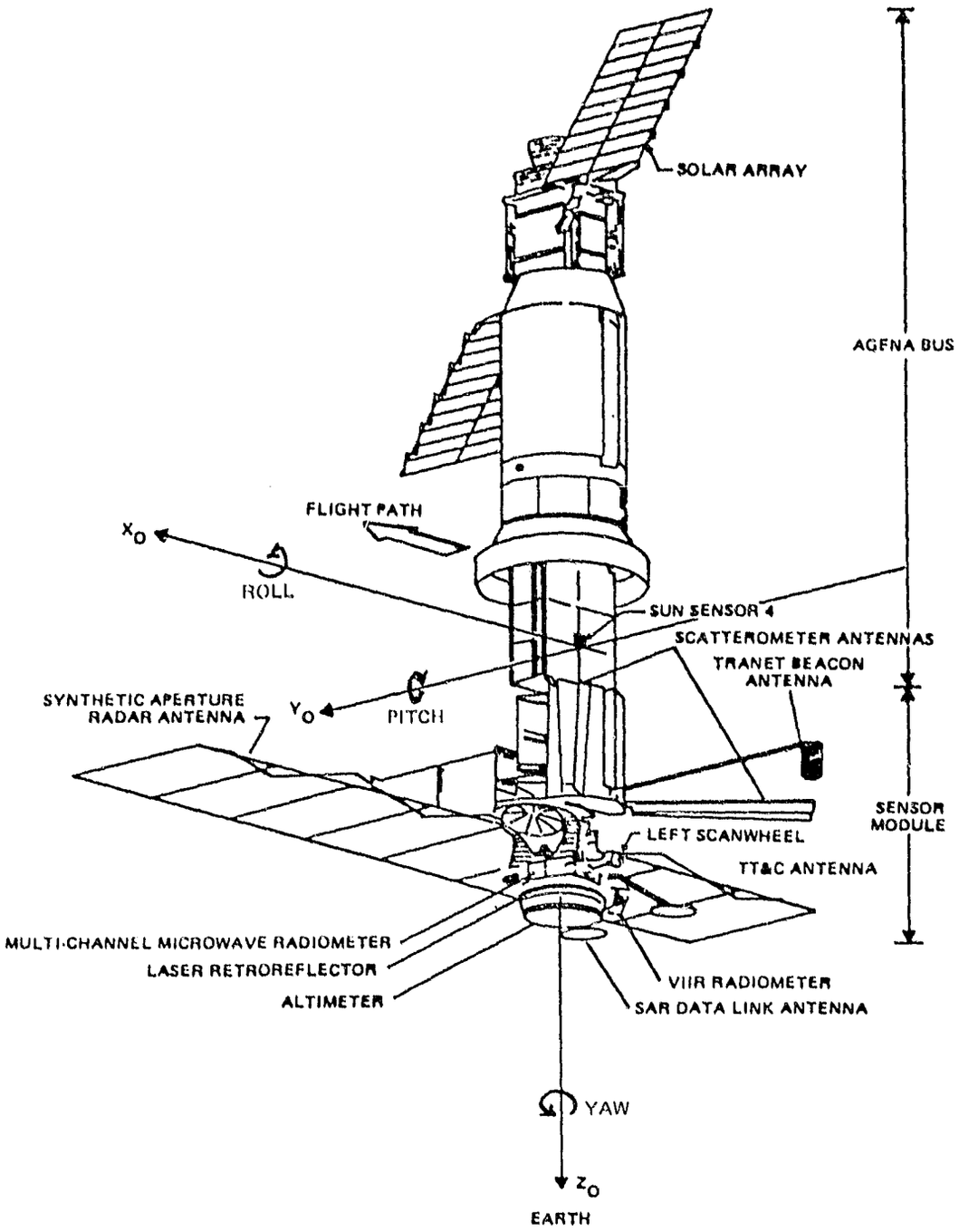

Figure 2-1. On-Orbit Seasat Configuration

contained in the orbit plane, the Y-axis pointed in the direction opposite of the orbit momentum vector, and the Z-axis pointed in the direction of the Earth. For the geocentric orbit reference system, the Z-axis pointed to the center of the Earth (where the Earth rotation axis intersects the equatorial plane), or the Z-axis was the negative of the orbit radius (position) unit vector. With the Y-axis parallel to the negative of the orbit normal, the X-axis was derived from the Y and Z axes, and was approximately in the inertial direction of flight. For the geodetic coordinate reference frame, the Z-axis was pointing to the Earth, but it was normal to the local horizontal plane at the subsatellite point. The oblateness of the Earth caused a position-dependent angular offset between the geodetic and geocentric coordinates.

B. ATTITUDE DETERMINATION HARDWARE AND SOFTWARE

Figures 2-2 and 2-3 (from Reference 2-2) show the locations and orientation of the Scanwheel* horizon sensors and the sun sensors on the Seasat spacecraft. Table 2-1 (from Reference 2-5) shows the actual alignment of this hardware with respect to SARA as measured on the ground before launch. These alignment values were taken into consideration in the ground processing of flight attitude telemetry.

1. Horizon Sensors (Scanwheels)

References 2-1 and 2-2 give detailed descriptions of the design and nominal operation of the Scanwheels. These devices provided the nadir reference for the OACS as well as the prime source of pitch and roll attitude data.

a. Pitch and Roll AD Accuracy Augmentation. If the horizon sensors were able to operate as a pair with no deviation from nominal design parameters, they would provide a geodetic reference to the OACS. Since the ground footprint software for science data processing requires attitude in geocentric coordinates, the least possible processing of pitch and roll attitude data would be the conversion from geodetic to geocentric coordinates. However, pre-launch analyses of horizon sensor error sources (References 2-6 and 2-7) revealed the need to augment pitch and roll AD accuracy with additional ground processing. Accordingly, GSFC built several extra capabilities into their ground AD software, including horizon sensor bias determination (Reference 2-8), and corrections (Reference 2-2) for biases and errors induced by systematic horizon radiance variations, orbital altitude variation, and Earth oblateness.

Table 2-2 shows the results of the Scanwheel bias determinations performed during the mission. The first set of results was obtained from the mission period immediately after reliable OACS operation was established on the right (single) Scanwheel, during which time the prime Control Logic Assembly (CLA)

*Tradename of Ithaco, Inc.

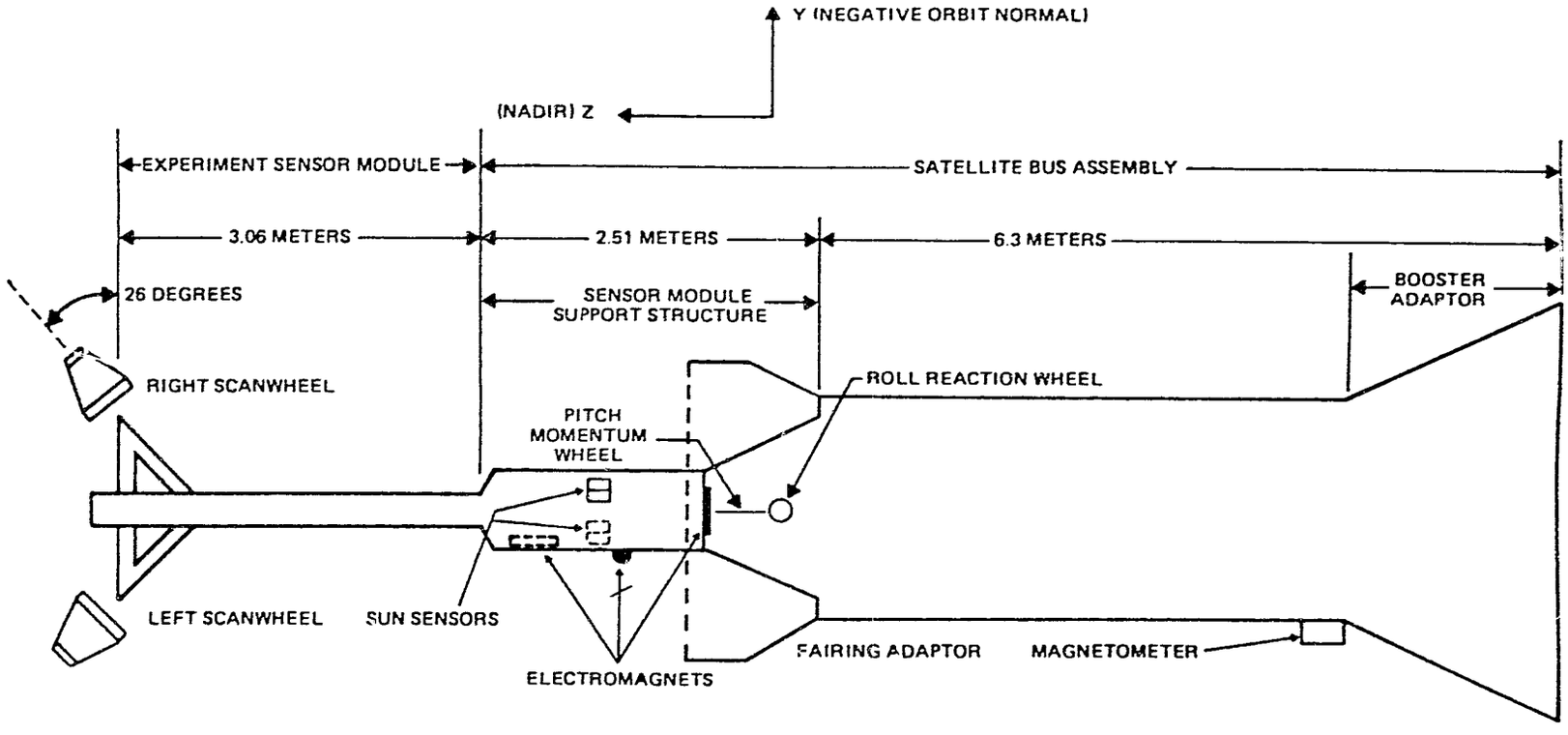

Figure 2-2. Positions of the Attitude Determination and Control Hardware in the Spacecraft Body Viewed with the Velocity Vector Out of the Plane of the Figure

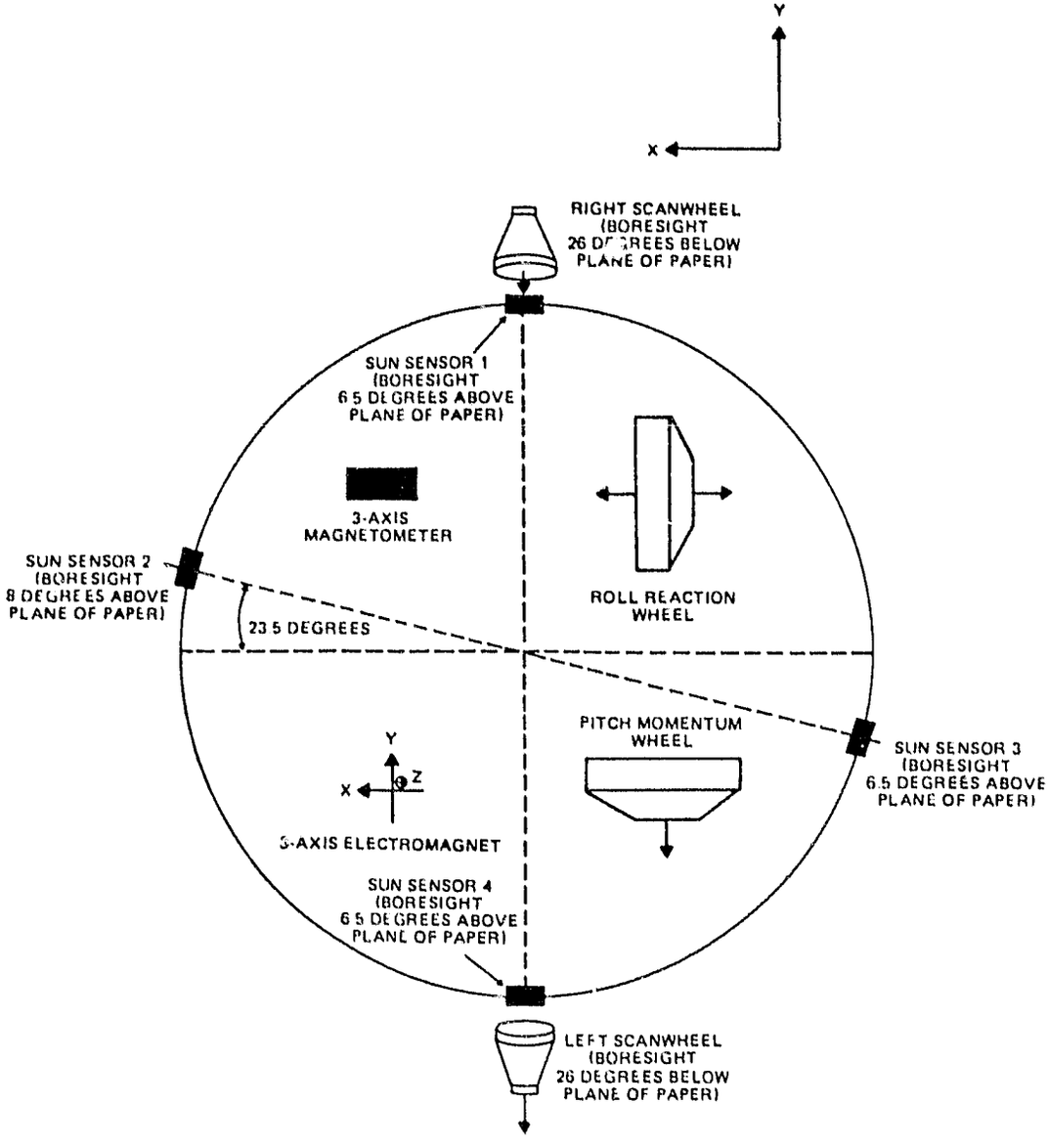

Figure 2-3. Positions of the Attitude Determination and Control Hardware in the Spacecraft Body Viewed Along the Spacecraft Z-Axis Toward the Earth

Table 2-1. AD Hardware Ground Alignment Data

AD Hardware	Euler Angles[a], deg						Measurement Uncertainty, deg (3σ)		
	Nominal			Measured					
	Clock (α)	Cone (β)	Twist (γ)	Clock (α)	Cone (β)	Twist (γ)	Clock (α)	Cone (β)	Twist (γ)
Right Scanwheel	90	64	0	89.9964	64.0092	0	0.0028	0.0025	0.0022
Left Scanwheel	-90	64	0	-90.0008	63.9908	-0.0022	0.0028	0.0025	0.0022
Sun sensor head 1 (S/N 1002)	90.0	96.5	-90.0	90.0158	96.4978	-89.9956	0.0025	0.0031	0.0033
Sun sensor head 2 (S/N 1003)	23.5	98.0	-90.0	23.5089[b]	98.0172[b]	-90.0125[b]	0.0025	0.0031	0.0033
Sun sensor head 3 (S/N 1001)	203.5	96.5	-90.0	203.4708	96.5153	-89.9745	0.0025	0.0031	0.0033
Sun sensor head 4 (S/N 1004)	270.0	96.5	-90.0	270.0036	96.4850	-89.9953	0.0025	0.0031	0.0033

[a]Angle definitions:

Clock (α) is a rotation about the Z-axis.
Cone (β) is a rotation about the rotated (due to α) Y-axis.
Twist (γ) is a rotation about the rotated (due to α and β) Z-axis.
The rotations are + or - based on the right-hand-thumb rule where the thumb is in the direction of the vector and + is a rotation in the direction of the fingers.
The rotations are from the nominal X,Y,Z spacecraft coordinate frame (α,β,γ sequence).

[b]Inflight calibration showed significant deviations from these values.

Table 2-2. Scanwheel Bias Estimates

Mission Period From Which Results Were Obtained	Mission Period to Which Results Were Applied[a]	CLA Power Supply Selected	Fine Pitch Bias		Fine Roll Bias	
			Estimate, deg	Uncert, deg (3σ)	Estimate, deg	Uncert, deg (3σ)
Days 186-209	Days 188-211	1	0.12	0.06	0.01	0.02
Days 229-233	Days 221-283	2	0.11	0.04	0.10	0.01

[a]For bias values used between days 220 and 226, see Section III-C.

power supply 1 was operating continuously. During days 220 and 221, sun interference with the Scanwheels resumed, and efforts to discover a favorable operating mode resulted in a permanent switch to CLA power supply 2. Redetermination of biases subsequent to that switch showed an unexpectedly significant difference in roll, apparently caused by the switch in power supplies. Definitive attitude processing corrected pitch and roll telemetry data for biases as a function of the CLA power supply, as shown in Table 2-2. Both sets of biases were obtained from sun sensor head 1 telemetry data.

Figure 2-4 shows typical factors that were added to pitch and roll telemetry data to correct for the effects of Earth oblateness and systematic horizon radiance variations in both axes, and for the effects of altitude variation in roll. This latter effect is due to orbital eccentricity and to differences between the mean orbital altitude and the altitude implied by the bias voltage, which in the OACS replaced the left Scanwheel attitude signal. In the nominal dual-Scanwheel mode, such variations would have had no effect to first order, since the same effect occurred on both sensors and they would have been automatically nulled by the differencing performed in onboard roll signal processing. The single sensor mode in which Seasat was operated made roll subject to significant altitude effects, as can be seen from the typical function (taken from a single revolution on 22 August 1978) shown in Figure 2-4. Actual correction for this effect was computed from the difference between 7168 km (3864 nm) and the actual satellite orbital radius; the actual radius was obtained from the definitive orbital ephemeris determined by GSFC for each revolution. Therefore, the correction applied to roll for this effect varied in phase and amplitude from that shown in Figure 2-4. Oblateness effects were also computed from definitive orbit data; these effects depended on the latitude of the subsatellite point, which is essentially normalized in Figure 2-4, so the actual oblateness correction varied only slightly from that shown.

Figure 2-5 gives examples, for 3 months, of the corrections added to pitch and roll telemetry data for AD errors induced by variations in horizon radiance. These corrections are specifically for right (single) Scanwheel operation, and are significantly different in roll than would be necessary (and were planned) for nominal dual-Scanwheel operation. The analyses reported in Reference 2-2 were reworked by GSFC immediately after the Seasat launch, when it became apparent that the nominal mode could not be used. This report, and the GSFC mission report, are the first documentations of the results of those reworked analyses. All definitive attitude files released in final form by GSFC were corrected with factors appropriate for single Scanwheel operation.

b. Example of Pitch and Roll Flight Data. Figure 2-6 shows, as an example, pitch and roll data from a single revolution (172) from day 190 (9 July 1978), both with and without corrections. Both plots were made from data at 5-s intervals, but a 5-s running average filter was used on the uncorrected graph, and a similar 120-s filter on the fully corrected plot. The latter mode was used for all definitive attitude files from day 188 through the end of the mission.

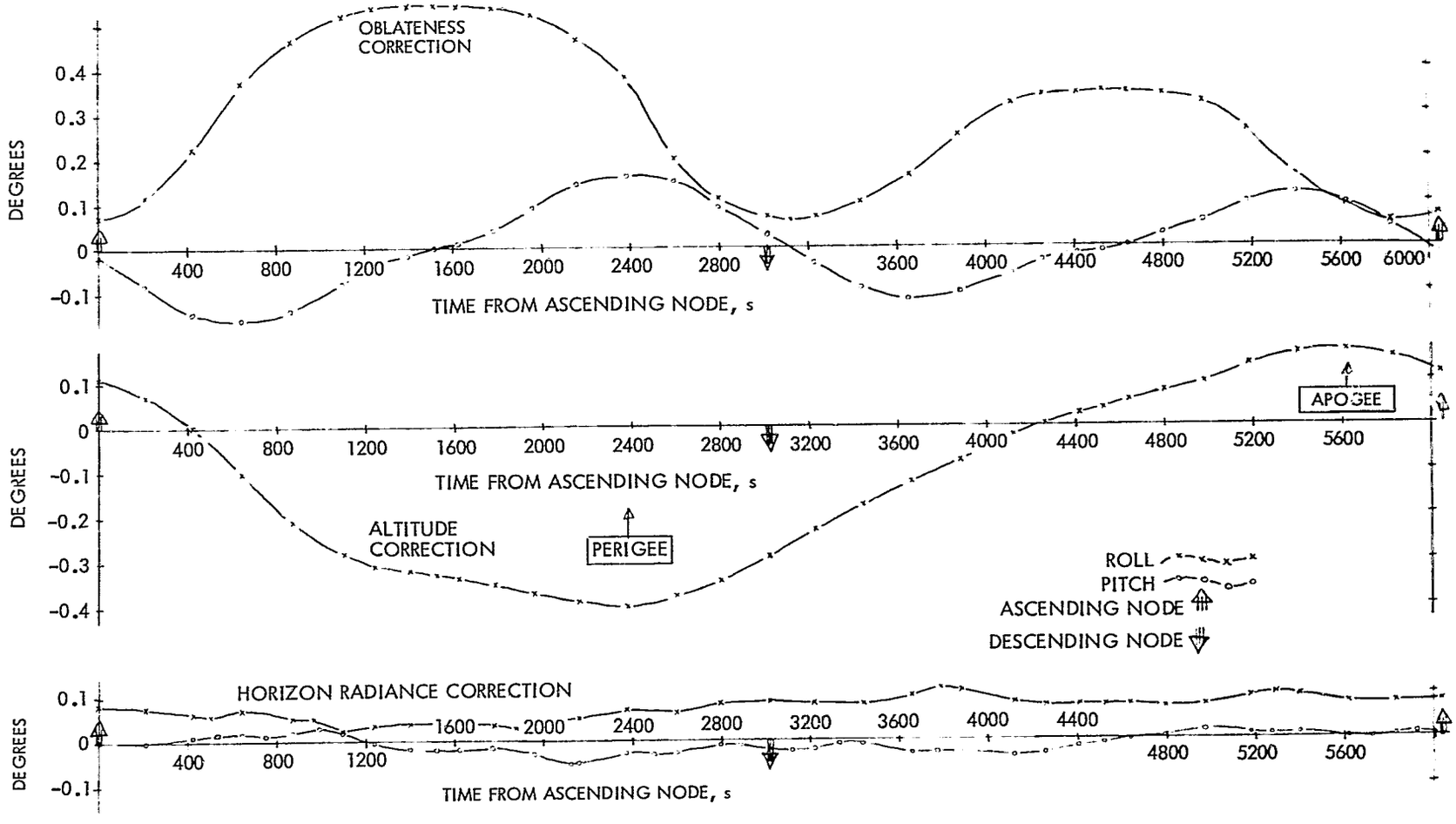

Figure 2-4. Telemetry Data Correction Factors for Pitch and Roll

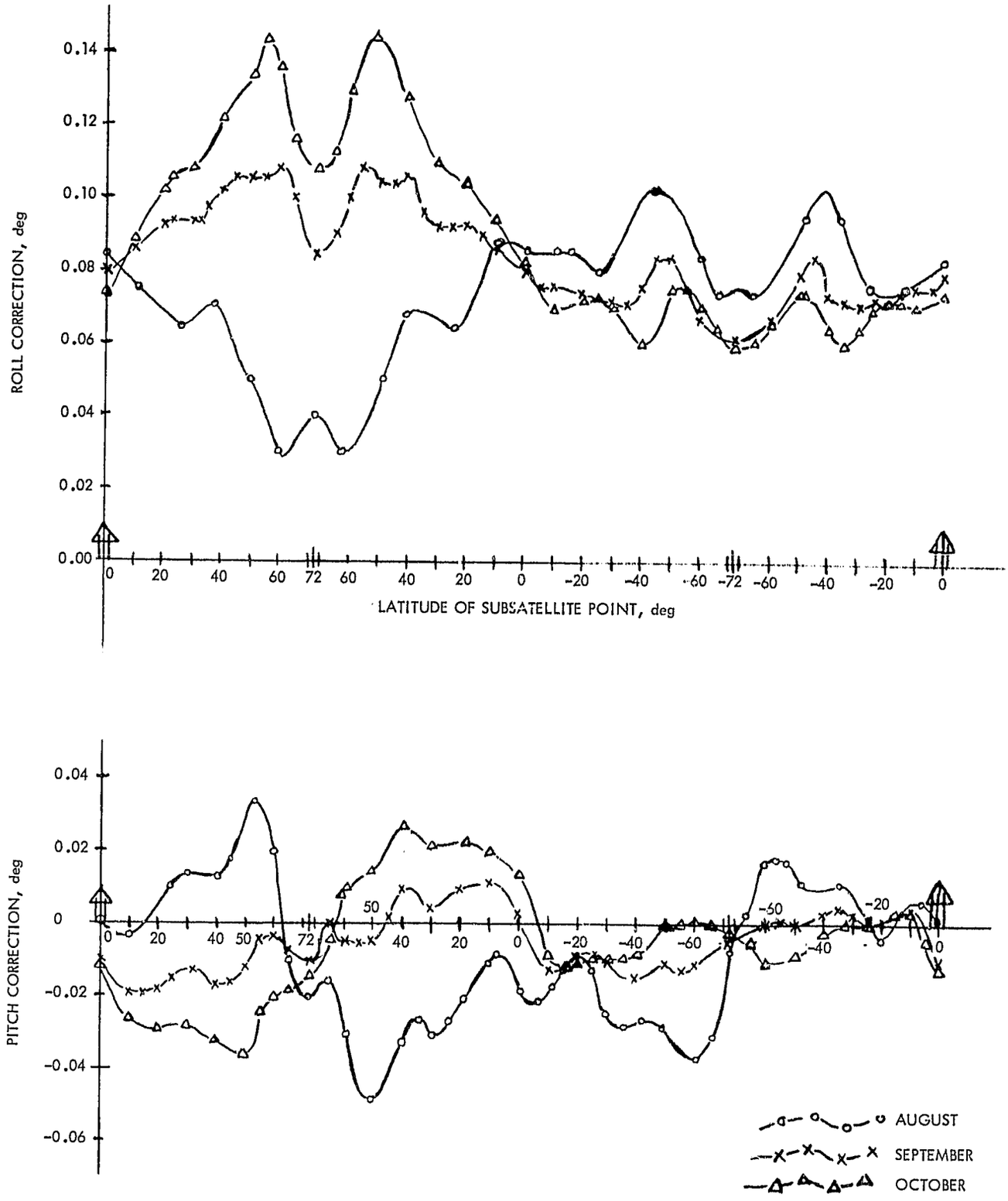

Figure 2-5. Horizon Radiance Corrections

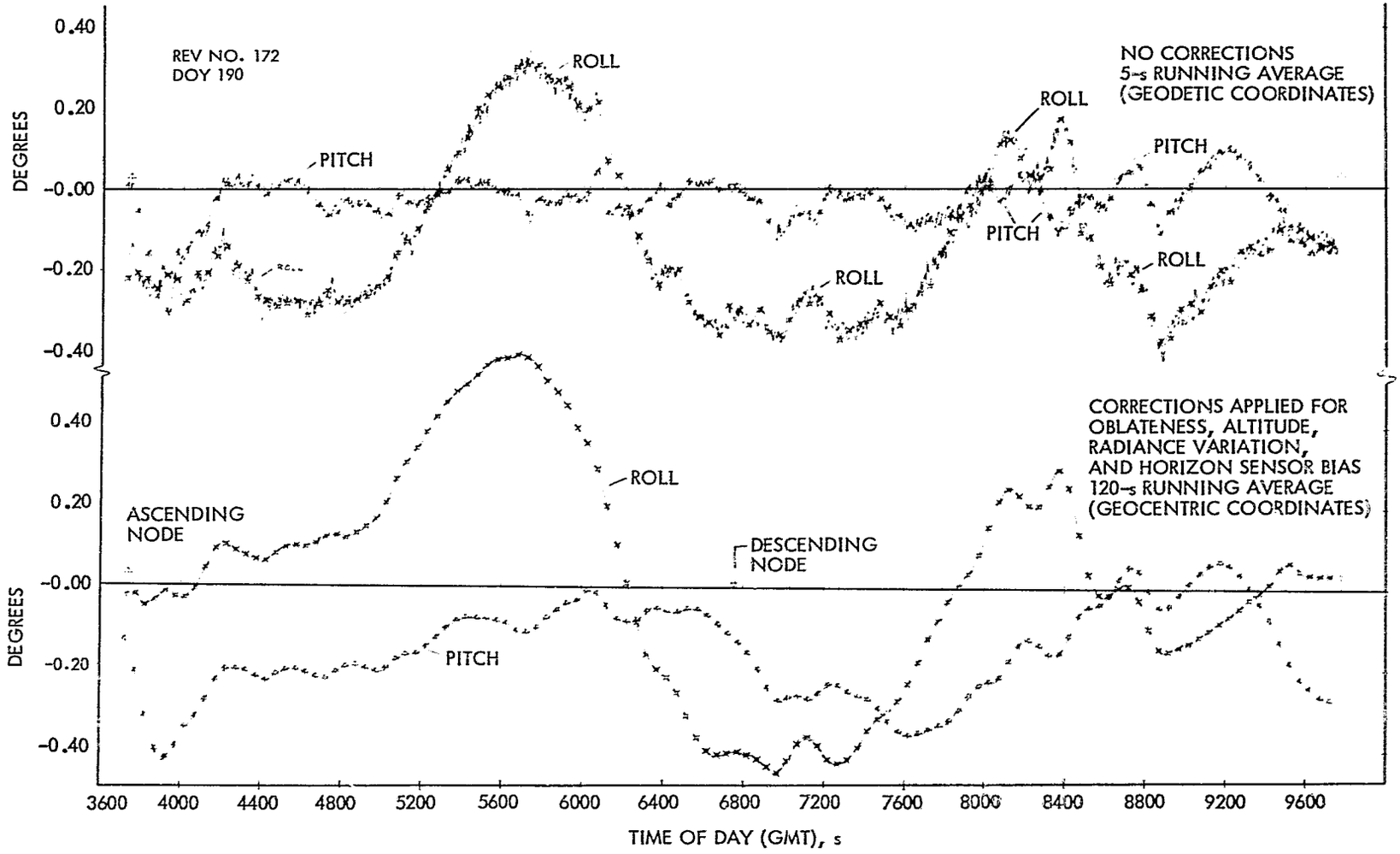

Figure 2-6. Corrected and Uncorrected Examples of Pitch and Roll Flight Data

The effects of pitch bias and oblateness corrections are easily seen from comparisons of Figures 2-4 and 2-6; this comparison for roll is not as obvious since the correction for altitude in Figure 2-4 is not the correct phase for rev 172, but the oblateness effect is fairly clear. "Cold cloud" effects are discussed in detail in Reference 2-9 but, as an example, note the positive 0.08-deg triangular function that occurs simultaneously in both axes at about 6100 s of day; this is the effect of a small cold feature observed by the threshold-setting portion of the trailing edge field of view (FOV) of the right Scanwheel. The 120-s running average has reduced the resulting attitude determination error from 0.08 deg to 0.03 deg, a reduction of about 60 percent. Shorter duration features would be filtered out more heavily, while longer duration features would have only their high-frequency components smoothed out. The effects on AD accuracy of the running average filter are discussed later.

2. Sun Sensors.

The Adcole sun sensor system consisted of two sets, each set containing two 2-axis sun sensor heads (Figure 2-7) and an electronics package to condition the sensor signals for digital telemetry. The resolution for each sensor axis was 1/256 deg, and the absolute accuracy was 0.05 deg (3σ) relative to the alignment mirrors. These sensors were not a part of the OACS, and were used only for yaw attitude determination and horizon sensor bias determination.

a. Sun Sensor Coordinate System. The sun sensor coordinate system (Reference 2-2) was defined so that the positive Z_S-axis was directed along the optical boresight of the sensor. The X_S and Y_S axes defined a plane normal to the Z_S-axis and were oriented as follows. The transformation from the SARA to the sensor axes was defined by an ordered 3-2-3 Euler rotation: clock angle rotation of the sensor about the SARA positive Z-axis, followed by a cone angle rotation about the new positive Y-axis, followed by a twist angle of -90 deg about the new Z-axis as shown in Figure 2-8. The difference between the measured twist angle and -90 deg is defined as the rotation angle. The X_S-axis is collinear with slit B of the two-axis sun sensor, and the Y_S-axis is collinear with slit A of the sun sensor as shown in Figure 2-9. Pre-launch measured alignment angles of these sensor axes with respect to SARA are given in Table 2-1.

b. Sun Sensor Fields-of-View. Figure 2-10 shows the FOV for each of the four sun sensor heads in the system. The coordinate system is spacecraft SARA, in a polar presentation with zenith (180-deg cone) at the center. The locus of nominal sun positions is given at intervals of 4 deg in sun beta angle over the course of the mission. Note that sensor head 4 never saw the sun, because the mission ended prematurely. The locations of the heads were chosen during the design phase to:

(1) Maximize the mission time for which the sun would be visible to the sensors.

(2) Ensure that every orbital revolution could have some sun observability.

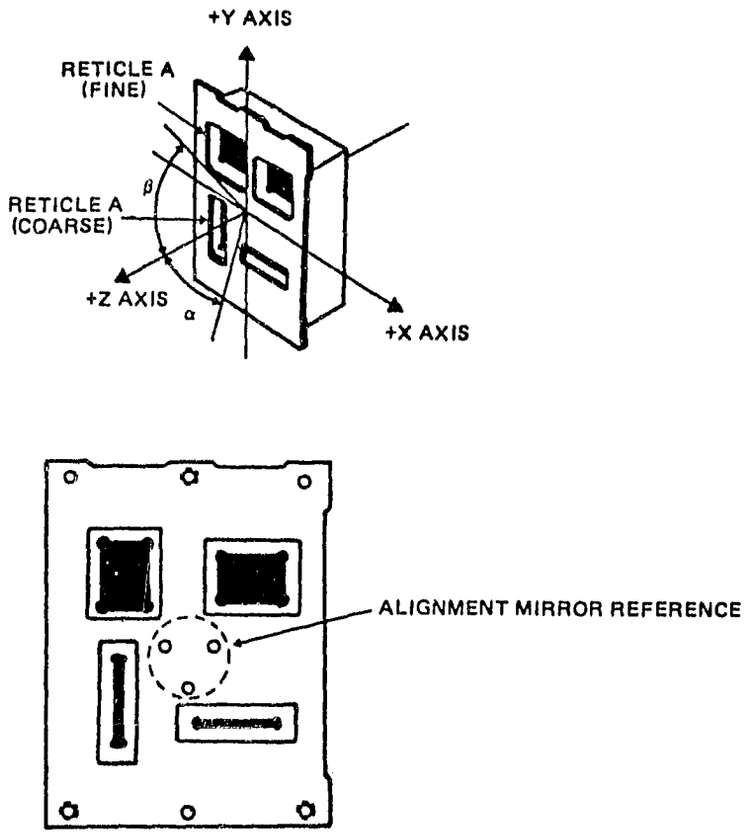

Figure 2-7. Fine Sun Sensor Head (Containing Two Independent One-Axis Sensors)

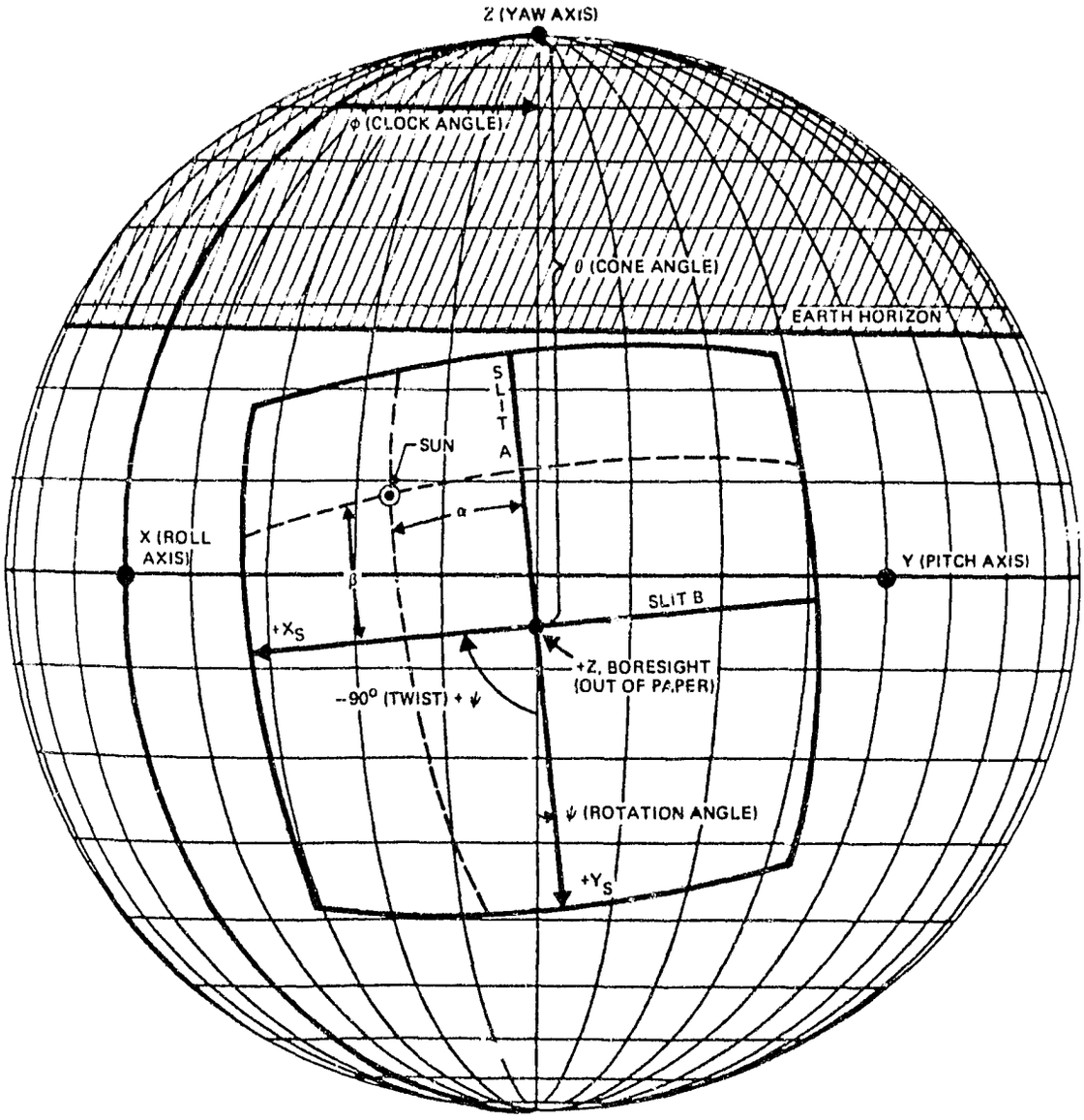

Figure 2-8. General Example of the Orientation of Two-Axis Sun Sensors in the SARA

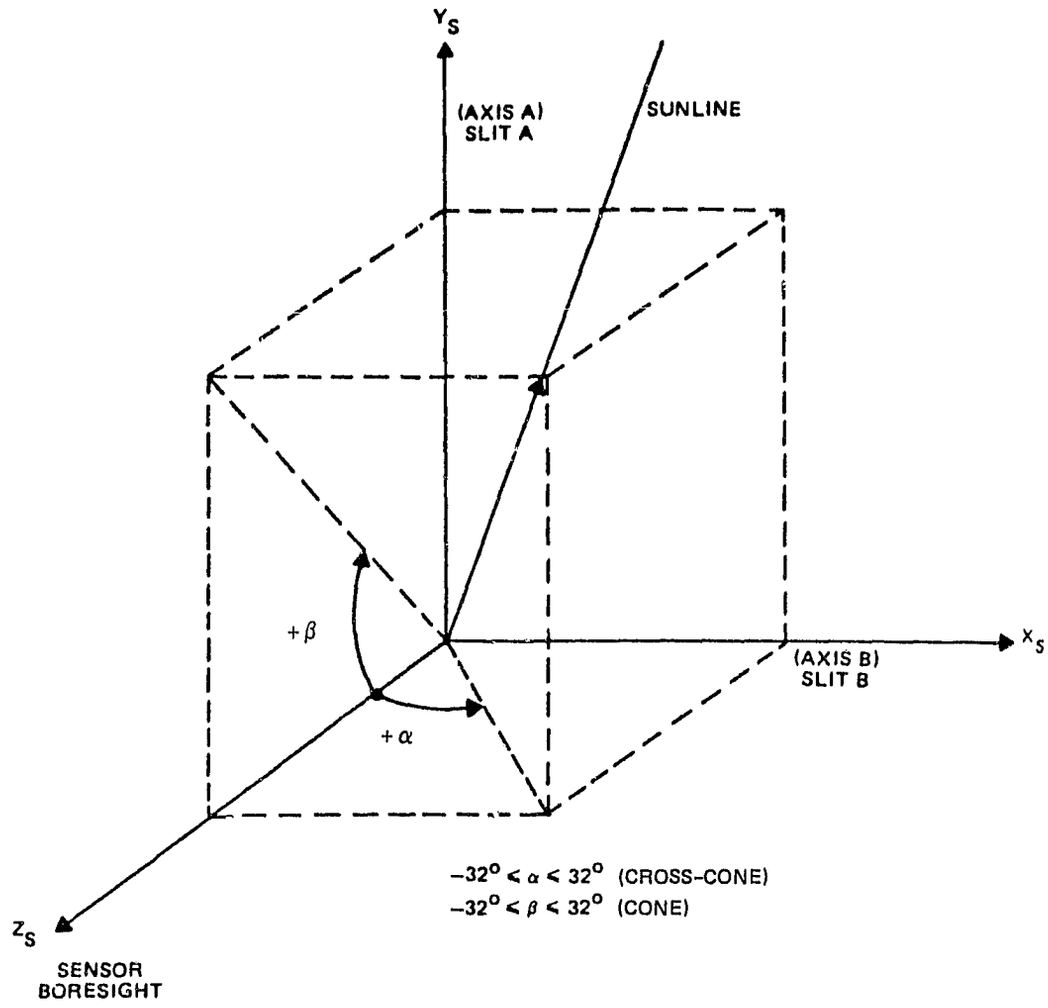

Figure 2-9. Two-Axis Digital Sun Sensor Reference Axes

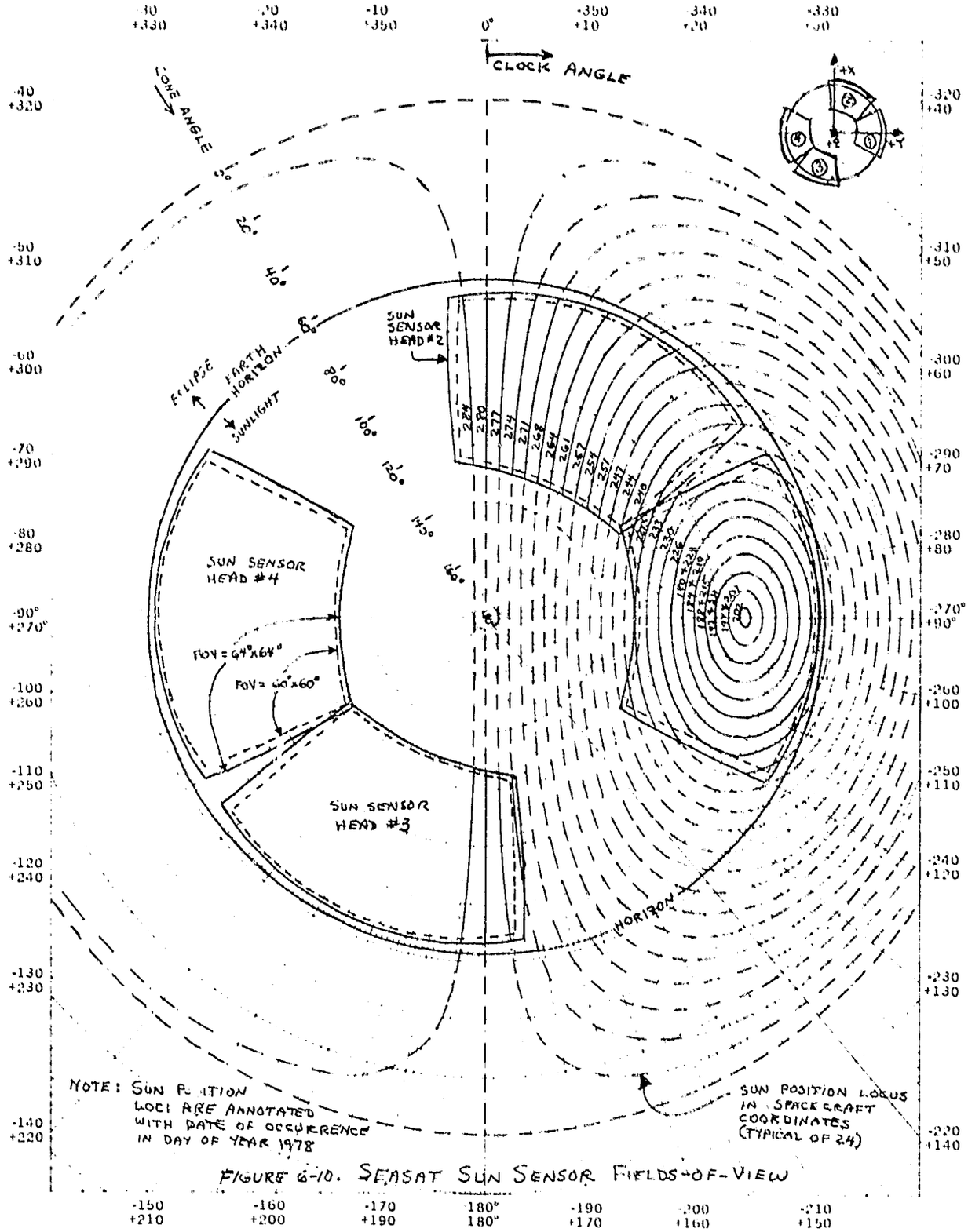

FIGURE 6-10. SEASAT SUN SENSOR FIELDS-OF-VIEW

Figure 2-10. Sun Sensor Fields-of-View

(3) Ensure a small FOV overlap between heads, where practicable, for relative calibration purposes.

(4) Keep all spacecraft structure out of the 64- by 64-deg FOV to avoid any interference or glint problems.

The final selected orientation met all of these criteria in a suboptimal but acceptable manner.

Figure 2-11 presents nominal sun sensor coverage as a function of mission time. Coverage is defined here as the time from ascending node and the subsatellite latitude over which a sun sensor (identified by number) could observe the sun, given the nominal 64- by 64-deg FOV, no significant attitude deviations, and expected sun beta angle at the time. Note the slight overlap of heads 1 and 2 near day 240. The meandering double line curves denote the times when the sun was within 1.5 deg of the right Scanwheel FOV, which will be discussed later.

In flight, the sun sensor FOV had to be cut off at 30 deg from boresight, leaving a 60- by 60-deg FOV. This was done by setting appropriate limit parameters in GSFC ground software. The cause for this action, which significantly reduced the mission time of sun observability, was that the sun sensor system produced telemetry signals for sun positions outside the ±32-deg boundary, and these signals were indistinguishable per se from honest readings for sun positions within the 30- to 32-deg band. That this could happen was apparently understood by LMSC and Adcole early in the design phase, but was not adequately communicated by them to JPL and GSFC. As a result, GSFC software as delivered incorporated no procedure for resolving the data ambiguity. When the problem was discovered, no time or resources could be committed to make the required software changes, so amputation was accepted as an expedient fix. It was still possible to reclaim this data through expert intervention by the software operator, but this resource-intensive method was used only for special occasions, such as for saving the FOV overlap region betweens heads 1 and 2 for calibration purposes. Figure 2-10 shows both the nominal 64- by 64-deg FOV and the 60- by 60-deg FOV realized in flight. (See Section 3.1.1 of Reference 2-9 for a detailed discussion of this problem.)

Actual sun coverage was affected by attitude deviations near the FOV boundary and by loss of telemetry data for any number of reasons. Figure 2-12 shows the actual sun coverage boundaries experienced on the mission, plus many, but not all, data gaps due to other causes and an outline of predicted sun sensor coverage. Figure 2-12 is provided to help identify the size and location of all major yaw attitude data gaps. Figures 2-11 and 2-12 can be compared by noting that the first quarter of each revolution is shown at the top of Figure 2-11 and at the bottom of Figure 2-12. Except for scale, all other factors are the same.

c. Yaw Determination from Sun Sensor Data. The algorithm used by GSFC to determine yaw attitude from sun sensor data is described in Reference 2-2. Digital sun sensor telemetry is converted to cone and cross-cone aspect angles (see Figure 2-9) by applying a polynomial function derived from ground calibrations. These two angles define the actual sun vector in sun sensor coordinates.

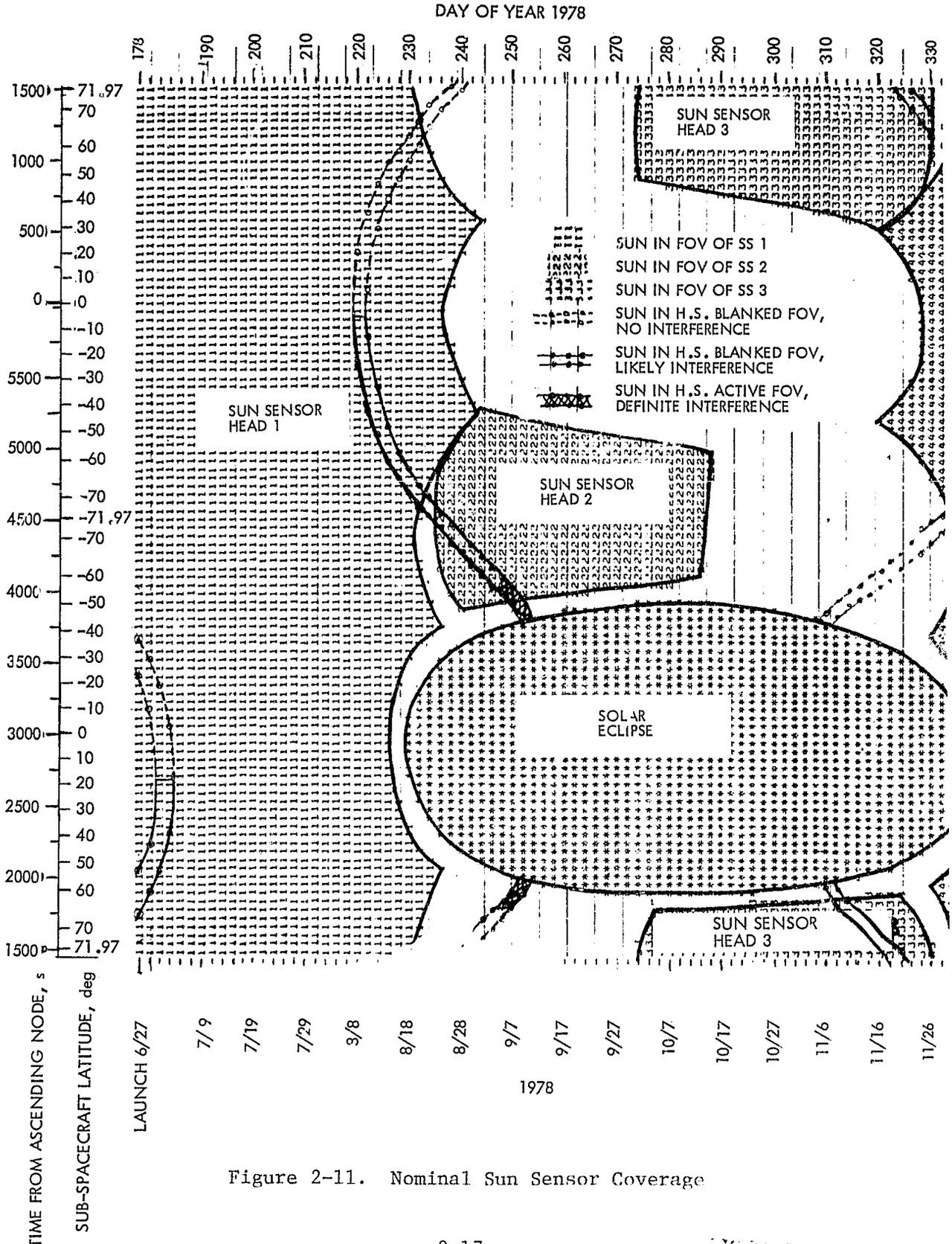

Figure 2-11. Nominal Sun Sensor Coverage

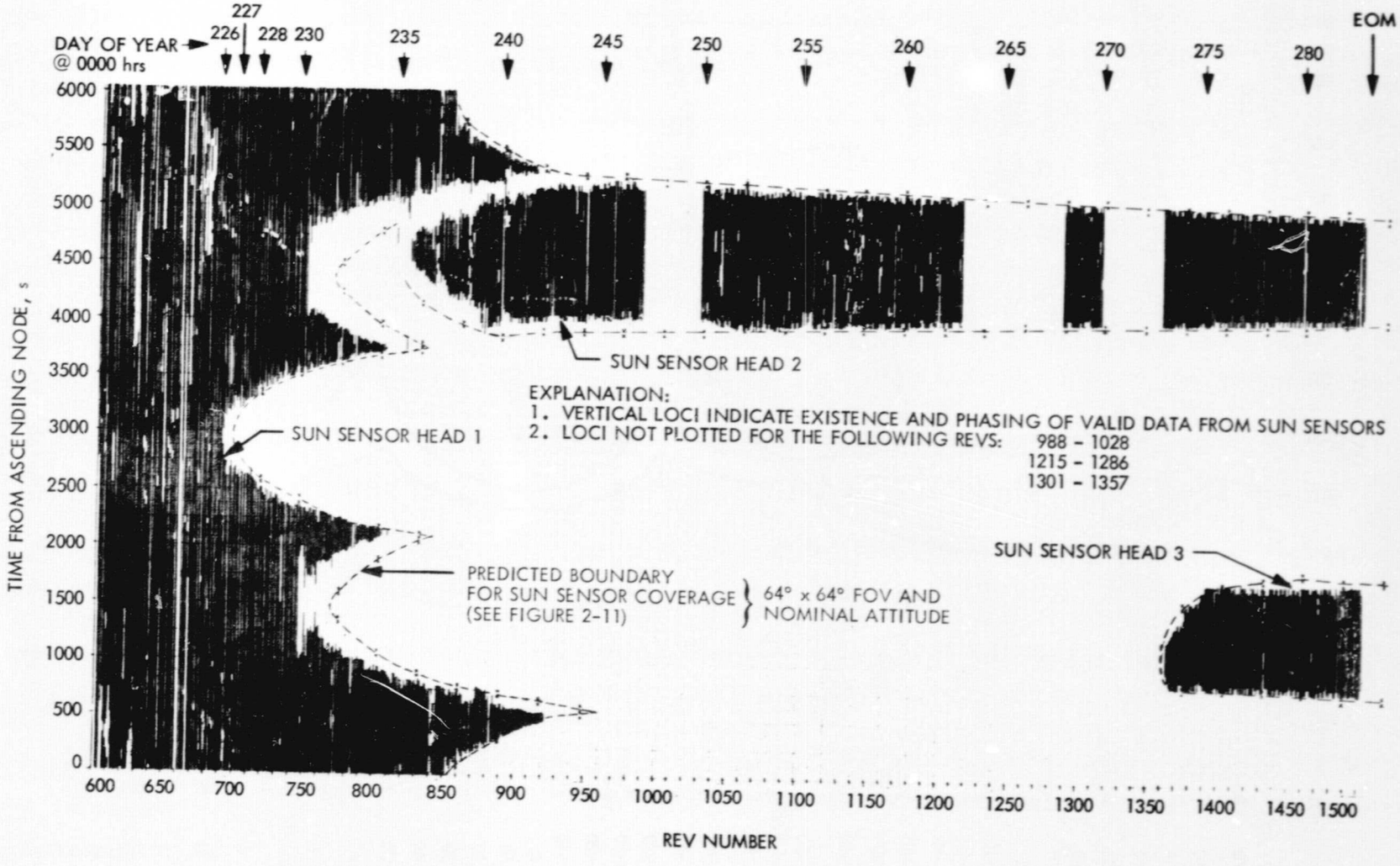

Figure 2-12. Actual Sun Sensor Coverage

The differences between the actual sun vector and the vector expected at that orbital position are assumed to be caused by attitude perturbations. Using pitch and roll data estimated from Scanwheel telemetry permitted a closed-form solution for yaw. The accuracy of yaw determination was, therefore, dependent on pitch and roll determination accuracy, and the position at that time of the sun within the sun sensor FOV.

When no sun sensor could see the sun, yaw could not be determined directly. An indirect method of interpolating these yaw gaps was used if telemetry data (including roll attitude) were available. This method will be described in the following paragraphs.

3. Yaw Data Gap Interpolation

The following information is adapted from Reference 2-10.

a. Summary of Method. Yaw data gap interpolation involves the problem of filling out the record of a real function of time, the measurement of which is desired to be continuous but which is arbitrarily discontinuous in its physical implementation. A typical application is completing the attitude data record of a nadir-pointing spacecraft in low planetary orbit where a sun sensor is chosen to be the attitude reference in one axis. Such a system will have attitude data gaps due to sensor FOV limits and occultations of the sun by the spacecraft and the planet. In the case of Seasat, maximum science return from the mission required complete attitude knowledge at every point in the orbit to an accuracy level 2.5 to 4 times better than the control of attitude. To produce continuous and accurate attitude determination by addition or substitution of star sensors would have been too expensive, as would have been the development and continuous use of an adequate spacecraft simulation on ground computers. Instead, a more limited amount of mission funds was devoted to the support of attitude determination, and those funds were used to extract as much attitude information (and, therefore, scientific return) as could be obtained under the circumstances.

This is a typical design trade-off, leading to a suboptimal but sufficient attitude determination system. The method developed to provide a reasonably good solution to the constrained data gap problem is generally applicable to any system characterizable by a Gauss-Markov process, and it produces a stable, closed-form solution under all conditions.

The general problem can be stated as follows: given the data record D(t) of a system parameter Y where at arbitrary times within the range of this record no direct observations of Y exist, provide sufficiently accurate estimates of Y using all available types of information that pertain to Y and describe the variance of the estimates.

The desired solution in the widest sense would provide estimates with variance less than or equal to the variance σ_D^2 of directly measured data.

The practical solution given here will provide estimates at all request times, the variance of which is maintained as close to σ_D^2 as the (variable) quality of input information will allow. The algorithm can be incorporated into a data processing system with little or no risk, and can be invoked reliably and automatically on a regular basis at a fixed, reasonable cost in throughput time. The products of the algorithm have predictable bounds of uncertainty. The algorithm was designed generally enough so that even after it was coded and incorporated into the data processing system, its output could be upgraded by making appropriate adjustment of its input parameters. The amount and quality of such algorithm support was dictated by cost constraints and the availability of the appropriate information.

The method uses three classes of information:

(1) Direct indicators of the system parameter Y when they exist, the measurements of which comprise the data record D(t), and the statistical extension of this record into time intervals of no direct measurement (data gaps) using a modification of standard autocorrelation techniques.

(2) An a priori predictor Y_p of the behavior of Y, based on the most accurate available model of system behavior. At the least, Y_p would describe only the design control limits of Y about its nominal value, and at the best would be a complete system model capable of exact prediction.

(3) One or more indirect indicators of Y based on observations of other system parameters. These functions may be used even if their errors are partially correlated.

The algorithm first extrapolates the available direct data D(t) into the data gap from both edges, de-weighting it exponentially as a function of distance from gap edge. The a priori predictor function Y_p is given increased weight as the extrapolation is de-weighted. The variance of this combined estimate is calculated on the basis of the stochastic process (first order Gauss-Markov) assumed for the variation of Y with respect to Y_p, the autocorrelation constant determined from the observed behavior of $(Y-Y_p)$, and all of the applicable measurement, noise, and parameter variability factors estimated a priori, outside the algorithm. The indirect measurement of Y (class 3, above) is treated as an estimate with errors that may be correlated with those of the extrapolation estimate. The correlation is estimated a priori (from previously observed behavior) and then used in combining the estimates in the linear mean-squares sense. The variance of the algorithm result will lie between the variance of the linear mean-squares optimal combination of estimates, as the anticipated minimum, and the variance of the most accurate component of the combination at the local time of the estimate, as the maximum.

b. Interpolation Techniques. Data interpolation is an old problem, and many techniques have been evolved. The following is a list of approaches that could be applied to the arbitrary data gap problem:

(1) Data Smoothing. When the time spanned by the periods of relatively continuous data is an appreciable fraction of the system time constant, and the periods of data outage are short in the same frame of reference, one of the many smoothing techniques can be used. Fourier series approximations and polynomial or spline fits to the data are appropriate techniques under the limiting conditions. As the data gaps get larger than the periods of observations, these techniques must be limited more strongly to their lower order terms, and accuracies drop rather rapidly.

(2) Extrapolation by Autocorrelation. To the extent that system behavior can be modeled via a stochastic Gauss-Markov process, the value of the system parameter at times greater than the last observation (and at times less than the next observation, by symmetry) can be inferred from the parameter's statistical correlation with itself. The true process must be nearly wide-sense stationary in the local time frame for meaningful estimates to be made, but the error caused by relatively small deviations from this condition can be handled in many cases by tracking the changes in autocorrelation and by appropriately scaling the estimation uncertainty. As time from the last observation increases, the information in the estimate decreases exponentially, and, therefore, in a practical sense its value disappears rather quickly.

(3) A Priori Prediction. A function or set of functions of time is used to predict the behavior of Y, based on a characterization of the system design and a prediction of the disturbances. If resources permit, a complete set of system equations is modeled, taking account all system internal characteristics and responsive to all external drivers and disturbances. Such a model is often expensive to construct and maintain, but can usually be made as accurate as desired. Less complete models are capable of less accurate results, given that no observations are noise-free. The minimum such model is an estimator of the mean behavior of the system parameter over all time. Given no observations of the system in operation, the maximum error of this estimator is the control limit of the system in its operational environment.

(4) Indirect Measurement. If there are other system parameters that are observable when the parameter of interest is not, some form of a system model may be used to relate the behavior of these parameters to the behavior of the desired function. A known cross-coupling of axes can be useful, as can a statistical correlation with the Y parameter that is believed strong in the local time frame. As an example, a nadir-pointing orbiter has an inertial cross-coupling between the two spacecraft axes (roll and yaw) in the orbit plane. The accuracy of such an estimate might be much less than that of a direct measurement and yet be useful, since it contains information near the time of interest. It is, therefore, more likely than the previously listed methods to show the results of random disturbances occurring in the data gap.

The hybrid method presented here to handle the arbitrary data gap problem includes aspects of all of the above techniques. When data gaps are short relative to the autocorrelation time (τ) of Y, the method becomes basically an exponential process of high accuracy. As gap length approaches and exceeds τ, the a priori function and indirect measurements have stronger effects on the total estimate, and eventually become predominant. In all cases, however, the estimates near the gap edges approach or exceed the accuracy of directly measured data, with uncertainty growing with distance from the last observation to error bounds that remain within system limits even for very large gaps. Unless the chosen system model requires it, no mode switches need be thrown to effect this broad range of performance. At each time point within the gap, the quality of the estimate is a fair approximation of the input information quality at that time.

c. Application to Seasat. The Seasat mission that began in June 1978 used the algorithm described below in its ground support of attitude determination. Seasat was a nadir-pointing Earth-orbiter with momentum bias perpendicular to the orbit plane (pitch). Control with respect to local nadir was obtained with horizon scanners, which were also the primary sources of attitude knowledge in pitch and roll. Rotation about the nadir (yaw) was limited by the stiffness of the momentum bias and the inertial cross-coupling into the controlled roll axis. Roll was, therefore, an indirect measure of yaw under steady-state conditions, although actual conditions made roll a relatively poor yaw indicator. Roll rate was numerically estimated from roll position data, and it was sometimes a relatively good indirect measure of yaw disturbances through the gyroscopic effect of the momentum bias. Direct measurements of yaw were obtained from the sun sensors. The length of the yaw data gap varied from 0 to 80 percent of orbit period in a relatively predictable pattern (Figure 2-12). Full computer simulation of the relatively complex Seasat control system and its environment for AD purposes was ruled out by cost constraints. Observation of yaw during full-data periods of the mission permitted a limited-capability empirical yaw predictor, and evaluation of roll and roll rate as indirect measures of yaw. No assessment of autocorrelation and cross-correlation was attempted.

d. Definitions.

t — Time from ascending node (the point in the orbit where the subsatellite point crosses the planet equator in a northerly direction).

t_1 — Time (in the above sense) at which the flow of directly observed data is interrupted; i.e., initial time for the data gap.

t_2 — Final time (in the above sense) for the data gap.

$Y(t)$ — True yaw behavior as a function of t.

$Y_D(t)$ — Directly observed yaw data, as a time sequence.

$Y_p(t)$ — Function of t which predicts a component of yaw behavior. For Seasat, the following algorithm was used:

$$Y_p(t) = K_o + \sum_{i=1}^{4} K_i \cos(2\pi i t/P_o + \lambda_i)$$

where K_i, λ_i are scaling and phasing constants chosen empirically to minimize σ_c^2, and P_o is the orbital period.

σ_c^2 — Variance of $Y_p(t)$ with respect to $Y(t)$. The value chosen must be consistent with observed yaw behavior, the effects of predicted disturbances not modeled by $Y_p(t)$, and predicted system-imposed limits on $Y(t)$.

σ_D^2 — Variance of observed yaw data with respect to $Y(t)$; i.e., absolute measurement accuracy.

τ_1 — Autocorrelation time constant of pre-gap yaw data.

τ_2 — Autocorrelation time constant of post-gap yaw data.

$R(t)$ — Roll attitude data at time t.

$\dot{R}(t)$ — Roll rate numerically derived from smoothed roll attitude data near t.

$Y_3(t)$ Estimate of yaw at time t based on observations of roll and roll rate, computed through a model of the yaw/roll cross-coupling. The form of this set of effects was assumed for this analysis to be:

$$Y_3(t) = K_{YR}\, R(t + t_R) + K_{YRD}\, \dot{R}\, (t + t_{RD})$$

where K_{YR}, K_{YRD} are scaling constants, and t_R, t_{RD} are phasing constants, chosen empirically to minimize σ_3^2.

σ_3^2 Variance of $Y_3(t)$ with respect to $Y(t)$. It is evaluated as:

$$E\left\{\left[Y_D(t) - Y_3(t)\right]^2\right\}$$

less the measurement noise σ_D^2, where the expectation is taken as ensemble over multiples of orbital periods.

P_{I3M}, τ_c Scaling factor and time constant for assumed model of cross-correlation of errors in Y_3 and in the interpolation estimate Y_I (defined in text below).

To begin the construction of the estimation algorithm, treat the function $Y(t)$ as a stochastic process or sequence. Assert for these purposes that the deviations of observed data $Y_D(t)$ with respect to the a priori deterministic function $Y_p(t)$ are random or of unknown causes. This models $Y(t)$ as the sum of $Y_p(t)$ plus noise:

$$Y = Y_p + Y_r$$

where Y_r is a random variable modeled by a Gauss-Markov process having the following properties:

$$E\left\{Y_r^2\right\} = \sigma_c^2$$

$$E\left\{Y_D\right\} = Y_P$$

$$E\left\{(Y_D - Y_P)^2\right\} = \sigma_c^2 + \sigma_D^2$$

$$E\left\{Y_r(t + \Delta t) \cdot \left[Y_D(t) - Y_P(t)\right]\right\} = \rho(\Delta t) \cdot \sigma_c^2$$

By the Gauss-Markov assumption:

$$\rho(\Delta t) = e^{-|\Delta t|/\tau}$$

The equation for the measurement of $Y_r(t + \Delta t)$ by the observation $Y_D(t)$ is:

$$Y_D(t) - Y_p(t) = \rho(\Delta t) \cdot Y_r(t + \Delta t) + n$$

The expectations given above yield:

$$\sigma_n^2 = \sigma_D^2 + (1-\rho^2)\ \sigma_c^2$$

Then the estimate of $Y(t + \Delta t)$ obtained from $Y_D(t)$ is:

$$\hat{Y}(t + \Delta t) = Y_p(t + \Delta t) + \hat{Y}_r(t + \Delta t)$$

$$= Y_p(t+\Delta t) + \frac{\left[\dfrac{\rho\ [Y_D(t) - Y_p(t)]}{\sigma_D^2 + (1 - \rho^2)\ \sigma_c^2}\right]}{\left[\dfrac{1}{\sigma_c^2} + \dfrac{\rho^2}{\sigma_D^2 + (1 - \rho^2)\ \sigma_c^2}\right]}$$

$$\sigma_{\hat{Y}}^2 = \sigma_{\hat{Y}_r}^2 = \sigma_c^2 \left[\frac{\sigma_D^2 + (1-\rho^2)\ \sigma_C^2}{\sigma_D^2 + \sigma_c^2}\right]$$

where ρ in the above equations is the previously defined $\rho(\Delta t)$.

In the application of this estimation process to the data gap problem, there are two Y_D observations, one at each end of the gap. We can take advantage of this extra information by expansion of the previous expressions.

Let $$\rho_1 = e^{-|t-t_1|/\tau_1}$$

and $$\rho_2 = e^{-|t-t_2|/\tau_2}, \quad t_1 \le t \le t_2 \qquad (1)$$

Then

$$\sigma_I^2(t) = \left[\frac{1}{\sigma_c^2} + \frac{\rho_1^2}{\sigma_D^2 + (1-\rho_1^2)\sigma_c^2} + \frac{\rho_2^2}{\sigma_D^2 + (1-\rho_2^2)\sigma_c^2}\right]^{-1} \tag{2}$$

$$\hat{Y}_I(t) = Y_p(t) + \sigma_I^2(t)\left[\frac{\rho_1(Y_D(t_1) - Y_p(t_1))}{\sigma_D^2 + (1-\rho_1^2)\sigma_c^2} + \frac{\rho_2(Y_D(t_2) - Y_p(t_2))}{\sigma_D^2 + (1-\rho_2^2)\sigma_c^2}\right] \tag{3}$$

where the subscript I is used to indicate interpolation.

In the limit as $(t_2 - t_1)$ becomes much less than τ_1 and τ_2, $\hat{Y}_I(t)$ approaches a straight-line interpolation between $Y_D(t_1)$ and $Y_D(t_2)$. In the middle of data gaps much larger than $(\tau_1 + \tau_2)$, $\hat{Y}_I(t)$ approaches the value of the a priori function $Y_p(t)$, and the variance of $\hat{Y}_I(t)$ relative to $Y(t)$ approaches σ_c^2, which is the variance of $Y_p(t)$ relative to $Y(t)$.

The $\hat{Y}_I(t)$ estimate reflects the information contained in the data at the gap edges and in the a priori function Y_p. The set of indirect measurements of $Y(t)$ expressed by the previously defined function $Y_3(t)$ can be used to enhance the accuracy of $\hat{Y}_I(t)$. The degree of enhancement is inversely proportional to the amount of statistical correlation between Y_3 and Y_I.

A combination of estimators with correlated noise may be formed optimally with respect to their mean squared errors by using a set of multipliers that satisfy the orthogonality criterion. For the set of estimators $\hat{Y}_I$ and Y_3, the optimal combination estimator would require the characterization of the variance of Y_3 and the covariance of $\hat{Y}_I$ with Y_3 as a function of time. The estimator is:

$$\hat{Y}(t) = L_1(t)\ \hat{Y}_I(t) + L_2(t)\ Y_3(t) \tag{4}$$

$$\sigma_{Y_o}^2(t) = L_1^2(t)\ \sigma_I^2(t) + L_2^2(t)\ \sigma_3^2(t) + 2L_1(t)\ L_2(t)\ P_{I3}(t)\ \sigma_I(t)\ \sigma_3(t) \tag{5}$$

where

$$P_{I3}(t) = \frac{E\left\{Y(t) - \hat{Y}_I(t)\right]\left[Y(t) - Y_3(t)\right]\right\}}{\sqrt{E\left\{\left[Y(t) - \hat{Y}_I(t)\right]^2\right\} \cdot E\left\{Y(t) - Y_3(t)\right]^2\right\}}}$$

$$L_1(t) = \frac{\sigma_3^2(t) - P_{I3}(t)\,\sigma_I(t)\,\sigma_3(t)}{\sigma_I^2(t) + \sigma_3^2(t) - 2\,P_{I3}(t)\,\sigma_I(t)\,\sigma_3(t)}$$

$$L_2(t) = \frac{\sigma_I^2(t) - P_{I3}(t)\,\sigma_I(t)\,\sigma_3(t)}{\sigma_I^2(t) + \sigma_3^2(t) - 2\,P_{I3}(t)\,\sigma_I(t)\,\sigma_3(t)}$$

In many practical applications, and in particular for Seasat, a rigorous characterization of P_{I3} as a function of time is not necessary for suboptimal but adequate estimation accuracy. This is particularly true when the variances of the estimator components are widely disparate, in which cases the combination estimate strongly favors the more accurate component regardless of correlation values. For this reason, P_{I3} was set equal to zero for Seasat.

If $Y_3(t)$ has a sufficiently constant variance (σ_3^2) relative to $Y(t)$ over the local time domain of interest, σ_3^2 may be modeled as the ensemble average over that domain. This simplification is an economy in the design of the combination estimator, and was implemented for Seasat. Because of the simplifying assumptions on σ_3^2 and $P_{I3}(t)$, plus the possible modeling error in the $\hat{Y}_I$ estimate, the variance $\sigma_{\hat{Y}}^2$ calculated by equation (5) is expected to be an optimistic estimate of the true estimator variance. The expected upper bound on estimator variance is σ_3^2 or σ_I^2, whichever is smaller at the time of the estimate.

Equations (1) through (5), with the associated definitions of parameters and qualifying statements, constitute the yaw interpolation algorithm for Seasat.

e. Algorithm Performance on Simulated Data. Figure 2-13 shows some typical design simulation results for Seasat steady-state attitude in the roll/yaw plane. Roll, roll rate, and yaw data are displayed. From this data, other similar simulations, and knowledge of Seasat design, the parameters of the yaw estimation algorithm were estimated and are listed in Table 2-3. Because these values were based on analysis of only a limited number of simulations and no flight data, they were only preliminary for Seasat purposes. However, they were appropriate values for demonstrating the operation of the yaw estimation algorithm and its effectiveness on available simulation data.

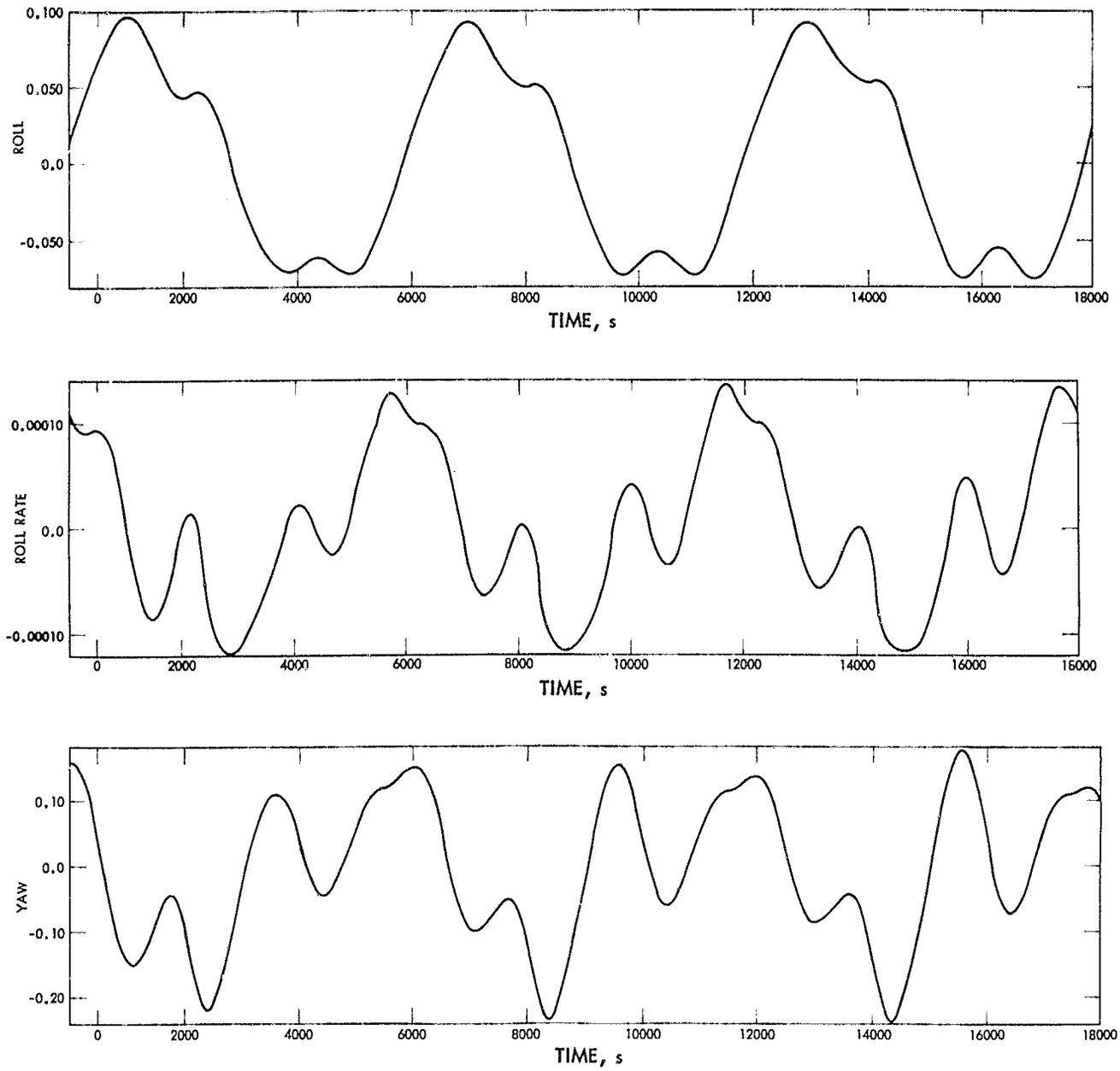

Figure 2-13. Simulated Seasat Attitude Versus Time

Table 2-3. Algorithm Parameter Values

Parameter	Estimated Value	Units
$K_0 = K_2 = K_3 = K_4$	0.0	deg
K_1	0.1	deg
P_0	5979	s
λ_1	+49	deg
$\lambda_2 = \lambda_3 = \lambda_4$	0.0	deg
σ_c	0.184	deg
σ_D	0.05	deg
$t_1 = t_2$	1000	s
t_R	2400	s
t_{RD}	400	s
K_{YR}	$1.6\rho_R$*	deg/deg
K_{YRD}	$1300 \cdot (1-\rho_R)$	deg/(deg/s)
σ_3	0.10	deg
P_{I3M}	0.65	none
t_c	500	s

*For the simulations studied, $\rho_R = 0$ tended to minimize σ_3^2. This was not true for flight data.

A developmental model of the algorithm was programmed in FORTRAN V and used to check out the concept. Figure 2-14 shows the estimator components with notation as defined previously for the algorithm applied to the data of Figure 2-13. An artificial yaw data gap was created between the time points marked t_1 and t_2, and the Y data points made unavailable to the estimator are indicated by a dashed line. Note that no attempt was made to fit slope and acceleration at the boundaries; though unaesthetic and contrary to system dynamics, the deviations caused by these breaks are properly accounted in the variance estimated by the algorithm, if the model assumptions are correct.

Figure 2-14 also shows the optimistic bound of predicted estimator error (solid curve, upper right) at 1σ and the actual deviation of the estimate from the (hidden) data versus time for the example. This is for illustration only, since a proper comparison would involve the ensemble of estimator deviations over a large number of sample data gaps. Such a comparison is made later.

Figure 2-15 illustrates algorithm performance on data gaps ranging from 0.7 to 1.8 autocorrelation time (τ) lengths. Figure 2-16 illustrates performance for data gaps of about 5τ, a situation that faced the estimation algorithm about 50 percent of the time it was used for Seasat (see Figure 2-11).

Overall performance of the major yaw estimator components is given in Figure 2-17 as three times rms error of each component with respect to true yaw, averaged over all data points from simulated gaps of the same length. The data gaps were artificially created in a uniform manner as a grid on the available simulation data, as a quasi-Monti Carlo approach. All yaw behavior as represented by these particular simulations was, therefore, given approximately the same opportunity to affect these performance statistics. Note the relatively strong performance of the interpolator ($3S_{Y_I}$) for shorter data gaps, with error growing to approach that of the *a priori* function ($3S_{yp}$) for larger gaps, as would be expected. Both the *a priori* prediction (Y_p) and the cross-correlation term (Y_3) have approximately constant statistics; these results are forced by the minimization of σ_2^2 and σ_3^2 performed before these sample statistics were taken. Note, finally, that in the 500- to 5000-s gap region the total yaw estimate statistics ($3S_y$) are always better than or equal to the best of its components, and not as good as the variance of the optimal combination estimate as predicted by the algorithm. The interesting divergence from this condition for shorter data gaps is due partly to the small number of samples that went into the statistics, and partly to the inaccuracy of long-scale ensemble averages of σ_3^2 and σ_2^2 with respect to these particular samples.

The final comparison is offered with a note of caution. The rms error of each estimator component was normalized to the rms value of yaw data itself for each sample data gap of the same length, and the average of these ratios is presented in Figure 2-18 as a function of data gap length. These comparisons are measures of the improvement offered by components of the yaw estimation algorithm over the rather simpler method of estimating yaw to be zero everywhere in the gap. It is an interesting comparison, and shows the significant improvements available, but the linearity of this relationship needs to be demonstrated on a wider range of signal amplitudes. More comprehensive estimates of performance level on flight data will be given in subsequent sections.

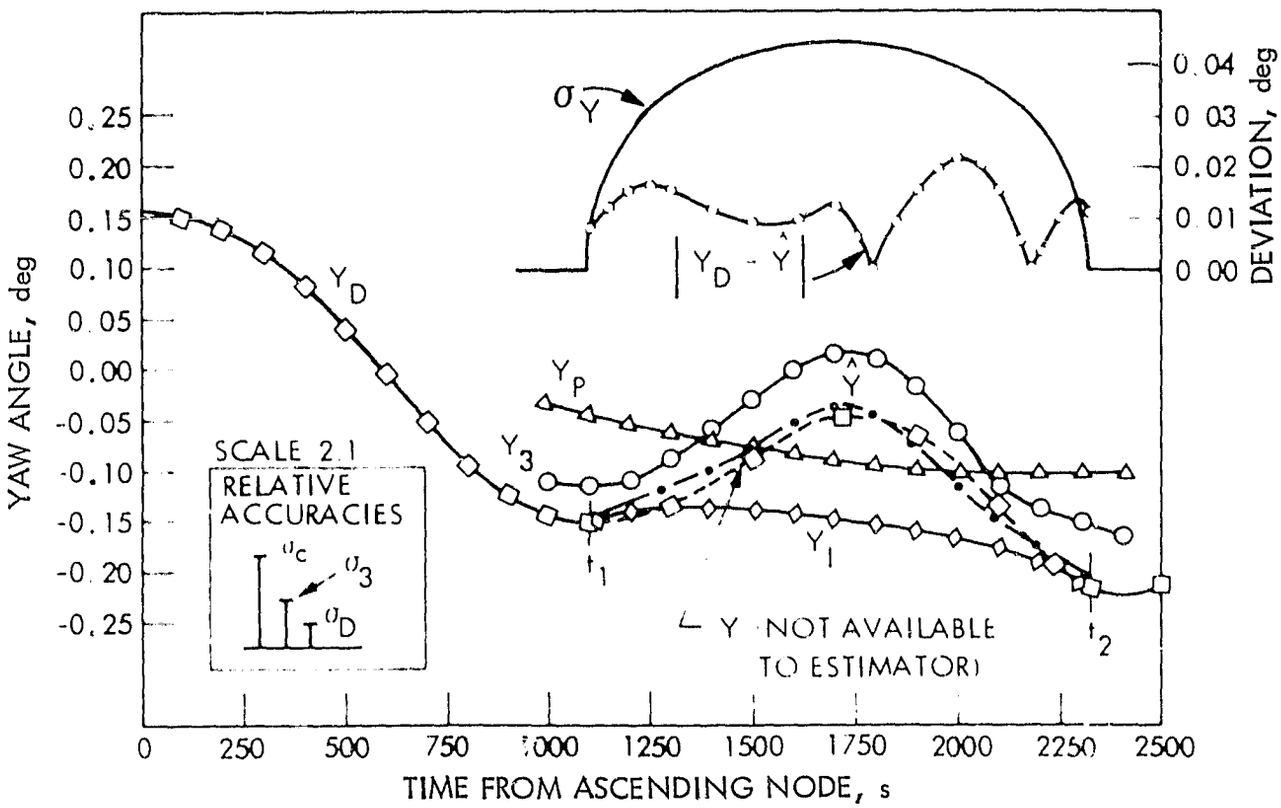

Figure 2-14. Typical Estimator Components

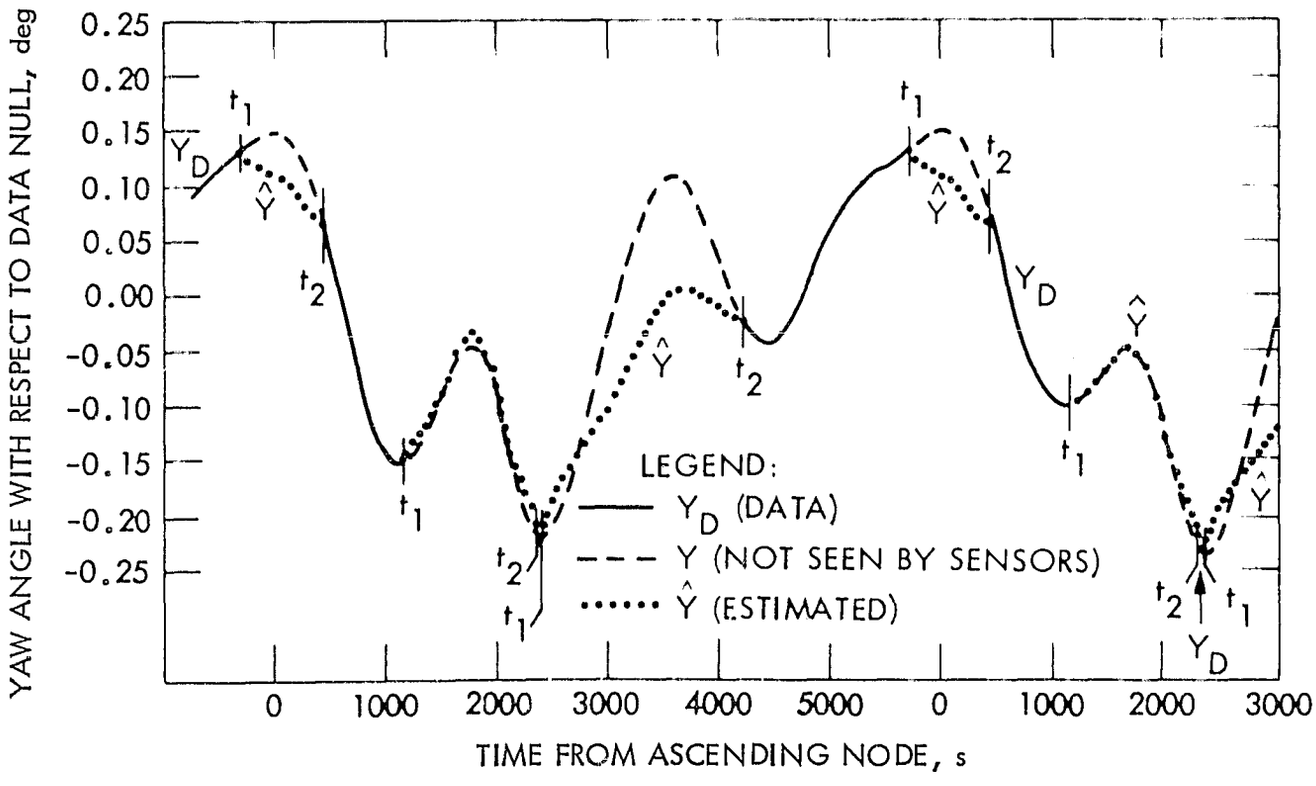

Figure 2-15. Typical Simulated Yaw Data Record, Example 1
(Data Gaps Filled With Estimates)

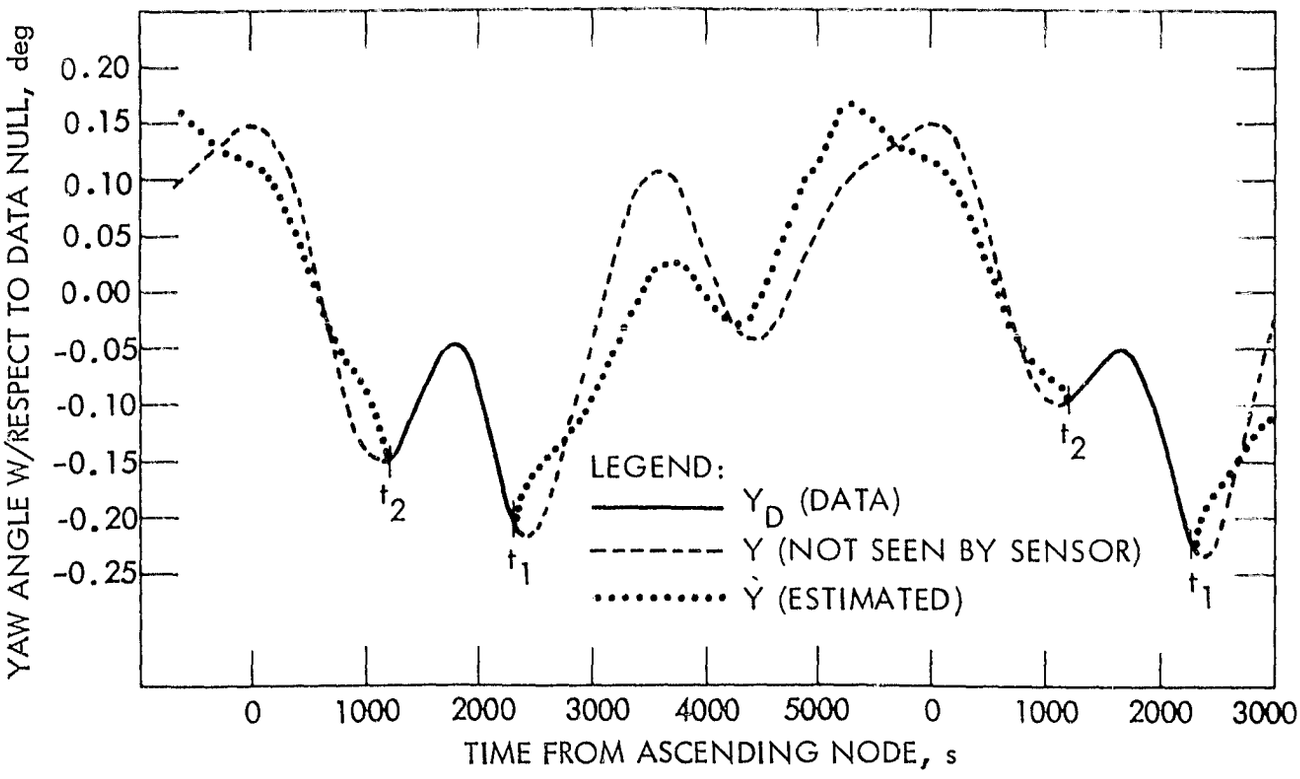

Figure 2-16. Typical Simulated Yaw Data Record, Example 2
(Data Gaps Filled With Estimates)

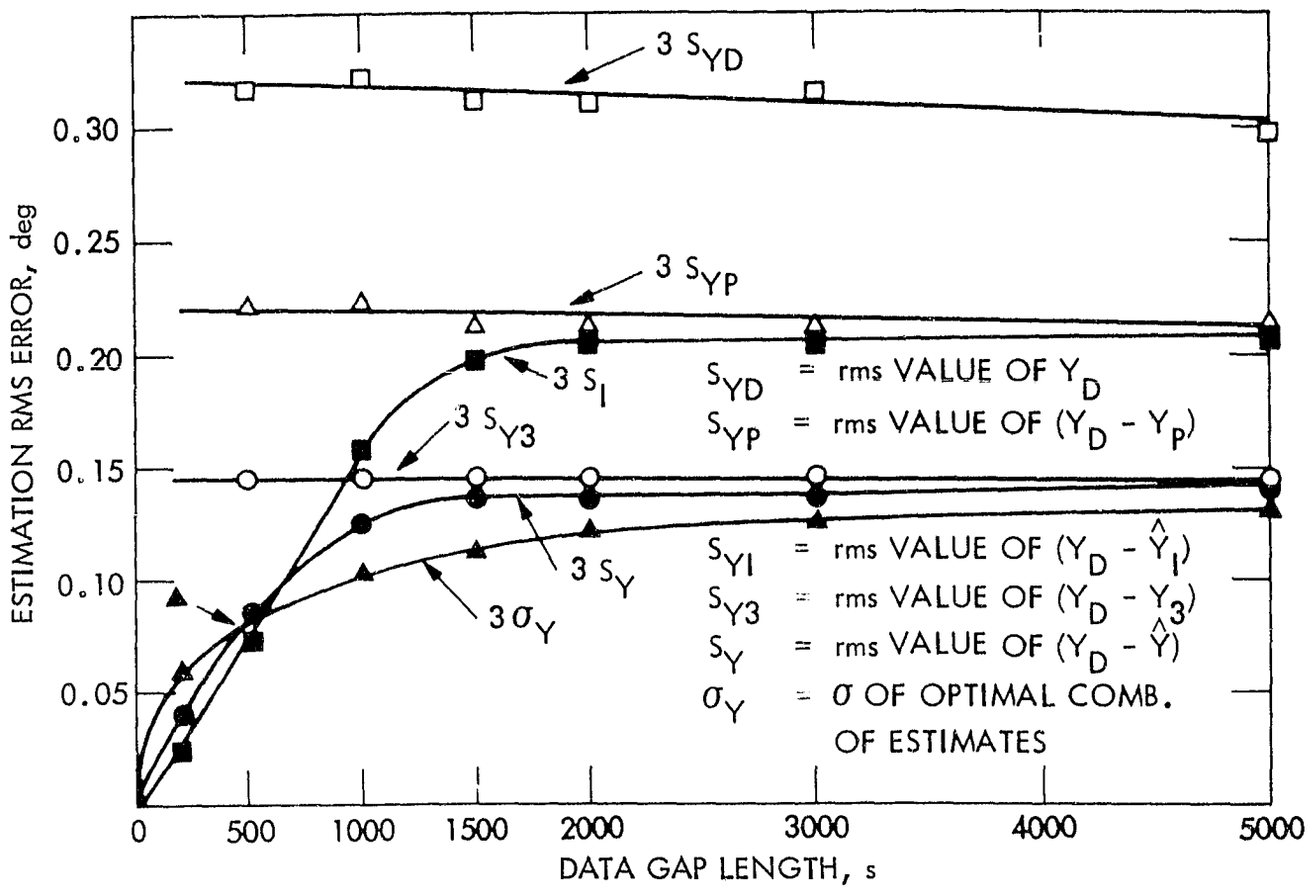

Figure 2-17. Yaw Estimator Performance Accuracy (on Simulated Data)

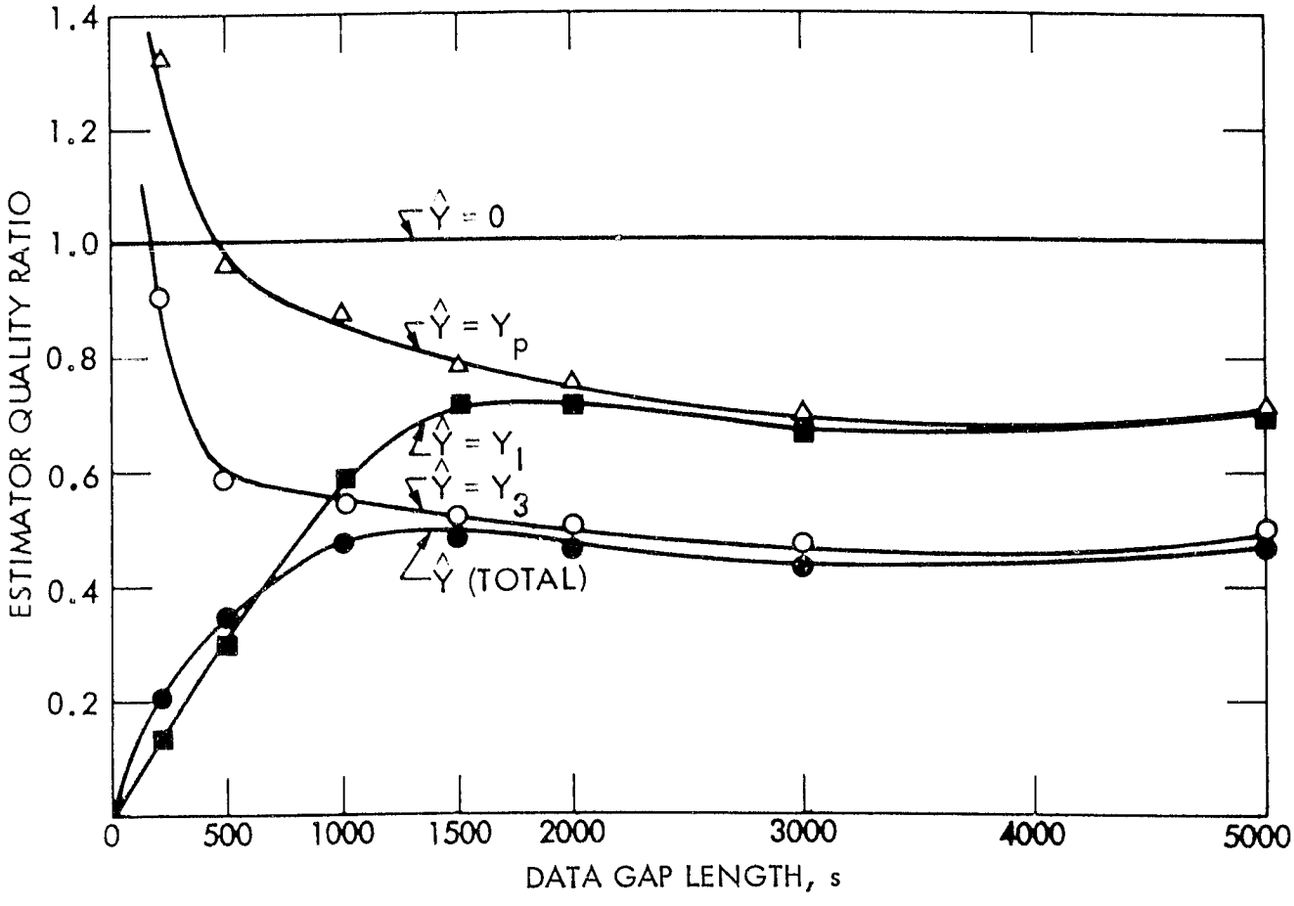

Figure 2-18. Yaw Estimator Quality

C. DEFINITIVE ATTITUDE FILE

1. Introduction

The Definitive Attitude File (DAF) is a record of the best estimates of spacecraft attitude defined on geocentric orbital reference axes as a function of time. The DAF was produced by Code 580 at GSFC and was recorded on an Attitude Orbit Tracking (AOT) tape generated for each day of the mission by the GSFC Information Processing Division (IPD). That tape was delivered by the Instrument Data Processing System (IDPS) at JPL. The DAF software capability was operational before launch on 27 June 1978, and the IPD capability was operational somewhat later. The functional flow of attitude data at GSFC is shown in Figure 2-19.

2. Functional Description

A file of determined satellite attitude spans the same satellite data day as the contents of the Telemetry Master Data File (TMDF). The file begins at 00:00:00:000 and ends at 24:00:00:000 GMT of the data day, according to requirements. Actual files deviate somewhat from this ideal, with the deviations always in the sense of less data.

Each data point of determined satellite attitude is expressed as a time (milliseconds of day), and the set of Euler angle rotations which at that time will convert to the SARA any vector expressed in the geocentric orbital reference axes defined as:

(1) Axis 1 (X): in the inertial direction of flight (derived from Y and Z).

(2) Axis 2 (Y): parallel to the negative of the orbit normal.

(3) Axis 3 (Z): toward the Earth center of mass.

The Euler angle rotations are in the 3, 1, 2 order of axes, which corresponds to satellite yaw, roll and pitch.

Yaw attitude at times the sun sensor can see the sun and pitch and roll at all times (subject to telemetry availability) were to be determined with a total absolute accuracy of 0.17 deg (3σ) for each axis, provided that all spacecraft error sources were meeting their attitude determination and control requirements. In flight, all attitude data was obtained in a non-nominal control mode, which degraded the accuracy of Scanwheel telemetry data. Therefore, although DAD software was designed to obtain the highest accuracy realizable from the data, the basic data quality was not good enough to permit attainment of the accuracy goal.

Yaw attitude at times the sun sensor system could not see the sun was determined with the yaw estimation algorithm described in the preceding paragraphs. Yaw determination accuracy during those times is whatever is provided by the algorithms.

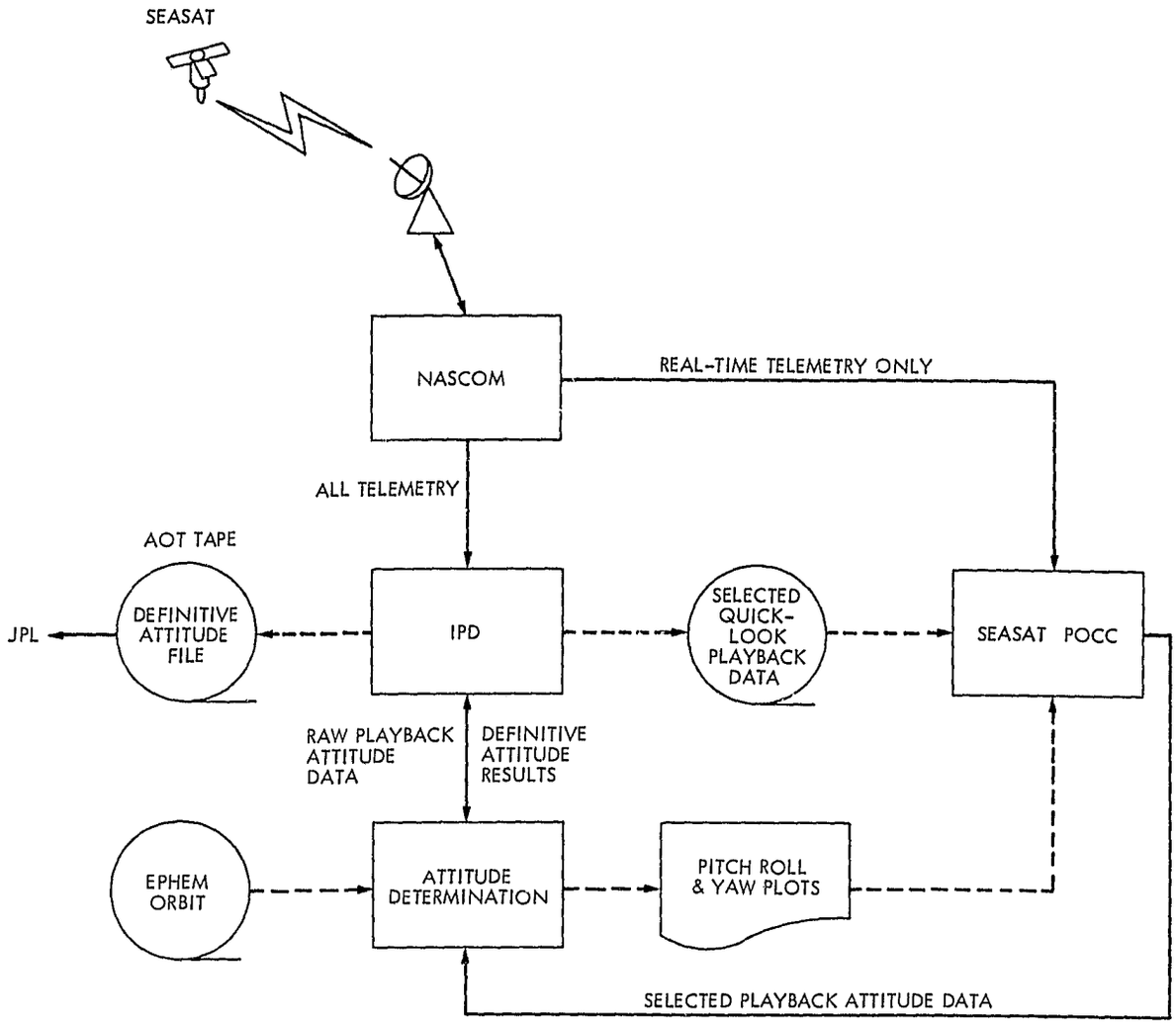

Figure 2-19. GSFC Attitude Determination Data Functional Flow Diagram

The time and frequency of the attitude points were selected to be synchronous with the Definitive Orbit File (DOF) data points. That is, since DOFs were provided on even minute time marks, the DAF contained data points at each of those times, and other attitude points were spaced between those times at 5-s intervals.

During periods for which no spacecraft telemetry exists in the TMDF, attitude points were not required, although they may have been included on the file. There were no zero-filled attitude logical records; i.e., data gaps were compressed out. Gaps are defined as time intervals when no telemetry exists.

3. File Organization and Contents

Each physical record in each DAF was 3476 bytes long. The first record was a header record. The remaining physical records each contained 144 attitude data sets. The organization of the header is shown in Figure 2-20, and its contents are listed in Table 2-4. The organization of the data records is shown in Figure 2-21, and their contents are listed in Tables 2-5 and 2-6.

Each physical record contains 144 logical records. There can be up to 121 data records for a 24-h period. The last record in such a case contains only the one data point at 24:00:00, and the rest of the record is filler.

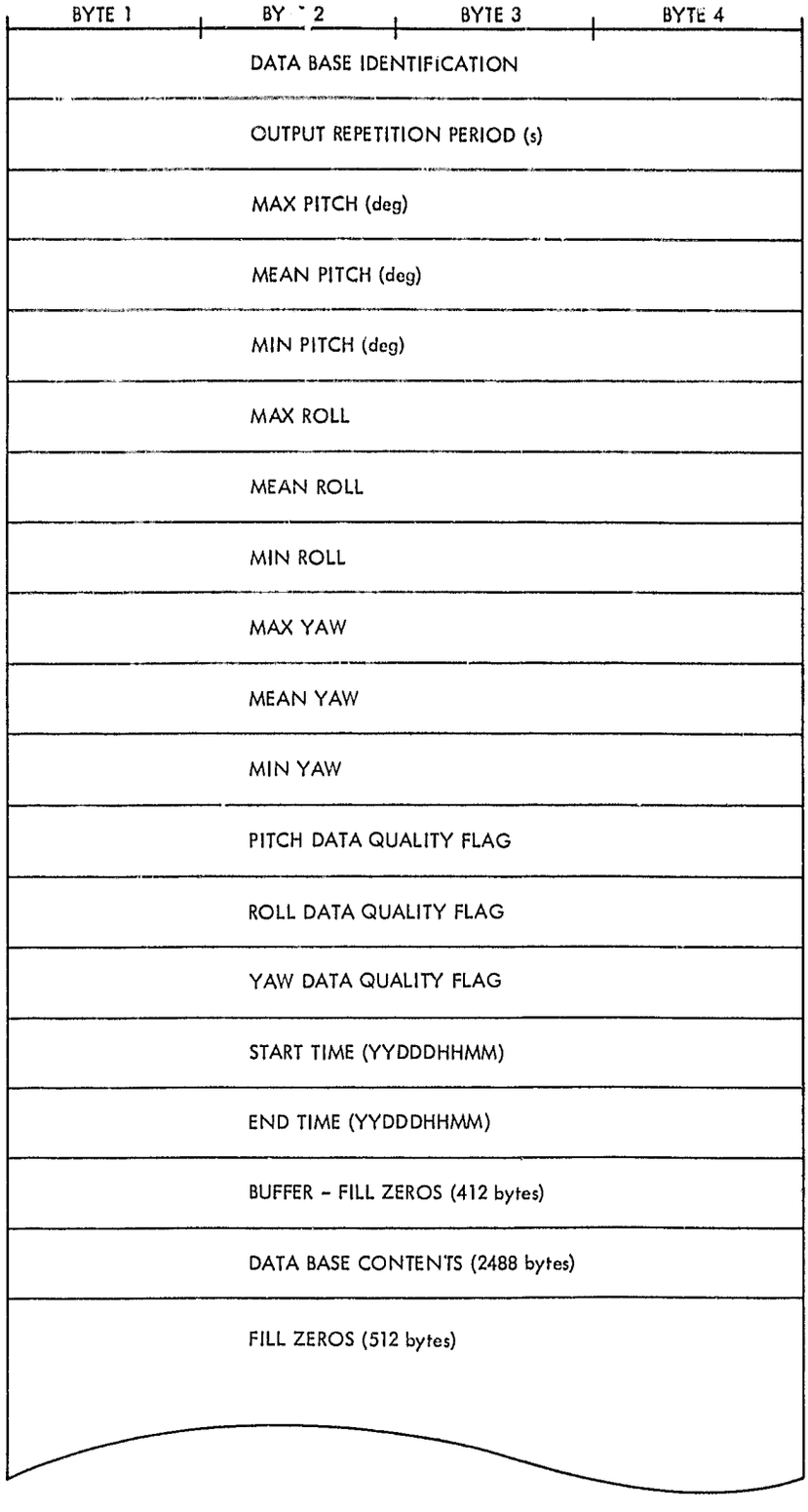

Figure 2-20. Definitive Attitude File, Header Record (Record 1)

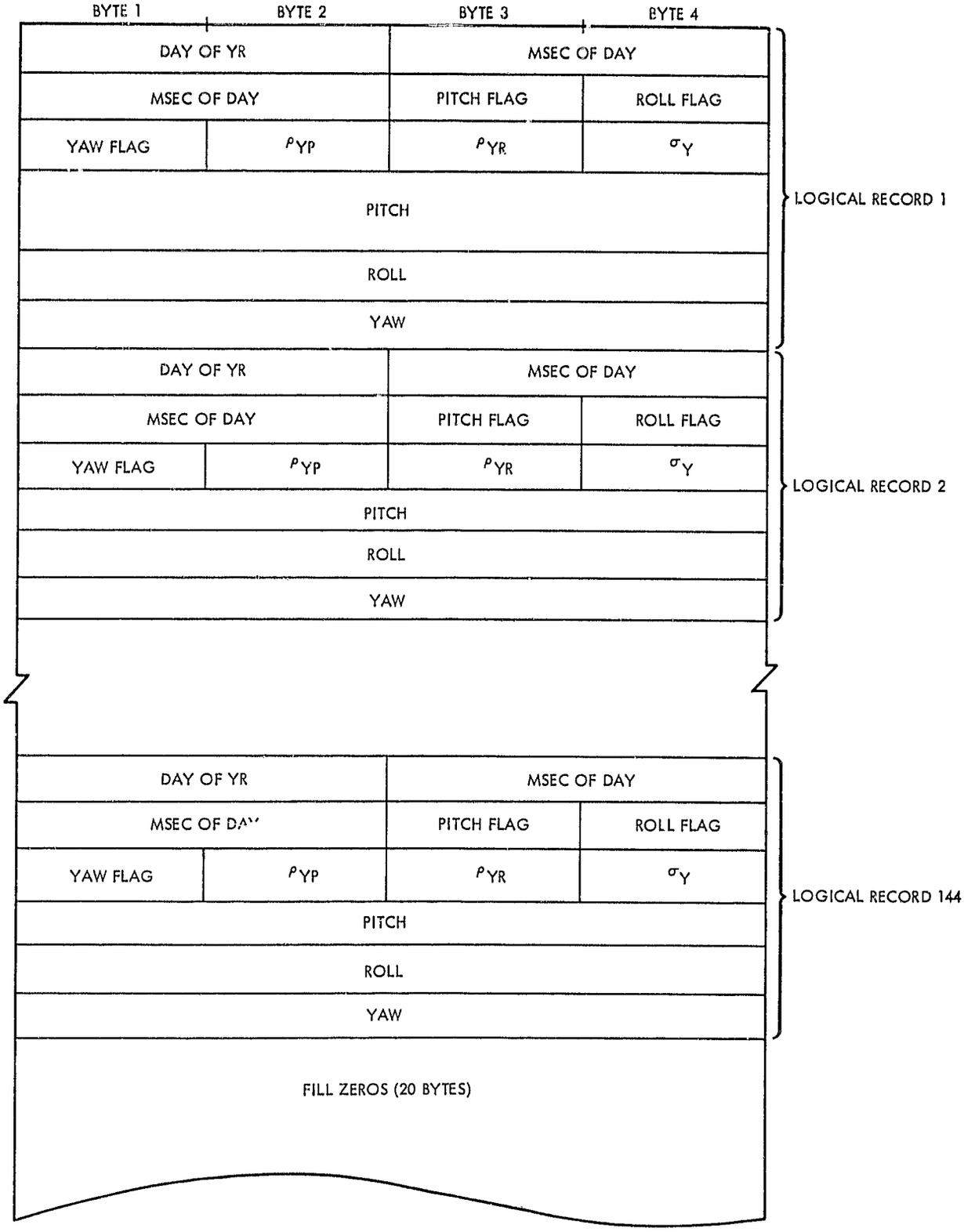

Figure 2-21. Definitive Attitude File, Data Records (Physical Records 2 through N)

Table 2-4. Definitive Attitude File Header Record Contents

Item	Label	Location, Byte Number	Data Type and Length, Bytes
1	DATA BASE IDENTIFICATION. Index number referring to data base being used. Increments by one each time data base modified	1	I*4
2	OUTPUT REPETITION PERIOD. Seconds between attitude points	5	I*4
3	MAX PITCH. Maximum value of pitch contained in file in deg	9	R*4
4	MEAN PITCH. Mean value of pitch data points contained in file in deg	13	R*4
5	MIN PITCH. Minimum value of pitch contained in file in deg	17	R*4
6	MAX ROLL (deg)	21	R*4
7	MEAN ROLL (deg)	25	R*4
8	MIN ROLL (deg)	29	R*4
9	MAX YAW (deg)	33	R*4
10	MEAN YAW (deg)	37	R*4
11	MIN YAW (deg)	41	R*4
12	PERCENT PITCH DATA FLAGGED FOR QUESTIONABLE DATA QUALITY	45	R*4
13	PERCENT ROLL DATA FLAGGED FOR QUESTIONABLE DATA QUALITY	49	R*4
14	PERCENT YAW DATA FLAGGED FOR QUESTIONABLE DATA QUALITY	53	R*4
15	Start time of FILE (YYDDDHHMM)	57	I*4
16	End time of FILE (YYDDDHHMM)	61	I*4

Table 2-4. Definitive Attitude File Header Record Contents (Continuation 1)

Item	Label	Location, Byte Number	Data Type and Length, Bytes
17	Filler (all zeros)	65 - 476	I*4
18-19	Angles between IR scanner boresight and spacecraft + Z-axis for scanner R and L ($\gamma_R = \gamma_L = 64$ deg)	477	R*4
20-21	Azimuth angles of IR scanner boresight measured in spacecraft X-Y plane from the spacecraft + X-axis for scanner R and L ($AZ_R = 90$ deg, $AZ_L = 270$ deg)	485	R*4
22	IR scanner cone angle ($\gamma = 45$ deg)	493	R*4
23	Flattening factor of Earth (f=0.00335281)	497	R*4
24	Equatorial Earth radius (Re = 6378.14 km)	501	R*4
25	Spare	505	R*4
26	Spare	509	R*4
27-28	Two yaw interpolation autocorrelation time constants (τ_1, τ_2)	513	R*4
29	Variance of yaw determination from sun sensor data (σ_D^2)	521	R*4
30	Variance of yaw prediction w.r.t. Y_D(σ_C^2)	525	R*4
31-32	Constant magnitudes for yaw estimate from roll and roll rate (K_{YR}, K_{YRD})	529	R*4
33-34	Constant phases for yaw estimate from roll (t_R, t_{RD})	537	R*4
35	Variance of Y3, yaw estimate from roll and roll rate, (σ_3^2)	545	R*4

Table 2-4. Definitive Attitude File Header Record Contents (Continuation 2)

Item	Label	Location, Byte Number	Data Type and Length, Bytes
36	Constant a priori predicted yaw (K_o)	549	R*4
37-40	Constant amplitudes of Fourier series for a priori yaw prediction $Y_p(K_i, i=1,2,3,4)$	553	R*4
41-44	Constant phases of Fourier series for a priori yaw prediction $Y_p(\lambda_i, i=1,2,3,4)$	569	R*4
45	Fundamental frequency of Fourier series for a priori yaw prediction ($\omega_o = 2\pi/$(orbital period))	585	R*4
46	Scaling factor of cross-correlation of errors in Y_3 and in Y_I interpolation estimate (P_{I3M})	589	R*4
47	Time constant of cross-correlation of errors in Y_3 and Y_I (τ_c)	593	R*4
48-50	Magnetometer bias field calibration coefficients (a,b,c)	597	R*4
51-59	Nine elements of magnetometer calibration matrix, [M]	609	R*4
60-71	Sun sensor alignment Euler angles ($\phi_i, \theta_i, \psi_i, i=1,2,3,4$)	645	R*4
72-143	Calibration parameters for sun sensors ($A^i_j, B^i_j, j=1,2,\ldots 9;\ i=1,2,3,4$)	693	R*4
144-306	Pitch and roll biases and telemetry conversion factors plus telemetry conversion factors for magnetometer data	981 - 1632	R*4

Table 2-4. Definitive Attitude File Header Record Contents (Continuation 3)

Item	Label	Location, Byte Number	Data Type and Length, Bytes
307	Proportional contribution to Y_3 for yaw estimate from roll (ρ_r)	1633	R*4
308-427	Various factors used in data processing	1637-3476	R*4 I*4

Table 2-5. Definitive Attitude File Data Record Contents

Location, Byte No	Label	Item Length, Bytes	Data Type
1-24	Logical record 1	24	
1-2	Day of year	2	I*2
3-6	Millisecond of day	4	I*4
7	Pitch data quality flag (See Table 2-6 for a detailed description)	1	I*1
8	Roll data quality flag - same as for pitch	1	I*1
9	Yaw data quality flag - same as for pitch	1	I*1
10	Yaw/pitch error correlation coefficient[a]	1	I*1
11	Yaw/roll error correlation coefficient[a]	1	I*1
12	Yaw determination accuracy (deg, 1σ)[b]	1	I*1
13-16	Pitch, deg	4	R*4
17-20	Roll, deg	4	R*4
21-24	Yaw, deg	4	R*4
25-48	Logical record 2 - same as bytes 1-24 for second point on file	24	
.	.	.	
.	.	.	
.	.	.	
3433-3456	Logical record 144	24	
3457-3476	Filler (all zeros)	20	

[a]Data Number: 0 = -1.00, 255 = +1.00

[b]Data Number: 0 = 0.000, 255 = 0.500

Table 2-6. Description of the Attitude Data Frame Quality Indicator Byte

Bit Number	Description	Value of Bit(s)
1-5	Number of data points divided by 2 that were used to obtain pre-averaged value	0-30
6	Attitude angle was measured	0
	Attitude angle was interpolated	1
7	Data was within "No" criteria during smoothing process	0
	Data was outside "No" criteria during smoothing process	1
8	Nominal mode was used to determine attitude angle	0
	Non-nominal mode was used to determine attitude angle	1

SECTION III

CHARACTERIZATION OF SEASAT ATTITUDE HISTORY

A. SUMMARY

The Seasat mission can be grouped into the five time periods described in the following paragraphs.

1. Initial Acquisition of Orbital Mode (9 Days)

The period from day 178 (launch) through day 187 was devoted to acquiring a nadir-referenced orbital attitude under control of the OACS, and to initial checkout of the scientific sensors. The events of this period are described in Reference 3-1 and Section VI of Volume II of this report. By the beginning of day 188, all sensors had been turned on and were operating together, and the spacecraft was stably controlled in attitude using only the right Scanwheel signal processor. Because attitude data from this period was not part of the scientific data record, no corrections were applied in ground processing.

2. First Quiescent Data Acquisition Period (32-1/2 Days)

From day 188 through the first half of day 220, no horizon sensor interference occurred. The calibration of science sensors and acquisition of data were pursued vigorously. OACS parameter trimming was completed on day 194, which reduced yaw excursions by a factor of 4 (approximately). All attitude data from day 188 on was fully corrected in ground processing.

3. OACS Mode Research (5 Days)

On day 220, the sun interference with horizon sensors resumed, as described in Reference 3-2. Until day 225, this period experienced a variety of responses to the horizon sensor difficulty, culminating in the use of Mode 5. Spacecraft attitude was considerably disturbed by all attempts to use the left signal processor. Mode 5 involved disconnection of the roll signal from the control loop, which proved the least disturbing method of coping with the interference.

4. Cruise in Mode 5 (30 Days)

From day 225 through day 255, Mode 5 was used to avoid horizon sensor interference. Pitch and roll were generally well-behaved, while yaw was perturbed every revolution by Mode 5 to excursions of 1-3 deg, mostly over the southern hemisphere of the Earth. All orbit adjustments were achieved during this period, which created different patterns of attitude perturbations on the 5 days affected by these maneuvers. Yaw attitude data gaps began to appear on day 226 and continued (as shown in Figure 2-12) to the end of the mission.

These data gaps were interpolated with the algorithm previously discussed. Sun sensor head 2 began to provide sun position data at about day 236 and by day 243 was the sole source of such data (head 1 gave data until day 243).

5. Second Quiescent Data Acquisition Period (27 Days)

On day 255, when all chance of horizon sensor interference had apparently passed, the use of Mode 5 was discontinued. Normal OACS operation, on the right signal processor only, then resumed. Pitch and roll behavior was similar to that in the first quiescent period after OACS trimming (days 195-220). Yaw behavior was also apparently similar, but directly visible only 900-1000 s each revolution from sun sensor head 2 until the last week of the active mission, when head 3 began providing a similar span of data in another phase of each revolution. Most of the yaw behavior was, therefore, inferred from the partial data by use of the yaw interpolation algorithm.

B. INFLIGHT ALIGNMENT CALIBRATION OF SUN SENSOR HEAD 2

1. Summary

In the last week of August 1978, the sun traveled the region in which the FOVs of sun sensor heads 1 and 2 overlapped. Figure 3-1 shows a sample of this data, with head 2 data mapped into the boresight reference frame of head 1 for direct comparison. Head 2 reads 0.14 deg less cross-cone and 0.11 deg less cone than head 1 for the same sun position. This was significantly larger than could be expected from the nominal error budgets, and precipitated a detailed investigation. No conclusion could be drawn from the overlap data alone, since it was obtained from such a limited area (one corner) of each head's FOV; the data allowed for only a two degree-of-freedom (DOF) solution to what was really a three DOF problem.

The sun angle difference between heads remained relatively constant during the approximately 1-week overlap period; therefore, its cause was likely to be some combination of fixed changes and errors in calibration and alignment, of either or both heads. The largest calibration residual measured at the manufacturer (Adcole) for any Seasat sun sensor was about 0.025 deg in either axis (cone or cross-cone); a worst-case combination of such errors could yield about 0.05-deg relative difference, clearly not the answer. The calibration history over the flight acceptance test sequence shows shifts of a few hundredths of a degree, on the same order as the calibration residual itself. Tolerance buildup could not furnish a logical explanation for the observed differences. The case for a fixed change or error in the alignment of head 2 was investigated and found compatible with observed phenomena. Though no cause for such misalignment could be proved, misalignment was demonstrated with confidence sufficient to warrant correcting data from head 2 for the calculated offset values.

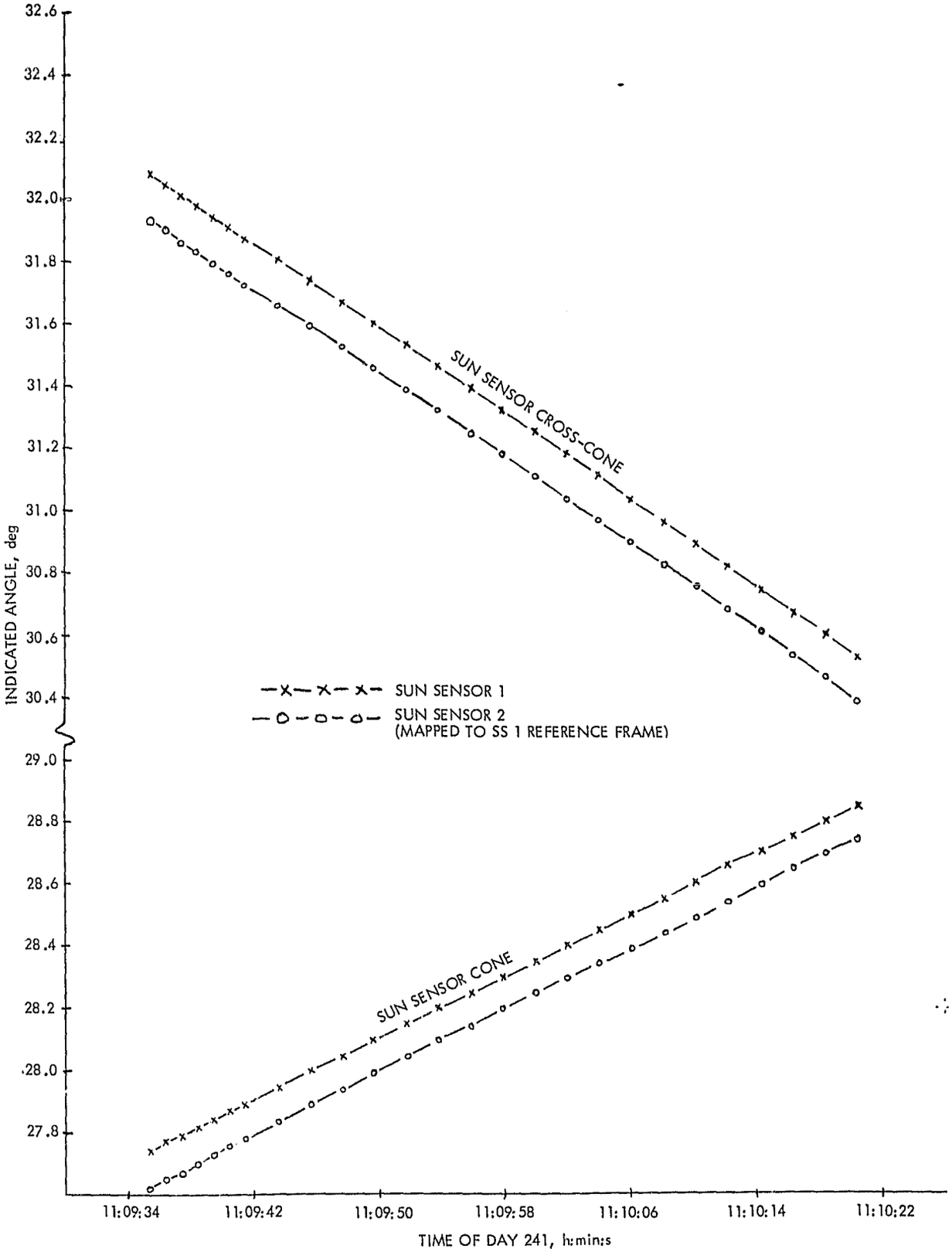

Figure 3-1. Sun Sensor Data by Overlap of FOV for Heads No. 1 and No. 2 (Sample)

2. Possible Causes of Data Anomaly

There were at least two possible causes of functional misalignment for any sun sensor head. One was the unseating of both fine reticles, perhaps caused by mishandling on the ground or a flight incident. There is a precedent for this explanation: one fine reticle of head 4 exhibited a 0.08-deg shift over vibration, ascribed to improper seating and corrected through rework and retest, and one fine reticle each in heads 1 and 3 showed smaller shifts over temperature, which were also improved by rework and retest. All of this occurred at the manufacturer's facility and none of it involved head 2. There were no checks of calibration performed after the units left Adcole, and, therefore, alignment stability was dependent on careful handling. Although the handling requirement ("... packaging ... shall be such that the unit will not experience environmental conditions more severe than those specified for flight.") would have protected the sun sensors if adhered to, no procedures were provided by LMSC to verify sensor integrity, other than the LMSC Quality Assurance (QA) stamp of approval. This is standard practice for low-cost projects, and leaves open the question of reticle shift.

Another explanation for sun sensor misalignment is an error or change in the orientation of the body of the sensor head. Heads 1 and 4 were mounted square to the side of the Sensor Support Module (SSM) in clock and elevated 6.5 deg above the horizontal in cone, requiring a very simple bracket mounting structure. Heads 2 and 3 were mounted at an angle of 23.5 deg in clock with respect to the sides of the SSM, and at 8.0 deg and 6.5 deg, respectively, above horizontal in cone. These mountings required a special small platform on which to mount the bracket, and in the case of head 2 several shims were required to reach the correct orientation. The complexity of mounting for heads 2 and 3 made them more liable to alignment problems, including inflight shifts. There is no evidence other than the observed data anomalies to either indicate or vindicate the mounting as the problem source, but it remains a possibility.

Other possible causes could be offered to explain the apparent sun sensor misalignment. However, no project resources could be made available to check them out, and the fact remains that the phenomena can be accounted for functionally as alignment offsets. The following sections describe the method used to estimate the magnitudes of these offsets and the effects on attitude data processing.

3. Alignment Calibration Method

a. Introduction. Misalignment of sun sensors can occur in three spatial DOFs, and may or may not be constant in time. The sun sensor FOV overlap data indicated a constant misalignment. However, the data was concentrated into a small range of sun angles, and therefore gave an accurate measure of only two degrees of freedom, with very poor definition of rotation about the sun line (the third DOF). Another kind of data was required to pin down the other DOF, and it was found in the comparison of pitch reconstructed from this same sun sensor head with pitch computed from Scanwheel data. Pitch computed from the sun sensor is dependent on information in the XZ plane only, to first order, and can

therefore be used to unambiguously relate sun sensor cone and twist errors. By selecting two sun sensor data sets produced by sufficiently different sun tracks, this pitch comparison affords a solution for the actual sun sensor cone and twist angles. Sun sensor clock for head 2 relative to head 1 can then be obtained by reference to data from the FOV overlap of the two heads.

The method outlined above depends on several factors. To ascribe misalignment values to head 2, the alignment of head 1 must be in flight insignificantly different from ground alignment. To validly use Scanwheel pitch as a basis of comparison, the right Scanwheel must have had a constant set of alignment errors, the mapping of which into pitch must have been well measured by sun sensor head 1 through the GSFC bias determination process.

b. Mathematical Basis

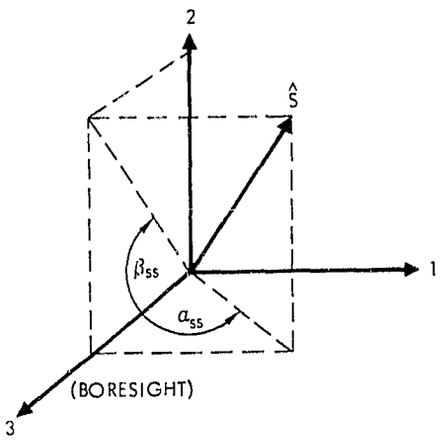

SUN SENSOR
COORDINATES

BY DEFINITION:

$$\left.\begin{aligned} \text{CROSS-CONE} \equiv \alpha_{ss} &= \tan^{-1}(S_1/S_3) \\ \text{CONE} \equiv \beta_{ss} &= \tan^{-1}(S_2/S_3) \end{aligned}\right\} \quad (1)$$

The cone and cross-cone angles defined above are direct outputs of the sun sensor. Using Equation (1), a unit sun vector ($\hat{S}$) can be constructed from sun sensor data:

$$\hat{S}(ssi) = \frac{1}{\sqrt{\cos^2\beta_{ss} + \sin^2\beta_{ss}\cos^2\alpha_{ss}}} \begin{bmatrix} \sin\alpha_{ss} & \cos\beta_{ss} \\ \cos\alpha_{ss} & \sin\beta_{ss} \\ \cos\alpha_{ss} & \cos\beta_{ss} \end{bmatrix} = K \begin{bmatrix} S_{s1} \\ S_{s2} \\ S_{s3} \end{bmatrix} = \begin{bmatrix} S_1 \\ S_2 \\ S_3 \end{bmatrix} \quad (2)$$

To express this vector in SARA coordinates, it is necessary to use the Euler angles of the alignment transformation:

$$\hat{S}_{Ri}(\text{SARA}) = \begin{bmatrix} \cos\alpha_{Bi} & -\sin\alpha_{Bi} & 0 \\ \sin\alpha_{Bi} & \cos\alpha_{Bi} & 0 \\ 0 & 0 & 1 \end{bmatrix} \begin{bmatrix} \cos\beta_{Bi} & 0 & \sin\beta_{Bi} \\ 0 & 1 & 0 \\ -\sin\beta_{Bi} & 0 & \cos\beta_{Bi} \end{bmatrix} \begin{bmatrix} \cos\gamma_{Bi} & -\sin\gamma_{Bi} & 0 \\ \sin\gamma_{Bi} & \cos\gamma_{Bi} & 0 \\ 0 & 0 & 1 \end{bmatrix} \hat{S}(\text{ssi}) \quad (3)$$

where α_{Bi}, β_{Bi}, γ_{Bi} are clock, cone, twist, respectively, and i indicates the sensor head from which the data was obtained.

The reconstruction of pitch from sun sensor data uses the observation model (Equation 4-166 of Reference 2-2):

$$-\sin p' \cos r' S_{R1} + \sin r' S_{R2} + \cos r' \cos p' S_{R3} = S_{03} \quad (4)$$

where

p' = true pitch = $p - p'_B$

r' = true roll = $r - r'_B$

p, r = pitch, roll data from Scanwheels corrected for Earth oblatness, S/C altitude, and systematic horizon radiance variation

p'_B, r'_B = true bias of pitch, roll

$\hat{S}_R = \begin{bmatrix} S_{R1} \\ S_{R2} \\ S_{R3} \end{bmatrix}$ = sun position observed by sun sensor, in SARA coordinates (Equation 3, above)

$\hat{S}_0 = \begin{bmatrix} S_{01} \\ S_{02} \\ S_{03} \end{bmatrix}$ = sun position determined from orbit parameters and time, in orbital coordinates

Pitch is reconstructed as the solution (p) of Equation (4) for α_B, r', $\hat{S}_R$, and $\hat{S}_0$ at a given time. To first order the sensitivity of this determination of pitch to the available sources of error is as follows (see Reference 3-3):

$$\left.\begin{aligned} C_1 &= \partial p/\partial \alpha_B = 0 \\ C_2 &= \partial p/\partial \gamma_B = -\cos(\alpha_s - \alpha_B)/\cos \alpha_s \\ C_3 &= \partial p/\partial \gamma_B = \sin(\alpha_s - \alpha_B) \sin \beta_B/\cos \alpha_s \\ C_4 &= \partial p/\partial \alpha_{ss} = \frac{-\cos \beta_s \sin(\alpha_s - \alpha_B)}{\cos \alpha_s} \quad \frac{1 - S_2^2}{S_3} \\ C_5 &= \partial p/\partial \beta_{ss} = \frac{\sin^2 \beta_s \cos^2(\alpha_s - \alpha_B) + \cos^2 \beta_s}{\cos \alpha_s \cos(\alpha_s - \alpha_B)} \end{aligned}\right\} \quad (5)$$

where S_2 and S_3 are as defined in Equation (2), and (α_s, β_s) are the clock and cone angles of $\hat{S}_R$:

$$\begin{aligned} \text{clock} = \alpha_s &= \tan^{-1}(S_{R2}/S_{R1}) \\ \text{cone} = \beta_s &= \cos^{-1}(S_{R3}) \end{aligned} \quad (6)$$

A determination of the sun sensor misalignment apparent about the pitch axis can be made by solution of this set of simultaneous equations:

$$\begin{pmatrix} p_{ssi} \\ \\ p_{ssj} \end{pmatrix} = \begin{pmatrix} p_i - p_B \\ \\ p_j - p_B \end{pmatrix} + \begin{pmatrix} C_{2i} & C_{3i} \\ \\ C_{2j} & C_{3j} \end{pmatrix} \begin{pmatrix} \Delta\beta_B \\ \\ \Delta\gamma_B \end{pmatrix} \quad (7)$$

where p_{ss} is pitch from sun sensor data, p and p_B are as defined for Equation (4), C_2 and C_3 are as defined in Equation (5), the subscripts i and j refer to different instants of time, and ($\Delta\beta_B$, $\Delta\gamma_B$) are the alignment changes in cone and twist. Given the relatively large stochastic errors to which p_{ss} and p are subject, care must be taken to reduce their effects before solving Equation (7). Accurate solution of this equation also depends on sufficient differences between the rows of the C matrix, which is obtained by judicious selection of the mission times for which data is analyzed.

Equation (7) solves for cone and twist independently of the sun sensor overlap data. To complete the analysis and solve for clock, map the sun vector observed simultaneously by both sensor heads to SARA as a common reference (Equations 2 and 3):

$$\hat{S}_{R1} = \left[T_{ss1}^{SARA}\right] \hat{S}_{ss1}$$

$$\hat{S}_{R2} = \left[T_{ss2}^{SARA}\right] \hat{S}_{ss2}$$

where T is the transformation matrix from the indicated sensor head to SARA. Since the two data vectors mapped to SARA represent the same sun vector:

$$\hat{S}_{R1} = \left(\hat{S}_{R2}\right)_{nominal} + \Delta\hat{S}_{R2} \tag{8}$$

If there were no anomalies, $\Delta\hat{S}_{R2}$ would be zero. By considering the transformation to SARA as composed of nominal plus small angular error components, equations can be obtained in terms of the desired solve-for quantities:

$$\left[T_{ss2}^{SARA}\right] = \begin{bmatrix} \cos\gamma_{B2} & -\sin\gamma_{B2} & 0 \\ \sin\gamma_{B2} & \cos\gamma_{B2} & 0 \\ 0 & 0 & 1 \end{bmatrix} \begin{bmatrix} 1 & 0 & \beta_B \\ 0 & 1 & 0 \\ -\beta_B & 0 & 1 \end{bmatrix} \begin{bmatrix} \cos\beta_{B2} & 0 & \sin\beta_{B2} \\ 0 & 1 & 0 \\ -\sin\beta_{B2} & 0 & \cos\beta_{B2} \end{bmatrix} \begin{bmatrix} 1 & -\gamma_B & 0 \\ \gamma_B & 1 & 0 \\ 0 & 0 & 1 \end{bmatrix} \begin{bmatrix} \cos\gamma_{B2} & -\sin\gamma_{B2} & 0 \\ \sin\gamma_{B2} & \cos\gamma_{B2} & 0 \\ 0 & 0 & 1 \end{bmatrix} \tag{9}$$

The nominal components of $\hat{S}_{R2}$ (and of $\hat{S}_{R1}$) are obtained by the nominal transformation from sun sensor to SARA coordinates. Thus:

$$\hat{S}_{R1} - \left(\hat{S}_{R2}\right)_{nominal} = \Delta\,\hat{S}_{R2} = \left[T_{ss2}^{SARA}\right]_{\Delta} \hat{S}_{ss2} = \begin{pmatrix} \Delta S_1 \\ \Delta S_2 \\ \Delta S_3 \end{pmatrix} \tag{10}$$

Taking the difference between the nominal and total (Equation 9) transformations for sun sensor head 2 gives the difference matrix, which is, to first order (using $\gamma_B \approx -90°$):

$$\left[T_{ss2}^{SARA}\right]_{\Delta} \cong \left[\begin{array}{c|c|c} \Delta\gamma_B \cos\beta_{B2} \cos\alpha_{B2} & -\Delta\beta_B \sin\beta_{B2} \cos\alpha_{B2} - \Delta\gamma_B \sin\alpha_{B2} & \Delta\beta_B \cos\beta_{B2} \cos\alpha_{B2} \\ \hline \Delta\gamma_B \cos\beta_{B2} \sin\alpha_{B2} & -\Delta\beta_B \sin\beta_{B2} \sin\alpha_{B2} + \Delta\gamma_B \cos\alpha_{B2} & \Delta\beta_B \cos\beta_{B2} \sin\alpha_{B2} \\ \hline -\Delta\gamma_B \sin\beta_{B2} & -\Delta\beta_B \cos\beta_{B2} & -\Delta\beta_B \sin\beta_{B2} \end{array}\right] \quad (11)$$

Rearranging Equations (10) and (11):

$$\begin{pmatrix} \Delta S_1 \\ \Delta S_2 \\ \Delta S_3 \end{pmatrix} = \begin{pmatrix} S_3 \cos\beta_{B2} \cos\alpha_{B2} - S_2 \sin\beta_{B2} \cos\alpha_{B2} & S_1 \cos\beta_{B2} \cos\alpha_{B2} - S_2 \sin\alpha_{B2} \\ S_3 \cos\beta_{B2} \sin\alpha_{B2} - S_2 \sin\beta_{B2} \sin\alpha_{B2} & S_1 \cos\beta_{B2} \sin\alpha_{B2} + S_2 \cos\alpha_{B2} \\ -S_3 \sin\beta_{B2} - S_2 \cos\beta_{B2} & -S_1 \sin\beta_{B2} \end{pmatrix} \begin{pmatrix} \Delta\beta_B \\ \Delta\gamma_B \end{pmatrix} \quad (12)$$

where S_1, S_2, S_3 are components of the unit sun vector observed by sun sensor head 2. Eliminating the dependence of the first and second rows:

$$\begin{pmatrix} \Delta S_2 - \Delta S_1 \tan\alpha_{B2} \\ \Delta S_3 \end{pmatrix} = \begin{pmatrix} 0 & S_2 (\cos\alpha_{B2} + \sin\alpha_{B2} \tan\alpha_{B2}) \\ -S_2 \cos\beta_{B2} - S_3 \sin\beta_{B2} & -S_1 \sin\beta_{B2} \end{pmatrix} \begin{pmatrix} \Delta\beta_B \\ \Delta\gamma_B \end{pmatrix} \quad (13)$$

This is easily solved as:

$$\Delta\gamma_B = \frac{\Delta S_2 - \Delta S_1 \tan\alpha_{B2}}{S_2 (\cos\alpha_{B2} + \sin\alpha_{B2} \tan\alpha_{B2})}$$

$$\Delta\beta_B = \frac{\Delta S_3 + \Delta\gamma_B (S_1 \sin\beta_{B2})}{-(S_2 \cos\beta_{B2} + S_3 \sin\beta_{B2})} \quad (14)$$

Therefore, cone and twist error in sensor 2 alignment can be solved from the sun sensor FOV overlap data as a function of clock angle (α_{B2}). Solution of cone and twist from pitch data is independent of clock. If sensor 2 was misaligned, the two solutions will intersect at the true clock angle of the sensor head 2 boresight.

c. Analysis of Data. Figures 3-2 and 3-3 show samples of pitch data from two revolutions on each of two widely separated days. The days were chosen to give maximum differences in sensitivity of reconstructed pitch to sun sensor alignment errors. Pitch is shown in Figures 3-2 and 3-3 both as reconstructed from sun sensor data and as determined from Scanwheel data. The latter is fully corrected except for the +0.11-deg bias measured earlier with sun sensor head 1; correction of Scanwheel data for this value of bias would widen the apparent separation of the two determinations of pitch. None of the data is filtered, but a smooth line was drawn by the "educated eyeball" method to facilitate comparison.

The scatter of points for reconstructed pitch in Figure 3-2 is due to roll IR noise and calibration residual error in the sun sensor cone axis; in Figure 3-2, Scanwheel pitch is scattered primarily by pitch IR noise. Between day 238 and day 282, the sun beta angle changed from about +51 deg to about -2 deg. Since the sensitivity of reconstructed pitch to roll determination error is approximately the tangent of the sun clock angle, the sensitivity on day 238 was about 1.2 to 1.8, while on day 282 the sensitivity was about 0.03 to 0.04. Therefore, in Figure 3-2, the reconstructed pitch shows larger effects of IR noise than Scanwheel pitch, where in Figure 3-3 the reconstructed pitch shows only sun sensor calibration residual error and no IR noise.

Figure 3-1 shows a sample of the sun sensor FOV overlap data. The comparison of cone and cross-cone angles between sensor heads is subject only to misalignment and residual calibration errors. To facilitate comparison between the two measurements of the same sun track, the cone and cross-cone data from sensor 2 were mapped through nominal alignment angles to the reference frame of sensor 1. From this data alone, the 0.14-deg difference between cross-cone and the 0.11-deg difference in cone could be ascribed to misalignments of those amounts in the fine reticles of one (or both) sensors, following the hypothesis of reticle shift. However, if reticle errors are mapped to their effect on reconstructed pitch, they fall far short (by a factor of 2-3) of explaining the differences between the two pitch determinations. For this reason, and because the alternate (misalignment) hypothesis fits all the data quite well, the reticle shift hypothesis can be discarded.

Figure 3-4 presents individual solutions to Equations (7) and (14), based on the premise of constant sensor 2 misalignment and a variety of data from Figures 3-1, 3-2, and 3-3. Each line represents the locus of cone and twist solutions available from either a single pitch comparison or a comparison of cone and cross-cone pairs for a single point in time. For each line, the actual position of the sun at that time was taken into account. Each line of overlap data solutions represents a range of sensor 2 clock alignment values, as indicated; the spread between lines (±0.01 deg) is due to sun sensor residual calibration error. The spread in the pitch comparison lines (±0.07 deg) is due

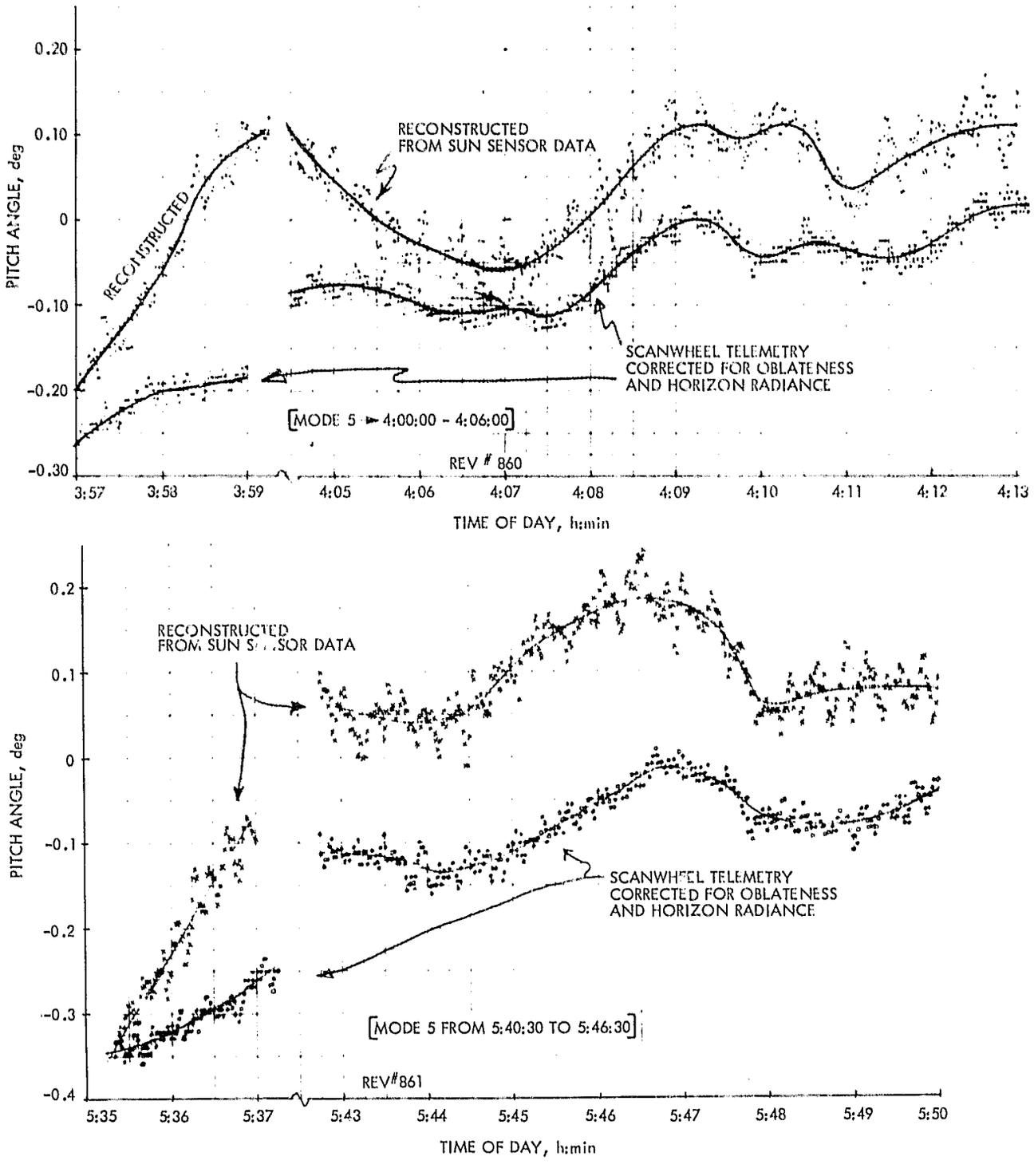

Figure 3-2. Pitch Reconstructed from Sun Sensor No. 2 Versus Scanwheel Pitch for Day 238

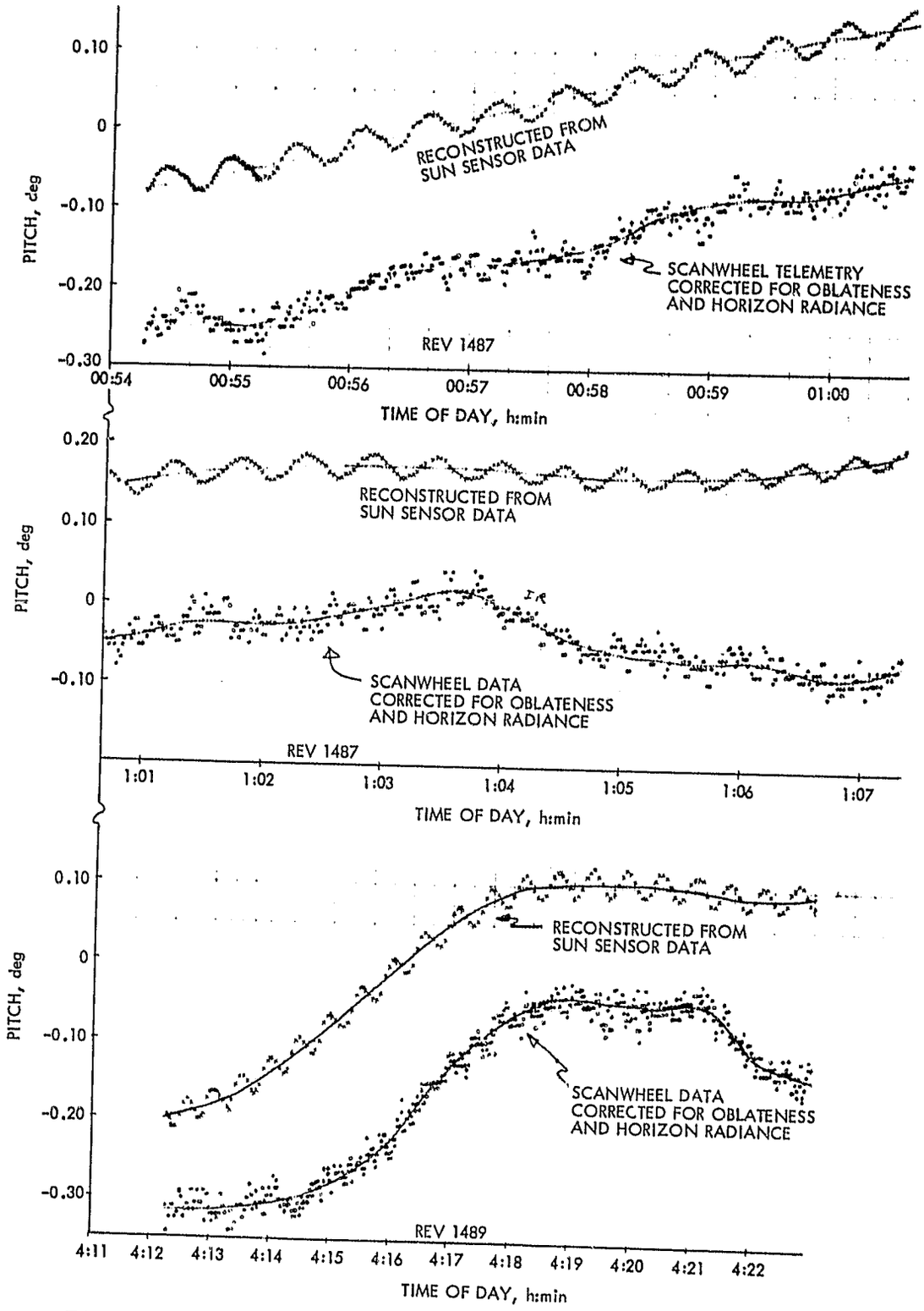

Figure 3-3. Pitch Reconstructed from Sun Sensor No. 2 Versus Scanwheel Pitch for Day 282

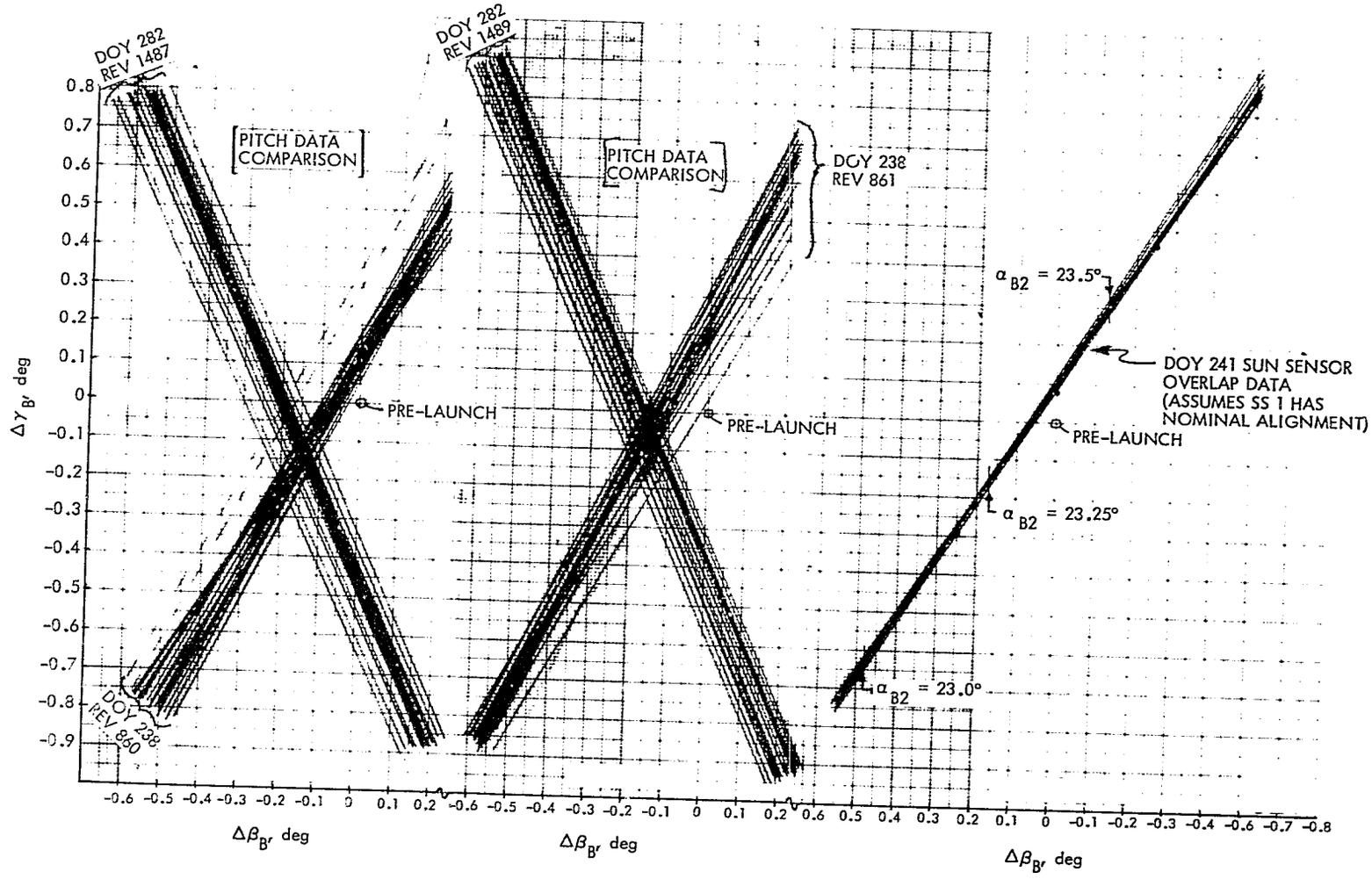

Figure 3-4. Individual Solutions for Sun Sensor No. 2 Misalignment in Cone and Twist

almost entirely to uncorrected errors in determining pitch (and roll for day 238) from Scanwheel data. The origin is marked "pre-launch" to show that the solutions sought are in terms of deviations from nominal alignment.

Figure 3-5 shows the least-squared-error solution lines obtained from the data of Figure 3-4. The single line for each day (238 and 282) represents the combination of both revolutions of data on that day. The intersection of those two lines is the solution to Equation (7) for cone and twist error. Not shown in Figure 3-5 is a comparison of reconstructed pitch to Scanwheel pitch on days 261 and 265; near these days, the sensitivity to twist was low, but the data tended to confirm cone error of approximately -0.15 deg. (See Section 3.1.2.2 of Reference 2-9.) Note that the solution locus from day 241 overlap data agrees within 0.01 deg with the solution from pitch data at a clock alignment of 23.265 deg; use of the new sensor 2 alignment values in GSFC processing of day 238 overlap data (same FOV area as day 241) showed that the data anomaly had been rectified. Therefore, data from three different days and three different areas of sun sensor 2 FOV all were explained satisfactorily by a constant alignment that differed substantially from the ground-measured values. This is the simplest explanation consistent with all of the data, and although no mechanism or scenario can be offered to account for its genesis, the misalignment of sun sensor head 2 is the most logical cause of the observed data anomalies. The final estimates from this inflight calibration are compared with ground-calibrated values in Table 3-1.

4. Effects on Definitive Attitude File

The disagreement between sensors 1 and 2 was discovered in September 1978. The spacecraft ceased operations in early October. Immediately after that event, GSFC processing of the data was halted on project request to organize the processing of extant flight data toward maximum scientific return. Detailed analysis of the sun sensor problem was delayed until GSFC processing could be resumed. When processing resumed in early November, emphasis was placed on the period between day 256 (13 September 1978) and the end of the mission (day 283, 10 October 1978). All DAFs for that period were completed before the results of the sun sensor misalignment analysis could be implemented. All yaw measurements during this period were obtained from sun sensor 2; therefore, all DAFs for this

Table 3-1. Sun Sensor 2 Alignment Calibrations

	Alignment Euler Angles, deg		
Calibration	Clock	Cone	Twist
Ground	23.509	98.017	-90.0125
Inflight	23.265	98.17	-89.89

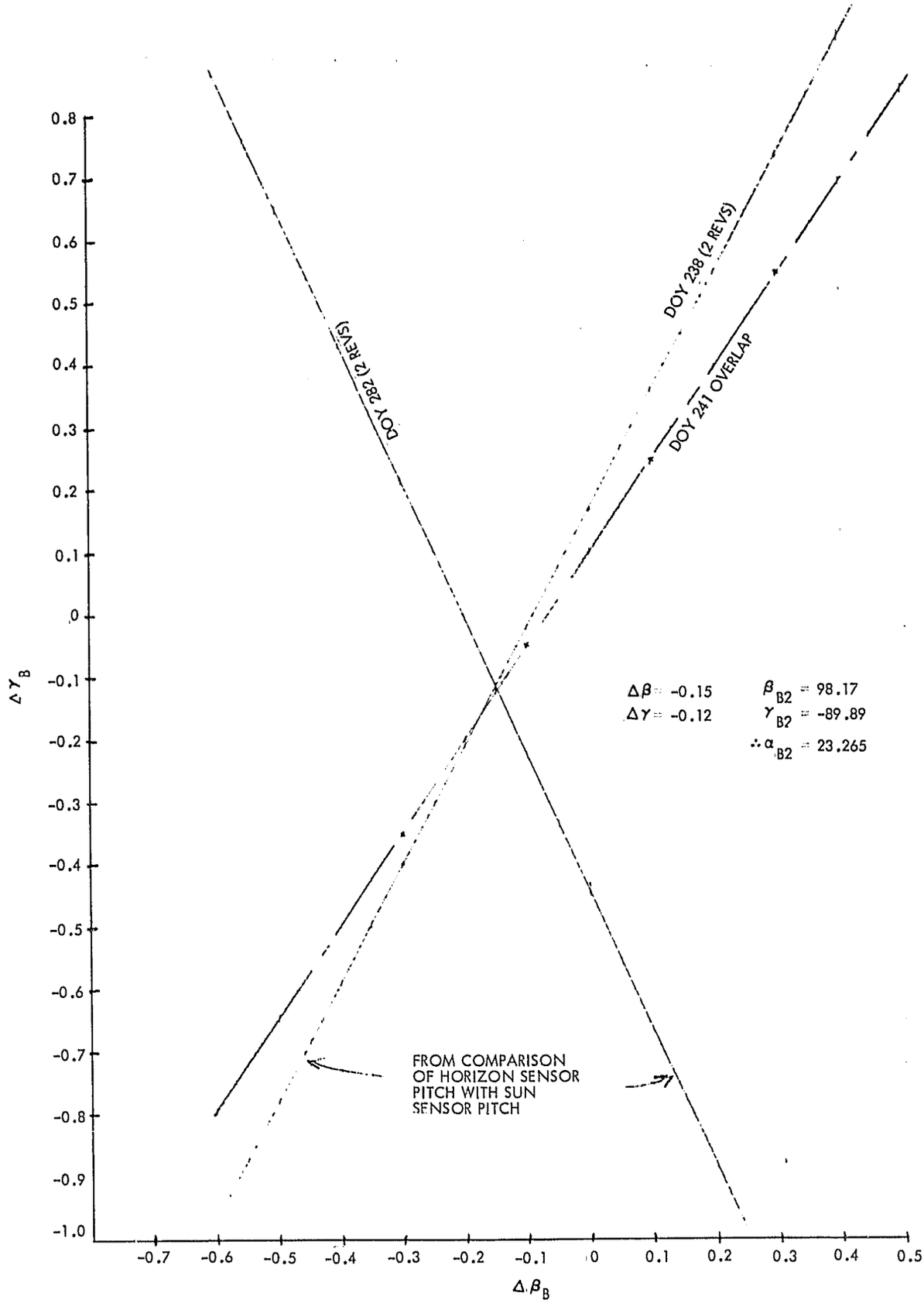

Figure 3-5. Least-Squared-Error Solutions for Sun Sensor No. 2 Misalignment

period have an additional yaw error source due to that sun sensor's misalignment. The project decided not to request reprocessing of the 27 files already produced, but to change the data base for processing of earlier data. (The data from day 220 to day 255 was next on the DAF processing schedule.) Therefore, because of the reorganized DAF production sequence, data from sun sensor 2 early in the mission was processed with ground-calibrated alignment values.

Since the differences between actual and nominal alignments have been determined for sun sensor 2, and the methods GSFC used for determining yaw are known, the effects of using incorrect alignments are deterministic. Figure 3-6 shows these effects for four representative days in the affected time period in the sense of the correction factor to be added to the DAF yaw value. The sun vector was within the sun sensor FOV from approximately 4100 s to 5100 s after ascending node in each revolution (actual times are shown in Figure 2-12). During this time, the effect of misalignment is the mapping of the alignment error into yaw as a function of sun position in spacecraft coordinates (described in Appendix B of Reference 3-3). For those times during a revolution when the sun was out of the sun sensor FOV, yaw was interpolated with the algorithm described in Subsection II-B-3. With this method, the effect of an error in yaw observation falls off exponentially with time, as shown in Figure 3-6.

The drop to zero correction in the north polar region for days 274 and 282 does not represent an increase in accuracy. Starting on day 272 (see Figure 2-12 for exact time), sun sensor 3 could sometimes see the sun. During those parts of each revolution, yaw was determined from sun sensor head 3, and, therefore, was not affected by sun sensor head 2 misalignment. However, analysis of pitch reconstructed from sun sensor head 3 data during this period showed approximately 0.1 deg difference from Scanwheel pitch (see Reference 2-9, Section 3.1.2.3). From previous arguments presented for head 2 anomalies, it would appear that head 3 was also misaligned, at least in either or both of cone and twist. Since there was no corresponding sun vector data from sun sensor FOV overlap during this period, and reconstructed pitch sensitivity to cone and twist errors remained relatively constant during the 9 days that head 3 was producing data, there was no way to separate cone from twist error, and no information at all about possible clock error. Reconstructed roll would have been useful in this analysis to separate cone from twist, but since the sun was near the orbital plane, roll from sun sensor data was extremely sensitive to all sun sensor errors and could not be trusted. In summary, no yaw correction could be calculated for sun sensor 3, and the anomaly observed in data from this head could be handled only by increasing the allocated uncertainty for yaw determined from that source. Attitude determination uncertainties will be discussed later in this report.

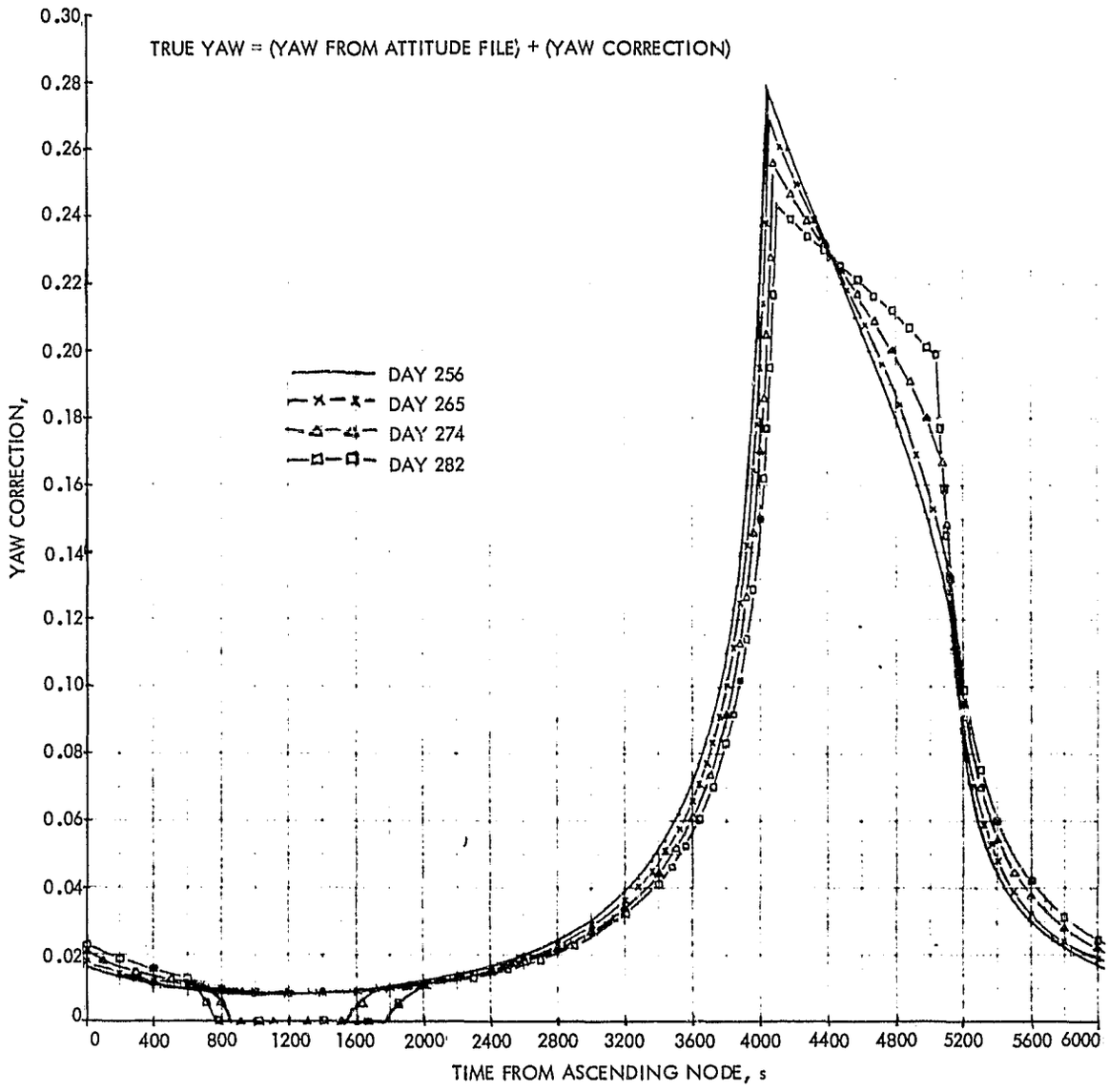

Figure 3-6. Correction to Yaw for Sun Sensor Alignment Error (Days 256-283)

C. ATTITUDE HISTORY

1. Method of Attitude History Characterization

All of the attitude history from days 188 through 283 (EOM) is presented rev-by-rev in an unpublished supplement to this report.* To facilitate comparisons within and between eras of the mission, a method was devised to characterize attitude history over spans of time relatively longer than one revolution. This method was also instrumental in evaluation of yaw interpolation accuracy (to be discussed later).

Figures 3-7 and 3-8 display (superimposed) all of the attitude history (14 revs) of day 206. The general trend of the data can be seen as a function of time from ascending node, as can the deviations from trend. Figures 3-9 and 3-10 display the mean (μ), the mean plus and minus the standard deviation ($\mu \pm \sigma$), and the outer bounds of the attitude behavior of each axis. The bounds are the outer envelopes from Figures 3-7 and 3-8; the mean and standard deviation was computed at intervals of 25 s from time of ascending node. It should be noted here that this σ is not AD uncertainty; rather, it is a measure of the deviation of the actual attitude from the daily mean attitude at the given time from ascending node. The accuracy to which these quantities are known is a separate issue to be addressed later in this report.

It can be seen from these illustrations that μ and σ describe a kind of inner bound of attitude behavior, and that the largest deviations from the mean are on the order of 2σ and sometimes 3σ. Figure 3-11 (from Reference 3-4) shows the geocentric representation of zero control error; since pitch and roll were controlled to a geodetic reference, zero control error in that frame maps to the non-zero function shown (perfect yaw would be always zero in both frames). The degree to which pitch and roll attitude behavior on day 206 met the ideal can be seen by comparing the characteristics shown in Figures 3-9 and 3-11.

Figures 3-12 through 3-15 illustrate day 249 in the same way as day 206 was shown in previous illustrations. (Note that the scale is [illegible] for Figures 3-7 through 3-13, while the scale of Figures 3-14 and 3-15 is [illegible] because of the larger maximum excursions.) Although the method of representation is the same, the characteristic behavior is different. The biggest difference is due to the attitude excursions induced by Mode 5 near 3800 s, which dominates behavior for the following 2000 s or so. Another difference is the brief horizon sensor interference effect near 1900 s, caused by the sun passing through the Scanwheel active FOV. Mode 5 was used to protect against this kind of interference from day 248 on. Yaw was directly observable for only the 1150-s period indicated, and was interpolated (as previously described) for the rest of each revolution. The relatively narrow range of deviations in the interpolated span is due to the limitations of the interpolation process: the smaller the deviations from the mean, the less information was used in forming the estimate.

---

*In custody of Dr. Hiroshi Ohtakay, Guidance and Control Section (343), Jet Propulsion Laboratory, 4800 Oak Grove Drive, Pasadena, CA 91103.

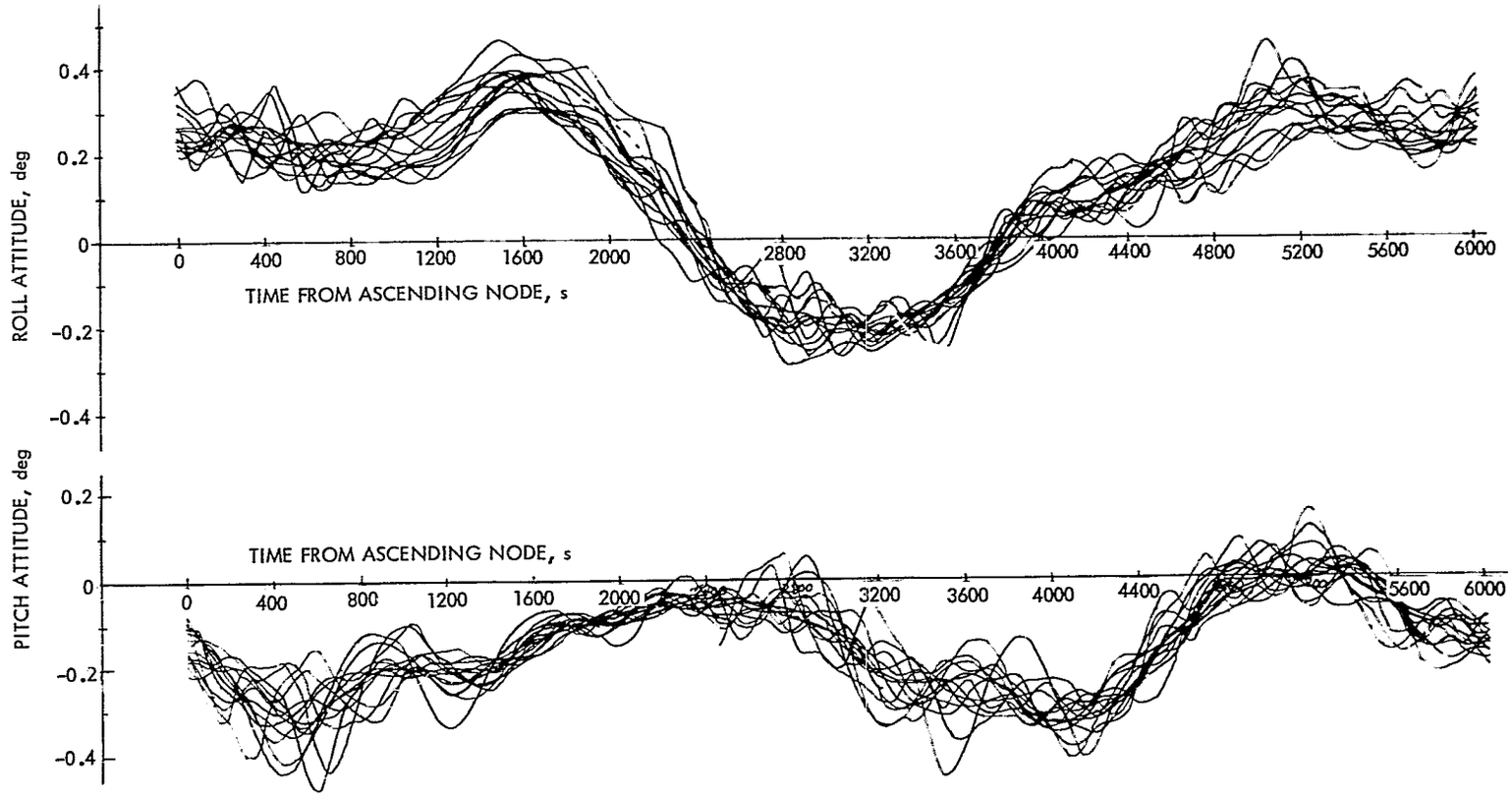

Figure 3-7. Composite Pitch and Roll for Day 206

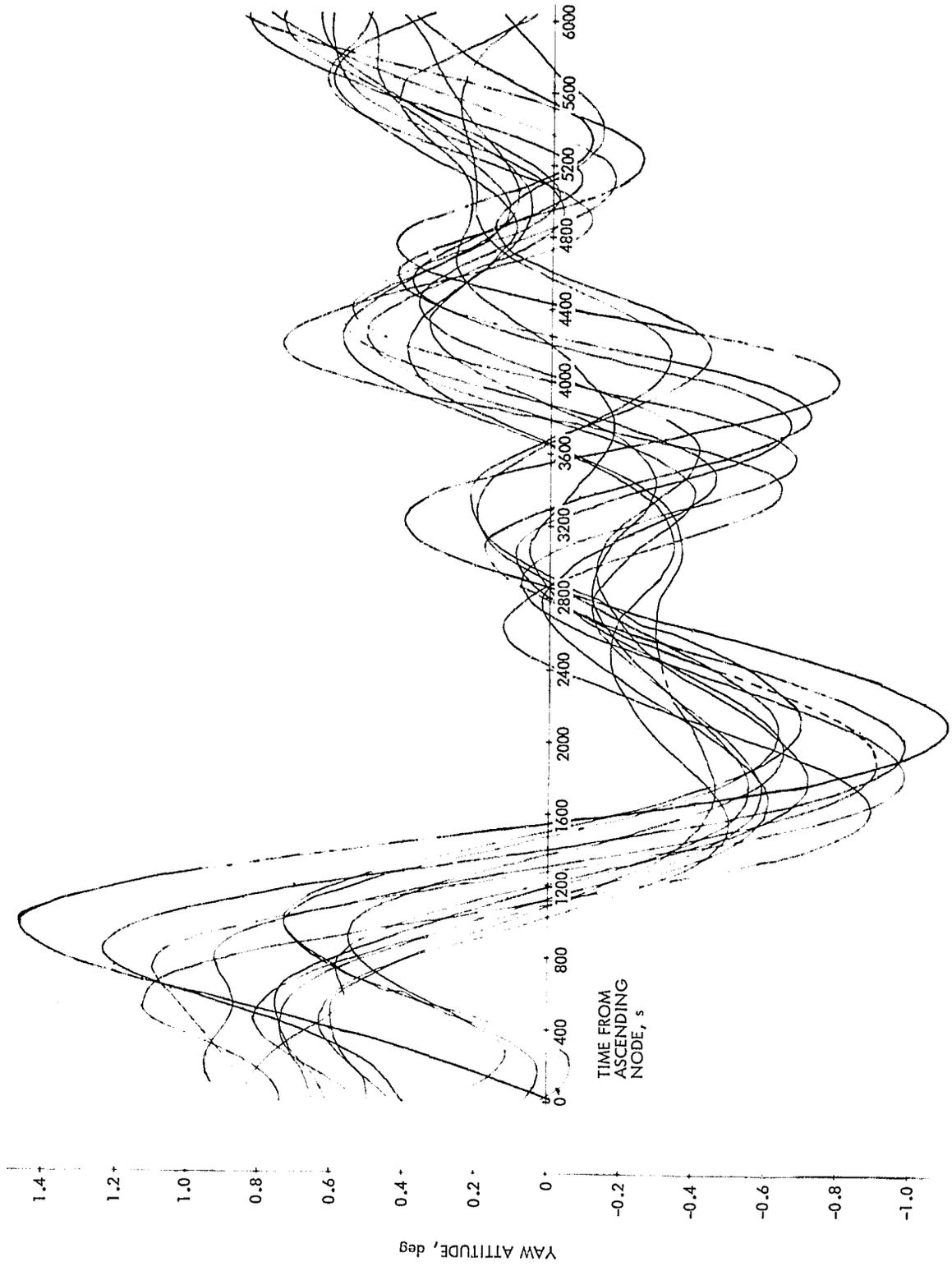

Figure 3-8. Composite Yaw for Day 206

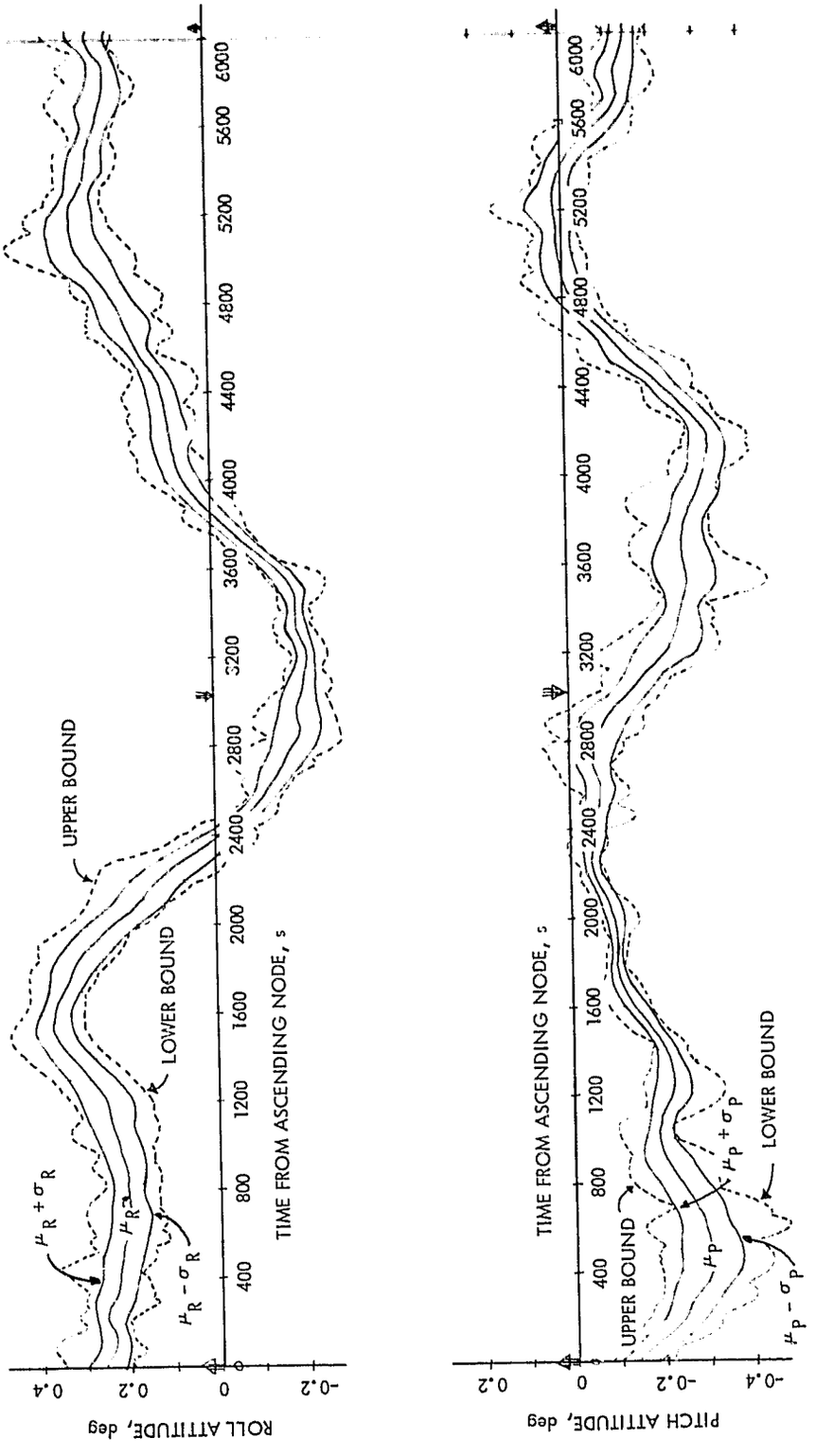

Figure 3-9. Pitch and Roll Envelopes for Day 206

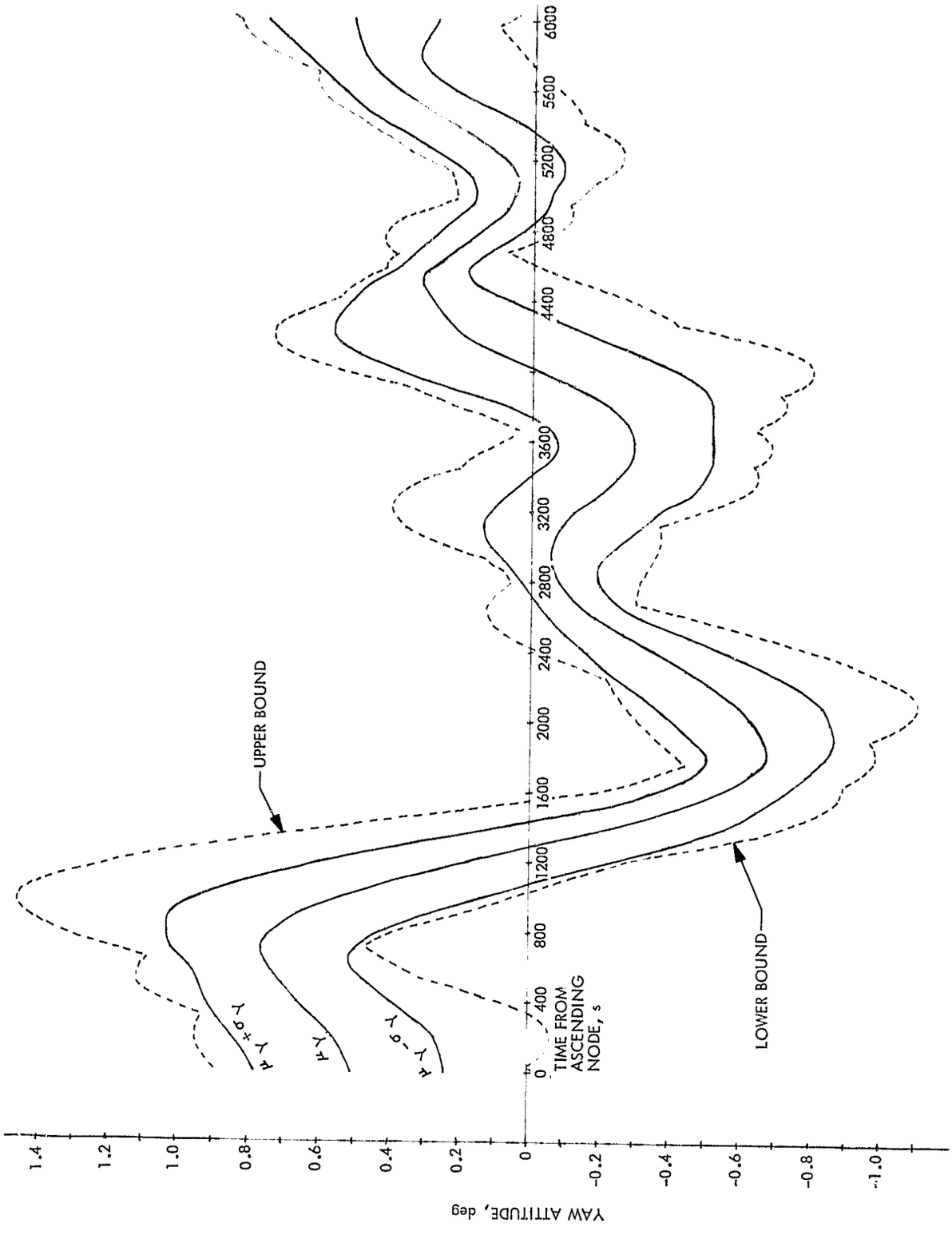

Figure 3-10. Yaw Envelopes for Day 206

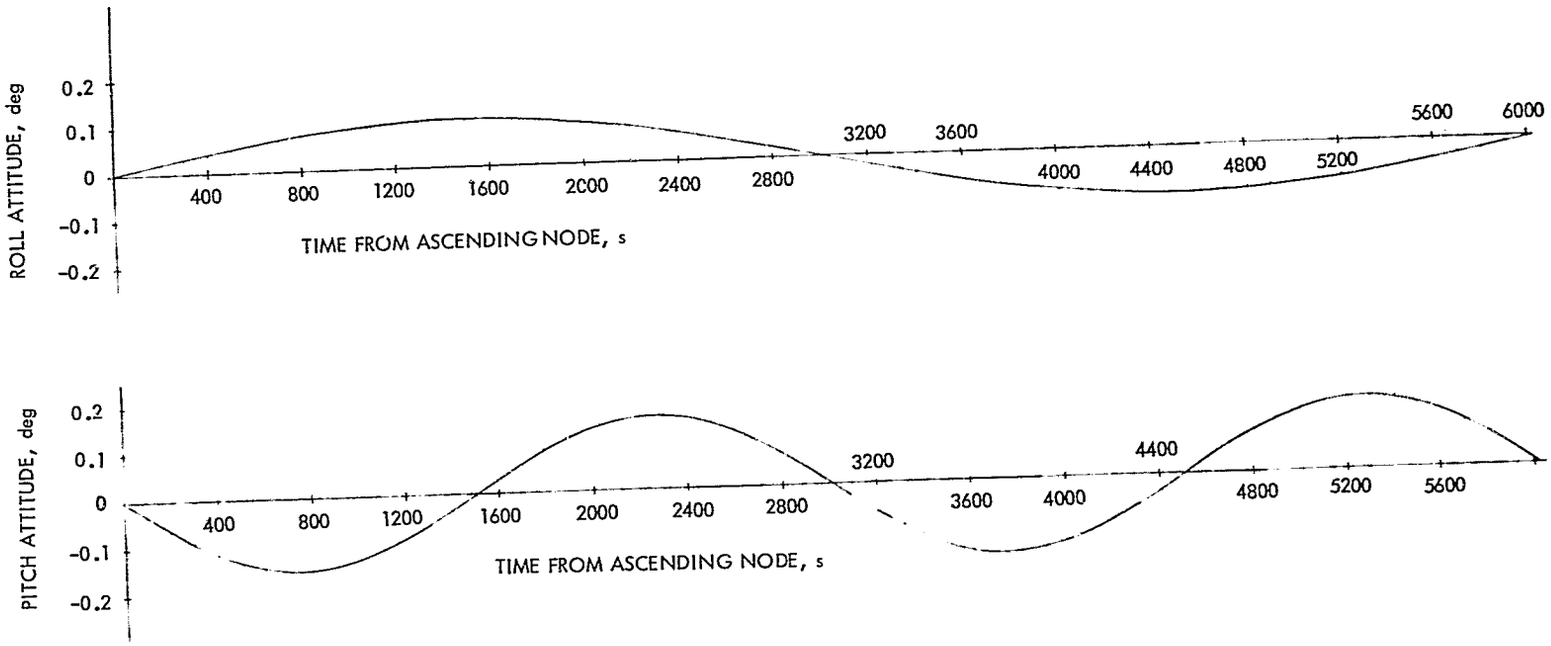

Figure 3-11. Null Geodetic Attitude in Geocentric Coordinates

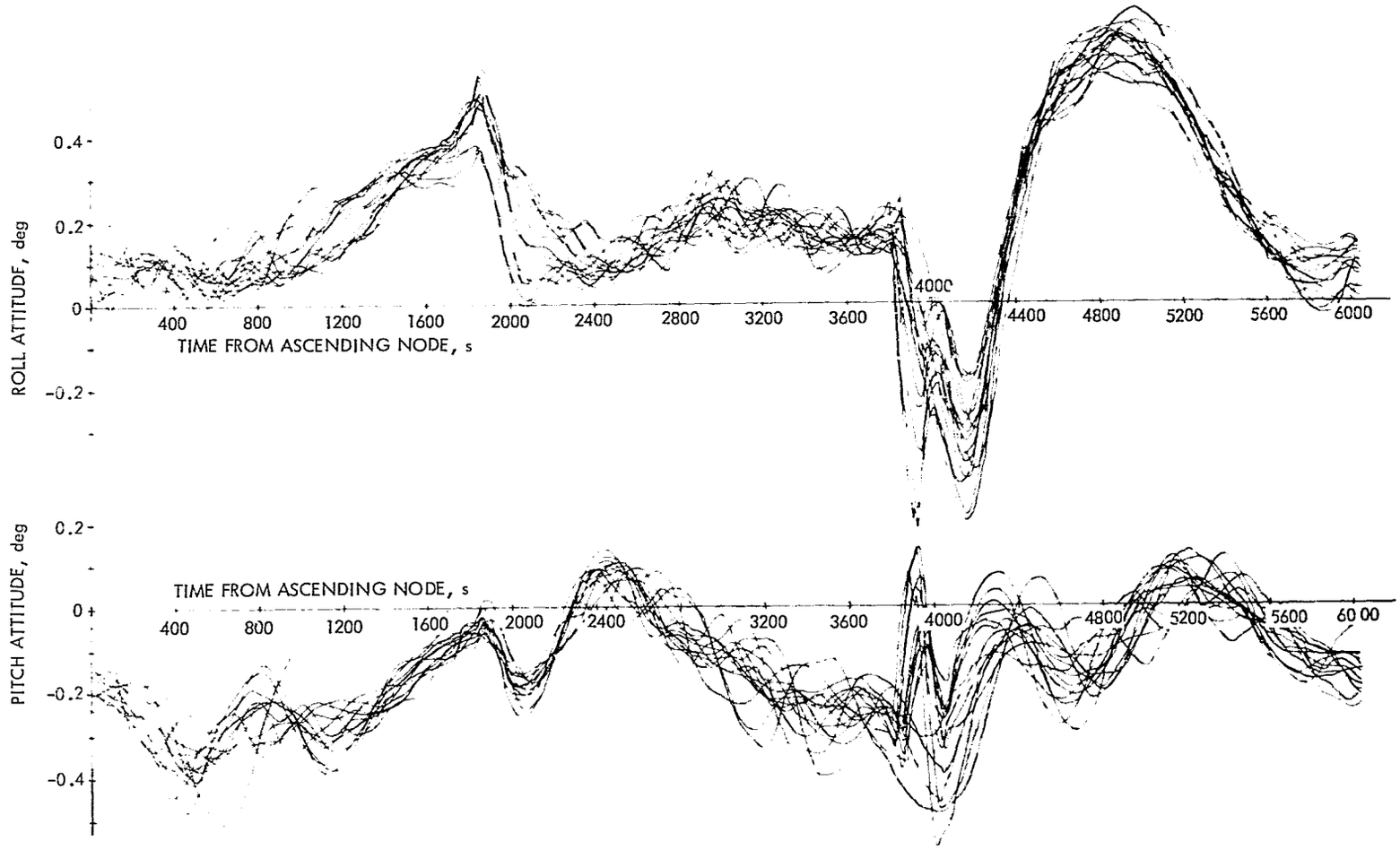

Figure 3-12. Composite Pitch and Roll for Day 249

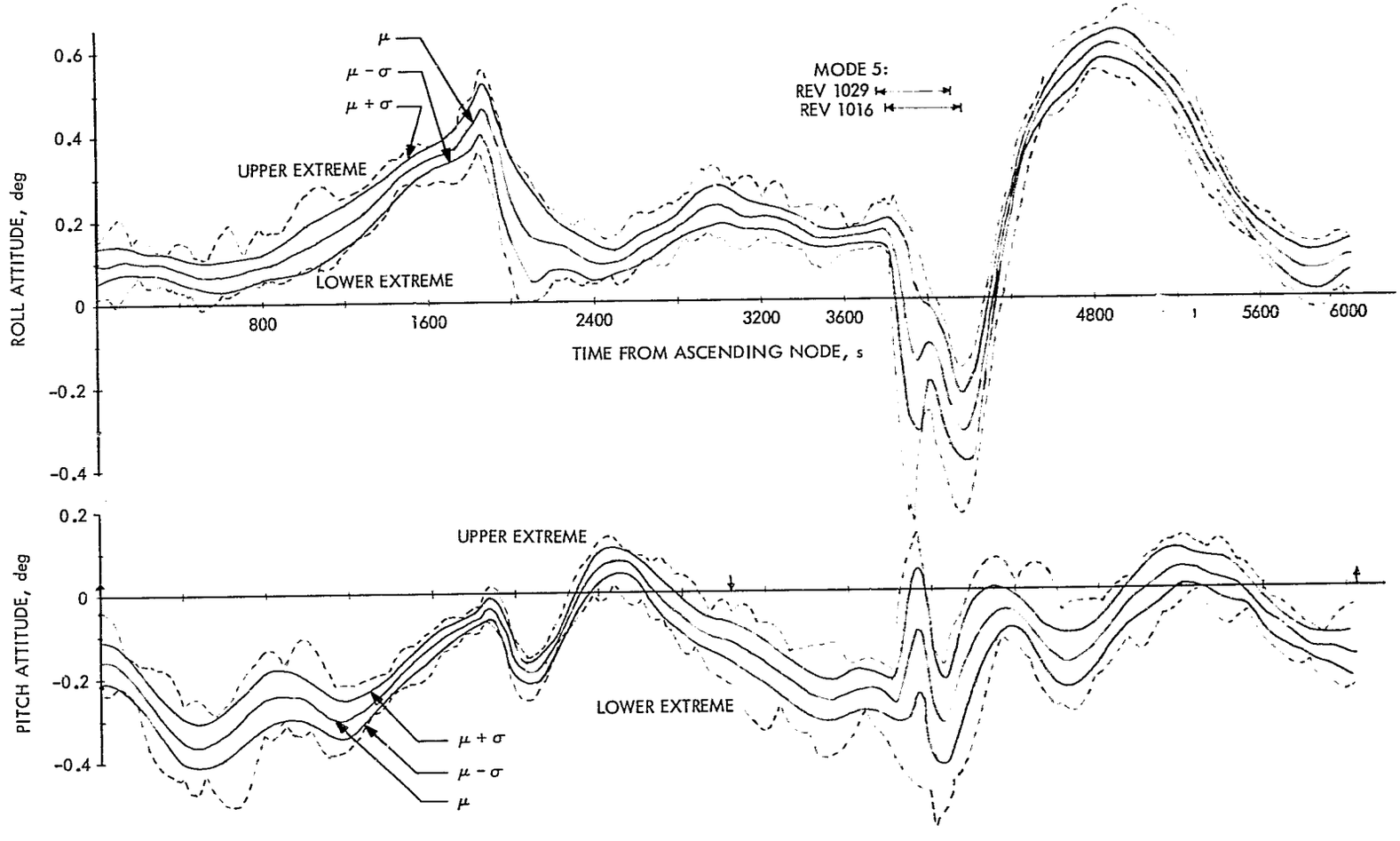

Figure 3-13. Pitch and Roll Envelopes for Day 249

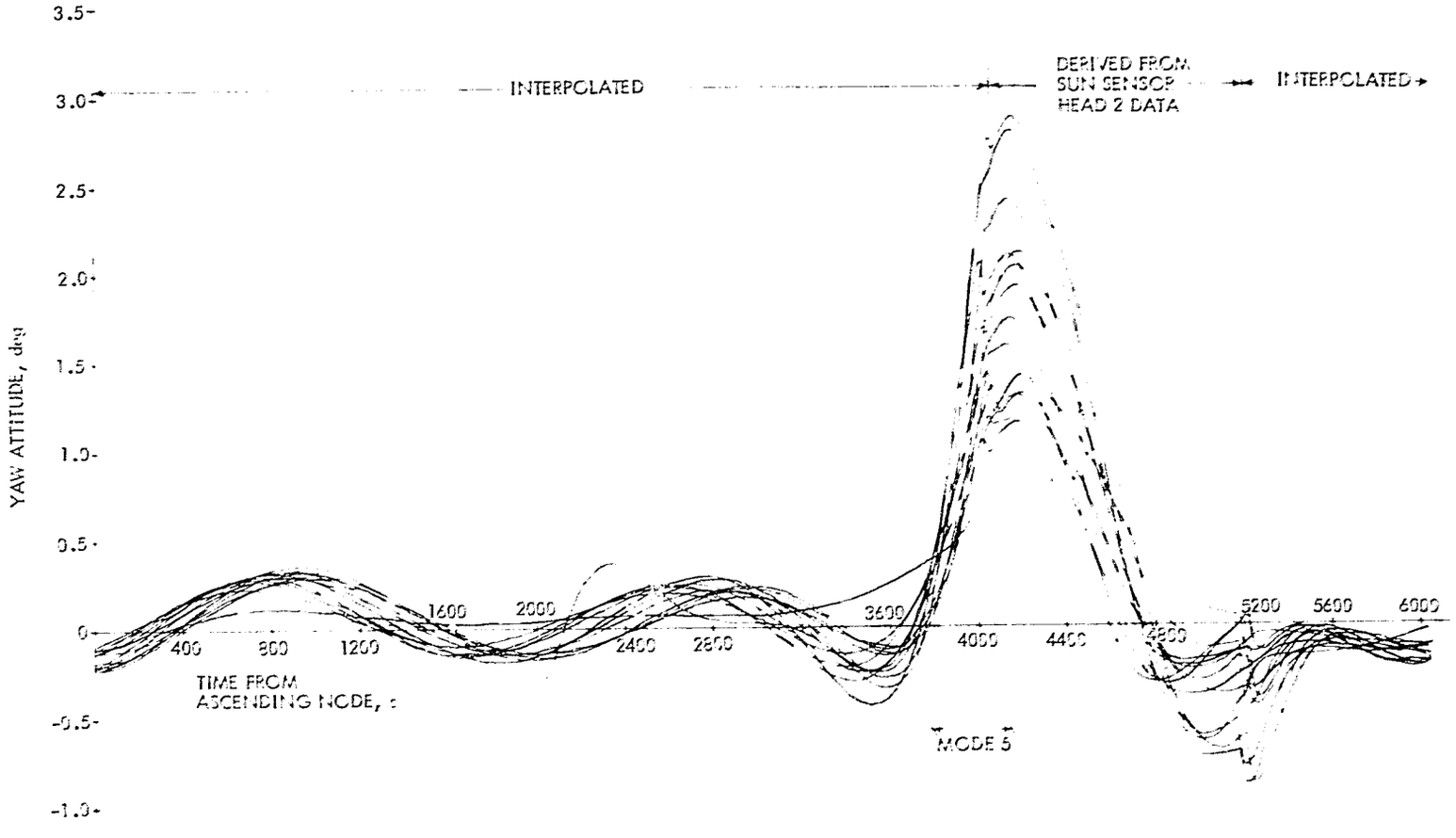

Figure 3-14. Composite Yaw for Day 249

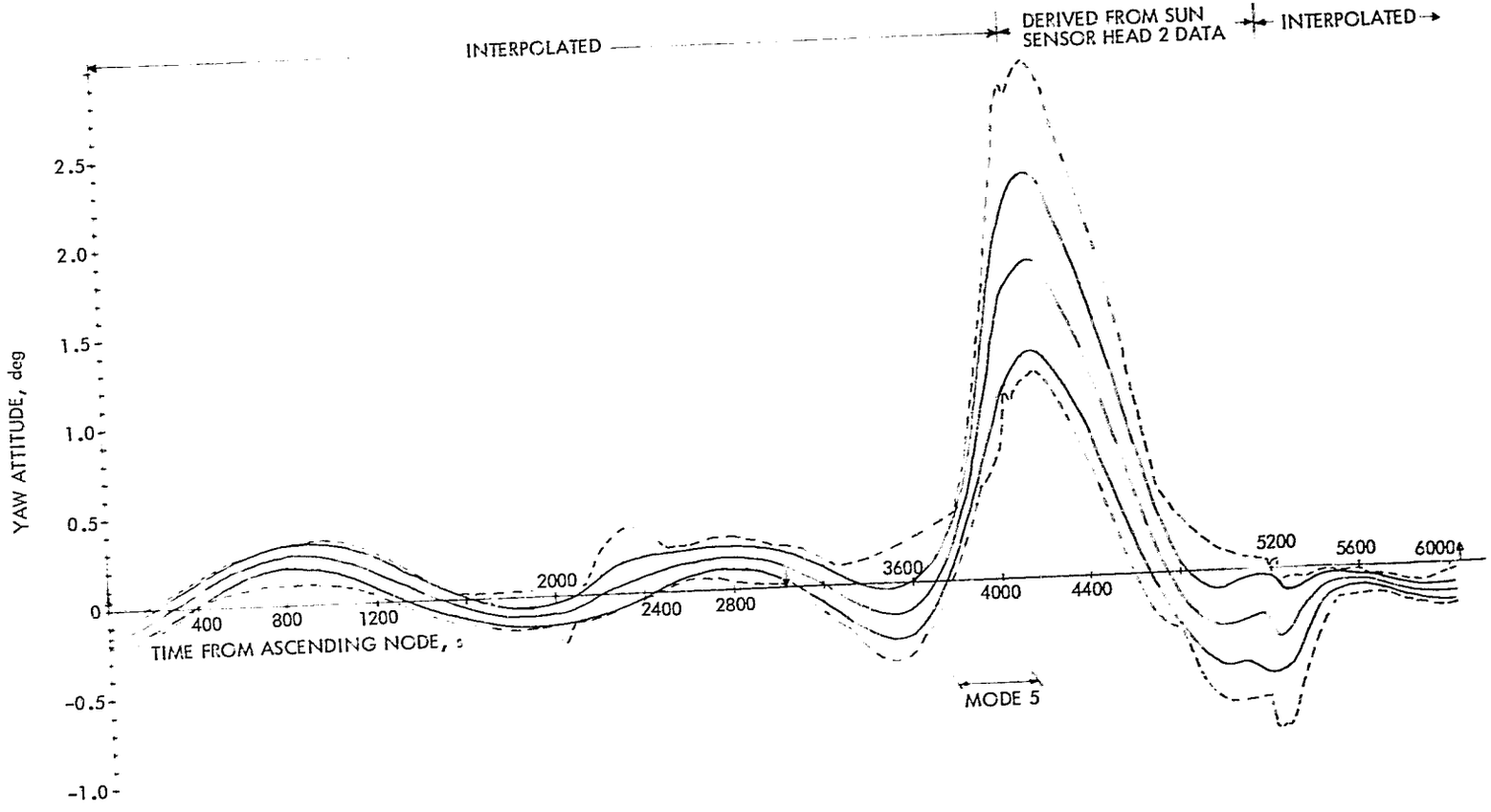

Figure 3-15. Yaw Envelopes for Day 249

Figures 3-16 and 3-17 are histograms for days 206 and 249 of attitude deviation from the mean taken every 200 s for every revolution represented by the previous illustrations. Each histogram represents a little over 400 points, taken from every phase of the attitude functions. All the histograms for day 249 show higher central peaks and longer tails than the day 206 histograms, the result of Mode 5 disturbances. The yaw function on day 249 is further distorted by the effect of yaw interpolation over most of each revolution; however, since the maximum excursion region was directly observed and this region tended to have the highest deviations from the mean, the tails of the frequency distribution are relatively undistorted. Comparing the yaw tails of days 249 and 206 shows that Mode 5 induced greater yaw variability. Pitch and roll under Mode 5 show not only longer tails, but also higher central peaks, which reflect the regularity of response to the Mode 5 commands.

Figure 3-18 shows the probability with which an attitude deviation in a given axis at any time would exceed a given multiple of the overall standard deviation for that axis. The smooth curves shown for each axis on days 206 and 249 were estimated graphically from the previous histogram data. The same function for the Gaussian distribution is included for comparison. The accuracy of the data functions in the high-sigma, low-probability region is limited by the small number of samples in this region. However, there are sufficient data to permit the following conclusions:

(1) For any axis at any time, there is approximately a 7 percent chance of an attitude excursion from the mean function of more than $\pm 1.65\sigma$ (for a normal distribution there would be 10 percent chance).

(2) For any axis at any time, the fiftieth percentile of attitude deviations from the mean function is at about 0.40σ (0.67σ for a Gaussian).

(3) There are several times more chances for a large deviation from the mean function under Mode 5 conditions than under usual conditions.

(4) For any axis at any time, the $\mu \pm \sigma$ envelope contains about 80 percent of attitude behavior.

Other conclusions could be drawn from Figure 3-18 with less confidence, but the above 4 conclusions are sufficient to put the $\mu \pm \sigma$ curves into perspective. To the degree described here, these curves can and will be termed "characteristic attitude functions." As such, they will be used to characterize spans of mission time within which conditions remained essentially constant.

2. First Quiescent Data Acquisition Period (Days 188-220)

This period is logically separable into two subperiods, which are divided by the completion of OACS trimming on day 194.

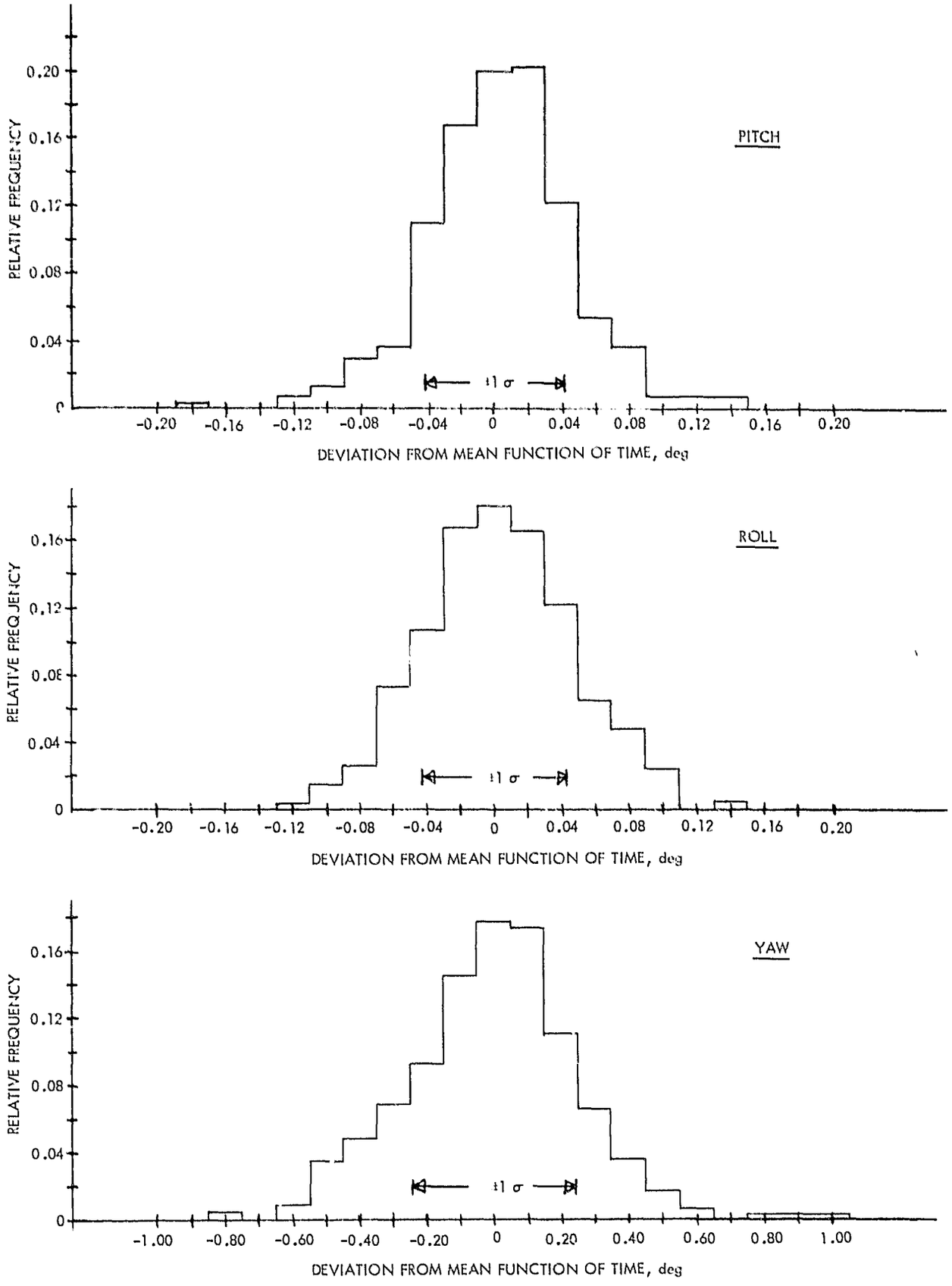

Figure 3-16. Histograms of Attitude Deviations for Day 206

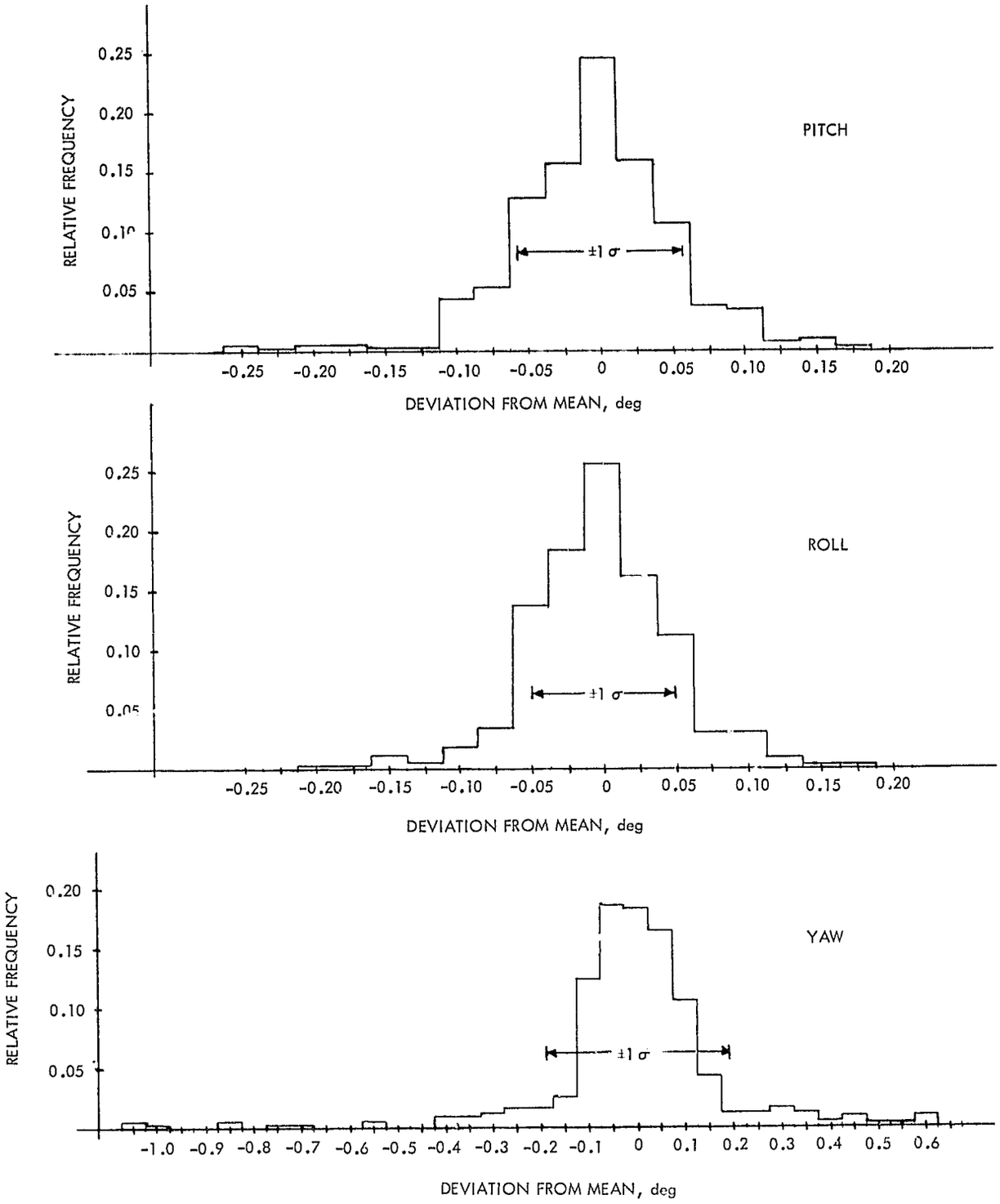

Figure 3-17. Attitude Histograms for Day 249

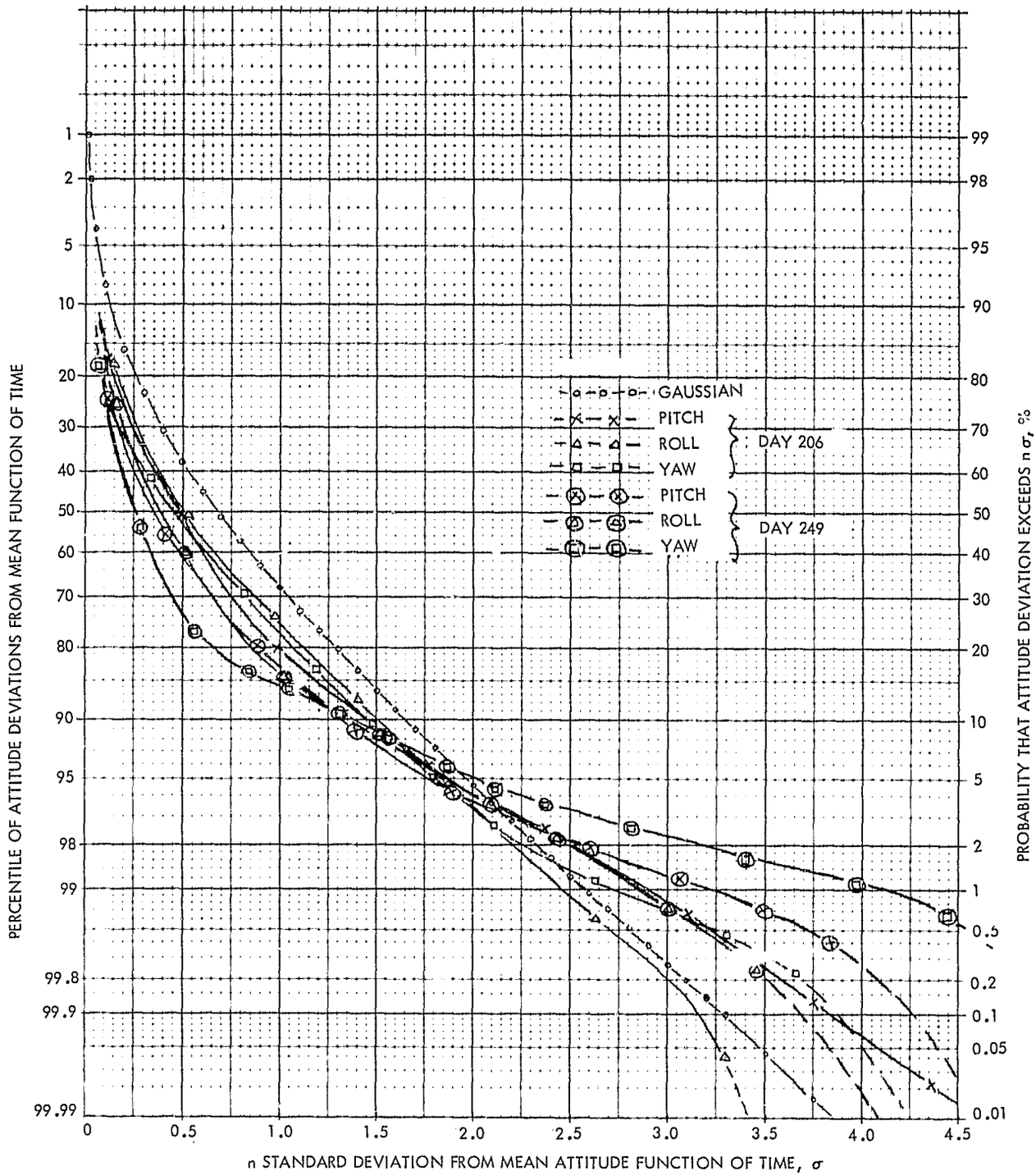

Figure 3-18. Significance of Attitude σ

a. OACS Trimming Period (Days 188-194). Figure 3-19 depicts the average attitude functions of time for each axis on each day of this period. Also shown are the contours of extreme $\mu \pm \sigma$ for this span of time. Note that pitch remained the same but roll and yaw changed significantly between days 191 and 192, when the first changes were made in OACS parameters. As an additional aid in evaluation of these functions, Figure 3-20 shows the pitch and roll average functions for day 188 as uncorrected, fully corrected geodetic, and fully corrected geocentric (same as in Figure 3-19). The uncorrected function is the spacecraft control system view of its own behavior, in a reference system which is geodetic but with systematic errors. The corrected geodetic function is the actual average performance relative to local vertical for that day.

b. Trimmed Quiescent Cruise Period (Days 195-220). Figure 3-21 shows the characteristic attitude functions for the quiescent period after the last OACS parameter change of day 194 and before the resumption of Scanwheel interference on day 220. Pitch in this period is indistinguishable from that of the earlier period, and remains essentially the same throughout this 25 days of cruise. This result was to be expected, since the previous parameter trimming was directed toward roll and yaw control and the only variable source of systematic error (horizon radiance variation) changed little on such a time scale. The roll characteristic function can be seen to change between the beginning and end of this period, due to the relatively rapid shift of apogee and perigee latitudes over time and the resultant phase shift of the roll altitude correction. Since the Seasat orbit nearly repeated itself in longitude every 3 days, the characteristic functions were plotted in groups of three consecutive days. The effects of longitude variation can be seen within these triplets for roll and yaw. Roll/yaw control coupling is evident in the variation of the yaw characteristic, which follows the variation of the roll characteristic. The regularity of yaw over this period plus the roll/yaw control coupling are the basis for yaw interpolation in the period after day 255. (This will be discussed later.)

3. OACS Mode Research Period (Days 220-225)

At approximately 08:52:00 on day 220, at the end of rev 605, sun interference with the right Scanwheel resumed. This precipitated a period of experimentation with OACS modes of operation to find the most acceptable means of minimizing the effects of this interference. A method frequently used was a switch to the left signal processor during the time that interference was expected (see Figure 2-11) for the right Scanwheel, in the often frustrated hope that the left Scanwheel would not receive interference at the same time as the right Scanwheel. This mode of interference avoidance was designated Mode 12. Also attempted were all combinations of primary and secondary Control Logic Assembly (CLA) power supplies. During revs 626 to 628 on day 221, both right and left Scanwheels were used simultaneously in the intended normal mode of operation; Figure 3-22 shows the effect of interference in this mode.

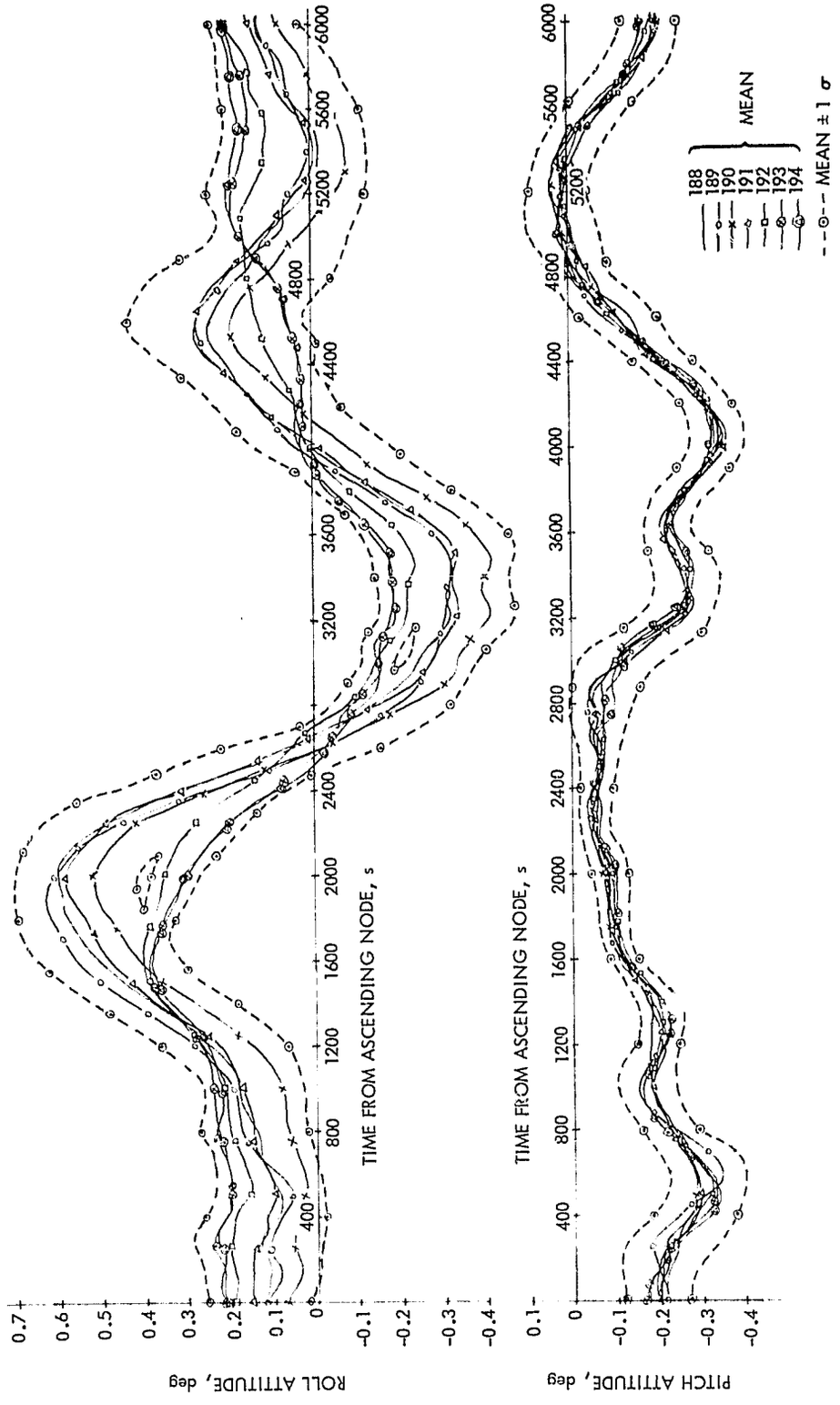

Figure 3-19. One-Sigma Attitude Envelopes for Days 188-194

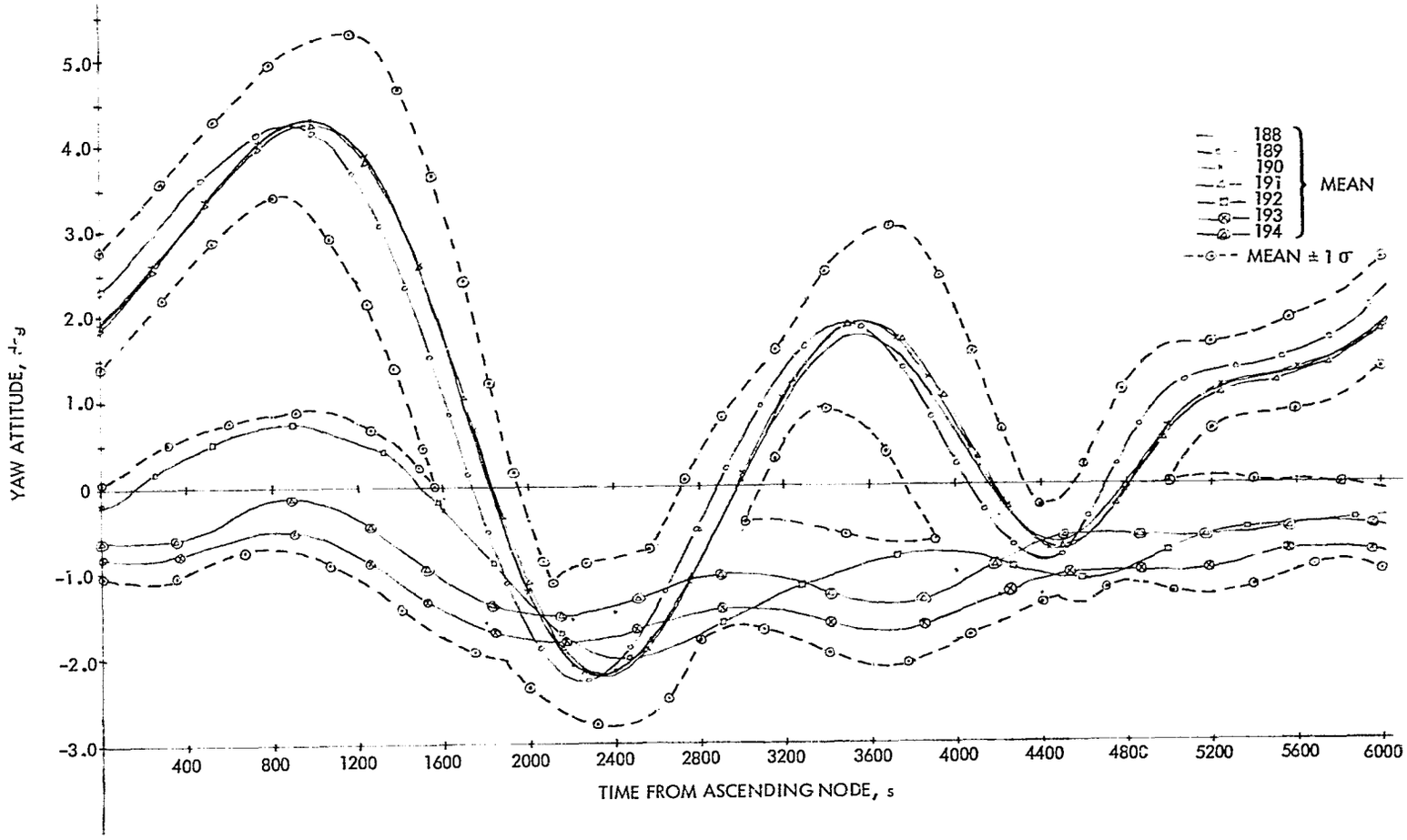

Figure 3-19. One-Sigma Attitude Envelopes for Days 188-194 (Continuation 1)

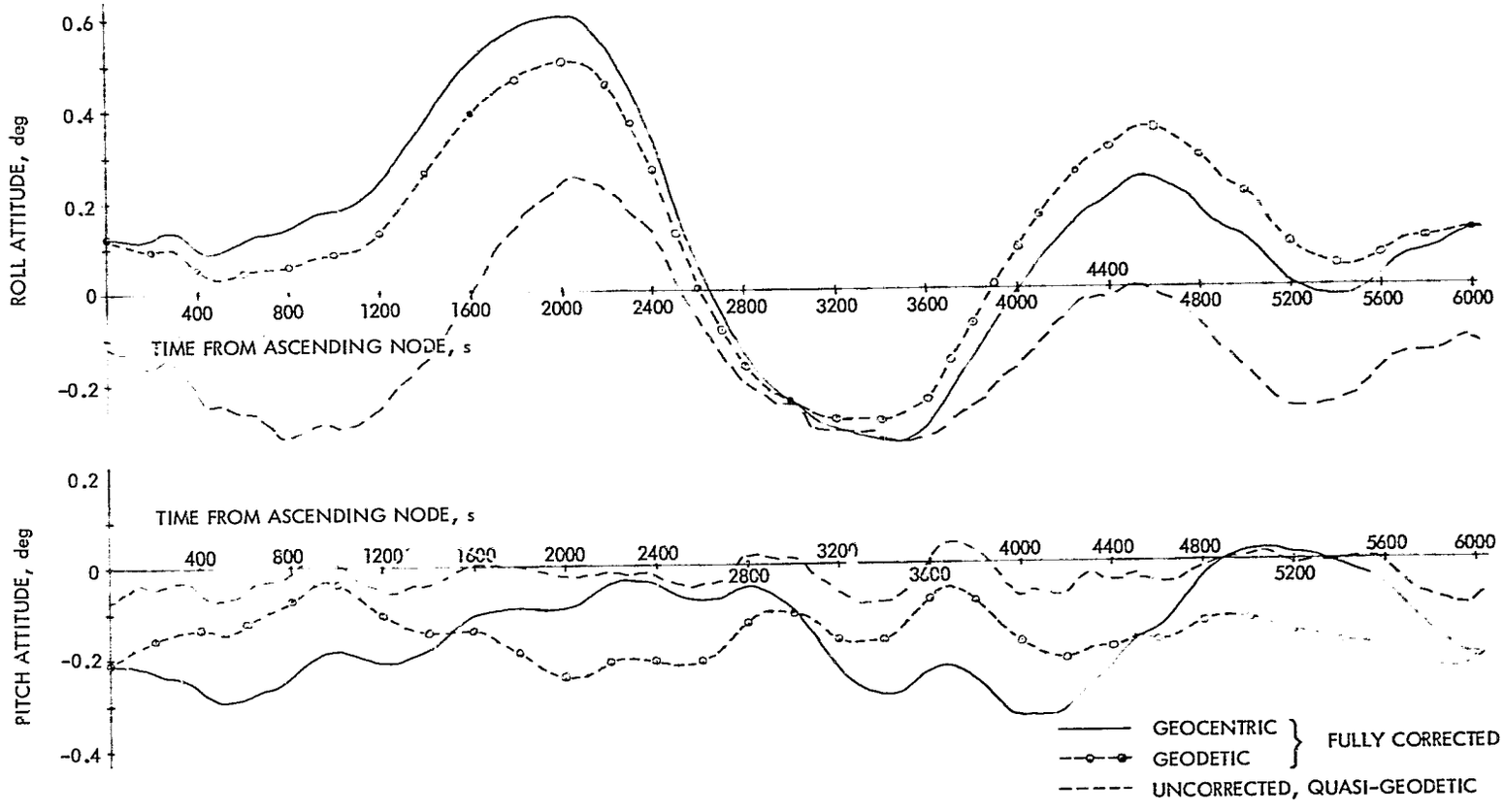

Figure 3-20. Corrected Versus Uncorrected Pitch and Roll (Mean for Day 188)

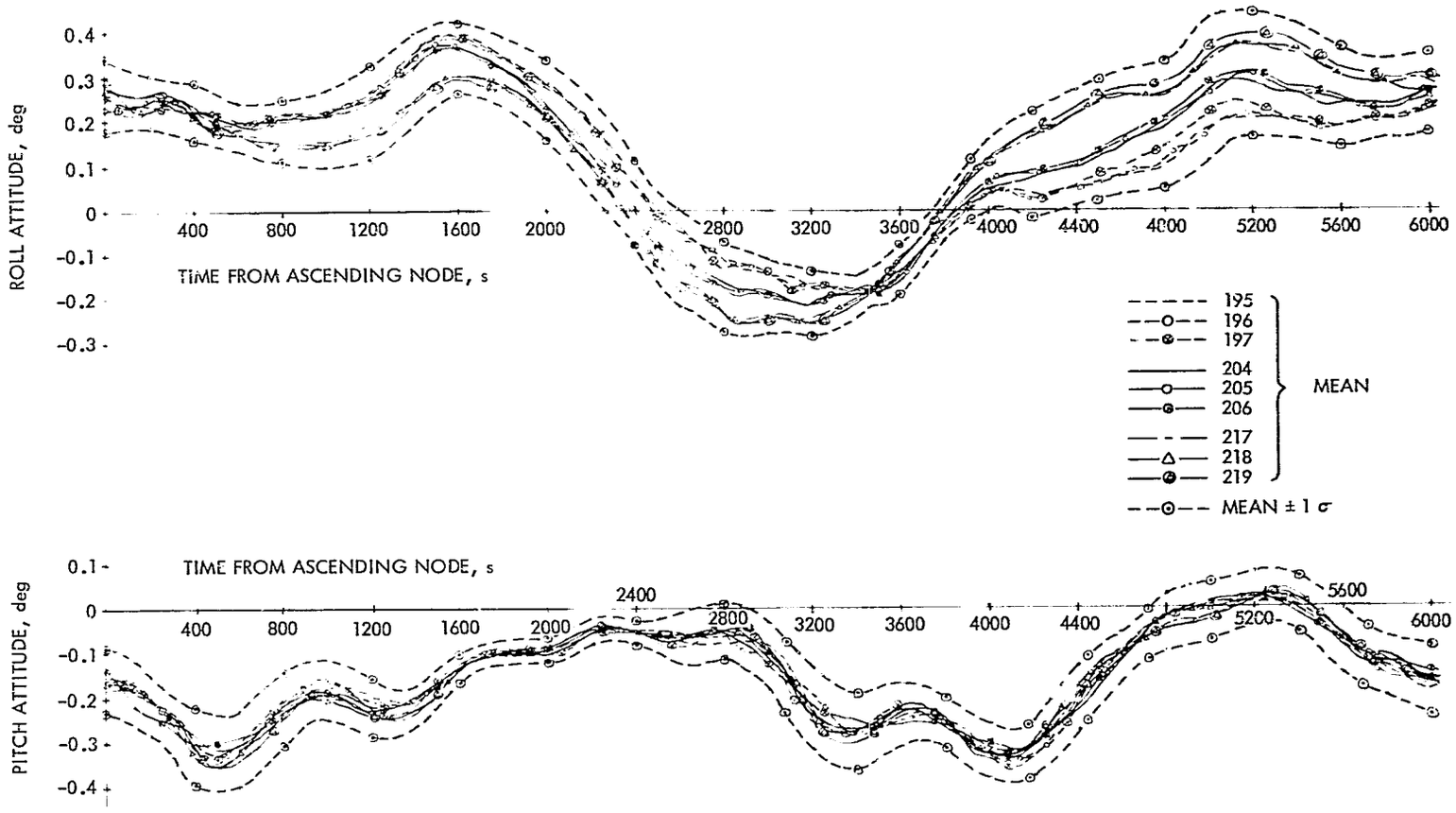

Figure 3-21. One-Sigma Attitude Envelopes for Days 195-219

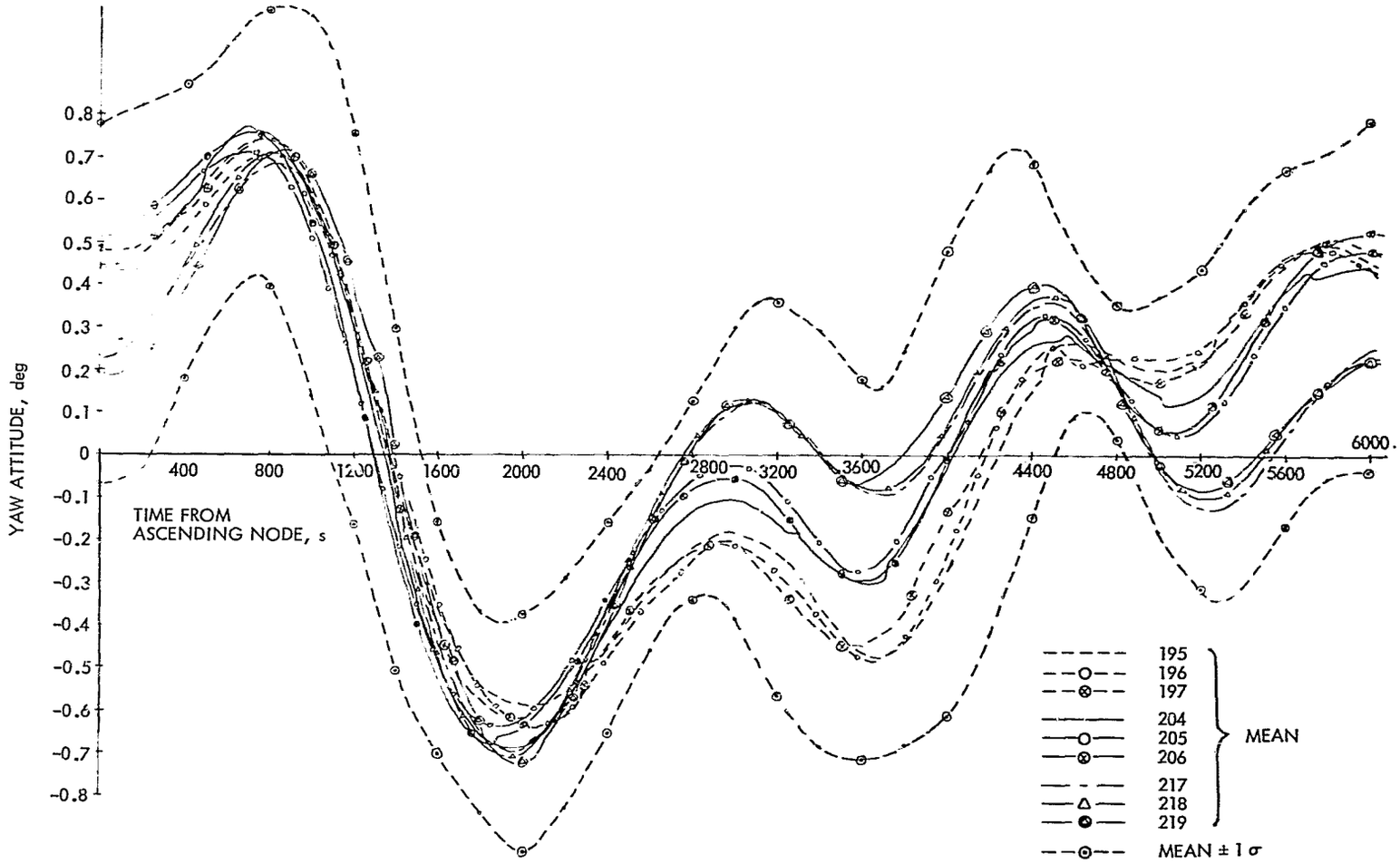

Figure 3-21. One-Sigma Attitude Envelopes for Days 195-219 (Continuation 1)

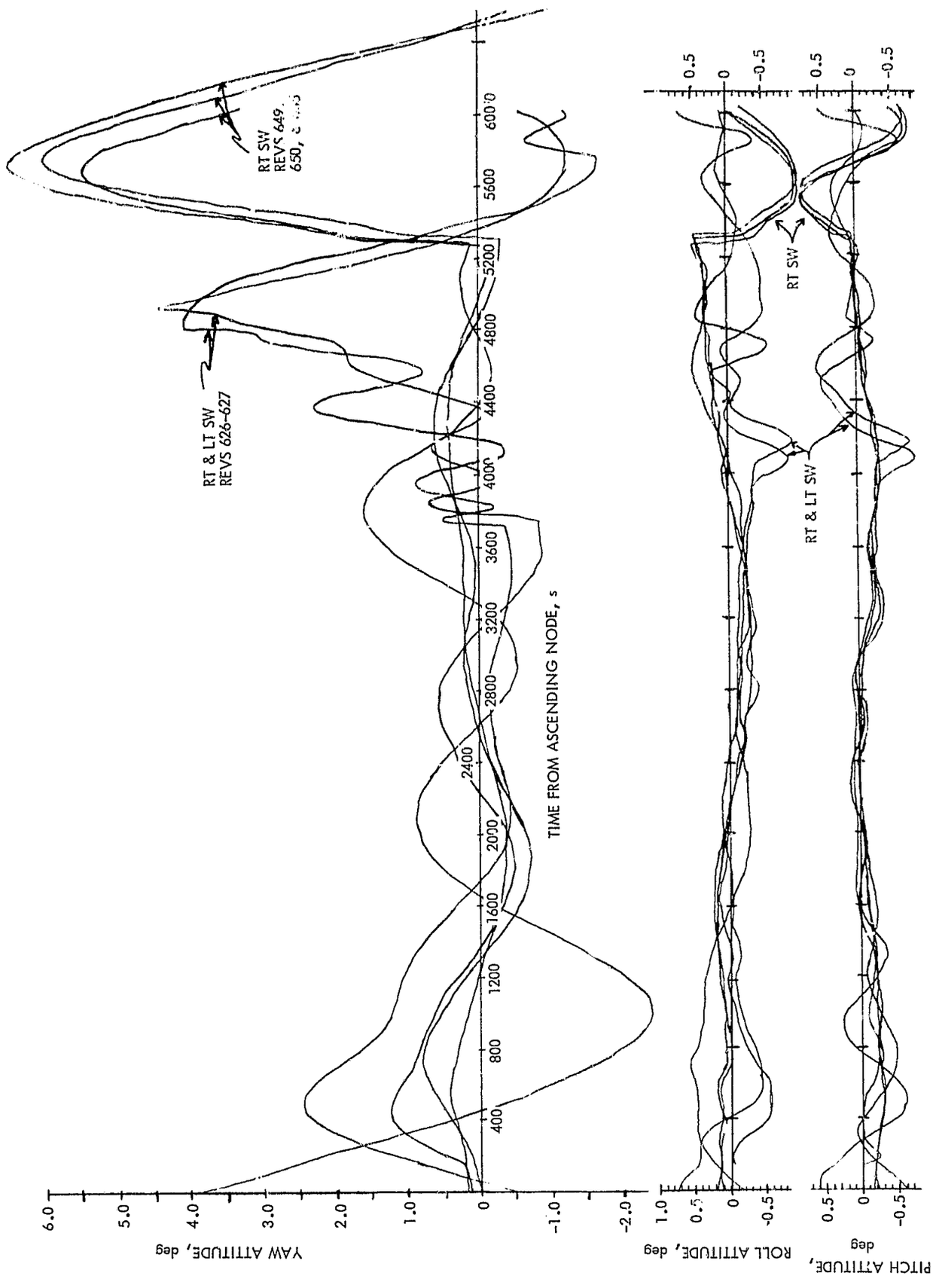

Figure 3-22. Examples of Scanwheel Interference (Days 221 and 223)

C-2

Figure 3-23 gives examples of attitude behavior when Mode 12 was used. Note the transients in all three axes when the signal processor switch was made. Pitch and roll from the left Seamwheel were each approximately 0.4 deg less (more negative) than the equivalent value from the right Seamwheel. The variation in this difference was about 0.3 deg, taken over the complete period in which Mode 12 was used. Review of the raw, unfiltered telemetry data indicated that the left Seamwheel experienced some level of sun interference almost every time it was switched in, which largely accounted for the observed transient. There was, in addition, some constant bias such as that observed for the right Seamwheel, but there were insufficient good data and available resources to permit a valid bias determination. Therefore, a bias value of zero was used in the production of all attitude records from the left Seamwheel. Table 3-2 shows the bias values applied to the data as a function of CLA power supply and signal processor selection. Table 3-3 shows times during which the Table 3-2 values were applied, and lists all OACS mode changes during this period.

Of all OACS control modes tried during this period, the "best" appeared to be what was called Mode 5, which was disconnection of the roll control signal during the expected period of interference. Figure 3-24 shows 5 revolutions at the end of day 225 during which this mode was applied. Although the scale for Figures 3-22 and 3-24 are different, these illustrations can be compared to see how Mode 5 improved overall attitude behavior in the presence of right Seamwheel interference. It can be seen that pitch became approximately normal, roll was roughly similar, and yaw excursions were reduced about 50 percent. When roll control was disconnected, on-board roll determination remained operative, so the interference could still be seen. Roll telemetry during Mode 5 showed a greatly reduced interference transient superimposed on the smooth attitude change due to the roll wheel momentum being driven toward the null (bias) value.

Table 3-2. Pitch and Roll Bias Values

Bias Set	Mode Select Status		Bias Values, deg			
	CLA Power Supply	Signal Processor	Coarse Pitch	Coarse Roll	Fine Pitch	Fine Roll
1	1	Right	-0.07	+0.02	+0.12	+0.01
2	2	Right	-0.02	+0.06	+0.11	+0.10
3	1 & 2	Right	-0.045	+0.04	+0.115	+0.045
4	Any	Left	0.0	0.0	0.0	0.0
5	Any	Right and Left	0.0	0.0	0.0	0.0

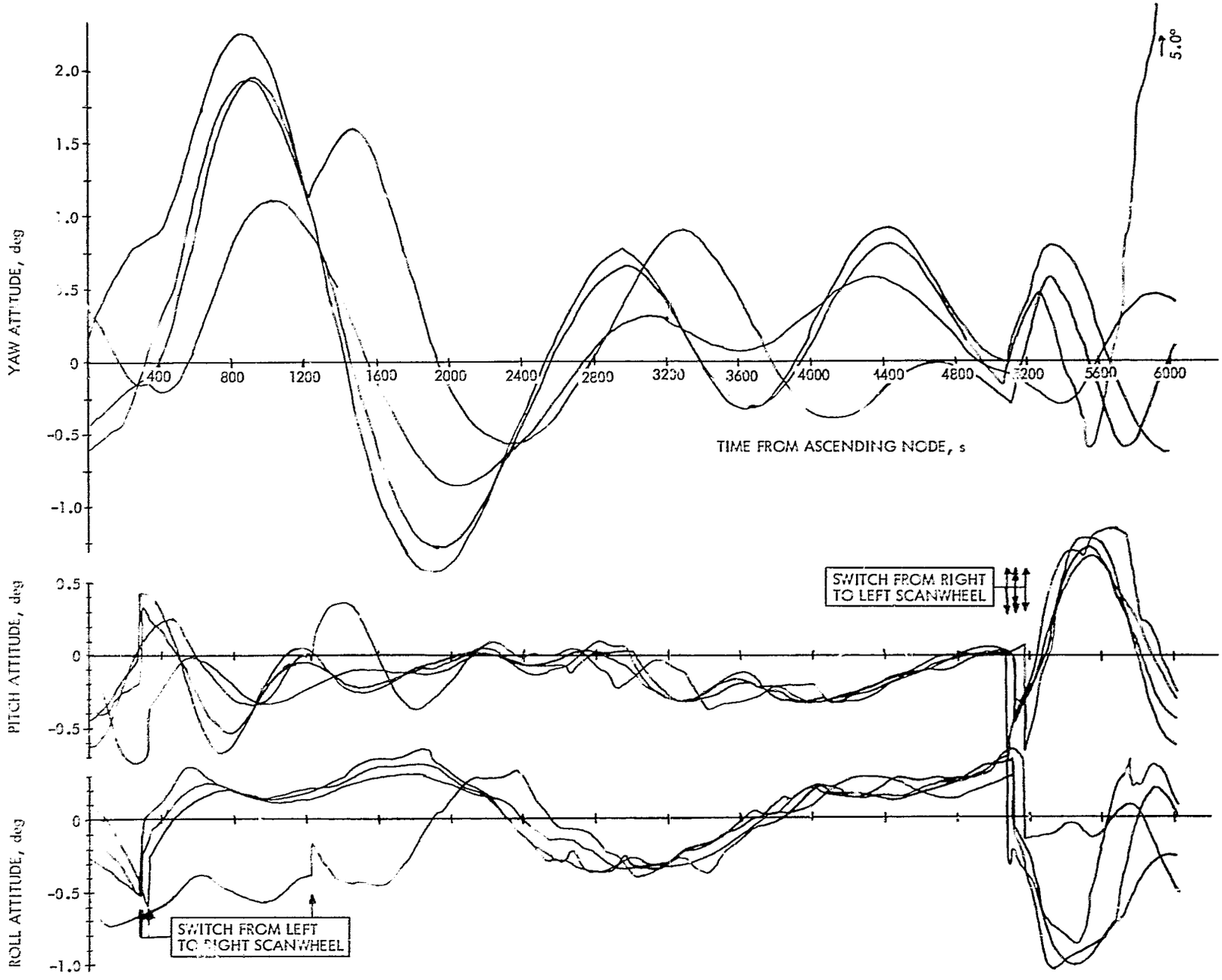

Figure 3-23. Examples of OACS Mode 12 (Day 220, Revs 608-611)

Table 3-3. OACS Mode Changes - Days 220 Through 225

Day (1978)	Event (GMT), Hr:Min:Sec	Mode Status Duration (Seconds From Ascending Node)		Mode Select Status			Pitch and Roll Bias Set
		From (Rev)	To (Rev)	CIA Power Supply	Signal Processor	Roll Attitude Signal	
to 220			5441 (607)	1	Right	Connected	1
220	17:06:01	5442 (607)	334 (608)	1 & 2	Left	Connected	4
220	17:11:47	335 (608)	5163 (608)	1 & 2	Right	Connected	3
220	18:52:01	5164 (608)	1225 (609)	2	Left	Connected	4
220	19:31:01	1226 (609)	5125 (609)	1 & 2	Right	Connected	3
220	20:12:01	5126 (609)	289 (610)	1 & 2	Left	Connected	4
220	20:51:07	290 (610)	5118 (610)	1 & 2	Right	Connected	3
220	21:32:31	5119 (610)	281 (611)	1 & 2	Left	Connected	4
220	22:12:37	282 (611)	5080 (611)	1 & 2	Right	Connected	3
220	22:52:31	5081 (611)	243 (612)	1 & 2	Left	Connected	4
220	23:32:37	244 (612)	5043 (612)	1 & 2	Right	Connected	3
220	00:13:01	5043 (612)	236 (613)	1 & 2	Left	Connected	4
220	00:53:07	237 (613)	5155 (613)	2	Right	Connected	2
220	23:00:00	5155 (613)	192 (614)	2	Right	Disconnected	2
220	23:23:00	193 (614)	5022 (614)	2	Right	Connected	2
220	23:43:31	5028 (614)	6017 (614)	1 & 2	Left	Connected	4
221	00:00:00	6017 (614)	609 (615)	1 & 2	Left	Connected	4
221	00:10:31	610 (615)	5049 (615)	1 & 2	Right	Connected	3
221	01:24:31	5050 (615)	652 (616)	1 & 2	Left	Connected	4
221	01:51:31	653 (616)	5023 (616)	1 & 2	Right	Connected	3
221	03:05:31	5023 (616)	694 (617)	1 & 2	Left	Connected	4
221	03:32:31	695 (617)	5094 (617)	1 & 2	Right	Connected	3
221	04:46:31	5095 (617)	676 (618)	1 & 2	Left	Connected	4
221	05:13:31	677 (618)	5116 (618)	1 & 2	Right	Connected	3
221	06:27:31	5117 (618)	699 (619)	1 & 2	Left	Connected	4
221	06:54:31	700 (619)	4959 (619)	1 & 2	Right	Connected	3
221	08:05:31	4960 (619)	542 (620)	1 & 2	Left	Connected	4
221	08:32:32	543 (620)	5251 (620)	2	Right	Connected	2

Table 3-3. OACS Mode Changes - Days 220 Through 225 (Continuation 1)

Day (1978)	Event (GMT), H:min:s	Mode Status Duration (Seconds From Ascending Node)		Mode Select Status			Pitch and Roll Bias Set
		From (Rev)	To (Rev)	CLA Power Supply	Signal Processor	Roll Attitude Signal	
221	09:51:00	5251 (620)	5851 (620)	2	Right	Disconnected	2
221	10:01:00	5851 (620)	5213 (621)	2	Right	Connected	2
221	11:31:00	5213 (621)	256 (622)	2	Right	Disconnected	2
221	11:49:00	256 (622)	5296 (622)	2	Right	Connected	2
221	13:13:00	5296 (622)	578 (623)	2	Right	Disconnected	2
221	13:35:00	578 (623)	165 (626)	2	Right	Connected	2
221	18:30:01	166 (626)	3690 (628)	2	Both	Connected	5
221	22:50:00	3690 (628)	1852 (629)	2	Right	Connected	2
222-224	00:00:00	1852 (629)	1432 (672)	2	Right	Connected	2
225	00:00:00	1432 (672)	4648 (675)	2	Right	Connected	2
225	05:55:30	4649 (675)	5549 (675)	1 & 2	Left	Connected	4
225	06:10:31	5550 (675)	4633 (676)	1 & 2	Right	Connected	3
225	07:35:53	4634 (676)	5534 (676)	1 & 2	Left	Connected	4
225	07:50:54	5535 (676)	4619 (677)	1 & 2	Right	Connected	3
225	09:16:16	4620 (677)	5520 (677)	1 & 2	Left	Connected	4
225	09:31:17	5521 (677)	4604 (678)	1 & 2	Right	Connected	3
225	10:56:39	4605 (678)	5505 (678)	1 & 2	Left	Connected	4
225	11:11:40	5506 (678)	1423 (681)	1 & 2	Right	Connected	3
225	15:05:30	1423 (681)	4835 (682)	2	Right	Connected	2
225	17:43:00	4835 (682)	5315 (682)	2	Right	Disconnected	2
225	17:51:00	5315 (682)	4826 (683)	2	Right	Connected	2
225	19:23:28	4826 (683)	5306 (683)	2	Right	Disconnected	2
225	19:31:28	5306 (683)	4816 (684)	2	Right	Connected	2
225	21:03:56	4816 (684)	5296 (684)	2	Right	Disconnected	2
225	21:11:56	5296 (684)	4806 (685)	2	Right	Connected	2
225	22:44:24	4806 (685)	5286 (685)	2	Right	Disconnected	2
225	22:52:24	5286 (685)		2	Right	Connected	2

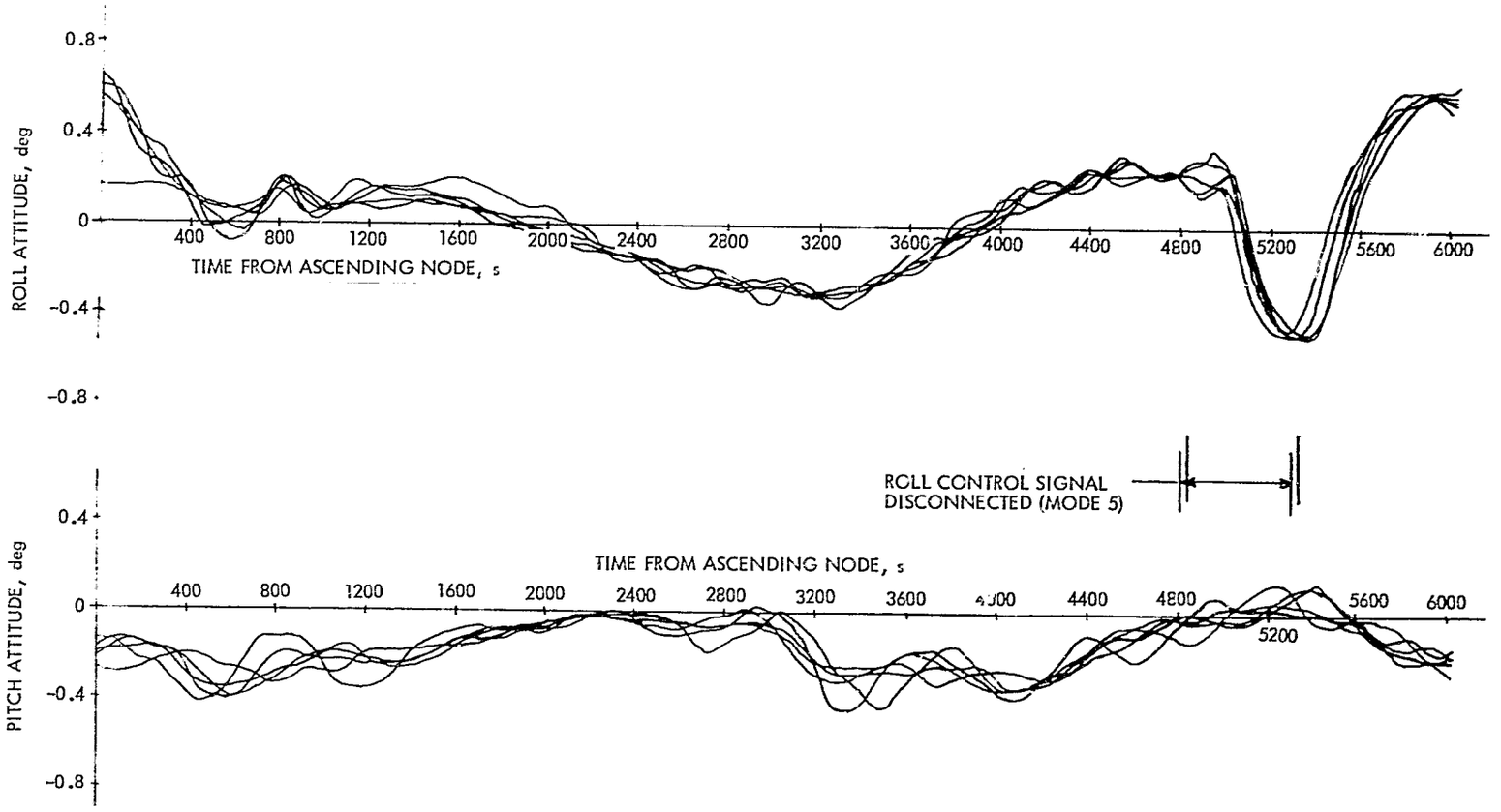

Figure 3-24. Examples of OACS Mode 5 (Day 225, Revs 682-686)

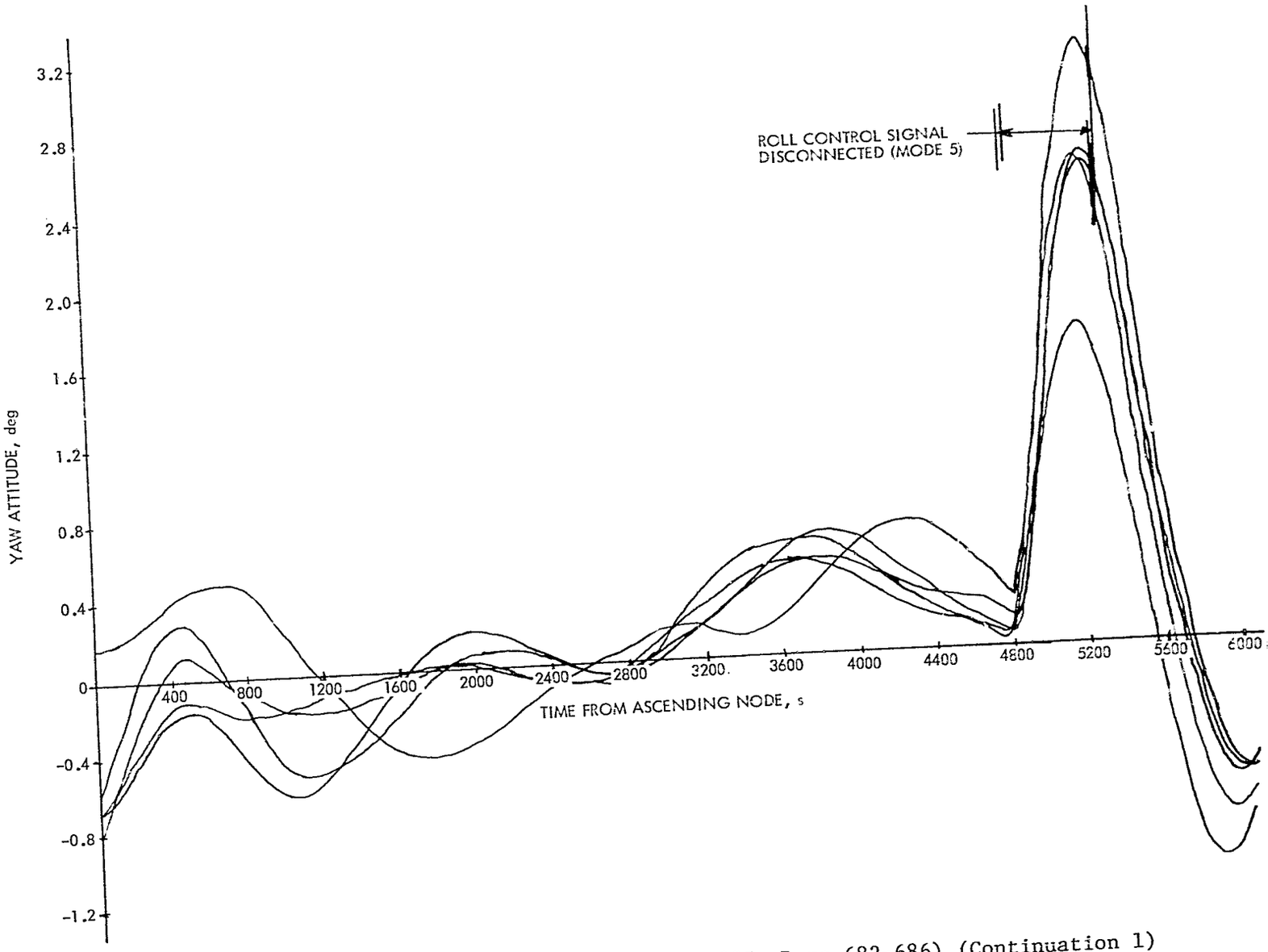

Figure 3-24. Examples of OACS Mode 5 (Day 225, Revs 682-686) (Continuation 1)

The yaw excursion was precession due to the roll torque acting on the pitch momentum bias. The pitch interference effect disappeared under Mode 5 (see Section 2.4 of Reference 3-5). The fact that the interference phenomenon moderated so strongly when the roll control signal was disconnected is a clue to the cause of the interference, but no resources have been applied to analyze this. Mode 5 was used to avoid the interference phenomenon from day 225 through day 255, when the geometry of the sun track finally precluded any intersection with the Scanwheel FOV.

4. Period of Cruise in Mode 5 (Days 225-255)

Mode 5 was used on a regular basis to moderate the effects of Scanwheel interference until the geometry of the sun track finally precluded any intersection with the Scanwheel FOV on day 255. The time points of roll control disconnect and reconnect were adjusted regularly to track the predicted times of such interference. Figure 3-25 shows the characteristic functions and the schedule for these mode switches over the early part of this period. The time span of disconnected roll control was 8 min from the latter part of day 225 until the end of day 226, and was 6 min thereafter. The phasing of Mode 5 was as shown in Figure 3-25. The experimentation to find the most beneficial phasing is evident both in the schedule and in the results (decreased excursions in roll and yaw) though the results are also aided by changes in sun track geometry.

Figure 3-26 shows the characteristic functions and Mode 5 schedule for the latter part of this period. On day 247 the sun track began to intersect the active FOV of the Scanwheel (near the Earth horizon), producing both pitch and roll disturbances near both leading and trailing edge horizon crossings. This phenomenon was expected from pre-launch analyses, and it lasted for 8 days. Beginning on day 248, Mode 5 was used for a 6-min span twice each revolution, as shown in the schedule of Figure 3-26. Interference in the active FOV had an obviously stronger effect on Scanwheel performance than interference in the blanked FOV, as can be seen by comparing Figures 3-25 and 3-26. Pitch by then had a marked response to both FOV crossings, roll response was about the same as previously, and yaw response was stronger. Because there was no sun sensor coverage (see Figure 2-12) for the northern FOV crossing, the yaw response to Mode 5 for that interval is not directly determinable. Figure 3-26 shows the results of the interpolation algorithm, which is of too low an order to accurately compute such a transient. The tightness of the 1σ boundary in this region is further evidence of the algorithm's low order. The southern FOV crossing was largely observed by the sun sensor and, therefore, is accurately portrayed. The roll response to the northern Mode 5 application is rather weaker than to the southern. An analysis of wheel speeds, if it were available, would probably show that Scanwheel speeds were near the bias value at the northerly roll disconnect and relatively far from bias at the other disconnect.

Figure 3-27 gives two samples of attitude behavior under control of ascent stage gyros with torque supplied by thrusters. The examples chosen were the calibration burns on days 227 and 235, and the plots are phased relative to start of the burn. Each burn was 60-s long, and the two burns were in opposite directions. This fact can be seen in the attitude response to thruster

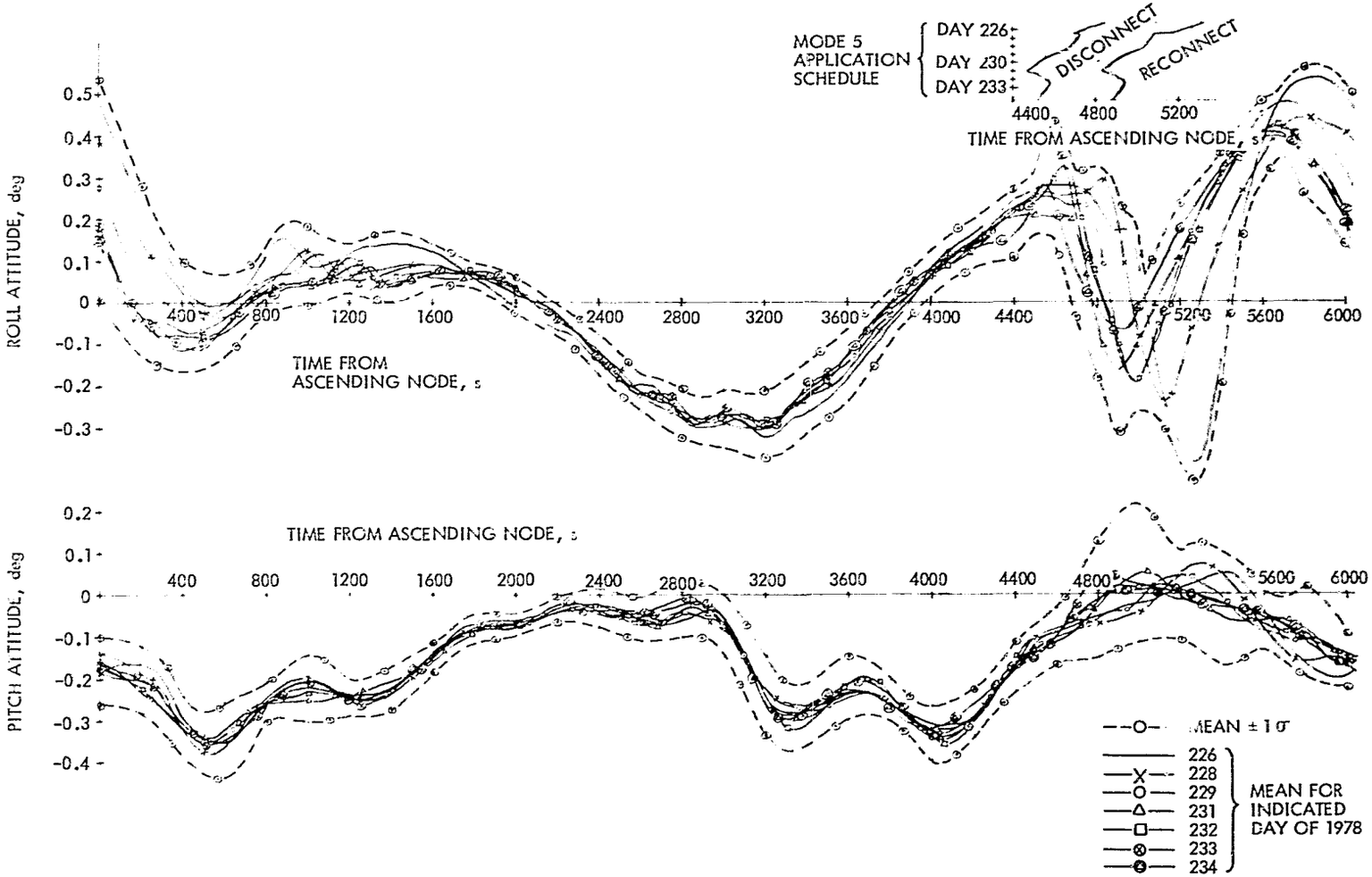

Figure 3-25. One-Sigma Attitude Envelopes for Days 226-234

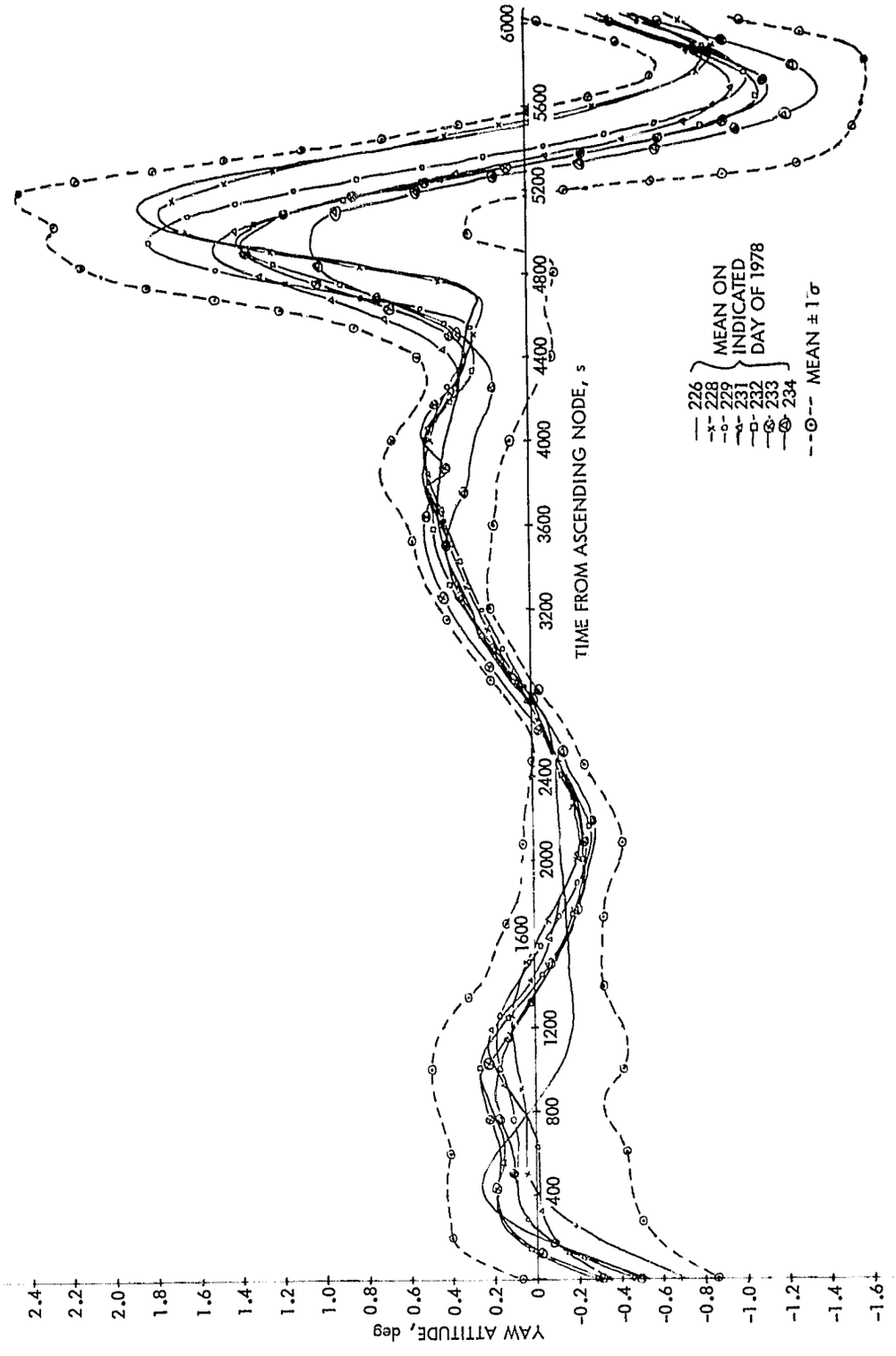

Figure 3-25. One-Sigma Attitude Envelopes for Days 226-234 (Continuation 1)

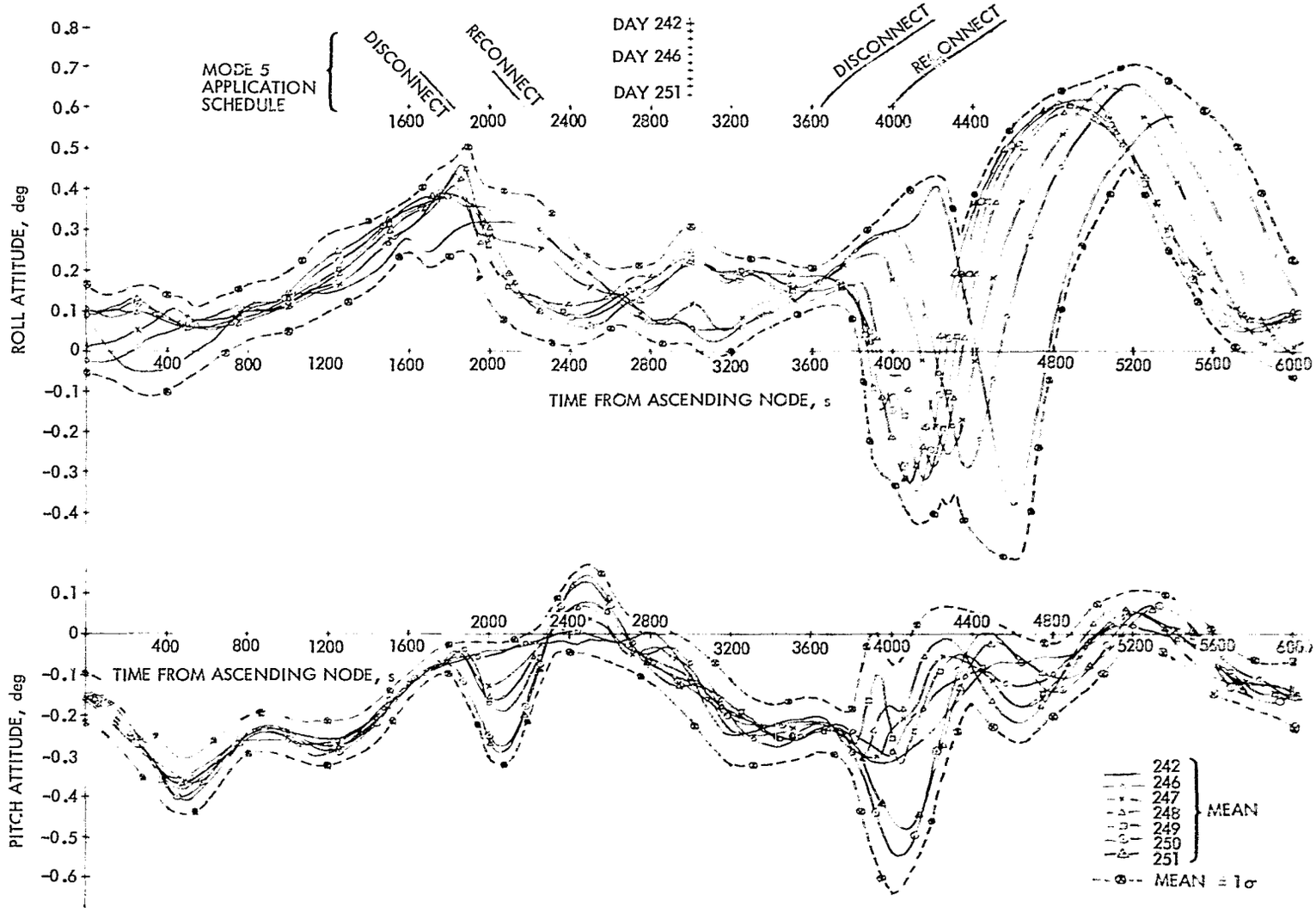

Figure 3-26. One-Sigma Attitude Envelopes for Days 242-251

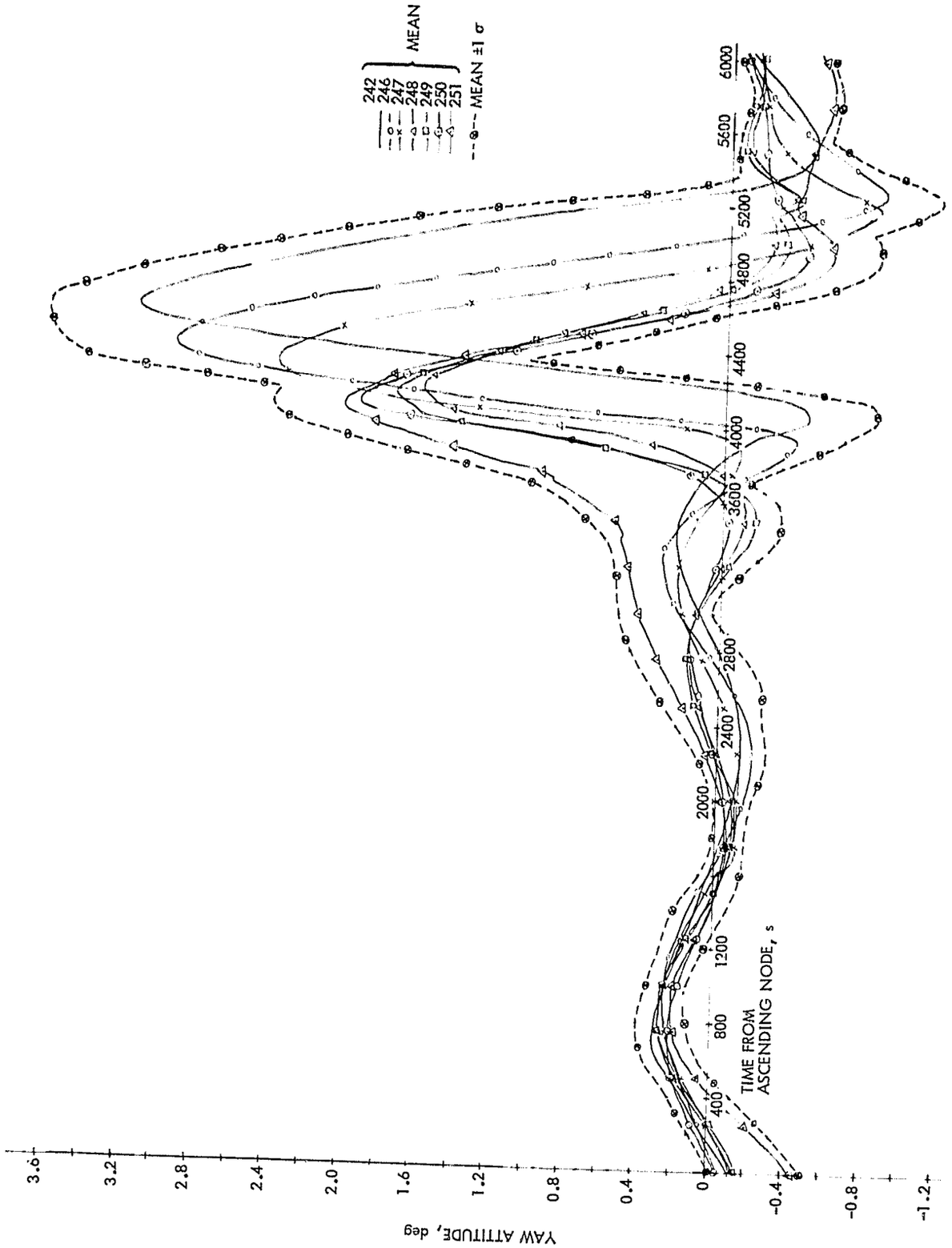

Figure 3-26. One-Sigma Attitude Envelopes for Days 242-251 (Continuation 1)

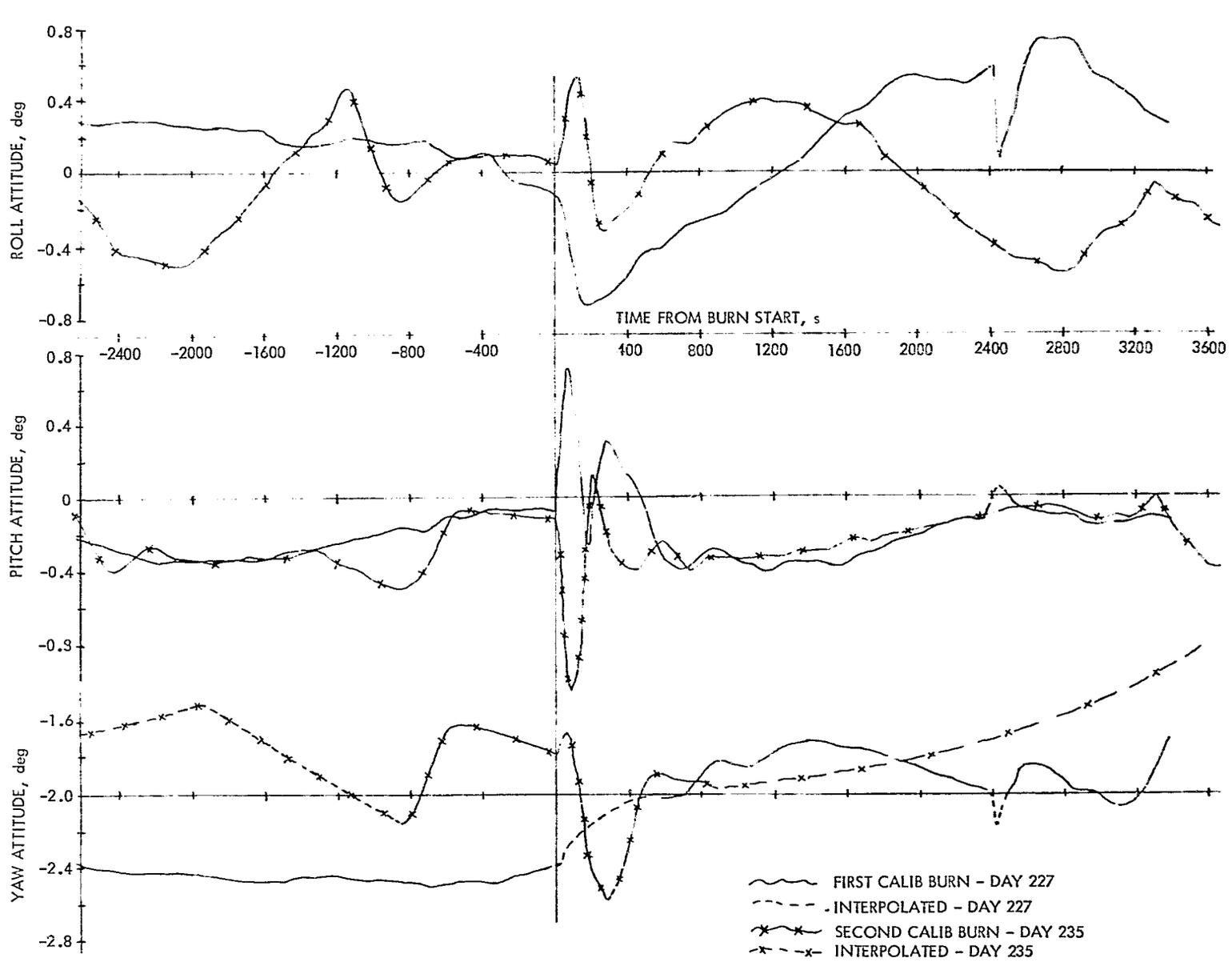

Figure 3-27. Attitude Behavior - RCS Control and Burns

misalignment with respect to spacecraft center-of-gravity. Note the -2 deg offset of yaw, caused by gyro misalignment. The transient observable at burn plus 2400 s on day 227 coincides with no recorded command. The switch from thruster/gyro to reaction wheel (normal mode) control occurred a little after burn plus 3000 s on both days, and resulted in a smooth changeover.

5. Second Quiescent Data Acquisition Period (Days 256-283)

Figure 3-28 shows the characteristic functions for the latter part of the mission. It can be termed quiescent because it includes no sun interference, no Mode 5, and no maneuvers. The operational mode was the same as in the first such period (days 195-219). Comparison of Figures 3-21 and 3-28 shows many similarities and some interesting differences. Pitch is almost identical; roll differs primarily in the phase of the altitude correction; yaw in the later period is mostly interpolated based on the average behavior in the earlier period, and looks similar for that reason. Yaw was directly observed (see Figure 2-12) by sun sensor head 2 near the south pole during each rev in this period, and by sun sensor head 3 near the north pole beginning around day 274. Note that the yaw interpolation algorithm, due to its lower order, tends to supply essentially the same estimated yaw function of time for all yaw data gaps. The accuracy with which this estimate represents true yaw behavior will be examined in subsequent sections.

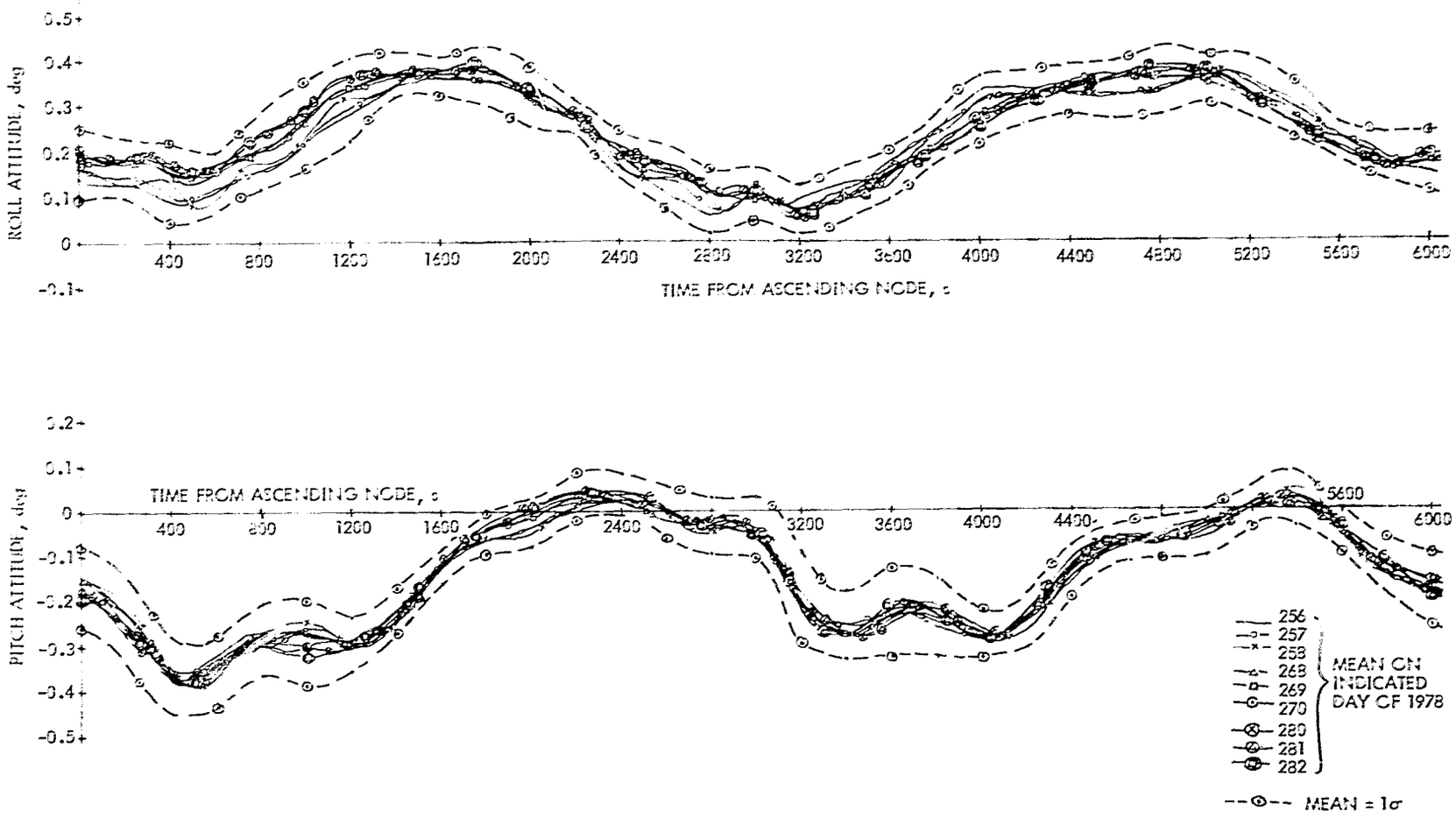

Figure 3-28. One-Sigma Attitude Envelopes for Days 256-282

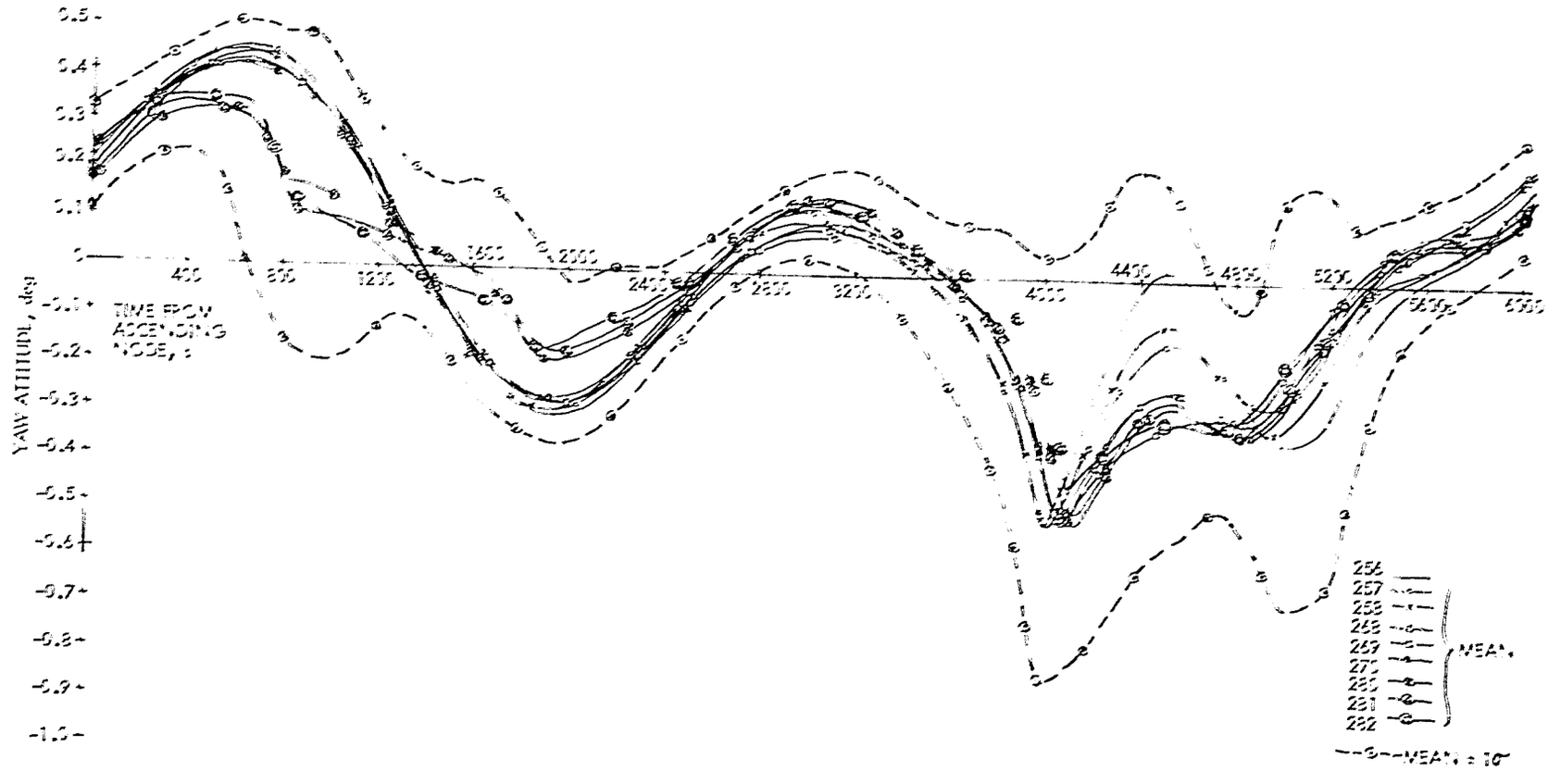

Figure 3-23. One-Sigma Attitude Envelopes for Days 256-282 (Continuation 1)

SECTION IV

YAW AD PARAMETER ESTIMATION

A. INTRODUCTION

In Subsection II-B-3, the Seasat yaw interpolation method was described. For the algorithm to have acceptable accuracy, JPL was required to specify for GSFC the values and time period of applicability of the constant parameters in Table 2-3. The JPL analysis that estimated these parameters was based on the repeatability of yaw as a function of sub-spacecraft latitude and as a function of a simplified model of yaw/roll cross-coupling. Data from the first trimmed quiescent cruise period (days 195-219) were used to estimate parameters for the second such period (days 256-283). Data from the early part of the Mode 5 cruise period were used to estimate parameters for the latter part of that period. Data from the first two propulsive maneuvers (days 227 and 230) were used to estimate parameters for all periods under RCS/gyro control.

B. DATA PROCESSING OVERVIEW

A set of undocumented developmental programs was used to help estimate yaw AD parameters from GSFC DAFs using the JPL Univac 1108 computer. The first step was to copy the DAF from the GSFC-supplied AOT tape to a Univac 1108-compatible tape; this process was performed on the JPL IBM 360 computer. Then the DAF (still in the IBM format) was processed by a Univac 1108 number-crunching program to produce (1) an edited (time and attitude values only) file in Univac 1108 "blank" format of all of the attitude records for the given day of data, and (2) a file, also in blank format, of the mean and standard deviation for each axis at 242 equally spaced phases of the orbit (integer multiples of 25 s from ascending node). The mean and standard deviation attitude functions were used to characterize attitude behavior as described in Subsection III-C; the mean function was also used in another Univac 1108 program to find the best (least-squared-error) fit truncated Fourier series for that day of data. The parameters of several such (daily) Fourier fits were evaluated to determine the most appropriate fit over several days to estimate the K_i parameters for the yaw interpolation algorithm. The edited file of all of the attitude data for a given day was processed by yet another Univac 1108 program to find the least-squared-error fit to the four parameters (two of magnitude, two of phase)of the simplified yaw/roll coupling model. The parameters of several of these fits were then evaluated to determine the most appropriate set to use for K_R, K_{RD}, t_R, and t_{RD} in the yaw interpolation scheme.

Because the Seasat OACS time constant (equivalent) in yaw was 3 or 4 times as large as the roll axis time constant, roll data had to be significantly smoothed before estimating the yaw/roll coupling parameters. The JPL estimation program used a cubic spline fit to roll on 300-s centers; GSFC AD software used a Chebychev polynomial instead of a spline fit but obtained similar results

The uncertainties of the Fourier fit predict and of the yaw/roll coupling model were also established. For the predict model, the following variances were summed:

(1) Actual attitude in the reference era with respect to its mean attitude function.

(2) Average (mean) function with respect to its Fourier approximation.

(3) Overall Fourier approximation with respect to the average function of available attitude data in the target era.

In the latter part of the Mode 5 cruise period, there were no applicable data from which to estimate item (3), so it was estimated as an arbitrarily large value for interpolations in that period only. The variance of the yaw/roll coupling model was estimated in a manner similar to that described for the predict, but item (1) was not included since actual, rather than average, data was used directly in estimating the parameters. The uncertainties estimated were used directly in the yaw interpolation algorithm.

C. DATA PROCESSING DETAIL

1. Fourier Series Approximation

To obtain a prediction function for yaw behavior, actual yaw data over a reference period of available data was characterized as a truncated (bias through fourth harmonic) Fourier series based on time from ascending node. Although the orbital period varied over the course of the mission (Figure 4-1), this created no first-order error for the predict function, since the Fourier series was expressed in terms of orbital central angle. Therefore, although the attitude data was expressed relative to time, it was analyzed and characterized in a time-normalized sense.

The program YAWFIT (which obtained the least-squared-error fit of the truncated series to a file of average yaw attitude versus time) would first subtract the effect of solar torque for the day the data was taken and add the solar torque effect for a given target data. The solar torque model used for this calculation was a simplified version of that published by LMSC as Reference 4-1, and the effects on spacecraft attitude were computed through a linearized OACS model as published in Reference 4-2. Required as inputs to the program were sun beta angle (Figure 4-2) and the orbital phase angle of sun nadir (Figure 4-3) for both the day the reference data was taken and for the day for which the predict would be made. The solar torques on the two days were generally quite different relative to each other, but in practice they accounted for only a minor proportion of total yaw behavior.

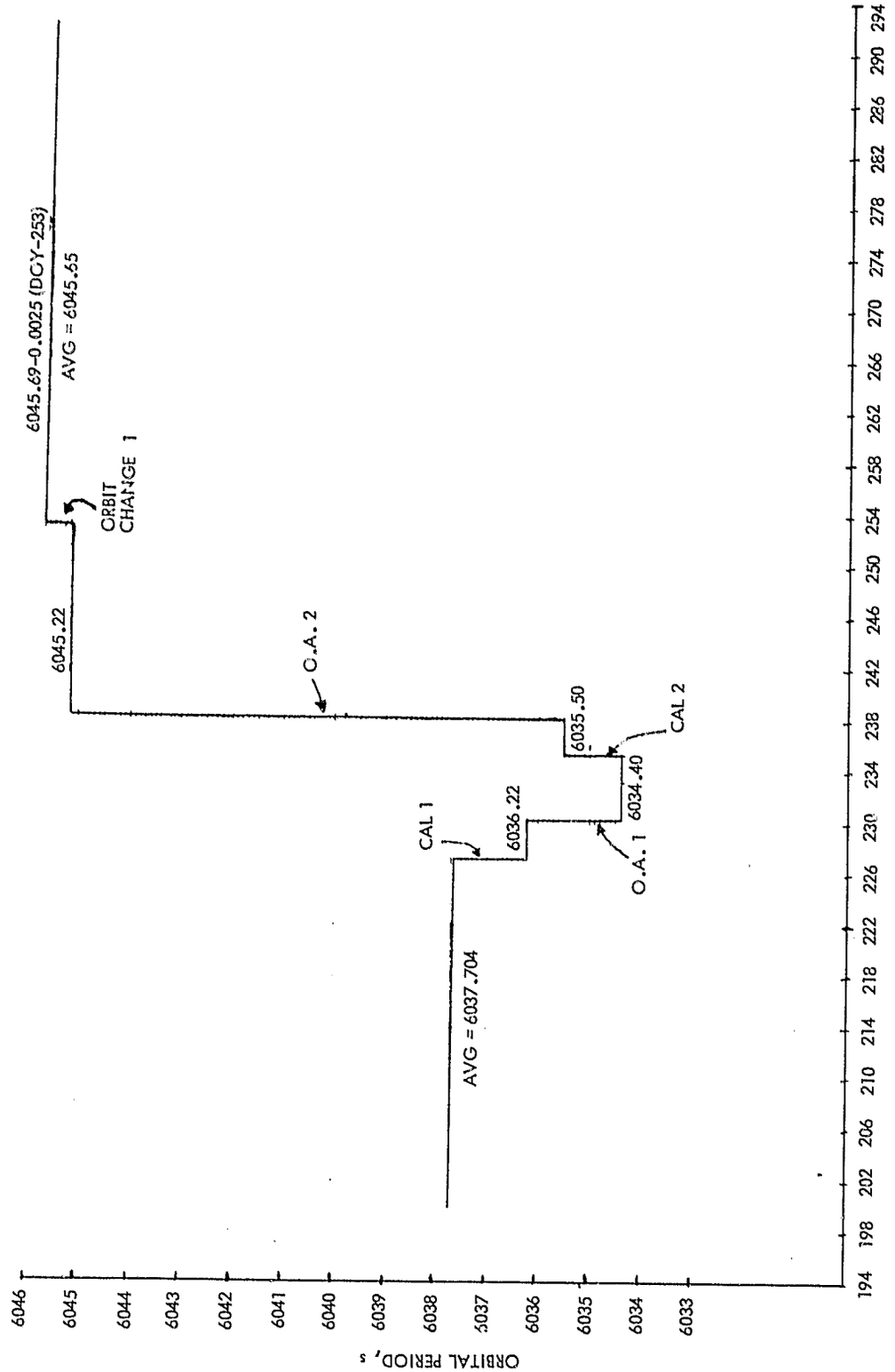

Figure 4-1. Seasat Orbital Period History

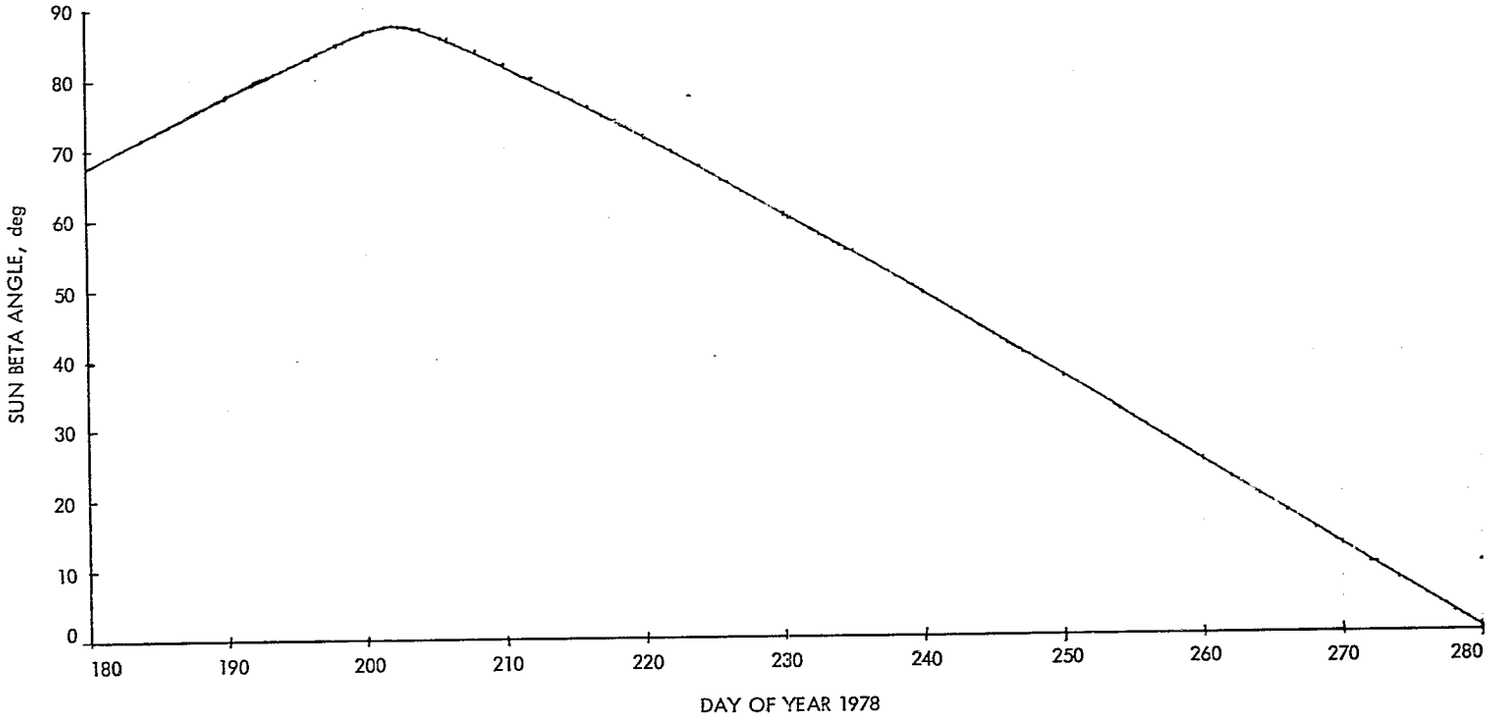

Figure 4-2. Sun Beta Angle History

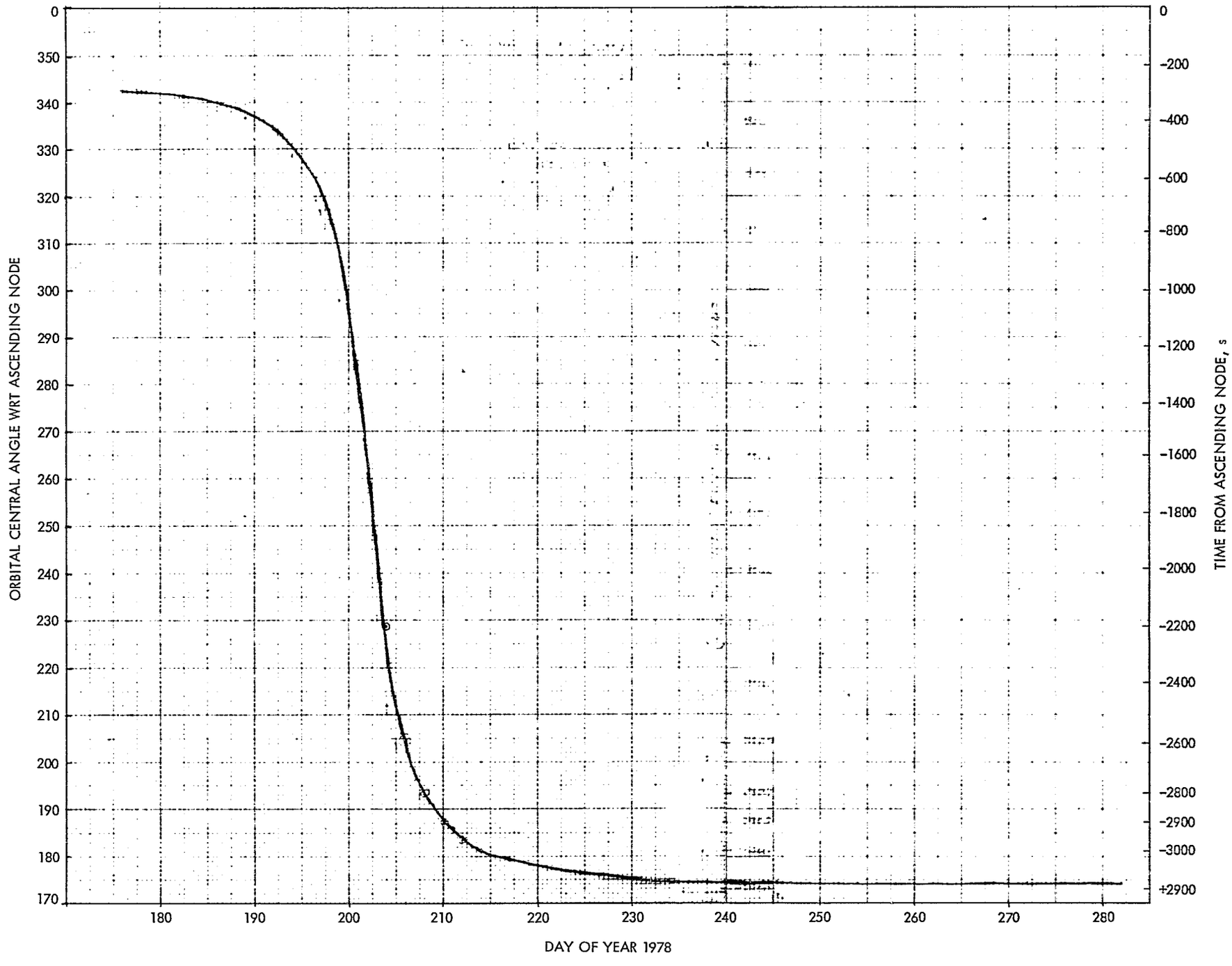

Figure 4-3. Sun Nadir Position Relative to Ascending Node

a. Quiescent Period. To prepare a predict function for the second quiescent period (days 256-282), the data of the first such period (days 195-219) was analyzed. Figure 3-21 gives examples of the average attitude functions in the reference period. Over 80 percent of the available data in this period was used in the analysis. Plots of individual Fourier term coefficients versus data day showed some cyclic behavior over the 25-day span, but the information was insufficient to justify extrapolation of the cycles to the target era 50-80 days later; therefore, the mean value over an apparent half-cycle was selected for each component to form the Fourier series characteristic of the reference era.

Figure 4-4 gives two examples of the average yaw function for a day in the reference period versus both the truncated Fourier approximation for that day and the truncated Fourier series used to characterize the entire reference period. The effect of series truncation at fourth orbital harmonic can be seen in the comparison of daily average function with daily Fourier approximation; overall standard deviation of this effect was near 0.04 deg. The differences between the individual Fourier approximations for days within the reference period and the overall Fourier series for that entire period has a standard deviation of about 0.10 deg. If the variation of actual yaw data with respect to the average yaw function for each day is taken into account, it is found that the overall truncated Fourier series can characterize the reference period yaw behavior with a statistical accuracy of about 0.27 deg (1σ).

This accuracy of characterization is actually a function of orbital phase, ranging from 0.11 deg to 0.40 deg (1σ), and is shown as an envelope about the overall Fourier function in Figure 4-5. To indicate this function's accuracy in predicting yaw behavior for the second quiescent period (days 256-283), the average yaw functions for several selected days within the later period are also plotted in Figure 4-5. Yaw was directly observable for only a part of each revolution because of sun sensor FOV limitations. The yaw plotted between 4100 and 5100 s was corrected for the alignment errors determined for sun sensor head 2 (see Figure 3-6). (Without this correction, these yaw functions would be approximately 0.2 deg more negative; that the correction improves the comparison with the first quiescent period adds confidence to the alignment analysis.) The yaw plotted between 850 and 1900 s is from sun sensor head 3; this head was apparently misaligned also (see Subsection III-C), but the range of data is insufficient to estimate the parameters. Therefore, the average data from this head should be viewed as subject to constant errors of undeterminable magnitude and direction, but probably within an envelope of ±0.25 deg or so. This error is, of course, in addition to the normal variation of yaw about its mean function.

From the data in Figure 4-5, it can be determined that the RMS error between the overall Fourier F(t) and the yaw functions for days 273 and 282 is about 0.44 deg, if only sensor head 2 data is used for the comparison. On other days, this error is less, but, for conservatism, the larger value was assumed. Taking this RMS error as one standard deviation and combining it with the overall σ_F from Figure 4-5 leads to a value of 0.55 deg as the conservative 1σ accuracy of F(t) in predicting yaw for the period of days 256-282.

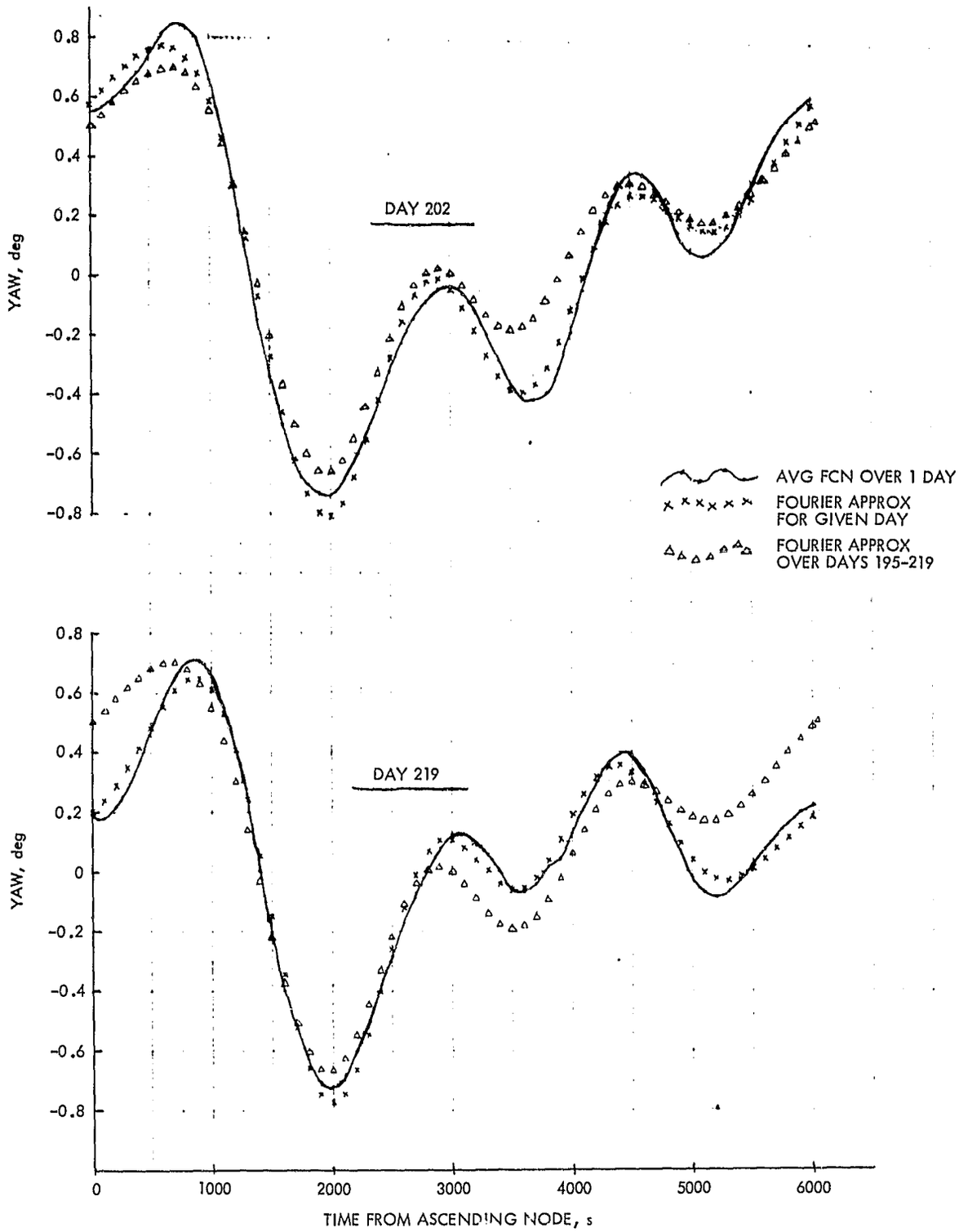

Figure 4-4. Daily Average Yaw versus Fourier Approximation - First Quiescent Period

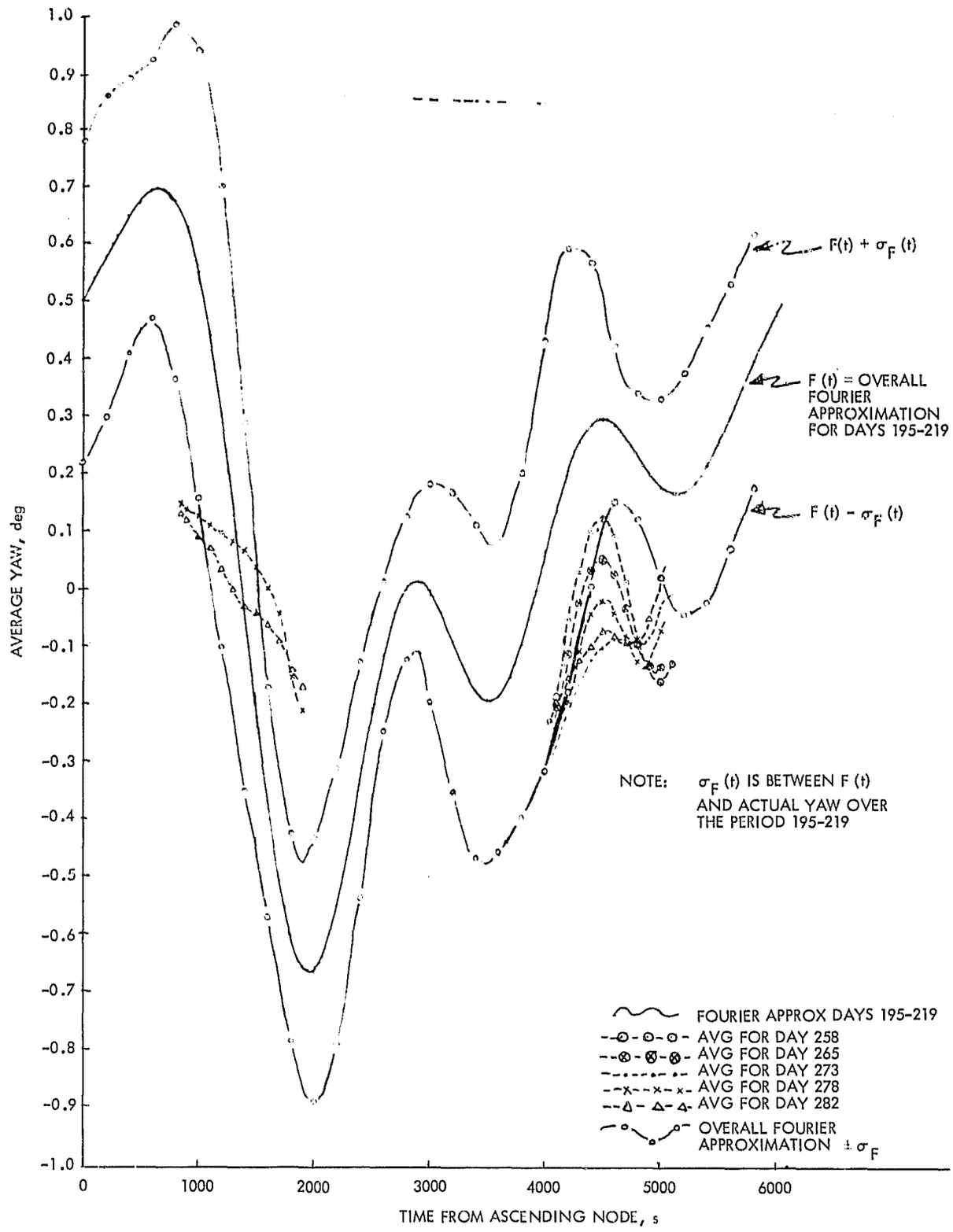

Figure 4-5. Daily Average Yaw versus Fourier Approximation - Second Quiescent Period

b. Mode 5 Period. In a manner similar to that described for the quiescent period, a truncated Fourier series was constructed to predict yaw for the varied yaw data gaps that occurred over the period of days 226-255. Such gaps began to appear at the very beginning and rapidly became so large that only days 226-229 have enough data to support Fourier analysis. Day 227 was excluded because several revolutions within that day were on RCS/gyro control, which has a quite different characteristic. The Fourier function which best fit days 226, 228, and 229 was then adjusted to emphasize the orbital phase covering the first 4000 s from ascending node and consequently de-emphasizing the last 2000 s. The reasons for this were threefold: (1) the period between 4000 and 5100 s from ascending node was usually covered by sun sensor data, so interpolation was not usually necessary; (2) the Mode 5 yaw excursion occurred regularly in the latter part of each revolution, and the truncated Fourier series cannot fit such a large excursion without being a poor fit to the rest of the data; and (3) the Mode 5 excursions varied significantly in orbital phase and amplitude, which meant that no constant predictor function could make a good fit except during a day or two of this mission interval.

Figure 4-6 shows the Fourier function chosen to represent yaw for the entire Mode 5 period, compared with the average yaw functions from the 3 days used to construct the function (Part 1 of Figure 4-6) and with the average yaw functions from several selected days subsequent to day 230. The average yaw functions are plotted only for data from the sun sensors, so the yaw data gaps are obvious. Part 2 of Figure 4-6 shows clearly how different the yaw behavior was in the latter part of the Mode 5 period compared to the beginning.

Figure 4-7 plots the RMS error of the selected overall Fourier function with respect to average yaw as a function of time from ascending node. Note that the lower curve, representing the time period between days 225-235, shows fairly good performance in the first 4200 s of a revolution, and much poorer performance in the interval containing the Mode 5 excursion. This was the intended result, for reasons given previously. The upper curve, representing the latter portion of the Mode 5 era, shows very much worse performance near the Mode 5 excursion, suggesting that performance in the orbital phase not observed by the sun sensor may also be significantly worse.

The data from Figure 4-7 was used to estimate the accuracy of the overall Fourier function for yaw interpolation in the Mode 5 period. Table 4-1 lists these estimates as functions of orbital phase and mission phase. Since the Fourier function was used to interpolate yaw primarily in the interval between 0 and 4000 s from ascending node, the 0.29-deg figure was used as 1σ for the day 226-235 period. There was no corresponding estimate for the day 236-255 period, because of the lack of sun sensor data in the appropriate orbital phases, so a default value of 0.75 deg (1σ) was used.

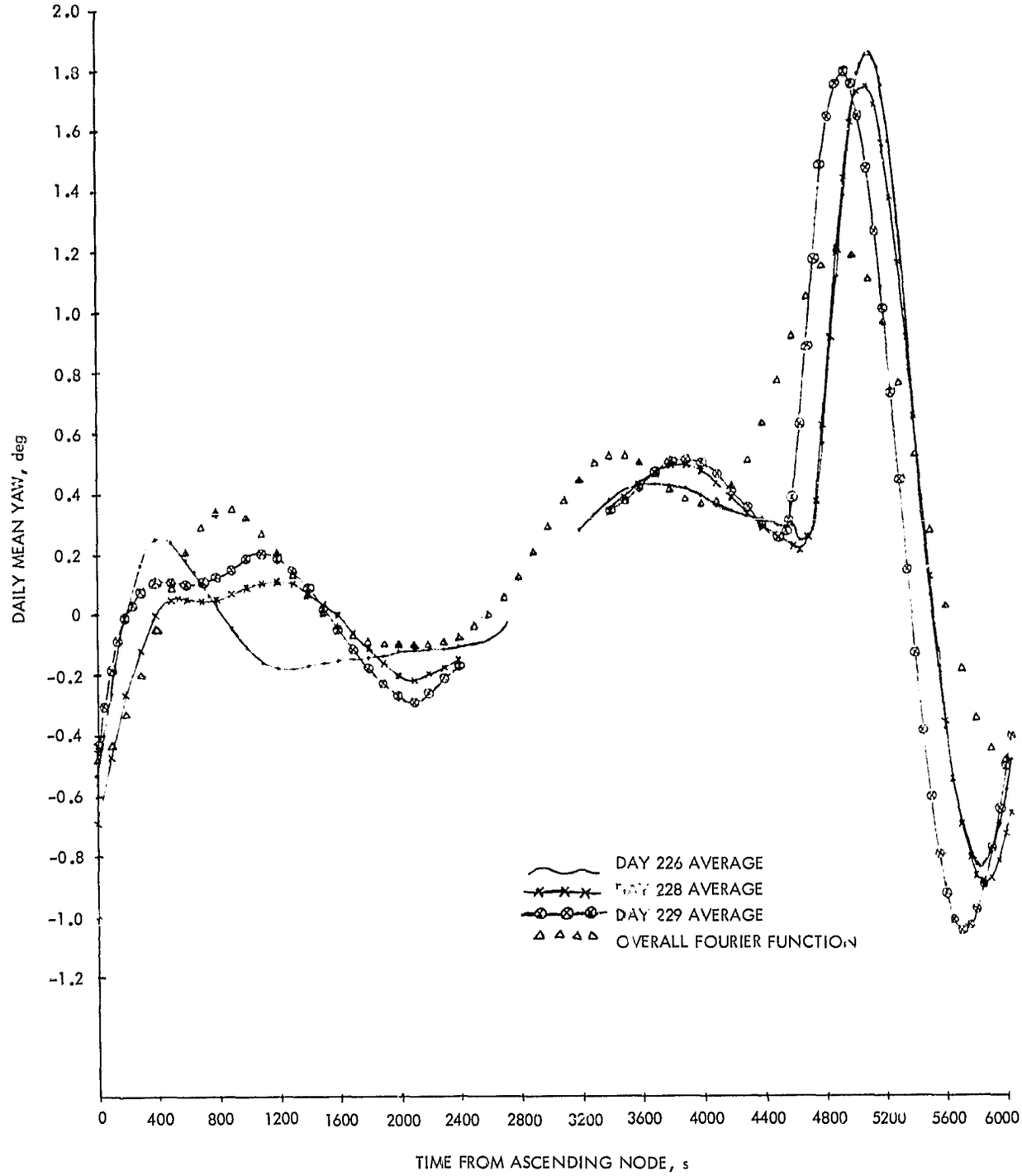

Figure 4-6. Overall Fourier Function versus Daily Mean Yaw for Mode 5

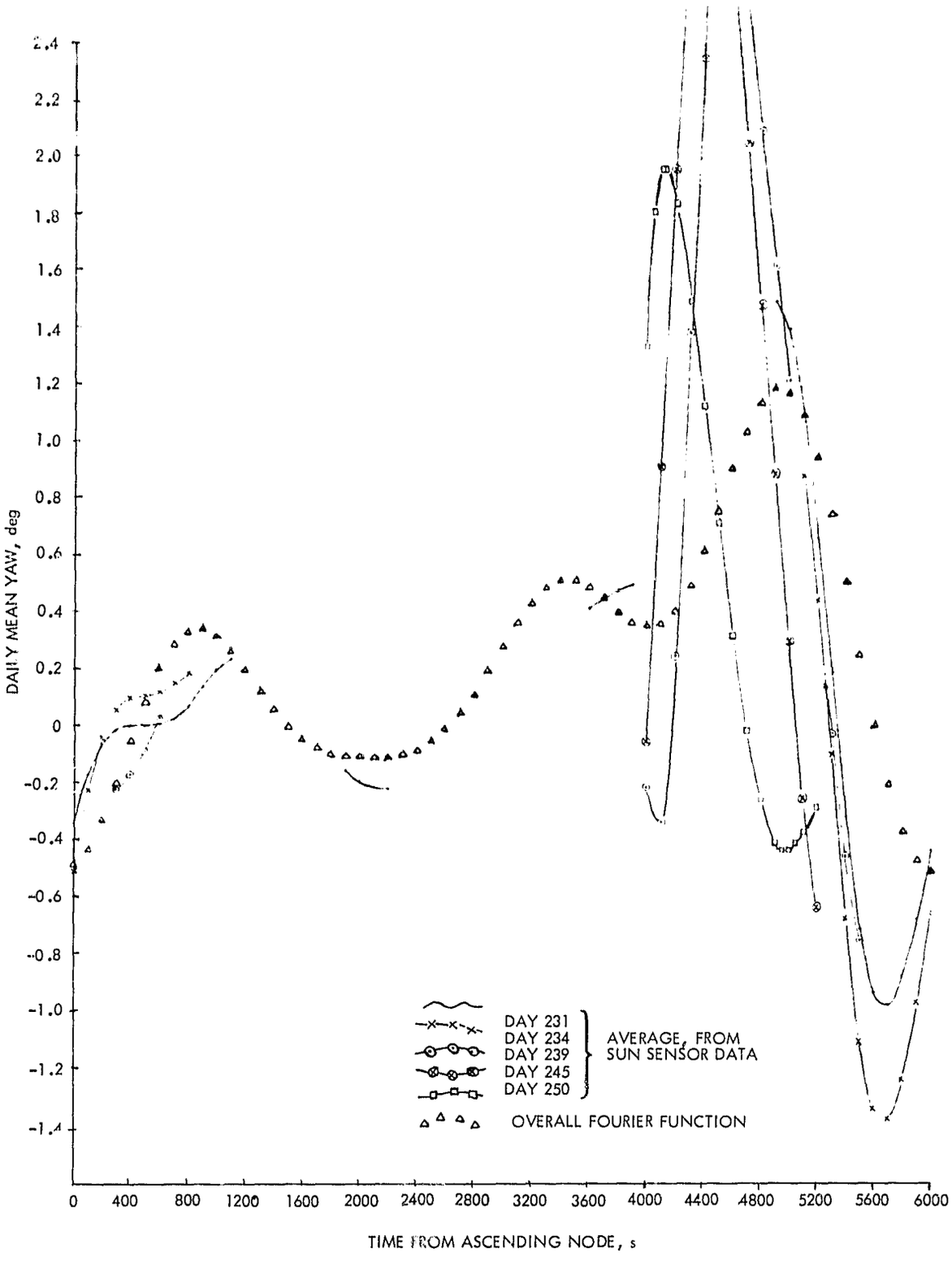

Figure 4-6. Overall Fourier Function versus Daily Mean Yaw for Mode 5 (Continuation 1)

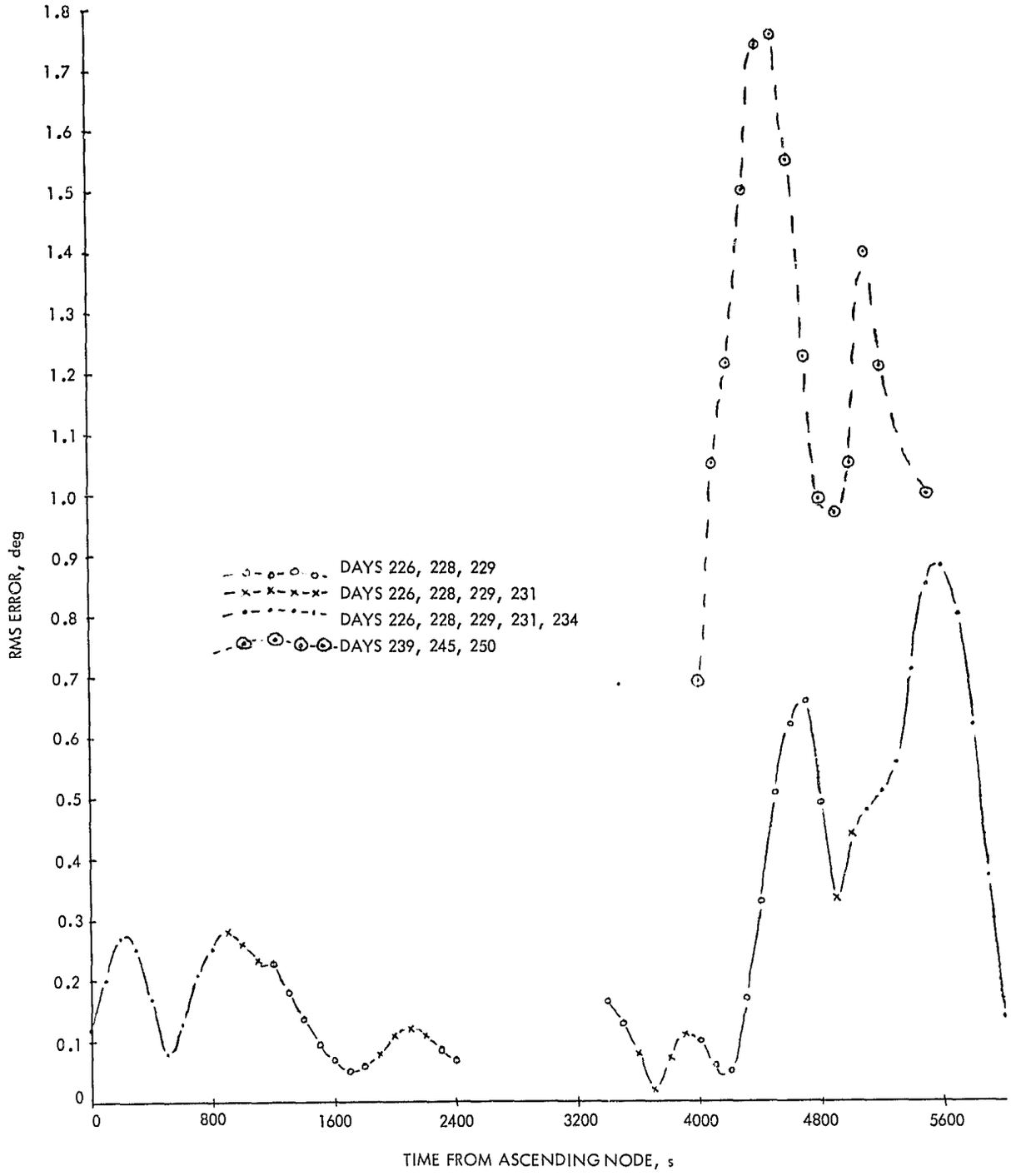

Figure 4-7. RMS Error of Overall Fourier Function with Respect to Daily Mean Yaw

Table 4-1. Fourier Function Accuracy for Mode 5 Period

Functional Relationship	RMS Error (deg) of Given Function per Orbital Phase (Seconds from Ascending Node)		
	Days 226 - 235		Days 236 - 255
	0 - 4000	4000 - 6000	4000 - 5200
Overall Fourier function relative to average yaw function	0.165	0.55	1.27
Actual yaw relative to average yaw function	0.23	0.39	0.42
Overall Fourier function relative to actual yaw	0.29	0.68	1.34

c. RCS Control Periods (Maneuvers). Yaw characteristic behavior under RCS/gyro control was quiescent, with small excursions relative to a mean value of -2.16 deg. This large mean offset was due to an unsuspected gyro misalignment. Since the dynamic behavior was apparently not a function of latitude or orbital phase, the Fourier function used to predict yaw for maneuver periods was simply the offset value, with all sinusoidal terms zeroed. The accuracy of such yaw estimation was calculated as 0.71 deg (1σ) by comparing the constant offset model with most of the available data from RCS control periods.

2. Roll/Yaw Coupling Model

Because of the pitch momentum bias, roll and yaw were coupled gyroscopically in addition to the inertial quarter-orbit coupling of a nadir-referenced spacecraft. The model used to estimate yaw from these relationships was a linear combination of roll and roll rate functions:

$$Y_3 = \rho K_{YR}\, R(t + t_R) + (1-\rho) K_{YRD}\, \dot{R}(t + t_{RD})$$

Parameter estimation was performed from data sets, each composed of a complete day's worth of data taken every 100 s. Yaw and roll data were each fit with a cubic spline, yaw on 200-s centers and roll on 300-s centers. The fit accuracy (1σ) during quiescent periods was 0.002 to 0.003 deg for yaw and about 0.02 deg for roll; for Mode 5 periods the fit accuracies were 0.01 to 0.03 deg and 0.03 to 0.05 deg, respectively. The lower fit accuracy for roll indicated that higher

frequency roll components were being filtered out by this process, which was desirable since only the lower frequencies were likely to be correlated with yaw. Evaluation of the spline at any time (t) produced an accurate value for position (Y or R) as well as rate ($\dot{R}$). The program used to estimate the parameters of the model in gain (ρK_{YR} and $(1-\rho)K_{YRD}$) and phase (t_R and t_{RD}) would search for the local minimum in the variance between Y_3, as defined above, and yaw data. For ea data set, three separate evaluations were made: one each for roll position (ρ=1) roll rate (ρ=0), and the combination of roll position and rate. From several suc evaluations a representative set of parameters was selected, and Y_3 from this representative set was compared again with several data sets to estimate the over all performance level.

a. Quiescent Period. Data from several days in the first quiescent period was analyzed to produce parameters for yaw interpolation in the second quiescent period. Since the orbital phase from 4100 to 5000 s after ascending node was normally observed by sun sensor head 2 in the latter period, yaw interpolation would not have to be performed for that orbital phase. Therefore, that interval was excluded from the parameter estimation process. The results suggested that for roll position alone, the gain (K_{YR}) should be 1.48 and the phase (t_R) about 1000 s. For roll rate alone, the gain (K_{YRD}) should be 750 with phase (t_{RD}) of 450 s. In combination, the value of 0.4 for the relative proportional factor (ρ) gave the best results. When this combination of parameters was checked in the Y_3 model against actual yaw data, for days 205, 214, and 218 (exclusive of the 4100- to 5000-s phase), the RMS error was 0.34 deg. Performance was also checked against available (preliminary) data from the second quiescent period. This data, from days 268, 274, and 282, had to be corrected for roll bias and sun sensor 2 misalignment before comparing with early data taken from sun sensor 1. However, the corrected data yielded RMS errors against the Y_3 model of 0.27 deg, which is the same result as a similar check against data from the same orbital phase in the first quiescent period. Therefore, it appears that the roll/yaw coupling model is as accurate on early quiescent period data as on the later data and, therefore, can be used with confidence to interpolate yaw data gaps.

Figure 4-8 shows two revolutions of yaw data from day 218, together with the Y_3 function from the corresponding roll data for each revolution. The revolutions were chosen to illustrate relatively good and relatively poor correspondence between Y_3 and true yaw. Note that Y_3 tends to stay in phase with yaw but can have significant amplitude errors. Figure 4-9 makes the same kind of comparison in the target era: the second quiescent period. As far as can be determined with the limited data available, Y_3 compares to yaw equally well in both quiescent periods.

b. Mode 5 Period. Because of the rapid growth of yaw data gaps in the early part of this period, only days 226-229 have enough data to justify parameter estimation. For the same reasons described for the quiescent periods, the interval between 4100 and 5000 s from ascending node was excluded from the

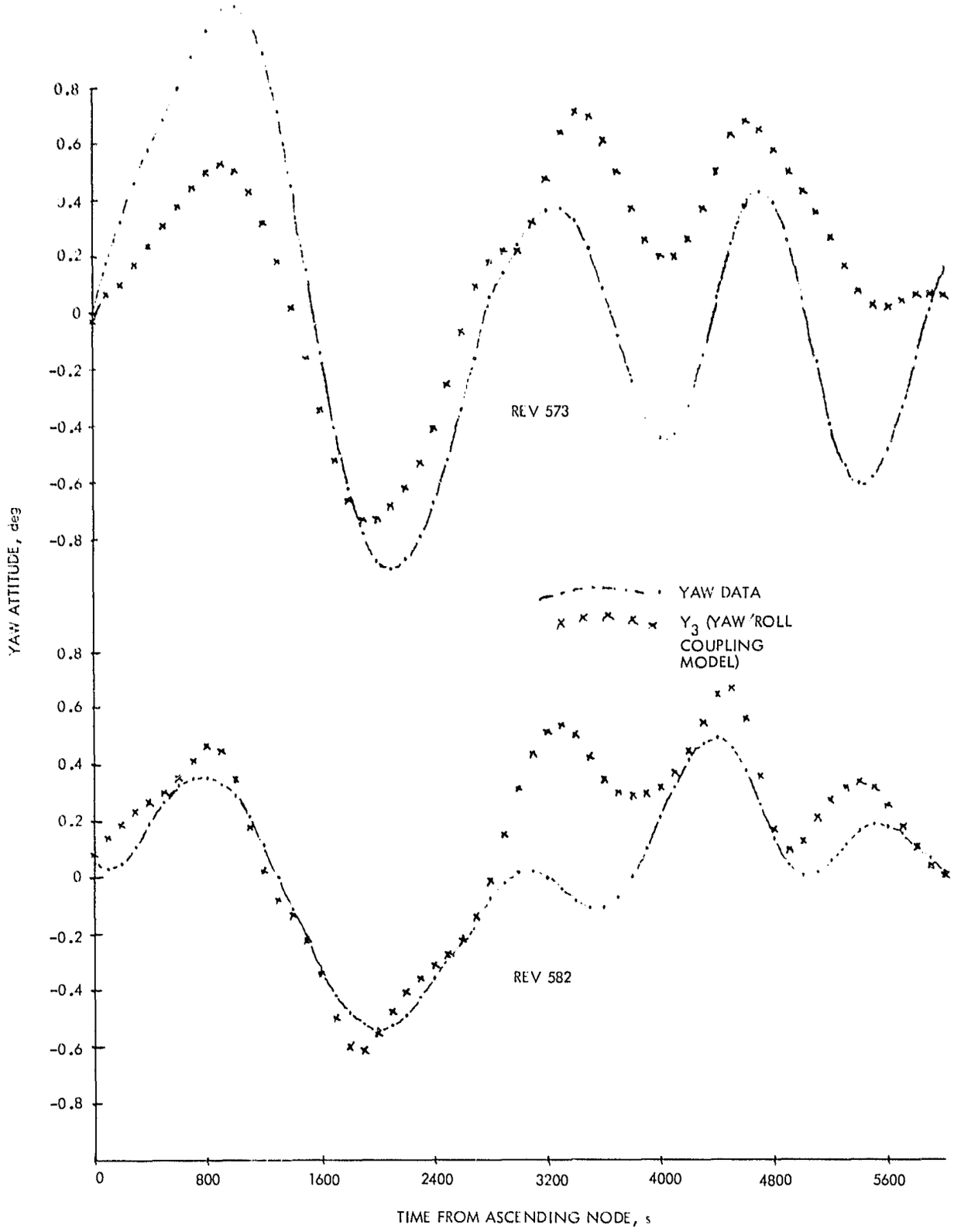

Figure 4-8. Examples of Y_3 versus Yaw - Day 218

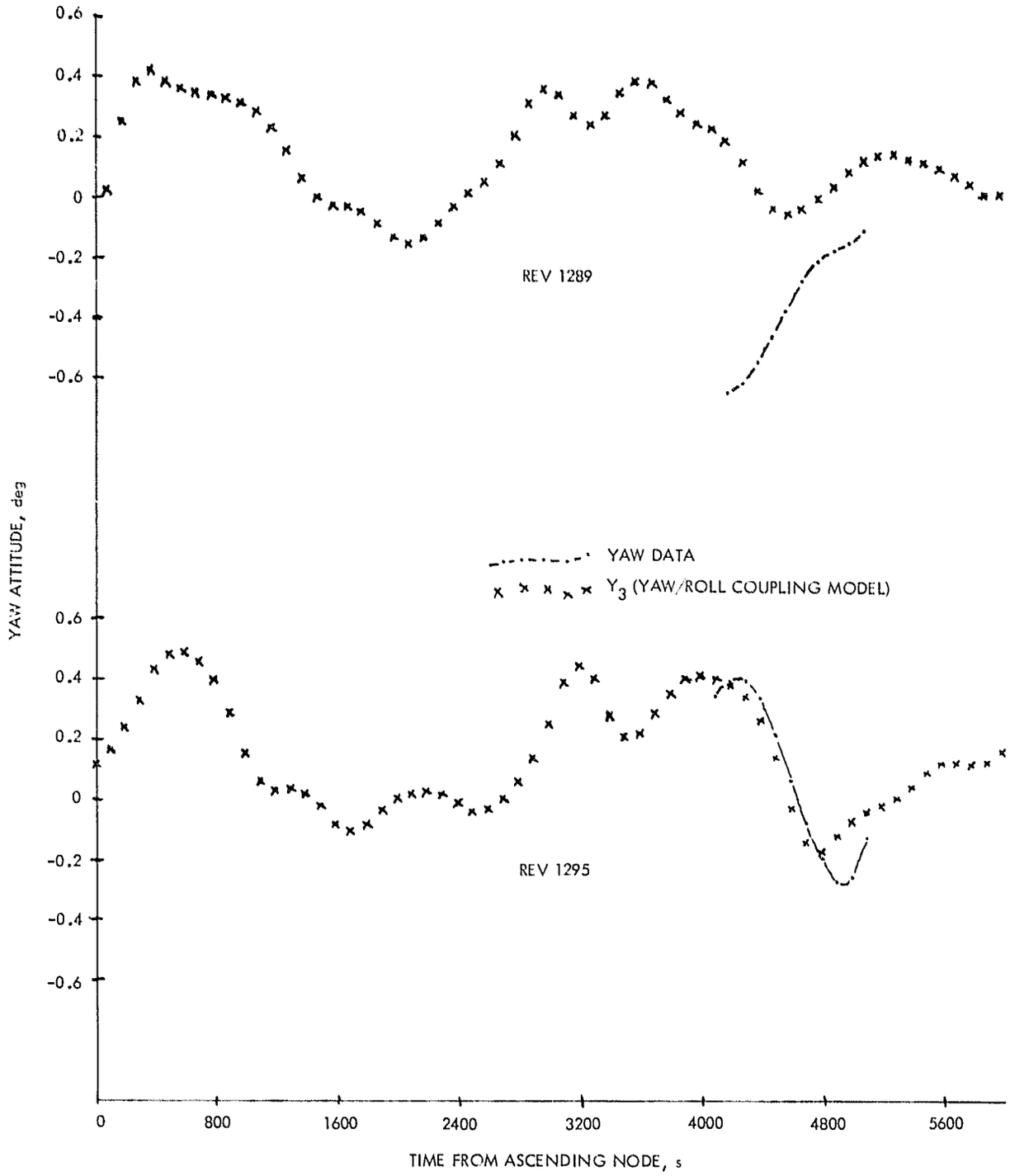

Figure 4-9. Examples of Y_3 versus Yaw - Day 268

estimation process. Day 227 was also excluded since a significant fraction of that day was spent on RCS/gyro control for an orbital trim maneuver. The analysis showed that the best parameters for roll alone were 1.50 in gain (K_{YR}) and 700 s in phase (t_R). For roll rate alone, the best parameters were 925 in gain (K_{YRD}) and 290 s in phase ($t_{R\dot{}}$). The best combination of the two was obtained with the proportionality constant ρ=0.2. For the day 226, 228, and 229 data, exclusive of the 4100- to 5000-s interval, the performance of this combination was about 0.26 deg RMS.

In the transmittal of these parameters from JPL to GSFC, the K_{YRD} and t_R values were inadvertently interchanged. All of the Mode 5 yaw data from day 227 through day 255 was interpolated, where required, with K_{RD}= 700 and t_R=925. The other parameters were as given above. Recheck of this (actual) yaw/roll model against the day 226, 228, and 229 data shows performance of 0.29 deg RMS rather than 0.26 deg RMS. Although this represents a loss of performance, it is not serious, and the difference is within the accuracy of the parameter estimation process.

Figure 4-10 shows three assorted revolutions of yaw data from the early Mode 5 period along with the Y_3 functions from the corresponding roll data. Y_3 is shown for both the best set of parameters and the set actually implemented. The difference in performance is difficult to see except during the Mode 5 yaw excursion. Note that the Y_3 function has an erroneous negative transient which is due primarily to roll rate behavior at the Mode 5 event; the Y_3 model describes fairly well the steady-state roll/yaw relationship, but does a relatively poorer job on transients. The accuracies quoted earlier do not include this transient response error.

Figure 4-11 gives two examples of yaw data compared with the actual Y_3 function for the latter portion of the Mode 5 period. Yaw data was limited to the 4000-5000 s interval for which Y_3 was not optimized, and, therefore, the comparisons are not favorable. Also, the phase of the Mode 5 event advanced regularly until it could no longer be observed by the sun sensor. Table 4-2 shows the accuracy of Y_3 in the 4100- to 5000-s interval for both early and late portions of the Mode 5 period. Those accuracies reflect performance under transient conditions; most of the revolution is more nearly at steady state, and the Y_3 parameters estimated from the early data can safely be assumed to represent yaw (outside the transient region) as well in the later portions of the Mode 5 period as in the earlier portions.

c. RCS Control Periods (Maneuvers). When the spacecraft was under RCS/gyro control, the misalignment of the yaw gyro caused a large fixed offset in yaw. Since the Y_3 model had no provisions for such offsets between mean roll and/or roll rate and mean yaw, the Y_3 model had over 2-deg RMS error during such periods. Therefore, Y_3 was not used for yaw interpolation during maneuvers.

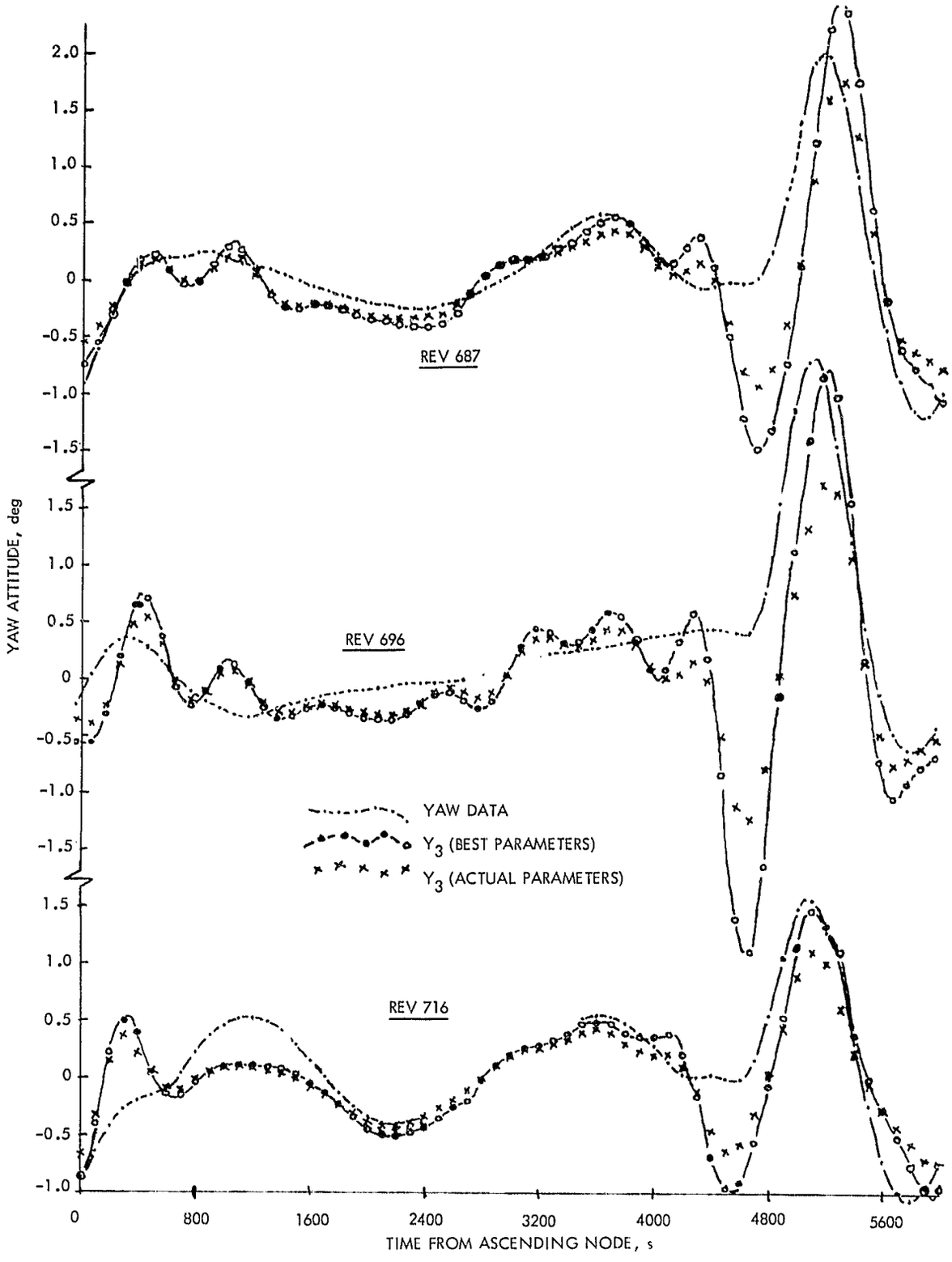

Figure 4-10. Examples of Y_3 versus Yaw for Early Mode 5 Period

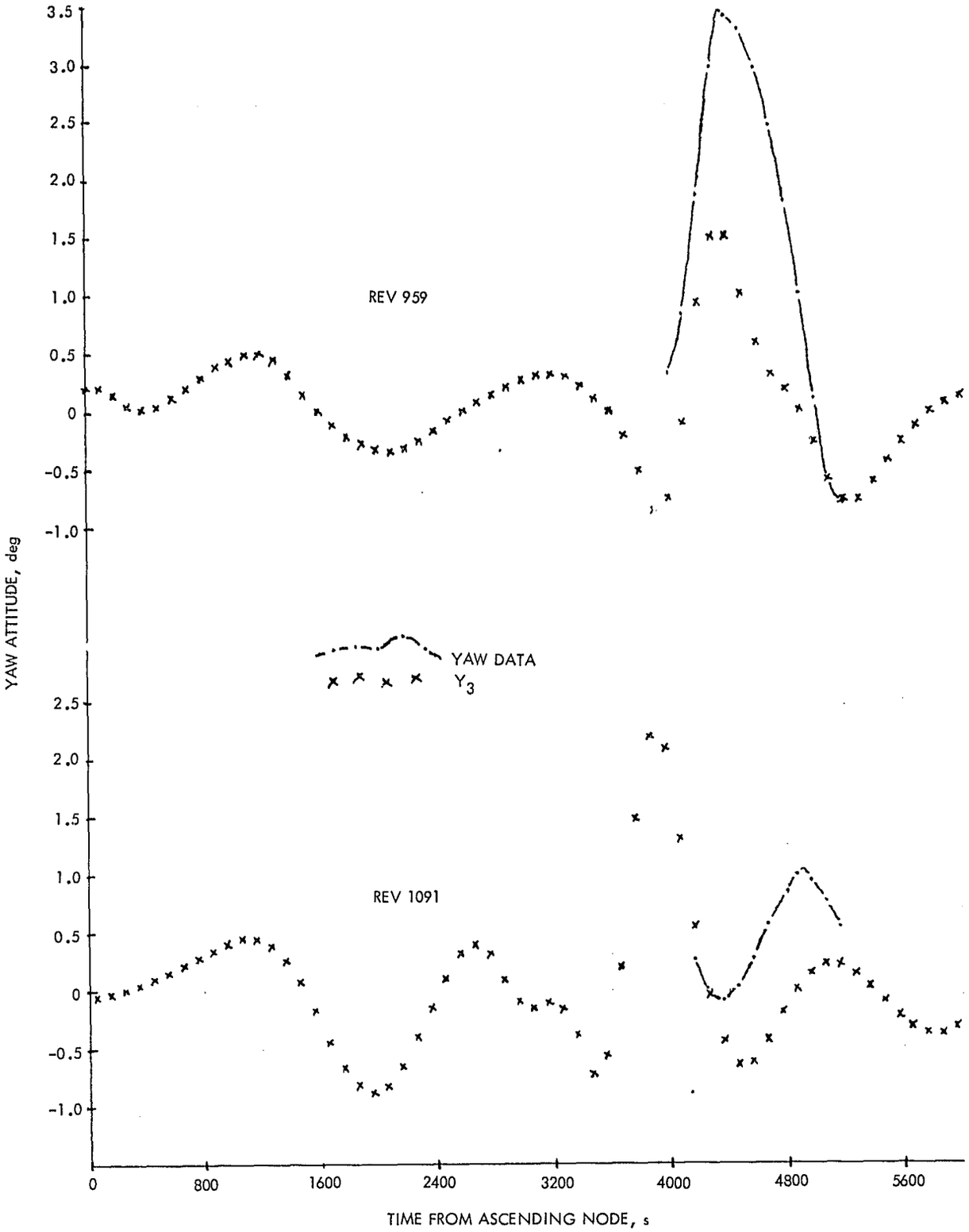

Figure 4-11. Examples of Y_3 versus Yaw for Late Mode 5 Period

Table 4-2. Y_3 Accuracy (deg) at 4100-5000 s From Ascending Node

Day of Year	Mean Error	Standard Deviation	RMS Error
226	-0.75	0.53	0.92
228	-0.62	0.35	0.71
229	-0.67	0.34	0.75
Overall (Early Mode 5)	-0.68	0.42	0.80
245	-1.36	0.69	1.53
254	-0.43	0.55	0.70
Overall (Late Mode 5)	-0.90	0.63	1.09

D. DATA BASE FOR YAW ATTITUDE DETERMINATION

Table 4-3 lists the values of yaw interpolation parameters and sun sensor head 2 alignment angles in each of the five AD data bases created for Seasat. Also given is the range of days of data to which each data base was applied. Table 4-4 lists the per-revolution applicability of data bases 3, 4, and 5 on maneuver days.

Table 4-3. AD Data Base Parameters

Parameter Description	Symbol	Parameter Value in Data Base: 1	2	3	4	5
Yaw interpolation parameters:						
Yaw autocorrelation time constants, s	τ_1, τ_2	1000	1000	1000	1000	1500
Variance of yaw (Y_D) from sun sensor data, deg^2	σ_D^2	$(0.05)^2$	$(0.05)^2$	$(0.05)^2$	$(0.05)^2$	$(0.05)^2$
Variance of yaw prediction w.r.t. Y_D, deg^2	σ_c^2	$(0.3)^2$	$(0.55)^2$	$(0.29)^2$	$(0.75)^2$	$(0.71)^2$
Constant magnitude for yaw from roll, deg/deg	$\kappa_{\gamma R}$	1.6	1.48	1.50	1.50	1.50
Constant magnitude for yaw from roll rate, deg/(deg/sec)	$\kappa_{\gamma RD}$	1300	750	700	700	700
Constant phase for yaw from roll, s	t_R	2400	1000	925	925	925
Constant phase for yaw from roll rate, s	t_{RD}	400	450	290	290	290
Variance of yaw from roll and roll rate, deg^2	σ_3^2	$(0.1)^2$	$(0.34)^2$	$(0.26)^2$	$(0.26)^2$	$(10.0)^2$
Constant a priori predicted yaw, deg	κ_o	0.0	0.106	0.260	0.260	-2.16
Amplitude of ω_o term of Fourier series for predicted yaw, deg	κ_1	0.0	0.401	-0.382	-0.382	0.0
Amplitude of $2\omega_o$ term of Fourier series for predicted yaw, deg	κ_2	0.0	0.243	-0.247	-0.247	0.0
Amplitude of $3\omega_o$ term of Fourier series for predicted yaw, deg	κ_3	0.0	-0.202	-0.338	-0.338	0.0
Amplitude of $4\omega_o$ term of Fourier series for predicted yaw, deg	κ_4	0.0	0.108	-0.159	-0.159	0.0
Phase of ω_o term of Fourier series for predicted yaw, deg	λ_1	49.0	15.49	-81.1	-81.1	-81.1
Phase of $2\omega_o$ term of Fourier series for predicted yaw, deg	λ_2	0.0	-64.43	3.1	3.1	3.1
Phase of $3\omega_o$ term of Fourier series for predicted yaw, deg	λ_3	0.0	49.18	4.8	4.8	4.8
Phase of $4\omega_o$ term of Fourier series for predicted yaw, deg	λ_4	0.0	70.40	50.9	50.9	50.9
Fundamental frequency of Fourier series for predicted yaw, rad/s	ω_o	computed daily from average ephemeris				
Scaling factor of Y_3 and Y_I cross-correlation error	ρ_{I3M}	0.0	0.0	0.0	0.0	0.0
Proportional contribution to Y_3 from roll	ρ_R	0.0	0.4	0.2	0.2	0.2
Sun sensor alignment Euler angles:						
Clock for sun sensor head #2, deg	ϕ_2	23.509	23.509	23.245	23.245	23.245
Cone for sun sensor head #2, deg	θ_2	98.017	98.017	98.170	98.170	98.170
Twist for sun sensor head #2, deg	ψ_2	-90.0125	-90.0125	-89.89	-89.89	-89.89
Data Base Applicability (days of year 1978)						
From		178	256	227	236	See
To		226	283	235	255	Table 4-4

Table 4-4. Data Base Applicability for Maneuvers

DOY	Rev	Event Times		YAWINT Data Base	Event Description
		From	To		
227	700-702	00:00:00	4:18:20	3	Normal (Mode 5)
	702	2:30:19			Start RCS
	703	4:19:50	4:29:10	5	Yaw Data Gap
	704	6:00:15	6:09:55	5	Yaw Data Gap
	705	7:41:08	7:42:08		Burn
	705	8:32:00			Stop RCS
	705	7:40:30	7:51:15	5	Yaw Data Gap
	706	9:21:10	9:32:05	3	Yaw Data Gap
	Subsequent			3	Yaw Data Gap
230	743-745	0:00:00	3:00:00	3	Normal (Mode 5)
	745	2:38:32			Start RCS
	745	2:40:45	2:59:10	3	Yaw Data Gap
	746	4:21:00	4:39:40	5	Yaw Data Gap
	747	5:44:25	5:50:10	5	Yaw Data Gap
	747	6:01:30	6:20:25	5	Yaw Data Gap
	748	7:24:30	7:31:10	5	Yaw Data Gap
	748	7:42:00	8:01:10	5	Yaw Data Gap
	748	7:46:58	7:48:22		Burn
	749	9:10:00			Stop RCS
	749	9:05:20	9:11:30	5	Yaw Data Gap
	749	9:22:40	9:41:40	3	Yaw Data Gap
	Subsequent			3	

Table 4-4. Data Base Applicability for Maneuvers (Continuation 1)

DOY	Rev	Event Times		YAWINT Data Base	Event Description
		From	To		
235	Up to 819	0:00:00	6:10:00	3	Normal (Mode 5)
	819	6:17:50	7:26:05	4	Yaw Data Gap
	819	6:39:27			RCS Start
	820	7:56:45	9:05:55	5	Yaw Data Gap
	820	9:20:36	9:21:36		Burn
	821	9:27:15	10:49:45	5	Yaw Data Gap
	821	10:12:02			RCS Stop
	822	11:18:10	12:21:20	3	Yaw Data Gap
	Subsequent			3	
238	Up to 862	0:00:00	7:53:20	4	Normal (Mode 5)
	862/863	7:41:55	7:52:40	4	Yaw Data Gap
	863	8:01:40	9:00:25	5	Yaw Data Gap
	863	8:10:27			Start RCS
	863	9:22:22	9:29:21		Burn
	864	10:00:02			Stop RCS
	863/864	9:22:40	9:32:50	5	Yaw Data Gap
	864	9:40:35	10:39:30	4	Yaw Data Gap
	Subsequent			4	
252	Up to 1072	0:00:00	24:00:00	4	Normal (Mode 5)
252	1072	23:25:32			Start RCS
	1071/1072	22:32:20	23:54:10	4	Yaw Data Gap

Table 4-4. Data Base Applicability for Maneuvers (Continuation 2)

DOY	Rev	Event Times		YAWINT Data Base	Event Description
		From	To		
253	1073	0:13:25	1:38:55	5	Yaw Data Gap
	1073	1:10:22	1:10:50		Burn
	1073	1:53:02			Stop RCS
	1073/1074	1:53:10	3:15:50	4	Yaw Data Gap
	Subsequent			4	

SECTION V

CHARACTERIZATION OF AD ACCURACY

A. SUN SENSOR ERROR SOURCES

Attitude determination in all three axes was affected by sun sensor errors. Pitch and roll were affected through the biases determined by comparison of Scanwheel output data with concurrent sun sensor data. The achieved accuracies of bias determination are demonstrated in Section 3.2.2 of Reference 2-9. Yaw AD accuracies will be explained in the following paragraphs.

The GSFC method of determining yaw attitude from sun sensor data is subject to three classes of errors: (1) coupling of roll and pitch AD errors into yaw AD, (2) sun sensor alignment errors, and (3) sun sensor observation errors. The error source mapping into yaw can be expressed as the first-order Taylor's expansion of the yaw estimate:

$$Y_e = Y_o + \sum_{i=1}^{n} \frac{\partial Y}{\partial \phi_i} \Delta\phi_i$$

where

Y_e = yaw estimate

Y_o = true yaw

ϕ_i = ith error source

For this case, there are seven error source groups: pitch and roll AD error, misalignment of the sun sensor boresight in spacecraft clock, cone, and twist, and sun sensor observation errors in the two sun sensor orthogonal coordinates cone and cross-cone. The sensitivities (first partial derivatives) of yaw to these error source groups are derived in References 2-2 and 3-3 and are summarized here:

$$\frac{\partial \text{ Yaw}}{\partial \text{ Roll}} = \frac{\cos \alpha_s}{\tan \beta_s}$$

$$\frac{\partial \text{ Yaw}}{\partial \text{ Pitch}} = \frac{\sin \alpha_s}{\tan \beta_s}$$

$$\frac{\partial \text{ Yaw}}{\partial \alpha_B} = -1$$

$$\frac{\partial \text{ Yaw}}{\partial \beta_B} = \frac{\sin (\alpha_s - \alpha_B)}{\tan \beta_s}$$

$$\frac{\partial \text{ Yaw}}{\partial \gamma_B} = \frac{\cos (\alpha_s - \alpha_B) \sin \beta_B}{\tan \beta_s} - \cos \beta_B$$

$$\frac{\partial \text{ Yaw}}{\partial \alpha_{ss}} = \frac{S_2^2 - 1}{\sin \beta_s \left[\cos \beta_B \cos \beta_s \cos (\alpha_s - \alpha_B) + \sin \beta_s \sin \beta_B\right]}$$

$$\frac{\partial \text{ Yaw}}{\partial \beta_{ss}} = - \sin (\alpha_s - \alpha_B) \left[\frac{1}{\tan \beta_s} + \frac{S_2}{S_3} \cos (\alpha_s - \alpha_B)\right]$$

$$S_2 = \cos \beta_B \sin \beta_s \cos (\alpha_s - \alpha_B) - \cos \beta_s \sin \beta_B$$

$$S_3 = \sin \beta_B \sin \beta_s \cos (\alpha_s - \alpha_B) + \cos \beta_s \cos \beta_B$$

where

α_s, β_s = clock, cone angles of sun in spacecraft coordinates

α_B, β_B, γ_B = clock, cone, twist alignment angles of sun sensor boresight in spacecraft coordinates

α_{ss}, β_{ss} = cross-cone, cone angles of sun in sun sensor coordinates

B. AD ERROR BUDGETS

References 5-1 and 5-2 give error budgets for Seasat attitude determination in all three axes. Reference 5-1 reflected the consensus of estimates from LMSC, GSFC, and JPL based on pre-launch expectations. Reference 5-2 was written after 6 weeks of orbital operations, and reflected changes of some estimates based on this operational knowledge. Further operational experience and thought by both

JPL and GSFC have produced further refinement of the AD error budgets. The GSFC estimates and their rationale are presented in Section 3 of Reference 2-9. The JPL estimates are summarized in Tables 5-1 and 5-2.

Table 5-1, which treats of pitch and roll AD accuracies, has several differences from a similar table in Reference 5-2. The allocation for Scanwheel noise after running-average filtering had been increased to 0.04 deg in Reference 5-2, but further operational experience indicated good performance with the 1.20-s period filter, so the allocation was returned to the 0.01-deg level. GSFC analyses (Section 3.4.6 of Reference 2-9) showed no Scanwheel speed-dependent effects greater than the 0.02-deg accuracy of their analytic method, so that allocation was reduced to 0.02 deg. The values for temperature variations and threshold stability had been increased by √2 in Reference 5-2 to allow for the possibly larger effects of operating on a single Scanwheel rather than the dual (nominal) system; operational experience has shown no reason to suspect larger effects, so the allocations were returned to the values of Reference 5-1. By similar reasoning the allocation for attitude computer drift was reduced to the low end of the range given in Reference 5-2. The bias determination error allocation was reduced to the values estimated by GSFC for the determinations they performed. The allocation for random horizon radiance errors has been made a function of subspacecraft latitude, based on GSFC analysis (Section 3.4.2 of Reference 2-9). Figure 5-1 shows the time function for this error budget and for the total AD accuracy of pitch and roll.

It should be noted that Table 5-1 applies only under the conditions which became normal for Seasat: single (right) Scanwheel operation, with no sun interference. There were periods of time during days 220-225 (and much later on rev 1117) when the left Scanwheel was used; there was an approximate 0.5-deg offset observable when Scanwheels were switched, and intermittent sun interference caused 2-deg errors. On the right Scanwheel from day 225 to day 255, there was an interference effect once a revolution (twice a revolution from day 246 to day 255), which was largely but not completely edited by the GSFC data processing system. Although this effect was small and probably negligible if it happened during Mode 5, there were some revolutions, among them revs 706-711 plus 812 and 863, when Mode 5 was not used, and the effects on final AD were on the order of 0.2-1.0 deg.

Table 5-2 gives the error budgets for yaw determination from sun sensor data. The budgets for individual error sources differ from those previously allocated in Reference 5-2 in three areas. Since temperature gradients were moderate compared to the maxima predicted before launch, the allocation for these effects was reduced by a factor of approximately 2 and applied only to the axis about which the maximum effect could be expected to occur. Alignment uncertainty was increased to account for the accuracy of inflight calibration of sensor head 2 and for the apparent bounds of misalignment of sensor head 3 (see Section 3.1.2 of Reference 2-9 and Subsection III-B). The contribution due to pitch and roll AD error was modified to correspond to actual Seasat experience on each sensor head. The total yaw AD error values shown in Table 5-2 are the result of mapping these error sources into yaw with the equations of Subsection V-A. The range of values given is the minimum to maximum values observed in such mapping over the entire range of sun positions experienced by Seasat.

Table 5-1. AD Error Budgets (3σ) for Pitch and Roll (for Operation on Right Seamwheel Only)

No.	Item	Pitch	Roll
1	Random horizon radiance variation	0.05-0.25	0.05-0.125
2	Noise after 120-s averaging	0.01	0.01
3	Seamwheel speed variation	0.02	0.02
4	Temperature variations	0.069	0.069
5	Threshold stability	0.069	0.069
6	Attitude computer drift and aging	0.066	0.066
7	Bias determination error	0.06	0.02
8	Bias determination observability	0.01	0.01
	Total (deg, 3σ)	0.14-0.28	0.13-0.18

Table 5-2. AD Error Budget (3σ) for Yaw (When Sun is Observable)

No.	Item	Sensor Head 1	Sensor Head 2	Sensor Head 3
1	Sun sensor accuracy (per axis)	0.05	0.05	0.05
2	Launch shock	0.01	0.01	0.01
3	Sun sensor alignment (per axis)	0.003	0.08[a]	0.25
4	Thermal distortion	0.025 (cone)	0.025 (twist)	0.025 (twist)
5	Pitch and roll AD error coupling into yaw AD error	0.000-0.197	0.000-0.148	0.000-0.109
	Yaw AD error (deg, 3σ)	0.051-0.205	0.096-0.208[a]	0.253-0.308

[a]Assumes that known misalignment is taken into account.

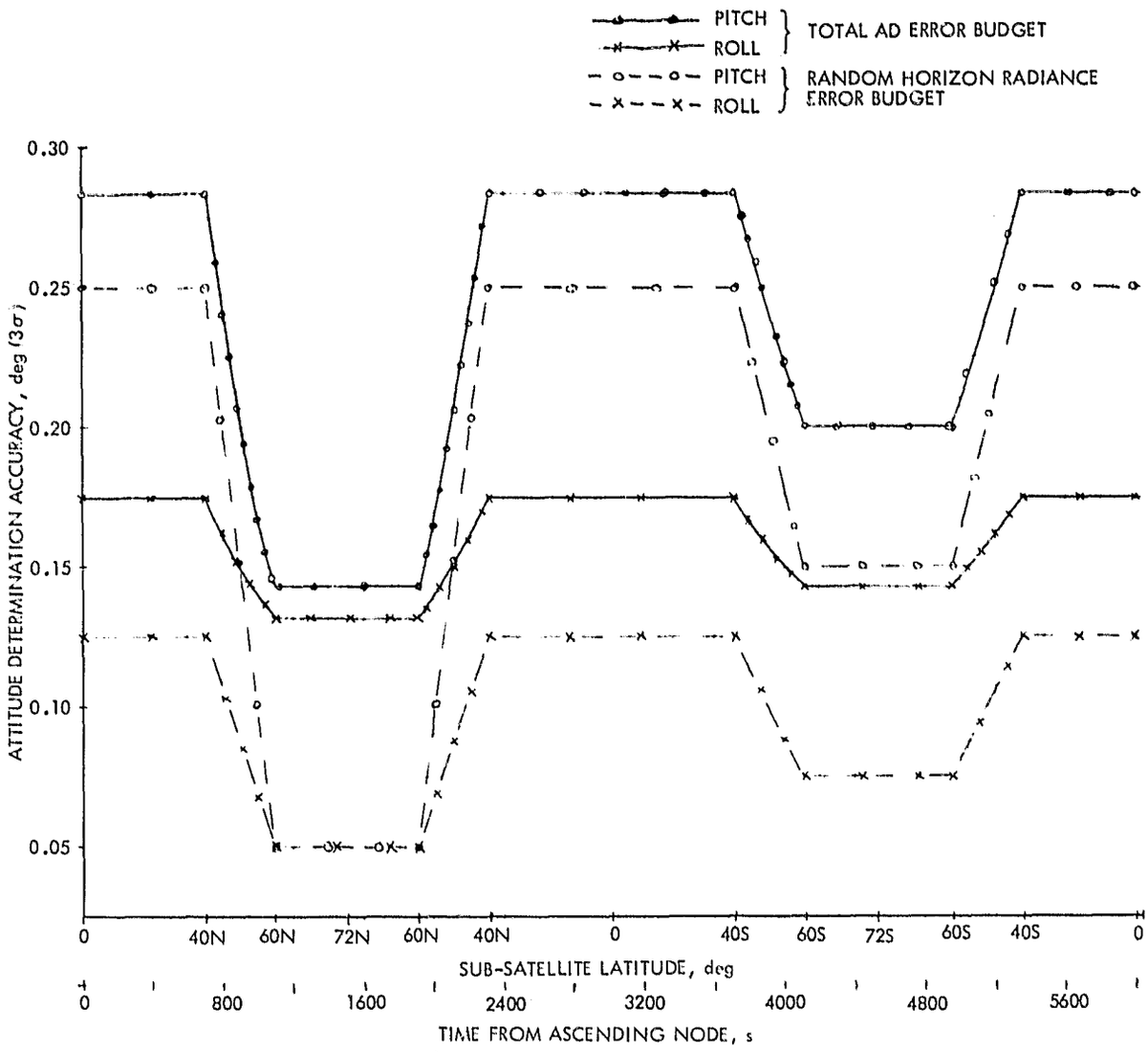

Figure 5-1. Pitch/Roll AD Accuracy Versus Time in Revolution

Note that Table 5-2 accuracies for sensor head 2 apply only if correction has been made for the measured misalignment of this head. Such correction was made in GSFC data processing up to day 255. Definitive attitude files for days 256-283 can be corrected by using the information in Figure 3-6. If the indicated correction is not applied to this data by the user, the accuracy estimate should be appropriately revised.

The yaw AD accuracy function of time is presented in detail in Figures 5-9 through 5-12.

C. YAW INTERPOLATION ACCURACY

The accuracy of the yaw interpolation process can only be inferred, not measured. By definition, it is a means of supplying an estimate at times no direct measurement is available, so there is no direct means of verifying the estimates made. However, an estimate of interpolation performance can be formed by comparing its performance against real data under simulated data gap conditions and making appropriate inferences.

1. Data Gap Simulations

a. Quiescent Period. Data from three consecutive days (214-216) of the first quiescent period, 37 revolutions in all, was used to simulate the attitude data conditions of the second quiescent period (days 256-283). The parameters of YAWINT data base 2 (see Table 4-2) were used to create an interpolated yaw estimate function for the orbital interval between -1040 and +4100 s from ascending node. This interval approximately covers the orbital phases of sun sensor data gaps in the second quiescent period (see Figure 2-12). To the extent that yaw/roll behavior is similar in the two quiescent periods, this simulation models yaw interpolation for days 256-283. Three consecutive days were chosen to average out the effects of longitudinal variation, since Seasat was in a near-3-day-repeat orbit. Figure 5-2 presents the results of this simulation as mean error (μ), mean plus and minus standard deviation of error ($\mu \pm \sigma$), and the extrema of error, all as functions of time from data gap start. Note that true yaw tends to be more positive than the interpolation in the northern hemisphere and more negative than the interpolation in the southern hemisphere. The average mean error over the entire simulated gap is -0.01 deg. Without corroborating evidence from an independent source (e.g., the SAR) of data from the day 256-283 period, the dynamic function of error has low confidence as a predictor for that period, and the mean error should be considered zero. Overall performance is 0.79 deg (3 RMS).

To estimate the similarity of actual (observable) yaw in the target era with simulated interpolated yaw, another comparison was made. The RMS error of interpolated yaw in the orbital phase 4100 to 5000 s from ascending node was evaluated for days 214-216 in the first quiescent period and for days 257, 258, and 268 in the second. Sun sensor data does generally exist in this orbital phase for the second period, and, therefore, a real performance estimate can be made. As it happens, this orbital phase is quieter (in yaw) than that

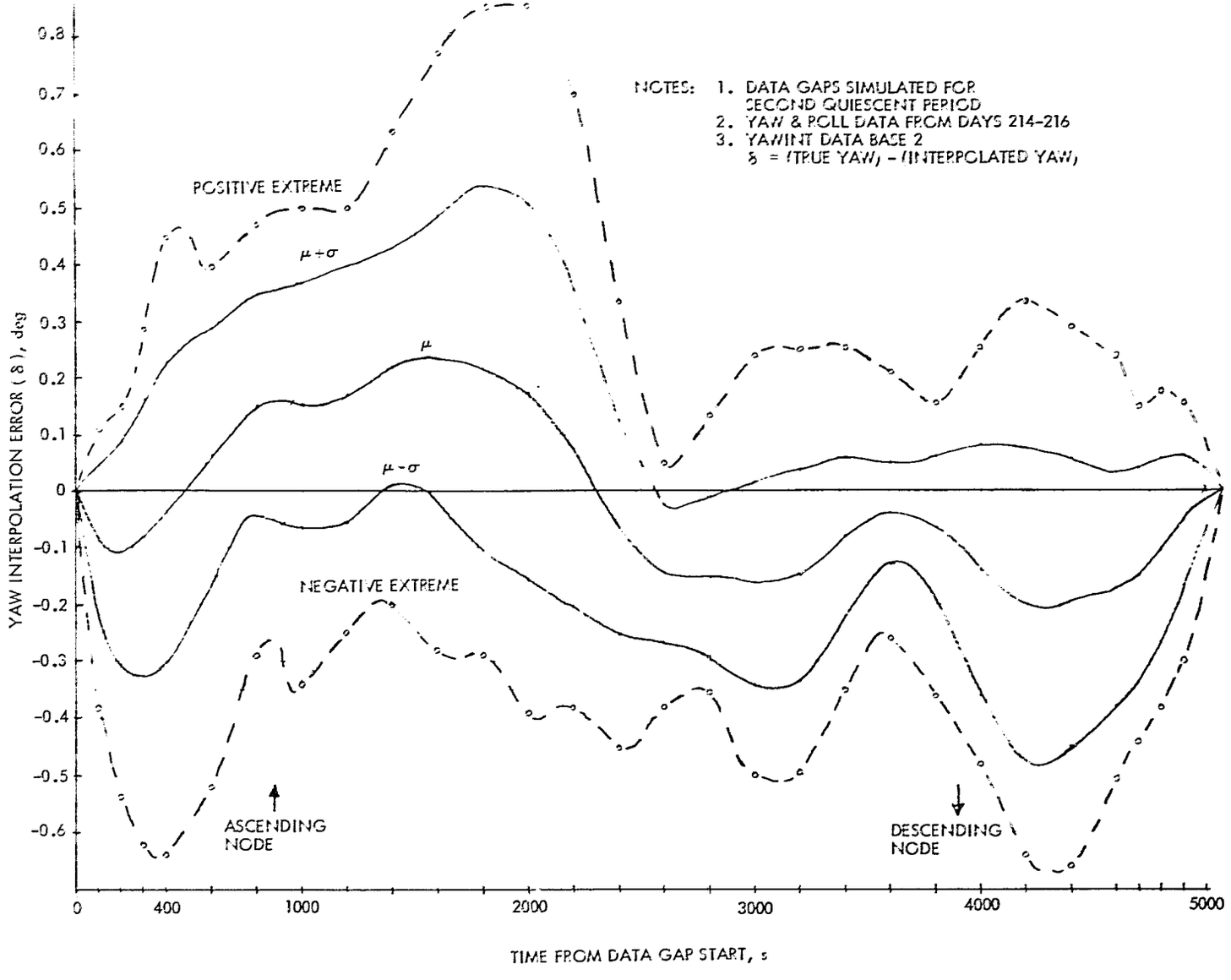

Figure 5-2. Yaw Interpolation Error

represented by Figure 5-2, at least for days 214-216. The comparison of results between the first and second quiescent periods is shown later in Table 5-3. There is an increase in RMS error for this orbital phase from the first period to the second. Treating this increase as due to a previously unaccounted independent error source, it would have a value of 0.53 deg (3 RMS). This can be RSS'ed with the 0.79 deg (3 RMS) overall performance in the simulated data gaps to infer 0.95 deg (3 RMS) for the real data gaps in the second quiescent period.

b. Mode 5 Period. As described above for the quiescent periods, data gaps were simulated for the Mode 5 periods. Since real data gaps had already appeared at the beginning of this era, only limited data was available for comparison. From day 225 to day 235, the actual data gaps varied considerably in number, size, and phase, as can be seen in Figure 3-13. By day 234, there was only one gap, and it was between 900 and 5050 s from ascending node. Using YAWINT data base 3 and the available data from days 228 and 229, the day 234 data gap was simulated. The results are shown in Figure 5-3. The pattern of error is obviously different from that of the quiescent period (Figure 5-2), driven mainly by the Mode 5 excursion in the latter part of the gap. The overall mean is about 0.03 deg and again should be considered zero.

Because of the significantly poorer interpolation performance near the Mode 5 excursion (which was in the southern hemisphere), better estimates of performance can be made by considering the Mode 5 region as distinct from the rest of the revolution. Accordingly, interpolation performance was estimated for data in the interval of 1200 s following the roll signal disconnect (Mode 5 start) and separately for the data in the rest of each revolution. Table 5-3 shows the results for yaw prediction (Y_p) from the Fourier series, yaw inferred from roll and roll rate (Y_3), and the overall yaw interpolation estimate ($\hat{Y}$). As can be seen in the table, interpolation performance is two to three times better away from the Mode 5 interval than near it. This means that scientific data from the northern hemisphere is much better served than that from the southern hemisphere; happily, the northern hemisphere also draws the most scientific interest.

Performance evaluations were made from available data throughout the day 225-235 period. For each individual day within that period, the appropriate accuracies can be obtained by interpolating Table 5-3. The data from days 232 and 234 tends to be concentrated in the low latitudes, so that their performance figures are biased toward higher uncertainties. A more appropriate set of values for the days between 230 and 235 are the overall figures given by the table for this period.

The orbital phase of the data gaps in the later portion of the Mode 5 period was almost the same as for the second quiescent period. Such data gaps were simulated, again on data from days 228 and 229, but using YAWINT data base 4. The results are shown in Figure 5-4. The overall mean error is now 0.08 deg, which may be significant. That this value is larger than for the other periods is due primarily to the poorer performance near the Mode 5 excursion. The interpolated estimate consistently undershot true yaw for large excursions, in order to minimize error for the more usual small excursions. The size of this undershoot was as large as 2 deg.

Table 5-3. Yaw Interpolation Accuracy (Middle of a Long Data Gap)

Performance (3 x RMS, deg) for Given Orbital Phase and YAWINT Data Base 2

Data Day	Sun Sensor Data Available in Target Era			Sun Sensor Data Not Available in Target Era		
	ΔY_p	ΔY_3	$\Delta\hat{Y}$	ΔY_p	ΔY_3	$\Delta\hat{Y}$
214	0.68	0.57	0.58	0.82	0.95	0.77
215	0.71	0.56	0.585	0.82	0.95	0.77
216	0.73	0.53	0.58	0.86	1.00	0.83
Overall	0.71	0.55	0.58	0.83	0.97	0.79
257	0.75	0.78	0.80			
258	0.86	0.73	0.73			
268	1.04	0.80	0.82			
Overall	0.89	0.77	0.79	0.99[a]	1.11[a]	0.95[a]

Data Day	Mode 5 Start + 1200 s				NOT (Mode 5 Start + 1200 s)			
	ΔY_p	ΔY_3	$\Delta\hat{Y}$ (d.b.3)	$\Delta\hat{Y}$ (d.b.4)	ΔY_p	ΔY_3	$\Delta\hat{Y}$ (d.b.3)	ΔY (d.b.4)
226	1.81	1.82	1.47		0.93	1.02	0.68	
228	1.62	1.94	1.45	1.79	0.82	0.91	0.62	0.81
229	1.79	2.01	1.67	1.90	0.82	0.93	0.63	0.84
232	2.46	1.60	1.85		0.83	0.72	0.63	
234	3.42	2.04	2.56		1.14	1.10	0.97	
Overall	2.32	1.89	1.84	1.84	0.92	0.94	0.72	0.82
250	3.84	1.91		1.89				
251	4.18	2.19		2.22				
Overall	4.01	2.05	NA	2.06	3.71[a]	1.19[a]	NA	1.24[a]

[a]Inferred from comparison of available data from appropriate orbital and mission phases.

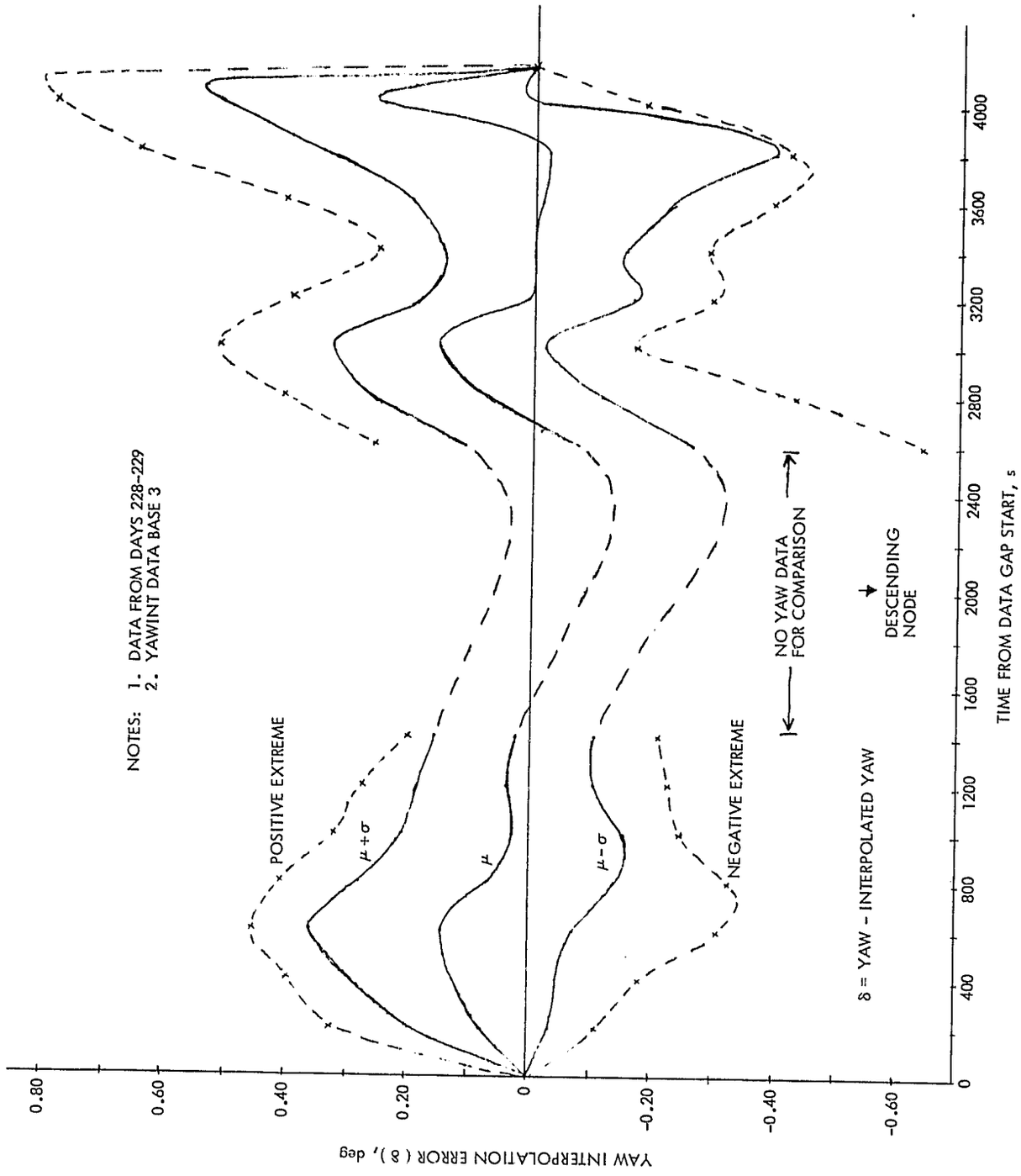

Figure 5-3. Yaw Interpolation Error Simulated for Day 234

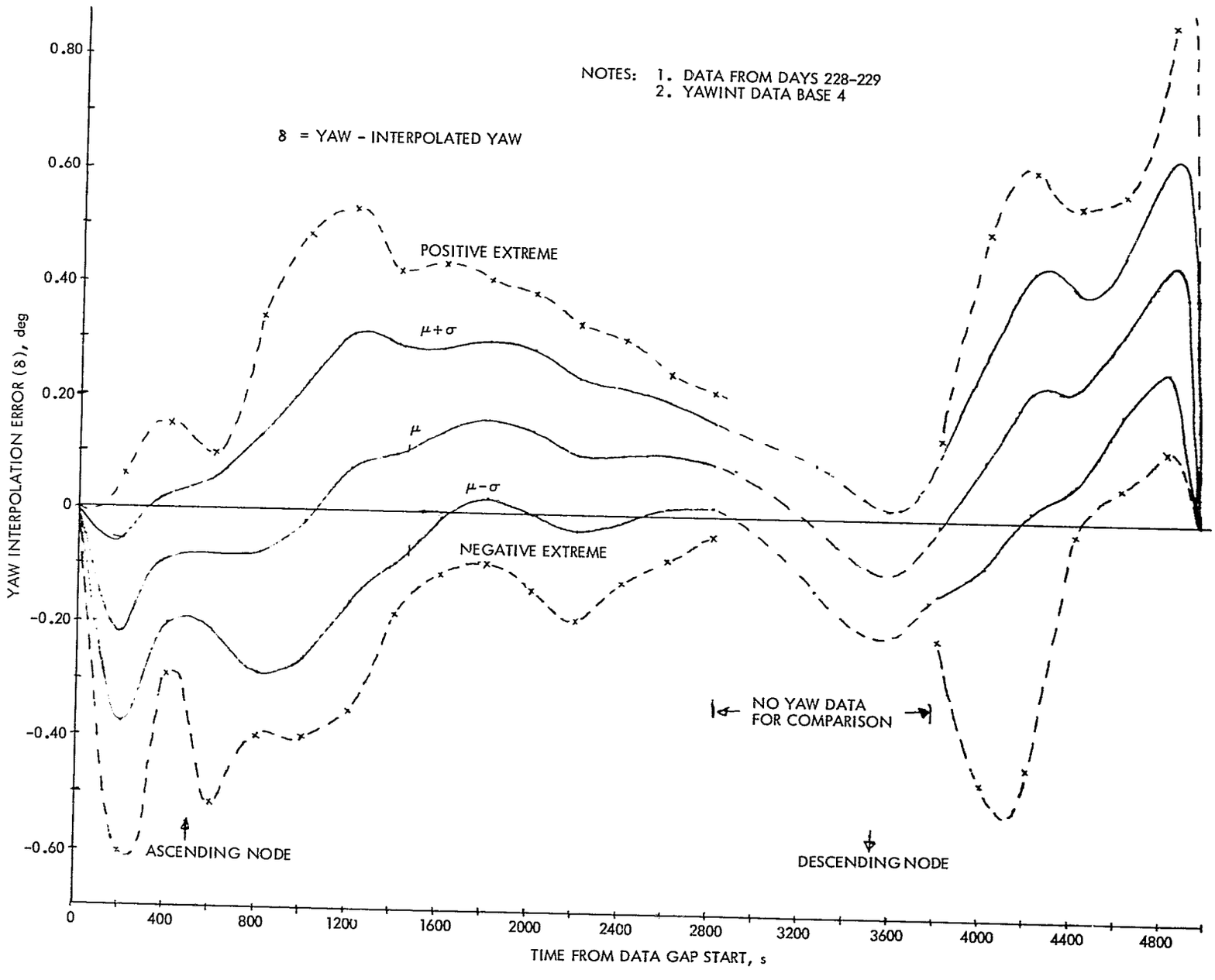

Figure 5-4. Yaw Interpolation Error Simulated for Days 242-255

In the later portion of the Mode 5 era, the only yaw behavior observable by the sun sensor was in the orbital phase disturbed by Mode 5. Comparison of available data from that time period with data from days 228-229 having the same phase relationship to Mode 5 start shows a decrease in interpolation performance from 1.84 deg to 2.06 deg (3 RMS). Following the rationale used for the quiescent period, this additional uncertainty can be attributed to another error source of value 0.94 deg (3 RMS). Combining this in an RMS sense with the 0.82-deg overall performance for days 228-229 leads to the estimate of 1.24 deg (3 RMS) for yaw interpolation performance outside the Mode 5 disturbance region.

2. Interpolation Error Distribution

The interpolation error of Figures 5-2 through 5-4 was analyzed to determine the relative frequency of various values of error. Figures 5-5 and 5-6 are the histograms resulting from this analysis, and incorporate 882 and 492 samples, respectively. The only truly significant difference between the two histograms is the mean shift due to Mode 5. The apparent deviations from the classical bell-shape are probably due to the small number of samples.

Figure 5-7 shows the distribution of RMS error with respect to orbital phase for the three simulated interpolation cases. As for the previous two figures, the scaling is correct only if true yaw behavior in the target (simulated) eras was identical to that in the reference eras. However, even if actual behavior is only similar to these simulations, it appears that RMS error is less in the orbital phase between $+72^{O}$N and descending node than in the rest of the revolution. This information could be used to give preference to data taken in this orbital phase, but was not used in the overall estimates (given in Subsection V-C-3) of yaw interpolation performance.

Figure 5-8 plots the cumulative distribution function of RMS interpolation error for four cases: (1) simulated second quiescent period, (2) simulated early Mode 5 period, (3) simulated late Mode 5 period, and (4) a Gaussian distribution. Each data set was normalized to its ensemble RMS value to help the comparison of distribution shapes. It is quite evident in Figure 5-8 that there is no significant difference between any of the functions and the normal distribution. The raggedness at high multiples of RMS is due to the paucity of samples. Therefore, RMS interpolation error can be understood as the standard deviation of a normal distribution, so that the ninety-ninth percentile is at 2.56 RMS, the fiftieth percentile is at 0.67 RMS, etc.

3. Yaw Interpolation Accuracy Versus Time

Figures 5-9 through 5-12 reflect all of the information in the preceding paragraphs, and they display yaw attitude determination accuracy as functions of orbital and mission phases. Figure 5-9 shows the early mission phases when the sun was continuously observable by sun sensor head 1. The variations in yaw AD accuracy are caused by the pattern of sun positions within the sun sensor FOV on the given day, but without regard to attitude deviations. Significant yaw excursions did occur previous to day 195 and after day 219; the former

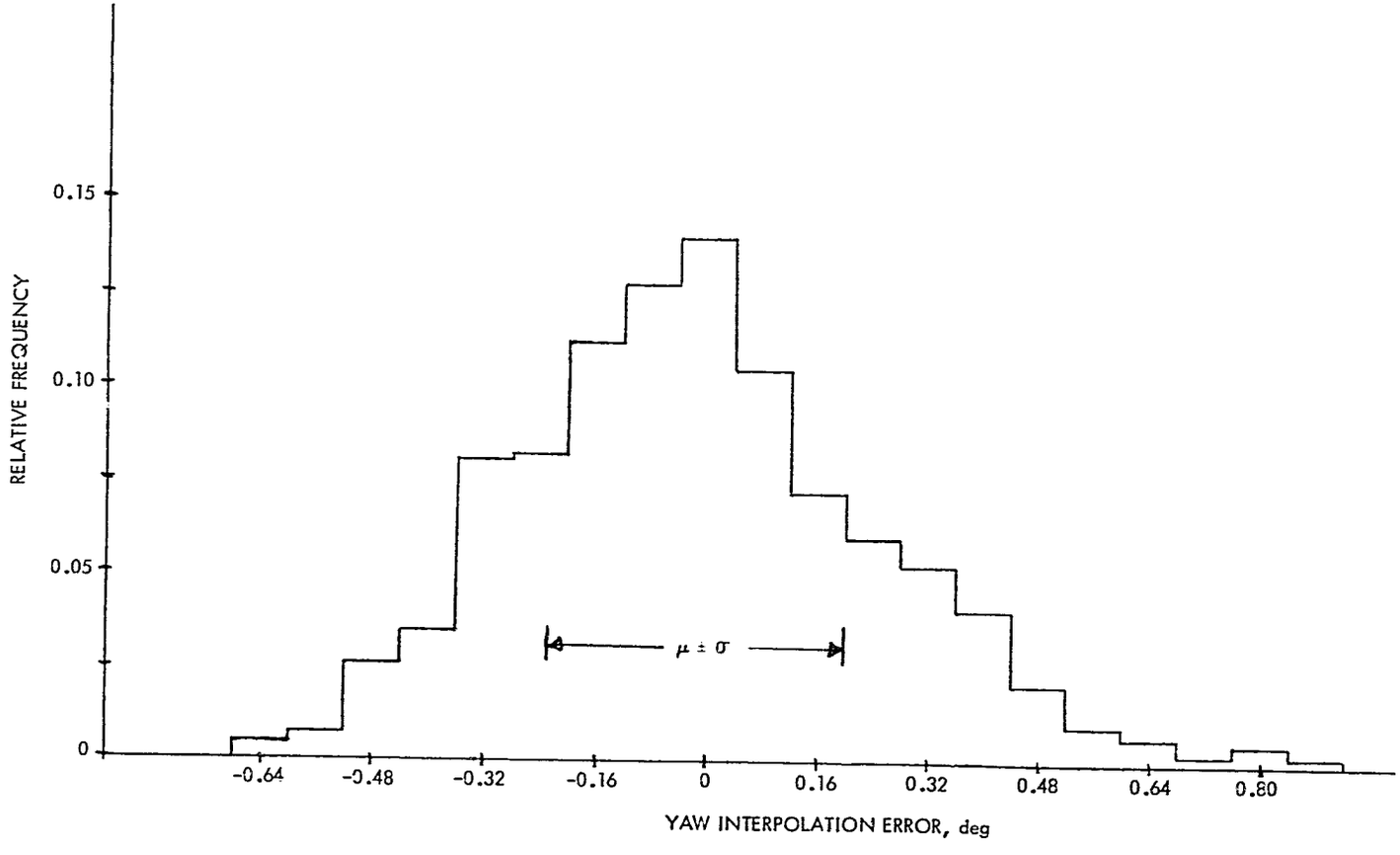

Figure 5-5. Histogram of Yaw Interpolation Error Simulated for Second Quiescent Period

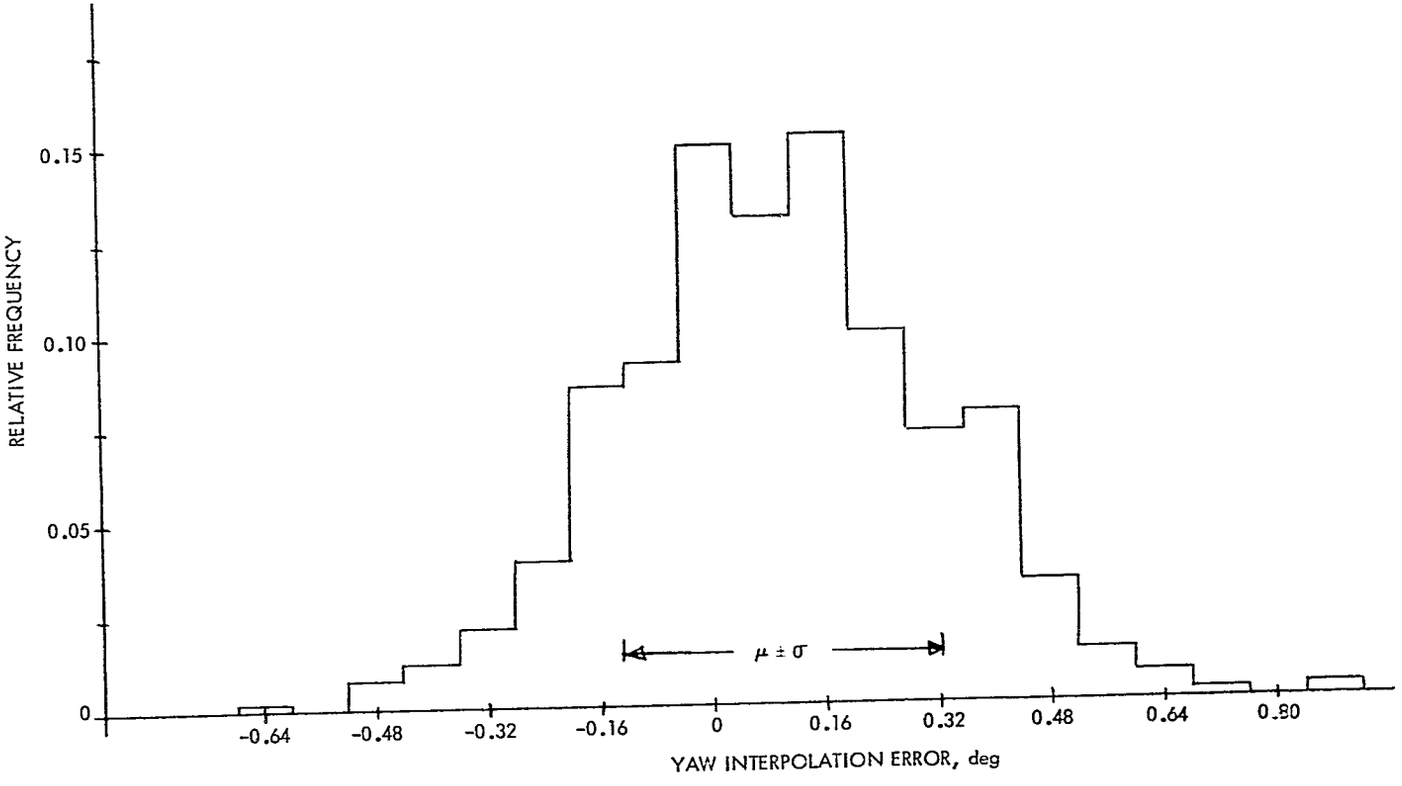

Figure 5-6. Histogram of Yaw Interpolation Error Simulated for Later Part of Mode 5 Period

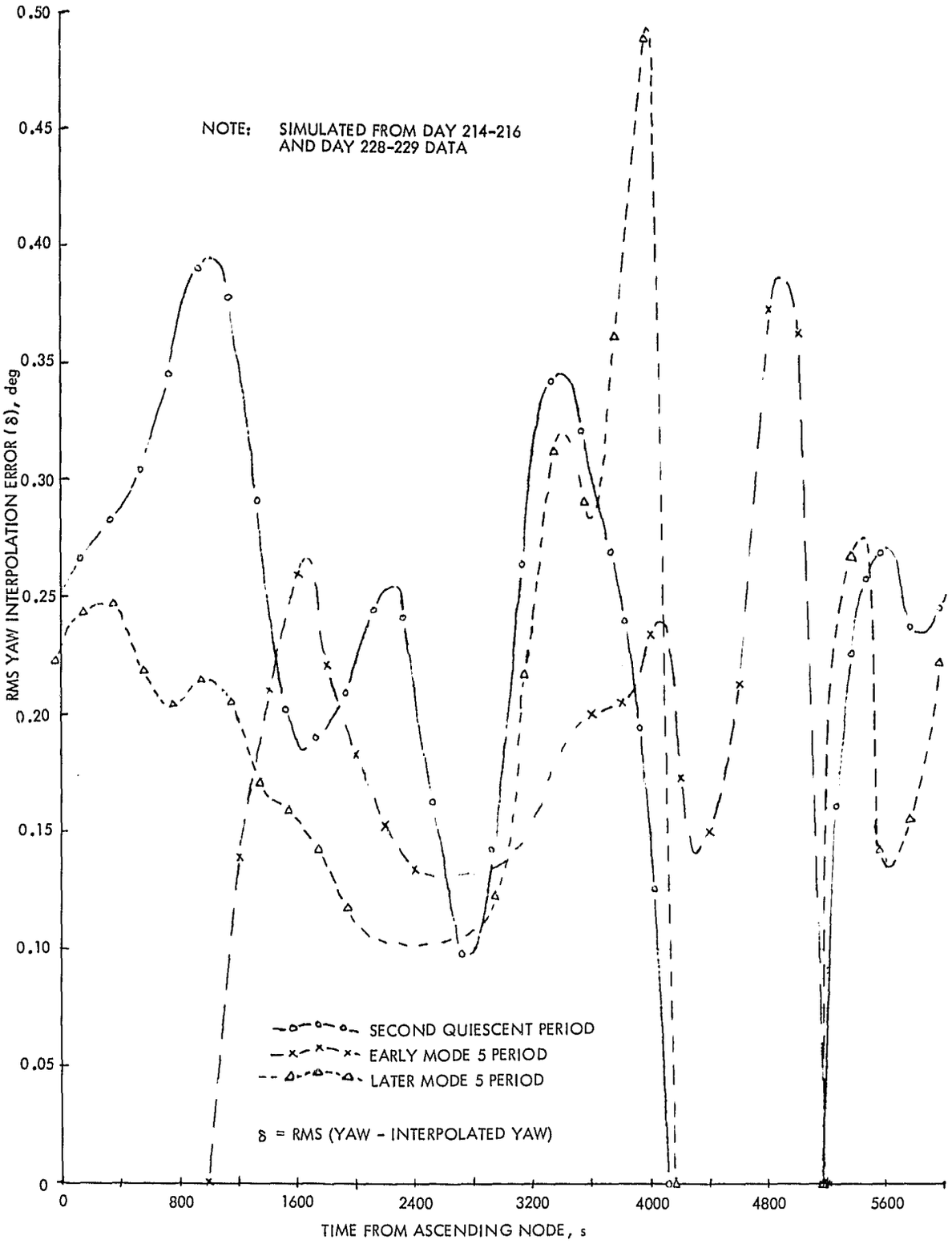

Figure 5-7. Yaw Interpolation RMS Error

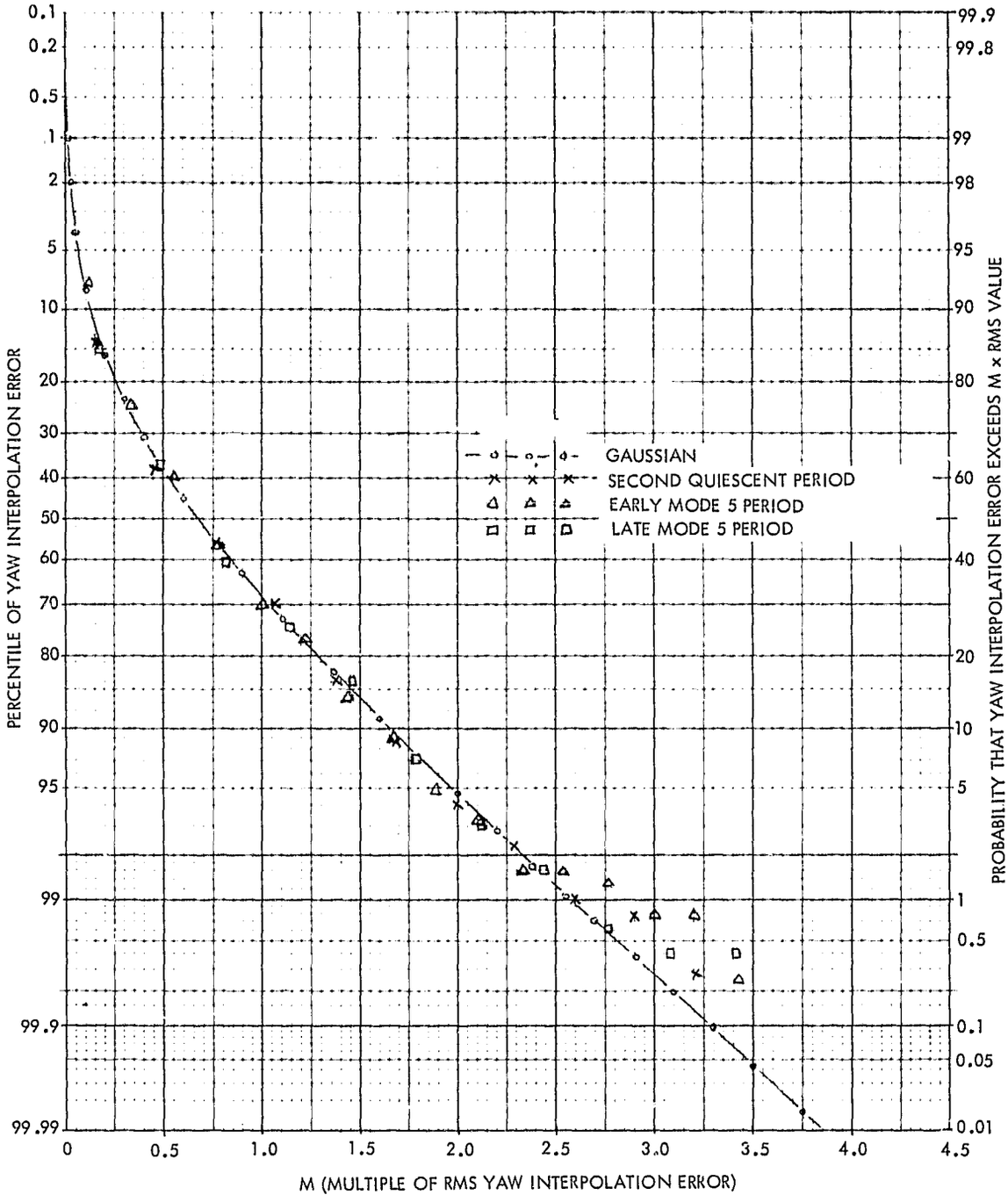

Figure 5-8. Significance of Yaw Interpolation Error RMS Value

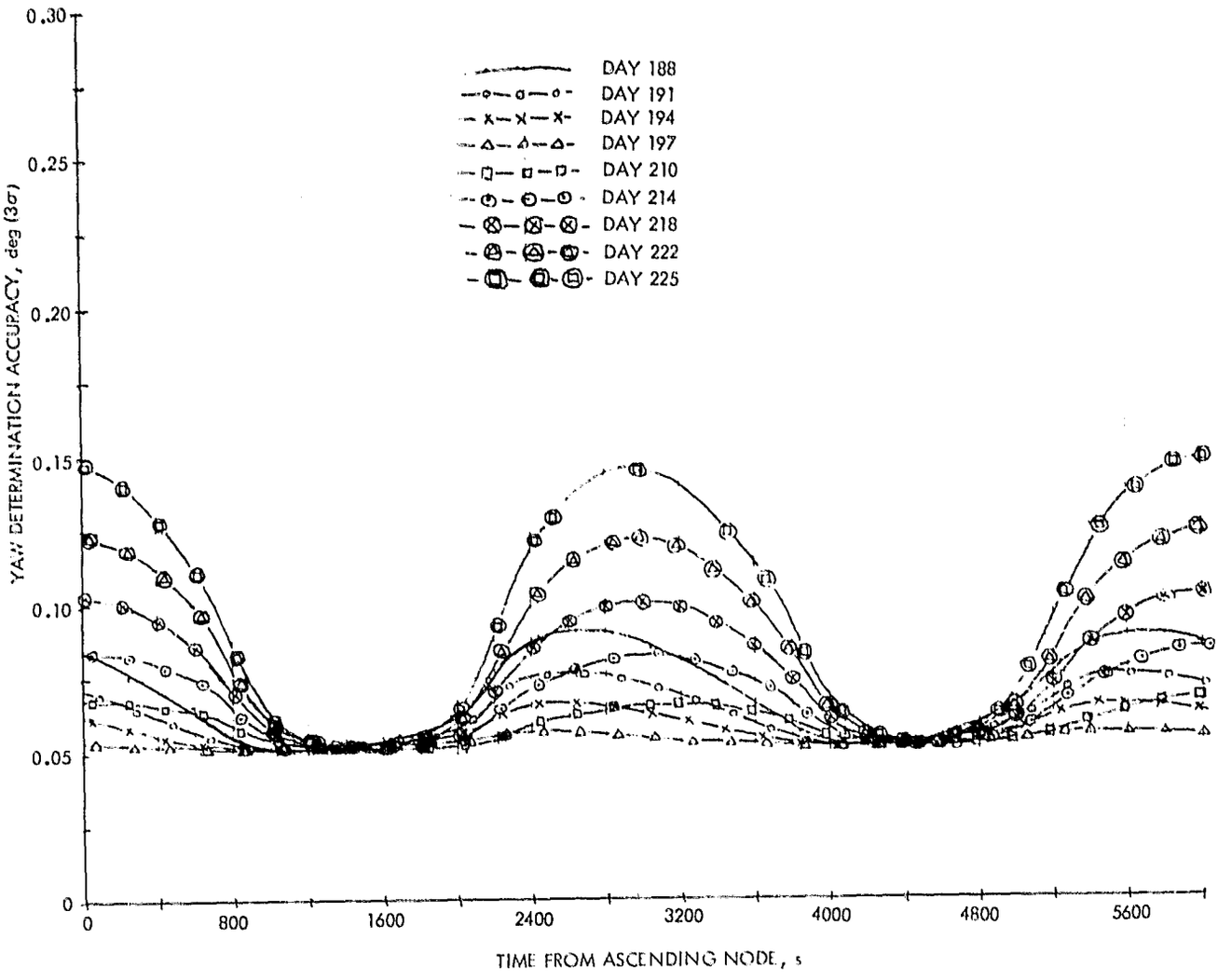

Figure 5-9. Yaw Determination Accuracy for Days 188-226

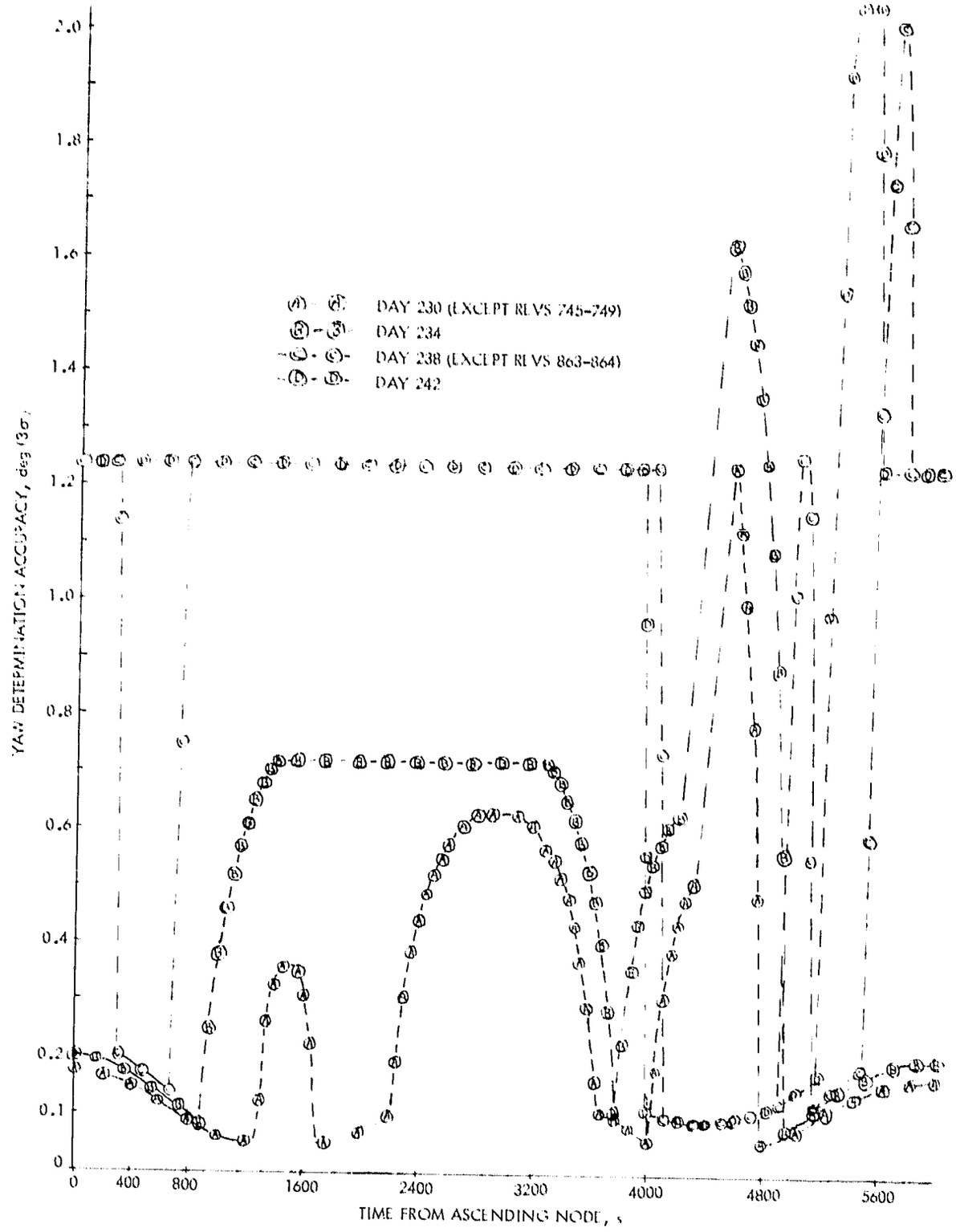

Figure 5-10. Yaw Determination Accuracy for Days 227-244

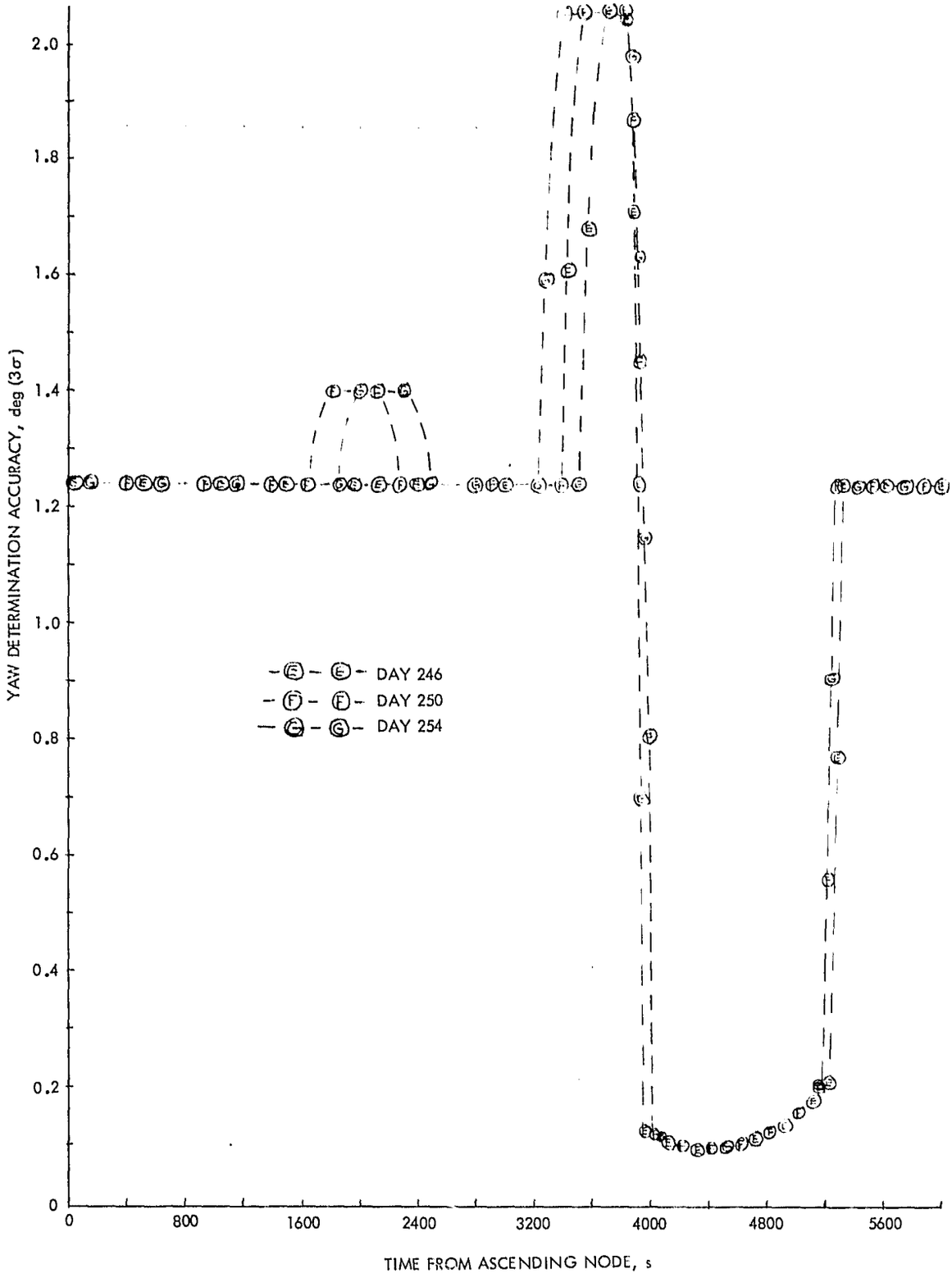

Figure 5-11. Yaw Determination Accuracy for Days 245-255

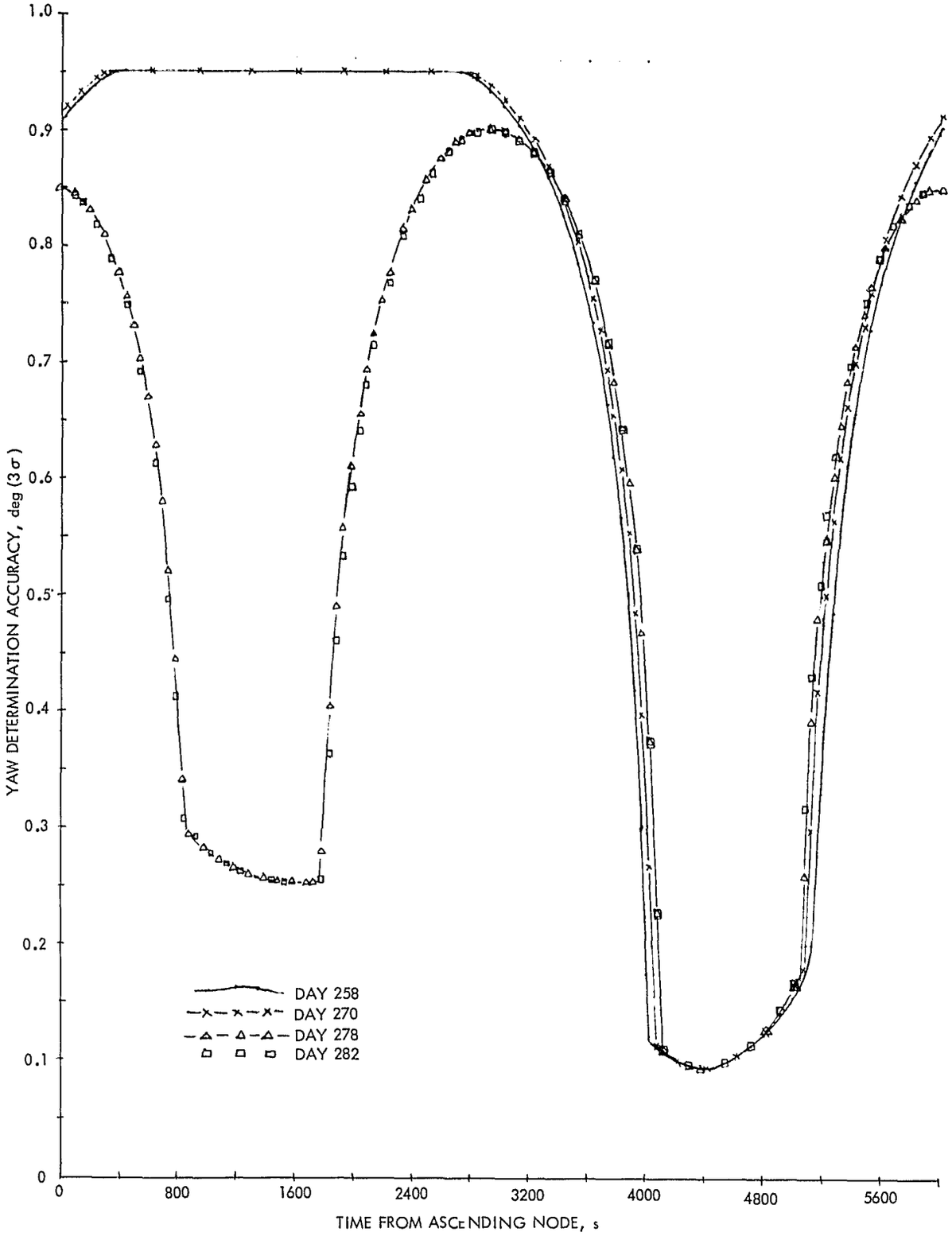

Figure 5-12. Yaw Determination Accuracy for Days 256-282

would cause no discernible change in Figure 5-9, but the latter would cause a shift forward in apparent mission phase of approximately a day for each positive degree of yaw. There were also some 15- to 20-min periods in several revolutions between days 220 and 225 when pitch and roll were seriously in error due to sun interference; the coupling of pitch and roll AD error into yaw could produce 1 to 1.5 deg of yaw AD error at those times. Allowance for these variations in accuracy would have to be done on a rev-by-rev basis, which is impractical in this report.

Figure 5-10 covers the mission period in which yaw data gaps began to appear and the transition to sun sensor head 2 occurred. The interpolation accuracy as a function of orbital phase was computed with the variance model described in Subsection II-B-3, using variance values inferred from Table 5-3. One variation from that model is the use of the Table 5-3 value for $\Delta\hat{Y}$ performance as the limiting variance value rather than the less conservative σ_{Y_0} computed by the model. Again, actual attitude deviations were not taken into account in this figure, so that the true pattern of accuracies can differ from that shown; however, Figure 5-10 is still a good guide to the accuracies available in this mission phase. These accuracies do not apply to those revolutions on days 227, 230, 235, and 238 when the RCS/gyro control mode was in force. Except for the half-rev transition (each way) between control modes, the yaw interpolation accuracy in the RCS/gyro mode was 0.7 deg (3 RMS).

Figure 5-11 shows the later portion of the Mode 5 mission period. All directly observed yaw data comes from sun sensor head 2. Accuracies were computed as described earlier for Figures 5-9 and 5-10, except that an additional uncertainty was inserted in the orbital phase during which Mode 5 was used in the northern hemisphere (see Subsection III-C-4).

Figure 5-12 covers the second quiescent period and includes the end of the mission. The scale is expanded by a factor of two compared to Figures 5-10 and 5-11 because of the smaller range of uncertainties to be expressed. Note that sun sensor head 3 produced data over the high northern latitudes during the last few days of the mission, starting around day 274.

SECTION VI

SUMMARY AND RECOMMENDATIONS*

A. SUMMARY

The first satellite built to observe the world's oceans, Seasat suddenly stopped sending data from orbit on 10 October 1978 after 105 days in space. In October, it was believed that a massive short circuit of the solar array rendered it unable to transmit or receive any signals. It was concluded finally that the loss of power was caused by a massive and progressive short in one of the slip ring assemblies. (The slip ring assemblies were used to connect the power system in the Agena with Seasat's rotating solar cell panels.)

Although the premature termination of the Seasat mission prevented observation of the change in sea conditions from season to season, a sufficient amount of flight data was obtained to evaluate the feasibility of the scientific aspects of the mission and to perform comprehensive post-launch attitude determination evaluations of the following: the Earth's horizon radiance model, cold cloud effects on IR data, the performance and the alignment accuracies of the attitude sensors and control system, and the capabilities of the Seasat attitude support software. Furthermore, the results of these analyses suggested the following recommendations for future mission support.

B. RECOMMENDATIONS

The following recommendations for attitude determination mission support hardware and software are derived from the Seasat mission support experience. The hardware recommendations deal primarily with the IR scanners and sun sensors, and some additional attitude sensing hardware is suggested. The software recommendations deal briefly with each aspect of the data processing to point out some of the handicaps in the operational support software. No comments are presented about the observed sun interference in the IR scanner.

1. IR Scanner Recommendations

The attitude determination error analysis demonstrated that the increased accuracy that was expected from the normalized threshold locator logic was nullified by the relatively broad band pass of the IR scanner optics. As a result of the broad band pass, atmospheric phenomena on the Earth's surface as low as 8 km (4.3 nm) altitude perturbed the threshold normalization voltage. The random errors thus introduced could not be modeled and exceeded the horizon radiance corrections being applied by the attitude determination software by a factor of 2. Although the normalized threshold system may have been necessary for attitude control stability (in that it reduced long-term fluctuations due to the seasonal/latitude-dependent radiance variations), a fixed threshold system,

*Based heavily on Section 5 of Reference 2-9.

assuming the same IR band pass, would have presented a more tractable problem for attitude determination. For the fixed threshold system, unmodeled cold cloud errors would have been greatly reduced and the errors in the model for the systematic radiance changes would have been no worse than those for the normalized threshold locator. Therefore, the attitude determination errors for the fixed threshold locator logic would have been smaller than those for the normalized threshold system.

The attitude error analysis completed 1 year before launch demonstrated that the 3σ error limits on attitude determination performance could not be met. The analysis was initiated and completed too late in the mission support to have any effect on the spacecraft flight hardware configuration. Although similar analysis performed by the spacecraft contractor much earlier in mission support had concluded that the error budget could be met, it is recommended here that such early analysis be performed by a third party or by the party responsible for attitude determination data processing.

2. Sun Sensor Recommendation

Given the problems that occurred with sunlight in the IR scanners and that resulted in control anomalies that reduced the effectiveness of the yaw interpolation algorithm, more comprehensive sun data coverage should have been provided. The six-sun sensor configuration proposed by GSFC before launch would have been invaluable for the determination of yaw, given the control problems that existed. Although sun sensor coverage near the zenith was discouraged because unfavorable geometry caused degraded accuracy, the addition of two or more sun sensors in this area would have provided increased sun data coverage near zenith, shorter sun data gaps, and a higher overall determination accuracy.

During the spacecraft design review, a request was made for information about the behavior of the sun sensors at the times when the sun traversed the edges of the FOVs. If this information had been communicated, significant problems in the data processing at these times could have been avoided. Software specifications to specifically eliminate or analytically correct anomalous data from the sensors, near and beyond the edges of the FOV, could have been implemented The obvious advantages would have been efficient and uninterrupted attitude data processing and possible extension, with some degraded accuracy, of the effective sun sensor FOV using the fine reticle telemetry data to angles as high as 60 deg from the boresight.

3. Yaw Interpolation Hardware Recommendations

Another alternative to the problem of yaw attitude determination and yaw interpolation involves the use of the yaw gyro as an attitude determination device. The yaw gyro was a critical instrument for yaw attitude control using hydrazine thrusters during orbit adjust maneuvers. For this reason, in addition to the fact that the gyro had a specified operating lifetime of no more than 30 days of continuous operation, the use of the gyro data in the attitude determination

system was negated. However, given the problems with yaw interpolation caused by the sun-interference-induced control anomalies, periodic use of the gyro data would have been invaluable for testing the yaw interpolation parameters and for evaluation of the interpolation absolute accuracy. In the pre-launch phase, during the attitude software specification process, some consideration was given to include the gyro telemetry data in the attitude telemetry record, but this data was excluded from the record because of space limitations on the input disk data set, and because there was low probability that the gyro would be available for this purpose. Magnetometer data, however, were included, even though the relative accuracy of this data, limited primarily by the resolution of the telemetry word, was known to be insufficient for mission support.

It is, therefore, concluded that during early mission support, a method of checking the yaw interpolation parameters at all phases of the mission should have been considered. A schedule of weekly or twice-weekly one-orbit runs with the yaw gyro "on," during low sun data coverage, could have been a nominal mission support procedure. A second backup yaw gyro package may have been required for this support, and, in the event that control anomalies had occurred, more frequent use of the gyro could have been justified.

4. Magnetometer Recommendations

Following the discovery that the yaw interpolation accuracy was being significantly degraded by the spacecraft control anomalies, magnetometer data was considered as a possible source of more accurate yaw attitude information. However, the following problems were encountered:

(1) The resolution of the telemetry word (4.4 milligauss) was insufficient and restrictive for accurate yaw attitude, particularly at the high latitudes when the horizontal field was low.

(2) The magnetometer triad was ground-calibrated against the sun data, on the full sun orbits, using a least-squares method, and unusually large biases were discovered along with evidence for sizable misalignment, crosstalk, or nonorthogonality of the triad.

It is, therefore, concluded that the telemetry word size for the magnetometer data could have been increased to be comparable to the noise in the magnetometers. A method of electronically nulling the biases on each axis of the magnetometer could have assisted the control system in dumping angular momentum. More accurate pre-launch calibration data from the manufacturer, or pre-launch calibration of the device once mounted on the spacecraft, would have been desirable.

5. Software Recommendations

Operationally, the Seasat Attitude Determination System (ADS) performed well after it was corrected for software errors and operational inconvenience. The Seasat ADS was composed of the following four subsystems: (1) Telemetry Processor (TP), (2) Definitive Attitude Determination System (DADS), (3) Log Interrogation and Data Management Utility (LIDM), and (4) Yaw Interpolation Utility (YAWINT).

The software was specified to be modular, with separate load modules for each major data operation. In view of the Seasat experience, this remains a recommended design feature if the number of subsystems required for daily mission support is small. Seasat operations personnel were able to learn the four subsystems required for attitude support, and analysis personnel were able to write detailed operations methods for four subsystems without difficulty.

The DADS could have been used only to apply corrections for biases, oblateness, and horizon altitudes. If no smoothing option had been applied to the data in the DADS subsystem and ephemeris-related operations could have been performed only at the output period, a considerable increase in the speed and volume of data processed in a single pass through the DADS could have been realized. Alternatively the array sizes required for data processing could have been reduced, possibly resulting in a maximum core requirement of 400K bytes for 30 min of data.

YAWINT, which performed yaw interpolation, could have been expanded into an output data smoother, incorporating whatever smoothing and interpolation method was necessary for all three functions (pitch, roll, and yaw). Methods such as Chebyshev fitting or spline fitting procedures to smooth the data and bridge the gaps in pitch and roll could have been specified as options. However, after viewing the repetitious pitch and roll functions from orbit to orbit throughout a given day, it became apparent that another method would have worked well; the average pitch and roll versus mean anomaly, for a given day's data, could have reliably bridged gaps of up to one orbit in length.

Computations for the log (such as minimum and maximum values) could also have performed by this subsystem. The logging functions specified for Seasat were extensive and comprehensive in their goals. During the early post-launch phase, no daily routine was established for data processing mission support, and because of excessive problems with the overall mission, analytical and software personnel were unable to monitor and quality assure the logging aspects of data processing. Therefore, the log was neglected and never met (nor was required to meet) the expectations of the specification. If the mission had continued, with time allocated for log functions maintenance in all subsystems, the log would have been invaluable in monitoring and perfecting the data processing procedures. However, for this mission, as for most missions in the early orbit phase, only a printed page of statistics for each day processed is necessary for the log. If this option had been available and no operational interface between the log and the operator would have been necessary, early mission procedures could have been simplified, Version 1 of the Seasat software could have been less complicated, and acceptance testing could have been simplified. Also, mission support programmers working on a later version of the software (scheduled for completion 3 to 6 months after launch) would have been ready and available to assist with software-related processing problems.

Further specific ground software recommendations are provided by GSFC in Section 5 of the Reference 2-9.

REFERENCES

2-1. Havens, W. F., and Ohtakay, H., "Attitude Determination System for a Nadir-Pointing Satellite," Journal of Guidance and Control, Vol. 1, No. 5, September-October 1978, pp. 352-358.

2-2. Nutt, W. T., Phenneger, M. C., Lerner, G. M., et al., "Seasat-A Attitude Analysis and Support Plan," GSFC Document X-581-78-9, April 1978.

2-3. Beach, S. W., Machnick, J., Radtke, D. D., et al., "Attitude Pointing Performance of the Seasat-A Orbital Attitude Control System - 5th Interim Report," LMSC Document GCS/3923/6211, 15 November 1976, pp. 5-8.

2-4. Ibid, pp. 8-10.

2-5. Markiewicz, B. R., "Revision of Attitude Sensor LMSC Optical Alignment Data," IOM 343-78-350, 28 March 1978 (JPL internal document).

2-6. Phenneger, M. C., Manders, C., et al., "Infrared Horizon Scanner Attitude Data Error Analysis for Seasat-A," Computer Sciences Corporation Document CSC/TM-77/6064, 28 July 1977.

2-7. Keithly, P. L., and Uplinger, W. G., "Effect of Clouds on Seasat-A Horizon Sensor," LMSC Document GCS/4001/6211, 13 July 1977.

2-8. Hotovy, S. G., "Evaluation of an Infrared Horizon Scanner Bias Determination Algorithm for Seasat-A," Computer Sciences Corporation Document CSC/TM-77/6130, 12 July 1977.

2-9. Manders, C. F., et al., "Seasat-1 Postlaunch Attitude Analysis," Computer Sciences Corporation Document CSC/TR-79/6008 (prepared for GSFC), June 1979.

2-10. Treder, A. J., "A Hybrid Technique for Spacecraft Attitude Interpolation with Arbitrary Attitude Data Gaps," Modeling and Simulation, Vol. 8, Proceedings of the 7th Annual Pittsburgh Conference, 21 April 1977, pp. 209-217.

3-1. Simcox, D. G., and Beach, S. W., "Summary of Seasat-A Flight Anomalies," LMSC Report GSC/4187/6211, 11 July 1978.

3-2. Machnick, J., and Beach, S. W., "Summary of Seasat-A Flight Anomalies (Second Occurrence)," LMSC Report GCS/4202/6211, 22 September 1978.

3-3. Treder, A. J., "Analysis of Attitude Determination Errors Due to the Sun Sensor System on Seasat-A," IOM 343-78-156, 9 February 1978 (JPL internal document).

3-4. Treder, A. J., "Approximate Conversion from Orbital Geocentric to Orbital Geodetic Coordinates," EM 343-414, 11 July 1979 (JPL internal document).

3-5. Bauer, T. A., "Seasat-A Mission Summary," IOM 312/78.8-123, 13 November 1978 (JPL internal document).

4-1. Gliebe, R. L., et al., "Solar Torque Update Analysis for Seasat-A," LMSC Report GCS/4039/6211, 30 September 1977.

4-2. Beach, S. W., and Simcox, D. G., "Linear Analysis of the Seasat Orbital Attitude Control System," LMSC Report GCS/3874/6211, 30 July 1976.

5-1. Treder, A. J., "Updated Summary of Seasat-A Attitude Determination System Performance Accuracy," IOM 343-78-098, 26 January 1978 (JPL internal document).

5-2. Treder, A. J., "Seasat-A Attitude Determination for Days 190-227," IOM 343-78-872, 8 August 1978 (JPL internal document).

APPENDIX

ABBREVIATIONS AND ACRONYMS

AD	Attitude Determination
ADS	Attitude Determination System
AOT	Attitude Orbit Tracking (Tape)
CLA	Control Logic Assembly
DAD	Definitive Attitude Determination
DADS	Definitive Attitude Determination System
DAF	Definitive Attitude File
DOF	Definitive Orbit File; Degrees of Freedom
EOM	End of Mission
FOV	Field of View
GSFC	Goddard Space Flight Center
IPD	Information Processing Division (GSFC)
IR	Infrared
JPL	Jet Propulsion Laboratory
LIDM	Log Interrogation and Data Management Utility
LMSC	Lockheed Missile and Space Company, Inc., Sunnyvale, CA
OACS	Orbital Attitude Control System
PDPS	Project Data Processing System
QA	Quality Assurance
RCS	Reaction Control System (LMSC)
RMS	Root-Mean-Square
RSS	Root-Sum-Square

SAR	Synthetic Aperture Radar
SARA	Satellite Alignment Reference Axes
SASS	Seasat Scatterometer System
SSM	Sensor Support Module
TMDF	Telemetry Master Data File
TP	Telemetry Processor
w.r.t.	with reference to
YAWINT	Yaw Interpolation Utility

NASA—JPL—Comi . L A . Calif